Advances in Acoustics and Vibration

Advances in Acoustic Sensing, Imaging, and Signal Processing

Guest Editors: Jafar Saniie, Mario Kupnik, and Erdal Oruklu

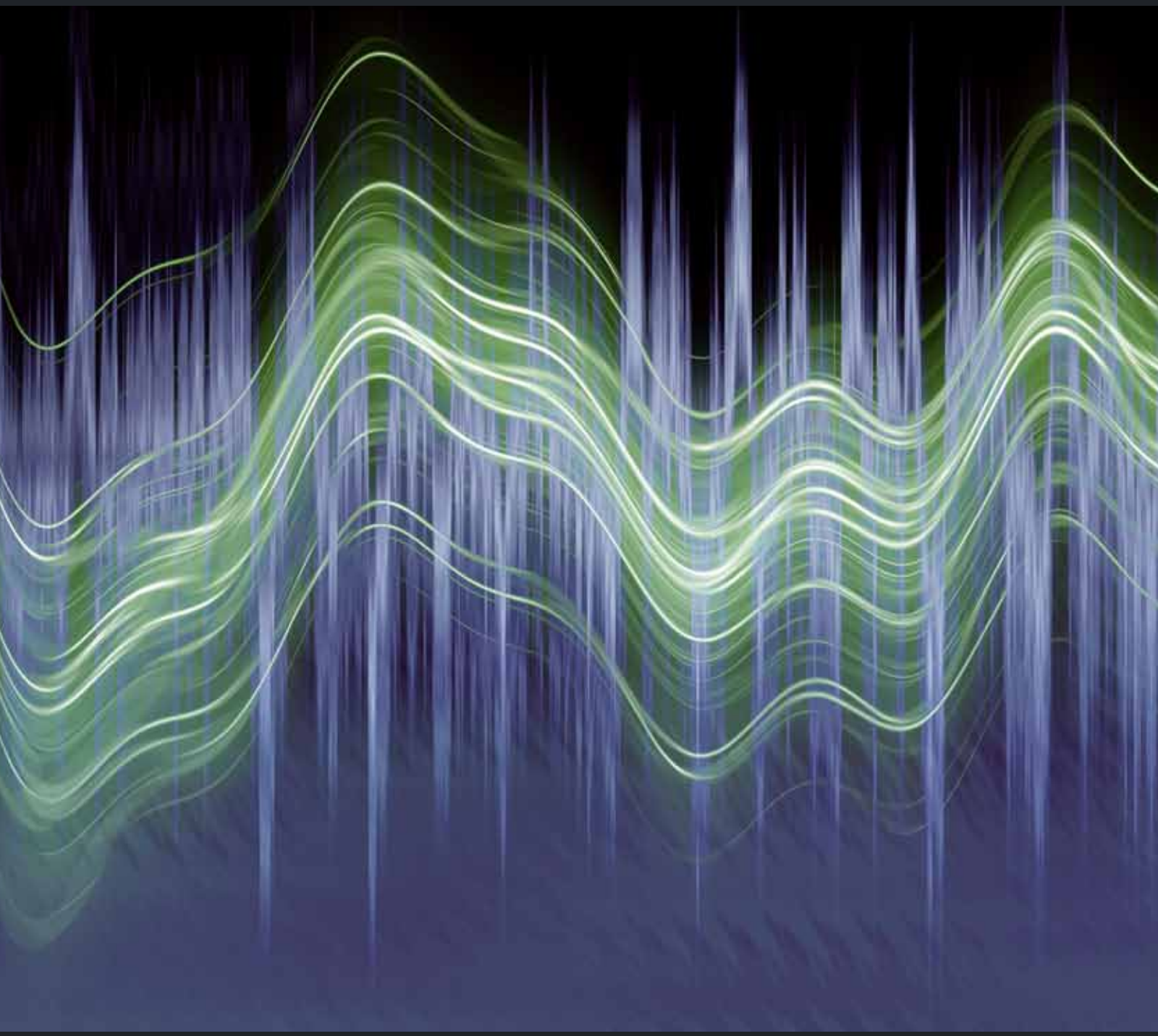

Advances in Acoustic Sensing, Imaging, and Signal Processing

Advances in Acoustics and Vibration

Advances in Acoustic Sensing, Imaging, and Signal Processing

Guest Editors: Jafar Saniie, Mario Kupnik, and Erdal Oruklu

Editorial Board

Contents

Hindawi Publishing Corporation
Advances in Acoustics and Vibration
Volume 2012, Article ID 901547, 2 pages
doi:10.1155/2012/901547

Editorial

Advances in Acoustic Sensing, Imaging, and Signal Processing

Jafar Saniie,[1] Mario Kupnik,[2] and Erdal Oruklu[1]

[1] *Department of Electrical and Computer Engineering, Illinois Institute of Technology, Chicago, IL 60616, USA*
[2] *Department of Electrical Engineering, Brandenburg University of Technology Cottbus, 03046 Cottbus, Germany*

Correspondence should be addressed to Jafar Saniie, sansonic@ece.iit.edu

Received 5 July 2012; Accepted 5 July 2012

The objective of this special issue is to address recent research trends and developments in the generation, acquisition, and processing of acoustic signals for industrial and medical applications. A substantial number of papers were submitted, and after a thorough peer review process, nine papers were selected to be included in this special issue. These papers cover important applications in acoustic sensing, including nondestructive testing of materials, enhanced ultrasonic imaging, underwater acoustic modeling, source mapping and communications. We believe that the original papers collected in this special issue highlight the contemporary topics in research related to acoustic sensing and imaging applications and will introduce readers to the latest advances in the field.

The paper by P. Etter presents a comprehensive review of contemporary underwater acoustic modeling methods. These advanced modeling techniques include forward and inverse applications, integrated-modeling approaches, non-intrusive measurements, and novel processing methods dealing with the changing ocean soundscape due to anthropogenic activity and natural factors.

The paper by P.-P. J. Beaujean and M. D. Staska, presents a computationally efficient underwater acoustic propagation model in a three dimensional rectangular duct closed at one end. The three-dimensional model presented in this paper provides a sufficient level of accuracy to be used in the simulation of an acoustic communication system operating between 15 kHz and 33 kHz, with the benefit of low computing requirements.

The paper by E. Sarradj analyzes the beamforming steering vector formulations for three-dimensional acoustic source mapping. In particular, four different steering vector formulations from the literature are examined, and their theoretical backgrounds are discussed. It is shown that no formulation produces both correct acoustic source location and correct estimates of their strength. This paper identifies the two formulations that yield the correct estimation of the source location at the cost of an insignificant error in the estimated source strength.

The paper by J. Sandhu et al. reports on the application of acoustography using acoustooptical sensors for mapping ultrasonic fields radiated from ultrasonic transducers. This study is critical to assess the radiated ultrasonic field characteristics, which can be affected by many factors, such as piezoelectric material inhomogeneity, lack of bonding, electrode design and contact placement, acoustic lens quality, and wear plate uniformity and adhesion.

The paper by C. Quinsac et al., first introduces the theory of compressive sampling, which has been shown to reduce data below the Shannon-Nyquist limit. Next, the authors present different methods to perform compressive sampling in the context of ultrasound imaging with encouraging results in 2D and 3D ultrasound images.

The paper by Y. Zhang et al., discusses ultrasonic flaw imaging via multipath exploitation. In the proposed approach, by identifying multipaths that reflect at the known top and bottom surfaces, virtual sensors can be identified. The locations of these sensors permit visualizations of the shadowed regions, which otherwise are difficult to obtain from only direct reflection signals. The proposed multipath exploitation is supported by analysis and verified by experimental data.

The paper by J. S. Ullom et al. presents a new speckle reduction method for improving the contrast-to-noise ratio in ultrasonic B-mode images. The proposed method is based on resolution enhancement compression and a frequency

compounding technique but it is enhanced to achieve higher axial resolution. Simulations and experimental measurements suggest that the proposed method can realize substantial improvements in terms of image visibility and enhance the boundaries between the target and the background.

The paper by Y. Lu et al. introduces a chirplet signal decomposition algorithm, based on fractional Fourier transform in order to analyze ultrasonic signals for NDE applications. Case studies and experimental results show that the proposed algorithm not only reconstructs the ultrasonic signal successfully, but also characterizes ultrasonic echoes and estimates echo parameters accurately.

The paper by R. Demirli et al., introduces a subspace-based approach for suppressing unwanted reverberations, enabling proper flaw detection and imaging. Two different cases are considered for the application of the proposed technique. The first case uses a set of flaw-free reference measurements of reverberation, whereas the second case is based on array measurements that contain flaws. For the first case, the clutter can be significantly removed with a negligible effect on the flaw echoes. In the second case that applies to ultrasound NDE imaging, it is demonstrated that the clutter can be mitigated by utilizing the array measurements without employing any reference data.

Acknowledgment

We would like to thank all the authors who contributed to this special issue. This publication would not be possible without the participation of our expert reviewers, who provided vital constructive feedback and criticism throughout the review process.

Jafar Saniie
Mario Kupnik
Erdal Oruklu

Hindawi Publishing Corporation
Advances in Acoustics and Vibration
Volume 2012, Article ID 874081, 12 pages
doi:10.1155/2012/874081

Research Article

Ultrasonic Flaw Imaging via Multipath Exploitation

Yimin D. Zhang,[1] Xizhong Shen,[2] Ramazan Demirli,[1] and Moeness G. Amin[1]

[1] *Center for Advanced Communications, Villanova University, Villanova, PA 19085, USA*
[2] *Electrical and Automatic School, Shanghai Institute of Technology, Shanghai 201418, China*

Correspondence should be addressed to Ramazan Demirli, ramazan.demirli@villanova.edu

Received 15 December 2011; Accepted 28 April 2012

Academic Editor: Erdal Oruklu

We consider ultrasonic imaging for the visualization of flaws in a material. Ultrasonic imaging is a powerful nondestructive testing (NDT) tool which assesses material conditions via the detection, localization, and classification of flaws inside a structure. We utilize reflections of ultrasonic signals which occur when encountering different media and interior boundaries. These reflections can be cast as direct paths to the target corresponding to the virtual sensors appearing on the top and bottom side of the target. Some of these virtual sensors constitute a virtual aperture, whereas in others, the aperture changes with the transmitter position. Exploitations of multipath extended virtual array apertures provide enhanced imaging capability beyond the limitation of traditional multisensor approaches. The waveforms observed at the physical as well as the virtual sensors yield additional measurements corresponding to different aspect angles, thus allowing proper multiview imaging of flaws. We derive the wideband point spread functions for dominant multipaths and show that fusion of physical and virtual sensor data improves the flaw perimeter detection and localization performance. The effectiveness of the proposed multipath exploitation approach is demonstrated using real data.

1. Introduction

Ultrasonic nondestructive evaluation (NDE) has traditionally used single-element sensors for material testing. Most flaw detectors utilize A-scan measurements obtained with monolithic transducers externally placed at different positions on or close to the surface of the material. The synthesized ultrasound array aperture, generated through scanning, provides a series of A-scan data whose intensity profile is used to generate a B-scan cross-section image. Two-dimensional (2D) sensor scanning (e.g., raster scan) over the material generates a collection of B-scan images to obtain a C-scan volume image. These 1D and 2D scanning processes require dedicated hardware to control precise sensor positioning and synchronized data collection. This scanning and imaging process has been typically conducted in laboratory conditions or in industrial material testing facilities using immersion testing techniques. We note, however, that this imaging process is not practical for field testing conditions.

Sensor arrays are more practical for field testing due to their increased coverage area, rapid data collection, and direct imaging capability. Although sensor arrays and beamforming techniques have been used in medical ultrasound for decades [1], their use in ultrasonic NDE has not begun until early 2000s [2]. Recent advances in transducer array manufacturing technology have permitted the use of sensor arrays in ultrasonic NDE, and have enabled significant improvements in the detection, localization, and classification of flaws inside a structure. These advances find wide applications in civil engineering and aerospace, automotive, and other transportation sectors [3, 4]. For example, a total focusing technique utilizes all the transmit and receive data in a 2D array to generate an image of material under consideration [5]. More recently multimode total focusing method is used to combine various wave propagation modes in imaging [6]. With the increased computational power and memory, it is expected that a large amount of data obtained with sensor arrays can be processed in a relatively short and acceptable time. Furthermore, offline processing of large volume data is tolerated in ultrasonic NDE due to the fact that the material structures generally do not change over the course of testing.

The existence of a flaw inside a limited size alloy gives rise to ghosts, which are false targets that appear due to the interreflections of the transmitted signals from the alloy boundaries and the target. Due to the prolonged distance travelled by these multipaths, the ghosts typically position outside the alloy boundaries. However, the ghosts that are located inside the alloy, if not properly identified, can cause clutter and false positives which could make visualization difficult, especially in the presence of multiple flaws. The ghosts may not only appear at positions different from the target location, but also present themselves with different image characteristics. This is attributed to the fact that reflections of ultrasonic signals which occur when encountering different media and interior discontinuities can be cast as direct paths to the target corresponding to the virtual sensors appearing on the top and bottom sides of the target. Some of these virtual sensors constitute a virtual aperture, whereas for others, the aperture changes with the transmitter position. The waveforms observed at the physical as well as the virtual sensors yield additional measurements corresponding to different aspect angles, thus allowing proper multi-view imaging of flaws. Each view has a different point spread function (PSF) and defocuses the target image depending on the location and angle of the respective virtual sensors.

In this paper, we consider multipath exploitations for ultrasonic imaging for the visualization of flaws in a material. In particular, our focus is the knowledge-based approach in which the alloy boundaries are assumed known and the adopted propagation model accurately represents the propagation and scattering phenomena inside the material. While multipath has traditionally been considered as troublesome in radar and wireless communications, significant efforts have been recently made to take advantage of multipath propagation. In wireless communications, diversity gains are obtained by various schemes, including multiple-input multiple-output (MIMO) and opportunistic communications (e.g., [7, 8]). In radar systems, the concept of multipath exploitation radar (MER) is being developed to increase persistent coverage over a large urban terrain. This is achieved by extending the tracking capabilities of existing radar sensor architectures beyond line-of-sight (LOS) using both multipath energy and knowledge of the urban scattering surfaces [9]. Some important results have been reported for urban non-LOS applications, indoor imaging, and other radar applications [10–12]. Multipath exploitation is also reported in acoustic focusing [13] and ultrasonic imaging [6]. Time reversal processing technique is also applied for target detection in a multipath propagation environment [14].

In the underlying ultrasound imaging applications, multipaths, when properly utilized, lead to (1) enlarging the array aperture for image enhancement using both physical and virtual sensors, (2) extension of angle of view of the narrow beamwidth of the ultrasound transducers, allowing improved visibility and array design flexibility, (3) multi-view observations of the flaw leading to better representations and characteristics of flaw volume and perimeter. It is noted that ultrasonic signals experience difficulty in penetrating a flaw, thus the aspect angle of the observation is limited unless access to other sides is available.

In this paper, multipath effects are examined using an aluminum alloy with artificial flaws. Different multipath realizations are considered and their virtual array geometries are identified. For each array geometry, the corresponding point spread function is developed and examined. In essence, exploitation of multipath information in ultrasonic imaging amounts to utilizing the different characteristics of the PSFs and fusing their collective viewing angles of the same target. We show that fusion of physical sensor data and virtual sensor data, due to multipaths, significantly improves flaw detection and characterization. The effectiveness of the proposed multipath exploitation approach is demonstrated through experimental examples.

The rest of the paper is organized as follows. Next section presents multipath propagation in materials with known cubic geometry. Section 3 describes ultrasonic imaging with multipath signals. Section 4 presents point spread function analyses of multipath signals. Section 5 discusses the multipath identification and association method. Section 6 presents experimental examples of multipath imaging. Section 7 concludes the paper.

2. Multipath Propagation Phenomenon

Ultrasound plane waves are subject to reflection and transmission from the boundaries of materials [15]. The propagation model for a beam of plane waves incident normally at a flat boundary is well known; part of the energy is transmitted to the support medium whereas the other part reflects back depending on the impedances of the medium and material. Normally incident propagation creates strong multipath (reverberation) in layered media. This propagation model has been extensively studied and exploited for nondestructive evaluation of layered materials (see e.g., [16]). The propagation model for a beam of plane waves obliquely incident to the medium boundary obeys the Snell's law. Assuming the impedance of the support layer (such as air) is much higher than the material, the majority of the incident energy reflects as longitudinal waves with the reflection angle equal to the incident angle, while a smaller portion of its energy is converted to shear waves. Shear waves reflect with a smaller angle and a lower speed than those of the reflected plane waves. In this paper, we consider longitudinal waves with specular reflections where the incident and reflected waves are coplanar with equal incident and reflected angles. As such, ray tracing models are utilized to predict the multipath signals.

While ultrasound wave reflections from material boundaries are explained with the Snell's law, the ultrasound scattering from material defects is more complex depending on the geometry and size of the object. An object whose size is comparable to the wavelength of the incident ultrasound wave is considered as a point reflector. Objects whose sizes are larger than the wavelength yield specular reflections. However, if the large object has sharp discontinuities or corners, wave diffraction phenomenon occurs at its extremities [15]. For example, an analytical diffraction model is

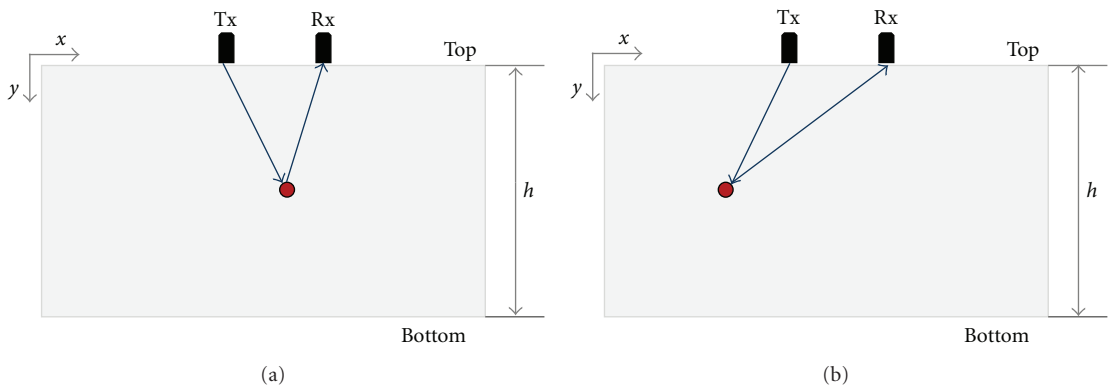

Figure 1: Direct paths when the target is between the transmit/receive pair (a) and outside of the pair (b).

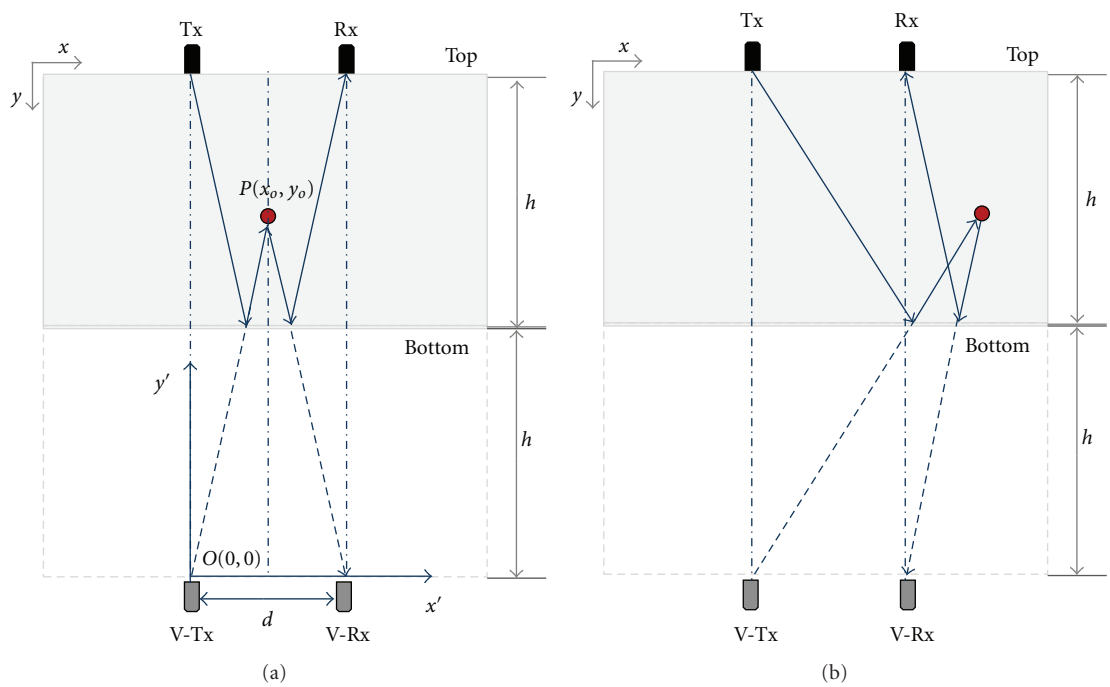

Figure 2: Multipath I when the target is between the transmit/receive pair (a) and outside of the pair (b).

developed for a penny-shaped crack in solids and verified experimentally by embedding a large penny-size crack in titanium [17]. In fact, there is a line of time-of-flight diffraction (TOFD) techniques used for flaw sizing based on estimating the time-difference-of-arrival of diffracted echoes from object boundaries [15]. Diffraction echoes are measured in a pitch-catch mode by positioning a pair of angle probes (transmitting and receiving transducers) far enough on the material's surface to see the extent of the crack. As such, measurements of diffraction echoes require angled and wide-beam ultrasound radiation and adjustment of the position of probes during acquisition. In this paper, we utilize direct and multipath specular reflections that can be observed with a fixed ultrasonic transducer array. These reflections are due to the plane waves which travel with a known uniform speed in materials.

We focus on multipaths due to bottom and top surface of alloys. In assuming wide alloys or limited transducer beamwidth, reflections from the sides of the alloy can be ignored. Thus, among a number of possible multipath patterns [15], we consider dominant two-way propagation patterns as illustrated in Figures 1, 2, and 3 where the black solid lines denote real paths and dashed lines imply virtual (image) paths. Figures 1(a) and 1(b) show the direct paths for two possible cases of the flaw. For the first case (a), the flaw lies inside the vertical strip defined by the transmit/receive transducer pair, whereas in the second case (b), the flaw is outside the strip. In Figure 2(a), reflections occurring at the bottom surface yield a W-shape propagation path. It can be equivalently represented by using the Λ-shape virtual path, with corresponding virtual transmit and receive transducers located at the bottom of the mirrored object. As such, in addition to the top view of the flaw accessed from the direct path, the exploitation of the multipath, in this scenario, will provide a bottom view of the flaw. On the other hand,

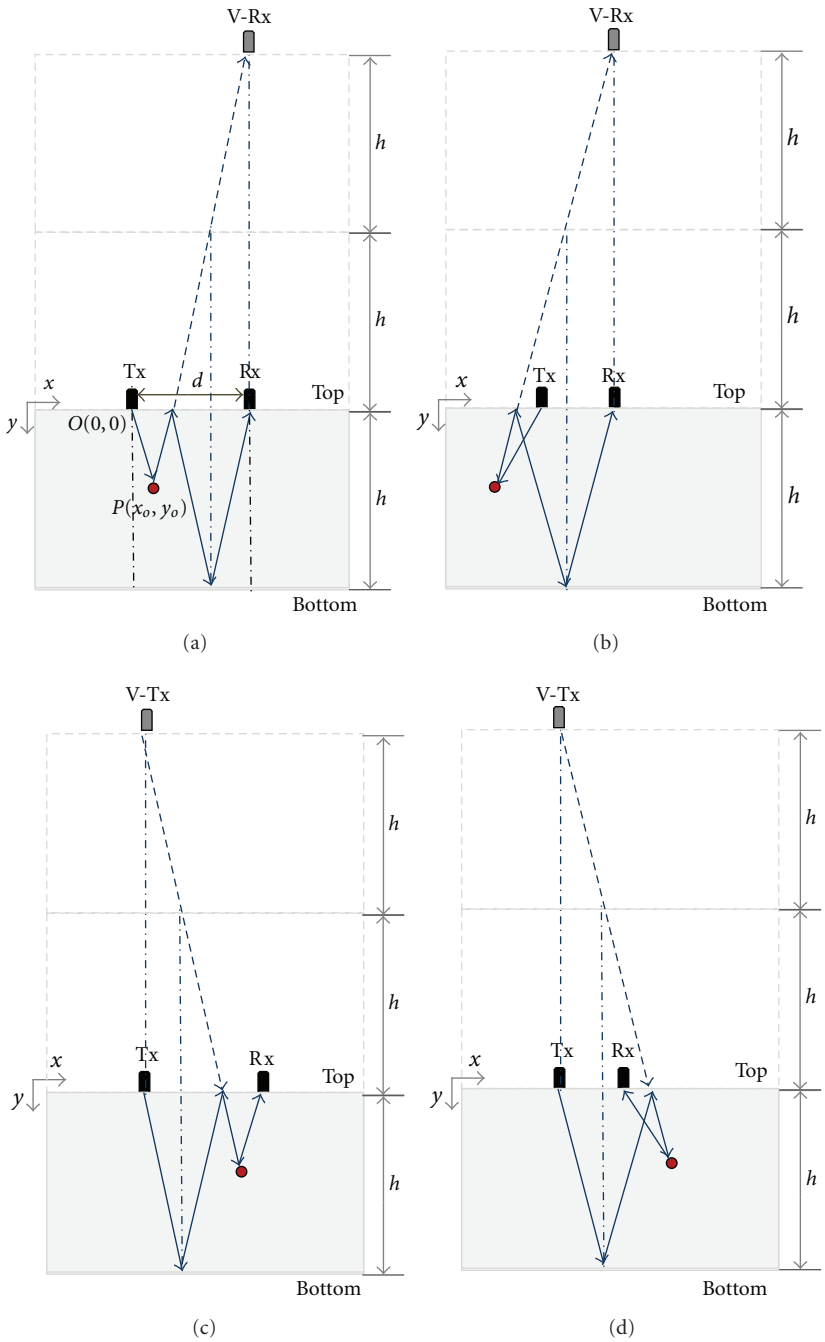

Figure 3: Multipath II-A with the virtual receiver when the target is between the transmit/receive pair (a) and outside of the pair (b). Multipath II-B with virtual transmitter when the target is between the transmit/receive pair (c) and outside of the pair (d).

the multipath II-A pattern depicted in Figures 3(a) and 3(b) include reflections from the top and bottom surfaces of a one-way path (shown in Figure 3(a) for the path from the flaw to the receive transducer) which results in a virtual position of the receive transducer with a different top view of the flaw. Multipath II-B pattern, depicted in Figures 3(c) and 3(d), includes top and bottom reflections only between transmit transducer and the flaw (not from the flaw to the receive transducer), which results in a virtual position of the transmit transducer with a different top view aspect of the flaw.

The ranges for various multipath signals can be predicted based on the known depth of the alloy (h) and transmit/receive sensor coordinates. We show in the Appendix that multipath I and II-A signals (those depicted in Figure 2(a) and Figure 3(a)) approximately lie in range $[2h\ 4h]$, when h is much larger than the distance between the T/R sensor pair, d. Multipath I and II signals coincide when the target is exactly at the center of the alloy inside the T/R pair strip, that is, when the target is at the coordinates $x = d/2$, $y = h/2$. For all other cases, multipath I and multipath II signals will be separable.

3. Signal Model and Ultrasonic Imaging

3.1. Signal Model. We consider an ultrasonic imaging system, where a single transducer transmits a wideband waveform, and several other transducers receive echoes from the tested material. This process is repeated for all transducers in the system. By the virtue of sequential waveform transmission and nonoverlapping nature of the transmitted signals, the transmitted signals can be separated at the receivers. As such, a multiple-input multiple-output (MIMO) system is implemented which allows a virtual aperture to by synthesized [18]. The MIMO system configuration outperforms traditional array configurations in target resolution and detection, especially, when the signal-to-noise ratio (SNR) is high. In this paper, we do not address the MIMO aspect of the imaging system, as it is implicit in our approach. Rather, we focus on another form of virtual sensors generated by the multipaths. The latter allows different aspect angles to the target, allowing detection of the target boundaries and perimeters.

Denote the signal emitted from the transmit transducer as $s_T(t)$. Let N be the total number of transducers. The signal received at the nth receive transducer corresponding to the mth transmit transducer position is denoted as $r_{mn}(t)$, where $m = 1,\ldots,N$ and $n = 1,\ldots,N$ with $m \neq n$. The received signal $r_{mn}(t)$ is considered as the convolution of the transmitted signal, $s_T(t)$, and the respective propagation channel associated with the mth transmit transducer and the nth receive transducer, $h_{mn}(t)$. That is,

$$r_{mn}(t) = h_{mn}(t) * s_T(t), \tag{1}$$

where $*$ denotes the convolution operation.

3.2. Ultrasonic Imaging Based on Direct Reflection Path. We assume that the respective positions of the transmit-and-receive array elements are assumed to be known in a three-dimensional Cartesian space, that is, the mth transmit transducer is located at $T_m = (x_{Tm}, y_{Tm}, z_{Tm})$, and the nth receive transducer is located at $R_n = (x_{Rn}, y_{Rn}, z_{Rn})$. The coordinate system is shown in Figure 4. Consider a region of interest (ROI) which is a two-dimensional cross-section under the linear array and corresponds to the plane as shown in Figure 4. We utilize a receive mode backprojection beamforming algorithm to construct internal images of materials [19]. The imaging can be performed in coherent or noncoherent sense [20]. Coherent imaging takes the amplitude and phase information into consideration when adding the signals received at each sensor, whereas only the amplitude information is incorporated in noncoherent imaging. The signal that is reflected from a hypothetical target located at the position $P(x_P, y_P, z_P)$ is then received with different delays at each receiver. The signal corresponding to the direct reflection path recorded at the nth receive transducer is given by

$$r_{mn}^{[d]}(t) = a_{mn}^{[d]}(P) s_T\left(t - \tau_{mn}^{[d]}(P)\right), \tag{2}$$

where $a_{mn}^{[d]}(P)$ is the reflectivity of the flaw that also accounts for the propagation loss, and $\tau_{mn}^{[d]}(P)$ denotes the delay for

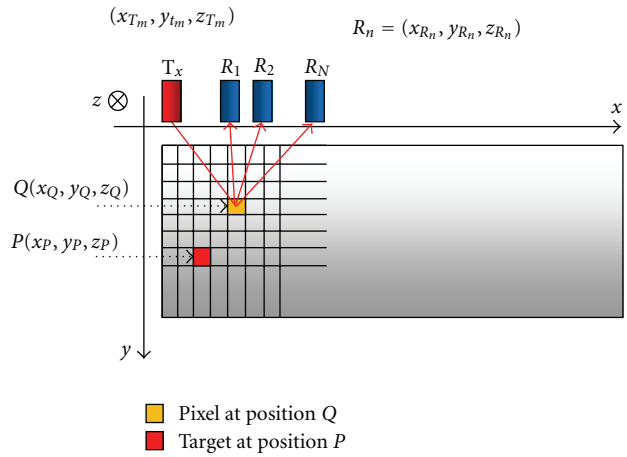

Figure 4: Transducer array and imaging geometry.

the signal to travel from the mth transmit transducer T_m to the target at P and then from location P to the nth receive transducer R_n. The superscript $^{[d]}$ is used to emphasize the direct reflection path. Assuming a homogeneous material with ultrasonic propagation speed of v in the material (the variation of the speed in the material and its compensation is considered in [18]), the time delay corresponding to any pixel Q in the image, located at (x_Q, y_Q, z_Q), can be calculated as

$$\tau_{mn}^{[d]}(Q) = \frac{\left\|\left(x_{Tm}, y_{Tm}, z_{Tm}\right) - (x_Q, y_Q, z_Q)\right\|}{v} + \frac{\left\|(x_{Rn}, y_{Rn}, z_{Rn}) - (x_Q, y_Q, z_Q)\right\|}{v}, \tag{3}$$

where $\|\cdot\|$ denotes the Euclidean norm operation. This imaging principle is illustrated in Figure 4.

The image intensity $I(Q)$ of every pixel Q in the image is obtained by adding the weighted time-delayed $N(N-1)$ received signals and correlating the resulting signal with the transmitted signal. The weights influence the point spread function (PSF) and can be chosen to control the PSF main lobe and side lobe characteristics [18]. Therefore, the intensity at pixel Q, using coherent imaging technique, can be written as

$$\begin{aligned} I(Q) &= \left.\sum_{m=1}^{N} \sum_{\substack{n=1 \\ n \neq m}}^{N} w_{mn}^{[d]}(Q) r_{mn}\left(t + \tau_{mn}^{[d]}(Q)\right) * s_T(t)\right|_{t=0} \\ &= \left.\sum_{m=1}^{N} \sum_{\substack{n=1 \\ n \neq m}}^{N} w_{mn}^{[d]}(Q) a_{mn}^{[d]}(P) s_T\left\{t + \tau_{mn}^{[d]}(Q) - \tau_{mn}^{[d]}(P)\right\} * s_T(t)\right|_{t=0}, \end{aligned} \tag{4}$$

where $w_{mn}^{[d]}(Q)$ is the weight corresponding to the mth transmit transducer and the nth receiver transducer. The

cross-correlation performs matched filtering and improves the output signal-to-noise ratio (SNR).

3.3. Ultrasonic Imaging Based on Multipath Signals. Similar to the direct reflection, we now consider three types of multipaths that are associated with the target located at $P = (x_P, y_P, z_P)$. The signal at the receive transducer R_n corresponding to the mth transmit transducer is given by

$$r_{mn}^{[i]}(t) = a_{mn}^{[i]}(P) s_T\left(t - \tau_{mn}^{[i]}(P)\right), \tag{5}$$

where the superscript $^{[i]}$ with $i = 1, 2, 3$ denotes the index of multipath I, multipath II-A, and multipath II-B, respectively.

Denoting h as the height of the metallic object, the time delays corresponding to a point target P, located at (x_P, y_P, z_P), can be, respectively, calculated for the direct and multipaths as follows.

Direct reflection path

$$\tau_{mn}^{[d]}(P) = \frac{\left\|\left(x_{Tm}, y_{Tm}, z_{Tm}\right) - (x_P, y_P, z_P)\right\|}{v} + \frac{\left\|(x_{Rn}, y_{Rn}, z_{Rn}) - (x_P, y_P, z_P)\right\|}{v}. \tag{6a}$$

Multipath I

$$\tau_{mn}^{[1]}(P) = \frac{\left\|\left(x_{Tm}, 2h - y_{Tm}, z_{Tm}\right) - (x_P, y_P, z_P)\right\|}{v} + \frac{\left\|(x_{Rn}, 2h - y_{Rn}, z_{Rn}) - (x_P, y_P, z_P)\right\|}{v}. \tag{6b}$$

Multipath II-A

$$\tau_{mn}^{[2]}(P) = \frac{\left\|\left(x_{Tm}, y_{Tm}, z_{Tm}\right) - (x_P, y_P, z_P)\right\|}{v} + \frac{\left\|(x_{Rn}, y_{Rn} - 2h, z_{Rn}) - (x_P, y_P, z_P)\right\|}{v}. \tag{6c}$$

Multipath II-B

$$\tau_{mn}^{[3]}(P) = \frac{\left\|\left(x_{Tm}, y_{Tm} - 2h, z_{Tm}\right) - (x_P, y_P, z_P)\right\|}{v} + \frac{\left\|(x_{Rn}, y_{Rn}, z_{Rn}) - (x_P, y_P, z_P)\right\|}{v}. \tag{6d}$$

Note that these multipaths, when processed using the actual transducer positions, will result in images outside the ROI. For multipath exploitations, however, we will synthesize their respective images using the virtual transducer positions, respectively, located at $T_m^{[1]} = (x_{Tm}, 2h - y_{Tm}, z_{Tm})$, $R_n^{[1]} = (x_{Rn}, 2h - y_{Rn}, z_{Rn})$ for multipath I, $T_m^{[2]} = T_m = (x_{Tm}, y_{Tm}, z_{Tm})$, $R_n^{[2]} = (x_{Rn}, y_{Rn} - 2h, z_{Rn})$ for multipath II-A, and $T_m^{[3]} = (x_{Tm}, 2h - y_{Tm}, z_{Tm})$, $R_n^{[3]} = R_n = (x_{Rn}, y_{Rn}, z_{Rn})$ for multipath II-B. In this way, multipath images will align and display the true position and size of the flaw. Specifically, multipath I image visualizes the bottom view of the flaw, whereas the other two images visualize the flaw from the top view.

4. Point Spread Functions

The virtual sensors reveal different segments of the flaw by the virtue of being placed at distinct positions from their physical sensors counterparts. Additionally, the new positions of the virtual sensors could be closer or farther from the target than the physical array sensors. As such, different segments of the flaw may be imaged with different resolutions. To demonstrate this fact, we drive in this section the point spread functions (PSFs) associated with the direct path, multipath I, and multipath II for a MIMO array configuration comprised of N ultrasonic transducers. The PSF is the response of the array imaging system to a point target. It captures the imaging characteristics of an array hence will be used herein for assessing the imaging performance associated with the direct path and multipaths. The PSF at an imaging point Q is derived in the frequency domain [19] considering an ideal point target located at P

$$I(Q) = \sum_{m=1}^{N} \sum_{\substack{n=1 \\ n \neq m}}^{N} w_{mn} \int_{\Omega} R_{mn}(f) S^*(f) e^{j2\pi f \hat{\tau}_{mn}(Q)} df, \tag{7}$$

where $R_{mn}(f)$ is the Fourier transform of the signal received by the nth receiver due to the mth transmitter, $S(f)$ is the Fourier transform of the transmitted waveform, w_{mn} is a weighting applied to the signal received by the nth receiver due to the mth transmitter, Ω is the bandwidth of the waveform, and $\hat{\tau}_{mn}(Q)$ is the estimated total propagation delay of the signal in traveling from the mth transmit element to the imaging point Q, and then back to the nth receive element. If we assume no dispersion, no attenuation, and monochromatic waveforms, the received signal can be written as

$$R_{mn}(f) = S(f) e^{-j2\pi f \tau_{mn}(P)}, \tag{8}$$

where $\tau_{mn}(P)$ represents the delay due to the target at P when a pulse is emitted from the mth transducer and the back-scattered signal is received from the nth transducer. We assume an ideal pulse with bandwidth B, that is, $|S(f)| = 1$, for $f_o < f < f_o + B$. Such a pulse can be closely emulated with a windowed Chirp function. The pulse bandwidth is sampled with frequencies as $f_k = f_0 + k\Delta f$ for $k = 0, \ldots, N_f - 1$, where N_f is the number of frequencies and $\Delta f = B/N_f$. Inserting (8) into (7) and sampling the bandwidth with the available discrete frequencies, the pixel value at imaging point Q (i.e., the PSF) can be written as follows:

$$I(Q) = \sum_{m=1}^{N} \sum_{\substack{n=1 \\ n \neq m}}^{N} w_{mn} \sum_{k=1}^{N_f - 1} e^{j2\pi(f_0 + k\Delta f)(\hat{\tau}_{mn}(Q) - \tau_{mn}(P))}. \tag{9}$$

It can be observed that the PSF highly depends on the target location P, the transducer array geometry and its characteristics, and the number of frequencies used in synthesizing the pulse. As such, these factors determine beamforming image quality. It is important to note that, given the wavelength, flaw range, and array extent, it is clear that we deal, in this paper, with a near-field problem. As

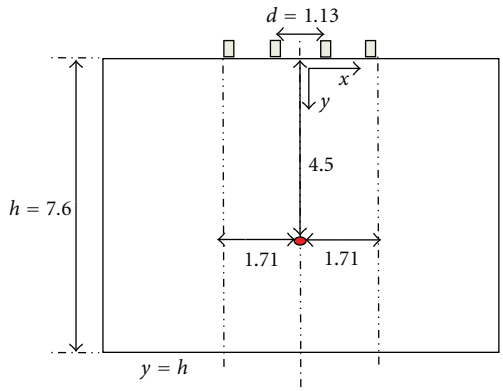

Figure 5: Simulated imaging configuration used for PSF computations (units are in cm).

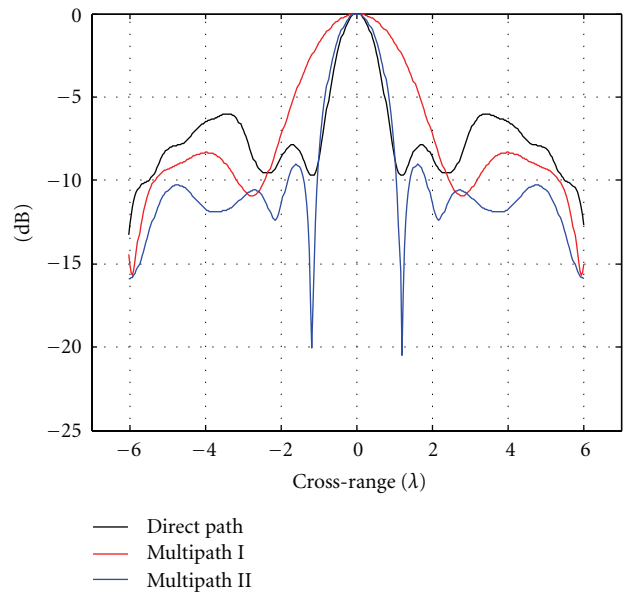

Figure 6: Cross-range PSFs for direct path (black line), Multipath I (red line) and Multipath II (blue line) based on wideband chirp excitation for the point target with the imaging array in near field as shown in Figure 5.

such, the image cannot be simply cast as a convolution of the PSF and spatial extent of the flaw. However, the PSF in the underlying problem remains indicative to image quality and can reveal the expected defocusing or blurring of the target associated with different multipaths.

In order to assess multipath imaging performance, we derive the PSFs due to multipath I and II and compare these to that of the direct path for near-field ultrasound flaw imaging. A simulated sensor array configuration for imaging a point target in a metallic alloy is illustrated in Figure 5. This simulation is intended to emulate experimental imaging conditions in our lab. A point target is assumed to be at the location (0, 4.5) cm in the near-field of a 4-element linear transducer array where the center point of the array denotes the origin (0, 0). The transducers are spaced with 1.13 cm (4λ) where $\lambda = 2.82$ mm is the wavelength of the propagating sound. The aperture of the transducer array is 12λ. A wideband chirp signal of length 50 ms with a 2.25 MHz center frequency and 2 MHz bandwidth is used to emulate an ideal pulse transmission.

First, we compute the PSF for the direct path based on the array geometry shown in Figure 5 and wideband chirp excitation. The intensity of the image point Q (9) is computed along the cross-range of the target and within the array aperture $[-6\lambda\ 6\lambda]$. This PSF is shown in Figure 6 in a solid black line. For computing the PSF of multipath I and II, we utilize virtual transmitter and receivers due to these multipaths as shown in Figures 2 and 3. The delays corresponding to the targets ($\tau_{mn}(P)$) and the test point Q ($\hat{\tau}_{mn}(Q)$) for multipaths are computed based on these virtual transmitter and receiver locations. These delays are used in PSF computations (see (9)) for a set of test points along the cross-range of the target. The virtual array for multipath I is a mirror image of the physical array with respect to the $y = h$ axis (i.e., the bottom surface of the material) and is placed at $y = 2h$ axis. As such, Multipath I virtual array views the target from a larger distance than that is seen from the physical array. This causes the main lobe of the PSF to be widened compared to that of the direct path PSF, whereas the side-lobes are reduced. For computing multipath II PSF, we utilize virtual transmitters or receivers positioned at $y = -2h$ line. More specifically, for multipath II-A, the virtual receivers are positioned at $y = -2h$ line, while the transmitter stays at its original location. Similarly, for multipath II-B, the virtual transmitter is positioned at $y = -2h$ line, while the receivers stay at their original locations, as shown in Figure 3. The PSFs associated with these two multipaths are combined into one PSF, since these two multipaths are generally unresolvable. This PSF is shown in Figure 6 in solid blue line. While the main-lobe of the Multipath II PSF is almost identical to that of the direct path, the side-lobes are reduced markedly, hence offering an improved imaging performance.

5. Multipath Identification and Association

When the image of the direct reflection path is synthesized and the location of a potential flaw, P, is identified, it is possible to identify the region where the images associated with the multipaths are likely to be located. When the flaw is assumed to be a point target, the respective delays corresponding to different paths can be computed from (6b)–(6d). Note that the actual time delay may be affected by the flaw shape and size, inhomogeneous propagation characteristics, and even the surface couplings in the transducers. Therefore, the objective of multipath association is to identify the likely multipath signals in the received waveforms and then process these signals to synthesize the multipath images.

To help identifying the direct reflection and multipath signals, we consider the received signal waveforms in terms of different phases. The first and the second phases are separated by the time delay corresponding to the bottom reflection. For specular bottom reflection, the reflection point corresponding to the mth transmit

transducer $T(x_{Tm}, y_{Tm}, z_{Tm})$ and the nth receive transducer $R_n(x_{Rn}, y_{Rn}, z_{Rn})$ is located at $((x_{Tm} + x_{Rn})/2, h, (z_{Tm} + z_{Rn})/2)$. Ignoring the gap between the transducers and the top surface (i.e., $y_{Tm} = y_{Rn} = 0$), the kth and the $(k+1)$th phases are separated by the time delay $(1/v)[((x_{Tm} - x_{Rn})/2)^2 + (2kh)^2 + ((z_{Tm} - z_{Rn})/2)^2]^{1/2}$. In this way, the waveform corresponding to the direct reflection path is located in Phase I, whereas the first-order multipath waveforms illustrated in Figures 2 and 3 are located in Phase II.

Phases I and II are used in the backprojection imaging to align the target images corresponding to the different multipaths. Any signal returns received over Phase I will be attributed to the physical array, whereas the returns of delays longer than the two-way propagation time to the bottom of the alloy will be attributed to cases involving virtual sensors. It is important to note that, according to the multipath configurations depicted in Figure 3, there is always a combination of physical and virtual sensors when considering multipath II. Although multipath I and multipath II both lie in Phase II, one can separate them according to their respective time delays. It can be observed that the direct-path delay and multipath I delay are approximately equally positioned on both sides away from the delay corresponding to the alloy bottom, which is very evident in Figure 2. One can, therefore, apply a time window to isolate multipaths I and II, provided that they are separable, as it is the case in the underlying example.

6. Experimental Examples

6.1. Experiment Settings. This section provides the results of our experimental studies. An aluminum block (alloy number 6061) of dimensions 12 in × 6 in × 3 in (304.8 mm × 152.4 mm × 76.2 mm) is used as the test specimen. Figure 7 shows a horizontal hole with a diameter of 9.24 mm going through the block, which simulates a specular flaw.

The waveform generation and observation are performed using Acousto/Ultrasonics system manufactured by Physical Acoustics. A train of 3 ms chirp waveform pulses with a frequency range between 1 MHz and 4 MHz were generated using an ARB-1410 arbitrary waveform generating board equipped in system, and the return signals were recorded by two PCI-2 two-channel AE data acquisition cards equipped in the same system with a sampling rate of 40 MHz [21]. A 20/40/60 dB preamplifier from Physical Acoustics is inserted between each receive transducer and the respective receiver PCI board. Olympus V133-RM contact transducers with a 2.25 MHz center frequency are used as both transmitter and receivers [22]. Four uniform linear transducer positions separated by an interelement spacing of 11.43 mm are considered. When a transducer at one position is used for transmission, transducers at the other three positions are used for receiving. By sequentially changing the transducer functions, a combination of 12 observations are recoded to synthesize an MIMO system.

Because chirp waveforms are transmitted, the received signal is first compressed using matched filtering [23]. Then, the Hilbert transform is applied to the received signals to form their analytical signal expressions for multipath identification and imaging.

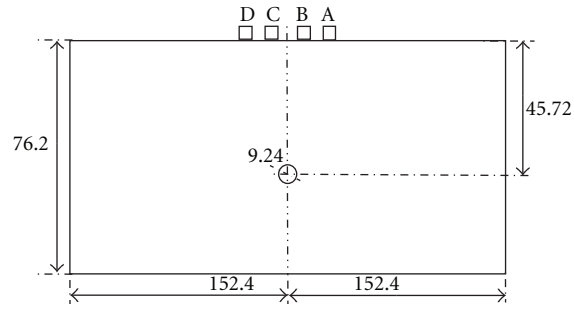

Figure 7: Dimensions of the aluminum alloy (unit: mm).

6.2. Results. The transducers are positioned on the top surface of the aluminum alloy ($y = 0$), and their x positions relative to the flaw center are, respectively, 17.145 mm (position A), 5.715 mm (position B), −5.715 mm (position C), and −17.145 mm (position D).

Table 1 summarizes the predicted and measured time delays of the direct and multipath signals from the flaw for all possible combinations of transmission and reception using the four transducers. The time delays are recorded for the flaw echo, echo from the bottom surface of the alloy, and multipath I and II echoes. The predicted time delays are calculated by tracing the direct and multipaths based on the geometry of the hole and transducer array as shown in Figure 7. The direct reflection echo from the flaw appears around 13.5 μs, whereas the multipath I echo appears around 32.3 μs. Multipath II-A and II-B echoes are both located around 37 μs and are generally unresolvable. As it is seen from the table, the measured time delays are in good agreement with the predicted time delays, indicating the validity of the multipath models.

Figure 8 shows the received waveform envelopes after matched filtering for all possible combinations of transmit/receive transducer pairs. It is evident that all waveform envelopes show clear direct reflection path (approximately between 13.0 and 14.0 μs) and bottom reflection (approximately between 24.1 and 24.6 μs), whereas the level of multipath signals depends on the transducer positions, because some multipaths corresponding to certain transducer positions may be obstructed by the hole itself. In general, the combination of using transducers positions A and D yields a higher multipath signal level.

Figure 9 shows the imaging results generated using different multipaths with the correct location and size of the flaw marked with a white circle. Figure 9(a) shows the image generated using the direct reflection path. The top of the hole is clearly identified. Multipath I yields an image showing the bottom of the hole, as depicted in Figure 9(b). Figure 9(c) shows the results obtained from multipath scenarios II. Since these images represent reflections at different sensor positions, image fusion can be applied. Figure 9(d) shows the fused image obtained by a simple sum of the previous three

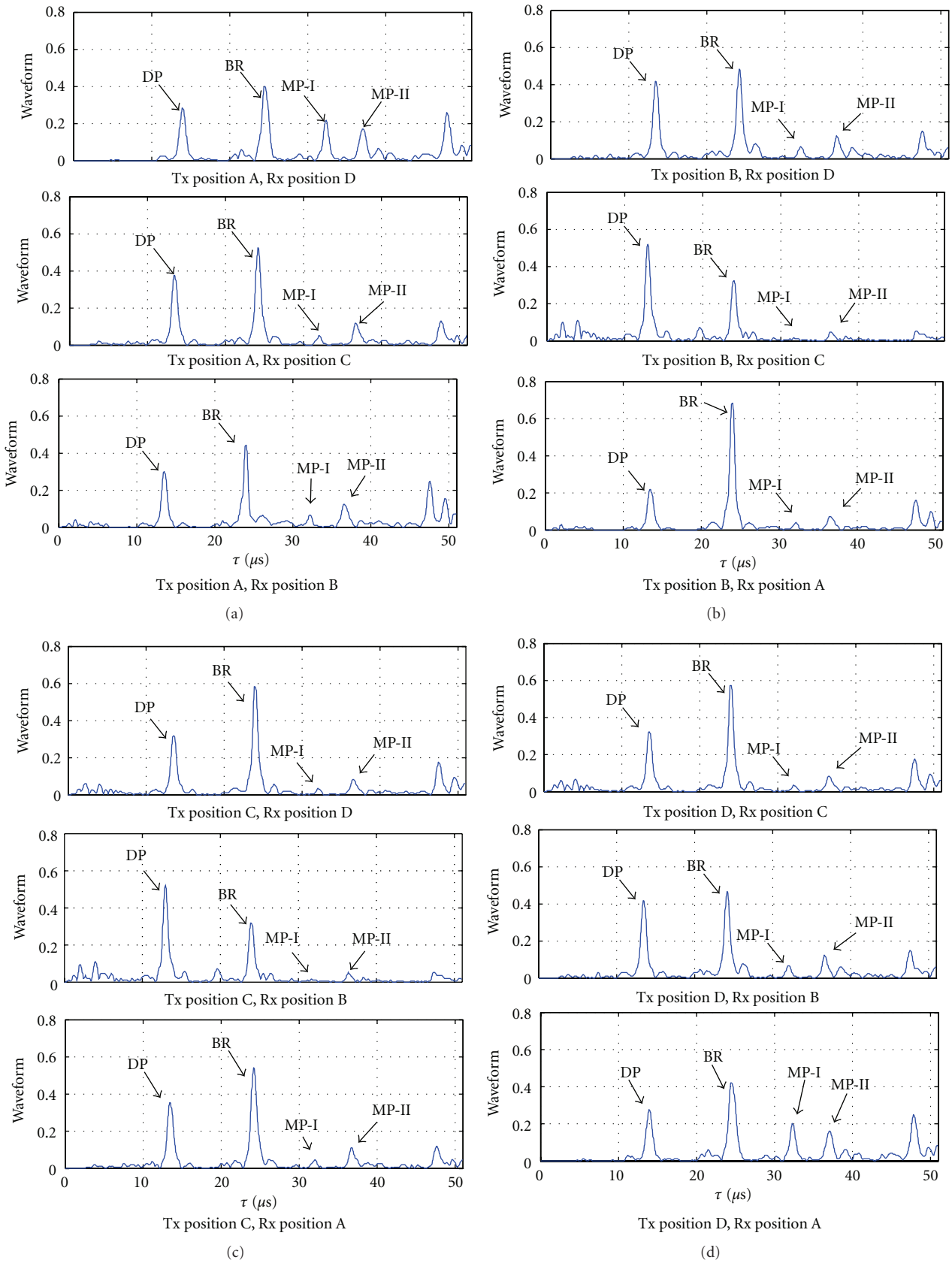

Figure 8: (a) Received waveform envelopes at sensors B, C, and D corresponding to transmitter A. (b) Received waveform envelopes at sensors A, C, and D corresponding to transmitter B. (c) Received waveform envelopes at sensors A, B, and D corresponding to transmitter C. (d) Received waveform envelopes at sensors A, B, and C corresponding to transmitter D.

Table 1: Predicted and measured time delays of multipath signals for the specular flaw shown in Figure 7 (unit: μs).

Transmit position	Receive position	Calculated time delay					Measured time delay			
		Bottom	Flaw	MP I	MP II-A	MP II-B	Bottom	Flaw	MP I	MP II-A/B
A	D	24.592	13.986	32.562	37.569	37.569	24.600	14.050	32.450	37.200
	C	24.265	13.513	32.364	37.465	37.096	24.280	13.550	32.180	36.880
	B	24.067	13.513	32.364	37.465	37.096	24.070	13.600	32.330	36.730
B	D	24.265	13.513	32.364	37.096	37.465	24.280	13.570	32.180	36.800
	C	24.067	13.040	32.166	36.991	36.991	24.070	13.030	32.180	36.520
	A	24.067	13.513	32.364	37.096	37.465	24.070	13.550	32.270	36.630
C	D	24.067	13.513	32.364	37.096	37.465	24.070	13.630	32.220	36.700
	B	24.067	13.040	32.166	36.991	36.991	24.070	13.030	32.380	36.500
	A	24.265	13.513	32.364	37.096	37.465	24.280	13.550	32.180	36.850
D	C	24.067	13.513	32.364	37.465	37.096	24.070	13.630	32.220	36.670
	B	24.265	13.513	32.364	37.465	37.096	24.280	13.550	32.180	36.800
	A	24.592	13.986	32.562	37.569	37.569	24.600	14.030	32.430	37.180

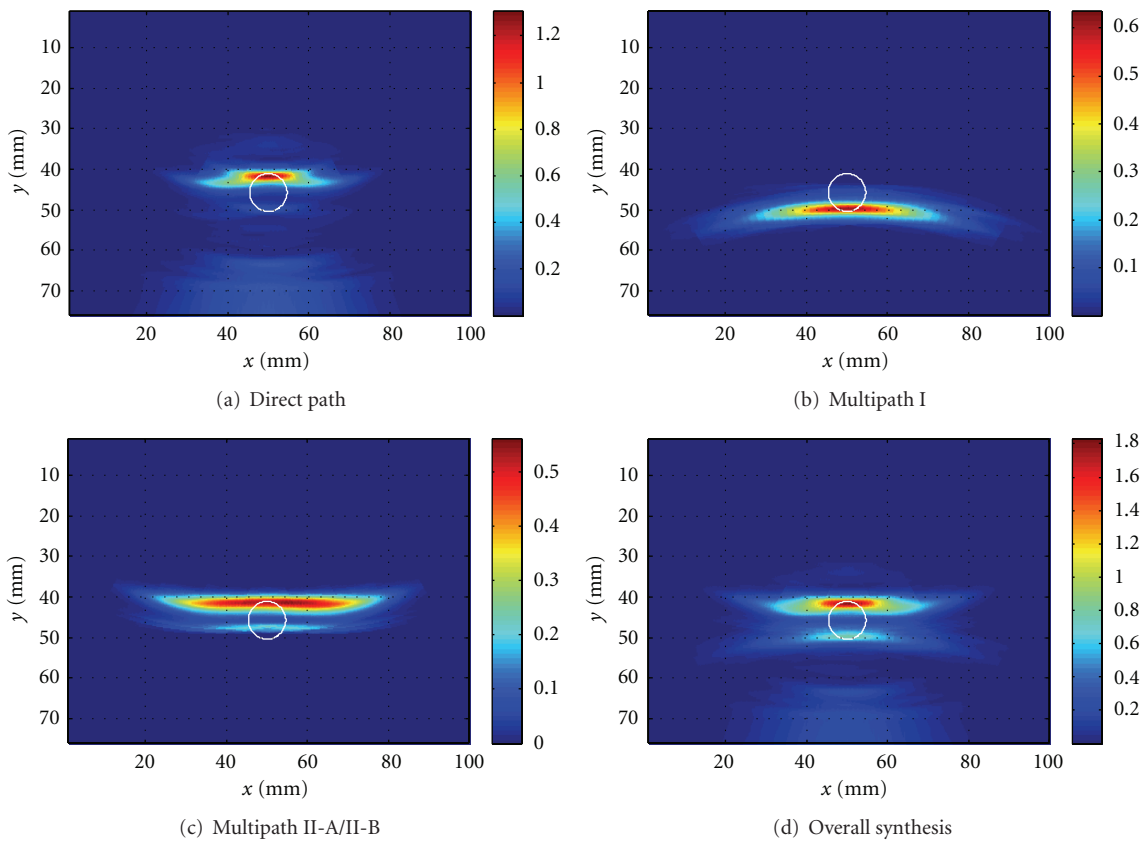

(a) Direct path

(b) Multipath I

(c) Multipath II-A/II-B

(d) Overall synthesis

Figure 9: Ultrasound imaging of a hole via multipath exploitation.

images. It is evident that the size of the hole is now revealed from the fusion result, which is otherwise unavailable if only the direct reflection observations were used.

7. Conclusions

Multipath propagation was explored in ultrasonic imaging for the purpose of nondestructive testing. Reflections from the flaw, when combined with reflections from the alloy boundaries, provide an opportunity to reveal segments of the flaw that are shadowed due the limited range penetration of ultrasound waves. Knowledge-based multipath exploitation was made possible by assumed known dimensions of a metallic alloy and resolvable signal arrivals. We focused on three categories of multipaths, all traced to reflections in the vertical plane including the transducers and flaw, and ignoring reflections from the alloy sides. By identifying multipaths that reflect at the known top and bottom surfaces, virtual sensors can be identified. The locations of these sensors permit visualizations of the shadowed regions

which otherwise is difficult to obtain from only the direct reflection signals. With the translation of the virtual sensor in both dimensions, more aspect angles to the target become available, aiding in the determination of the flaw type and perimeter. The point spread functions corresponding to the different multipath types were derived and shown to be different, causing the image quality to vary with multipath. The proposed multipath exploitation is supported by analysis and verified by experimental data.

Appendix

A. Minimum and Maximum Path Lengths for Multipath I and II

We show the minimum and maximum path lengths for multipath I (Figure 2(a)) and multipath II (Figure 3(a)). These minimum and maximum lengths will determine the range of the two-way propagation time delays from the transmitter and back to the receiver. This will, in turn, aid in separating multipaths from the direct path and associate them with their respective virtual arrays.

For multipath I, we fix the origin at the virtual transmitter (V-Tx) location and denote as $O\ (0,0)$. Then the flaw location P is assigned as (x_o, y_o) according to the (x', y') axis representation in Figure 2(a). Further, assuming the target is in the strip between the transducer and receiver pair and between the top and bottom surface, the target point P coordinates change in ranges as, $0 < x_o < d$ and $h < y_o < 2h$, where d denotes the distance between the transmitter and receiver, and h denotes the depth of the material. The total path length from virtual transmitter (V-Tx) to the target and from target to the virtual receiver (V-Rx) can be written as follows:

$$L_1(x_0, y_0) = \sqrt{x_0^2 + y_0^2} + \sqrt{(d - x_o)^2 + y_0^2} \tag{A.1}$$

We find the minimum and maximum values of this path via maxima points. By taking the partial derivative of the above equation with respect to x_o and setting it equal to 0 yields

$$\frac{\partial L_1(x_0, y_0)}{\partial x_0} = \frac{x_o}{\sqrt{x_0^2 + y_0^2}} - \frac{(d - x_o)}{\sqrt{(d - x_o)^2 + y_0^2}} = 0. \tag{A.2}$$

The maxima point x_o satisfying the above equation can be derived as $\tilde{x}_o = 0.5d$. It can be readily shown that the path length $L_1(x_0, y_0)$ is minimized at this maxima point. Similarly, taking the partial derivative of $L_1(x_0, y_0)$ with respect to y_o and setting it equal to 0 yields

$$\frac{\partial L_1(x_0, y_0)}{\partial y_0} = \frac{y_o}{\sqrt{x_0^2 + y_0^2}} + \frac{y_o}{\sqrt{(d - x_o)^2 + y_0^2}} = 0. \tag{A.3}$$

From the above equation, the maxima point can be found at $y_o = \tilde{y}_o = 0$. It can be readily shown that this point minimizes $L_1(x_0, y_0)$. Further, it can be seen from (A.1) that $L_1(x_0, y_0)$ is a monotonically increasing function of y_o. Since y_o changes in range, $h < y_o < 2h$, the path length $L_1(x_0, y_0)$ will be minimum at target location $(0.5d, h)$, and will be maximum at target locations $(0, 2h)$ and $(d, 2h)$. As a result, the minimum path length can be calculated as

$$L_1(0.5d, h) = 2\sqrt{(0.5d)^2 + h^2}. \tag{A.4}$$

Similarly, the maximum path length can be calculated as

$$L_1(0, 2h) = L_1(d, 2h) = 2h + \sqrt{d^2 + (2h)^2}. \tag{A.5}$$

Furthermore, assuming the material depth is much larger than the distance between the transmitter and receiver, that is, $h \gg d$, the minimum and maximum path lengths can be approximated as

$$\begin{aligned} \{L_1\}_{\min} &= L_1(0.5d, h) \cong 2h, \\ \{L_1\}_{\max} &= L_1(0, 2h) = L_1(d, 2h) \cong 4h. \end{aligned} \tag{A.6}$$

Therefore, multipath I will approximately be in range $[2h\ 4h]$ and its arrival time will be confined to the time interval, $[2h/v\ 4h/v]$, where v is the speed of sound in the material.

For multipath II, we first fix the origin at transmitter (Tx) location and denote as $O\ (0,0)$ (See Figure 3(a)). Then, the flaw location P is assigned as (x_o, y_o) according to the (x, y) axis representation in Figure 3(a). Further, assuming the target is in the strip between the transducer and receiver pair and between the top and bottom surface, the target point P coordinates change in ranges as, $0 < x_o < d$ and $0 < y_o < h$. Then, the total path length from the transmitter (Tx) to the target and from target to the virtual receiver (V-Rx) can be written as

$$L_2(x_0, y_0) = \sqrt{x_0^2 + y_0^2} + \sqrt{(d - x_o)^2 + (2h + y_0)^2}. \tag{A.7}$$

By taking the partial derivative of the above equation with respect to x_o and setting it equal to 0 yields

$$\frac{\partial L_2(x_0, y_0)}{\partial x_0} = \frac{x_o}{\sqrt{x_0^2 + y_0^2}} - \frac{(d - x_o)}{\sqrt{(d - x_o)^2 + (2h + y_0)^2}} = 0. \tag{A.8}$$

The maxima point x_o satisfying the above equation can be derived as $x_m = y_0 d/2(h + y_0)$. It can be readily shown that the path length $L_2(x_0, y_0)$ is minimized at this maxima point. Similarly, taking the partial derivative of $L_2(x_0, y_0)$ with respect to y_o and setting it equal to 0 yields

$$\frac{\partial L_2(x_0, y_0)}{\partial y_0} = \frac{y_o}{\sqrt{x_0^2 + y_0^2}} + \frac{2h + y_o}{\sqrt{(d - x_o)^2 + (2h + y_o)^2}} = 0. \tag{A.9}$$

From above equation, the maxima point minimizing $L_2(x_0, y_0)$ can be found as $y_o = \tilde{y}_o = 0$. Further, it can be seen from (A.7) that $L_2(x_0, y_0)$ is a monotonically increasing function of y_o. Since y_o changes in range, $0 < y_o < h$, the path length $L_2(x_0, y_0)$ will be minimum at target location $(x_m, 0)$, and maximum at locations $(0, h)$ and (d, h). As a result, the minimum path length can be calculated as

$$L_2(x_m, h) = x_m + 2\sqrt{(d - x_m)^2 + (2h)^2}. \tag{A.10}$$

Similarly, the maximum path length can be calculated as

$$L_2(0,h) = h + \sqrt{d^2 + (3h)^2},$$
$$L_2(d,h) = \sqrt{d^2 + h^2} + 3h. \tag{A.11}$$

Furthermore, assuming the material depth is much larger than the distance between the transmitter and receiver, that is, $h \gg d$, the minimum and maximum path lengths can be approximated as,

$$\{L_2\}_{\min} \cong 2h,$$
$$\{L_2\}_{\max} \cong 4h. \tag{A.12}$$

Therefore, multipath II-A will approximately be in range $[2h\ 4h]$ as in multipath I.

Acknowledgment

This research is supported by the National Science Foundation (NSF) under grant number IIP-0917690 and by The Ministry of Railways, China, under grant number 2011J011-E.

References

[1] K. E. Thomenius, "Evolution of ultrasound beamformers," in *Proceedings of IEEE Ultrasonics Symposium*, pp. 1615–1622, November 1996.

[2] B. W. Drinkwater and P. D. Wilcox, "Ultrasonic arrays for non-destructive evaluation: a review," *NDT & E International*, vol. 39, no. 7, pp. 525–541, 2006.

[3] L. W. Schmerr and S.-J. Song, *Ultrasonic Nondestructive Evaluation Systems*, Springer, 2007.

[4] R. Lasser, M. Lasser, J. Kula, D. Ecich, and R. Westernic, "Remote, simple nondestructive testing of composite defects with an ultrasound camera: a Boeing study," in *Procceedings of Composites*, Las Vegas, Nev, USA, February 2010.

[5] C. Holmes, B. W. Drinkwater, and P. D. Wilcox, "Post-processing of the full matrix of ultrasonic transmit-receive array data for non-destructive evaluation," *NDT & E International*, vol. 38, no. 8, pp. 701–711, 2005.

[6] J. Zhang, B. W. Drinkwater, P. D. Wilcox, and A. J. Hunter, "Defect detection using ultrasonic arrays: the multi-mode total focusing method," *NDT & E International*, vol. 43, no. 2, pp. 123–133, 2010.

[7] P. Viswanath and D. Tse, *Fundamentals of Wireless Communications*, Cambridge University, 2005.

[8] V. Tarokh, Ed., *New Directions in Wireless Communications Research*, Springer, 2009.

[9] "Multipath Exploitation Radar (MER)," DARPA, Solicitation Number: DARPA-BAA-09-01.

[10] E.-G. Paek, J. Y. Choe, P. A. Bernhardt, and J. Horlick, "High-resolution over-the-horizon radar using time reversal," Tech. Rep. NRL/FR/5317-09-10,180, Naval Research Laboratory, December 2009, http://www.dtic.mil/cgi-bin/GetTRDoc?AD=ADA514533&Location=U2&doc=GetTRDoc.pdf.

[11] S. Kidera, T. Sakamoto, and T. Sato, "Experimental study of shadow region imaging algorithm with multiple scattered waves for UWB radars," *PIERS Online*, vol. 5, no. 4, pp. 393–396, 2009.

[12] P. Setlur, G. E. Smith, F. Ahmad, and M. Amin, "Target localization with a single-antenna monostatic radar via multipath exploitation," in *Proceedings of the SPIE Conference on Radar Sensor Technology XV*, Orlando, Fla, USA, April 2011.

[13] A. Derode, P. Roux, and M. Fink, "Robust acoustic time reversal with high-order multiple scattering," *Physical Review Letters*, vol. 75, no. 23, pp. 4206–4209, 1995.

[14] J. M. F. Moura and Y. Jin, "Detection by time reversal: single antenna," *IEEE Transactions on Signal Processing*, vol. 55, no. 1, pp. 187–201, 2007.

[15] J. Blitz and G. Simpson, *Ultrasonic Methods of Nondestructive Testing*, Chapman & Hall, 1996.

[16] J. Saniie and D. T. Nagle, "Pattern recognition in the ultrasonic imaging of reverberant multilayered structures," *IEEE Transactions on Ultrasonics, Ferroelectrics, and Frequency Control*, vol. 36, no. 1, pp. 80–92, 1989.

[17] J. D. Achenbach, L. Adler, D. K. Lewis, and H. McMaken, "Diffraction of ultrasonic waves by penny-shaped cracks in metals: theory and experiment," *Journal of Acoustical Society of America*, vol. 66, no. 6, pp. 1848–1856, 1979.

[18] R. Demirli, X. Rivenq, Y. D. Zhang, C. Ioana, and M. G. Amin, "MIMO array imaging for ultrasonic nondestructive testing," in *Nondestructive Characterization for Composite Materials, Aerospace Engineering, Civil Infrastructure, and Homeland Security*, vol. 7983 of *Proceedings of SPIE Conference*, San Diego, Calif, USA, March 2011.

[19] M. G. Amin and K. Sarabandi, "Special issue on remote sensing of building interior," *IEEE Transactions on GeoScience and Remote Sensing*, vol. 47, pp. 1267–1268, 2009.

[20] Y. D. Zhang and A. Hunt, "Image and localization of behind-the-wall targets using linear and distributed aperture," in *Through the Wall Radar Imaging*, chapter 4, CRC Press, 2010.

[21] Physical Acoustics Corporation products, http://www.pacndt.com/index.aspx?go=products.

[22] Olympus NDT contact transducers, http://www.olympus-ims.com/en/ultrasonic-transducers/contact-transducers/.

[23] M. Skolnik, *Radar Handbook*, McGraw-Hill, 3rd edition, 2007.

Hindawi Publishing Corporation
Advances in Acoustics and Vibration
Volume 2012, Article ID 480473, 13 pages
doi:10.1155/2012/480473

Research Article

Fractional Fourier Transform for Ultrasonic Chirplet Signal Decomposition

Yufeng Lu,[1] Alireza Kasaeifard,[2] Erdal Oruklu,[2] and Jafar Saniie[2]

[1] *Department of Electrical and Computer Engineering, Bradley University, Peoria, IL 61625, USA*
[2] *Department of Electrical and Computer Engineering, Illinois Institute of Technology, Chicago, IL 60616, USA*

Correspondence should be addressed to Erdal Oruklu, erdal@ece.iit.edu

Received 7 April 2012; Accepted 31 May 2012

Academic Editor: Mario Kupnik

A fractional fourier transform (FrFT) based chirplet signal decomposition (FrFT-CSD) algorithm is proposed to analyze ultrasonic signals for NDE applications. Particularly, this method is utilized to isolate dominant chirplet echoes for successive steps in signal decomposition and parameter estimation. FrFT rotates the signal with an optimal transform order. The search of optimal transform order is conducted by determining the highest kurtosis value of the signal in the transformed domain. A simulation study reveals the relationship among the kurtosis, the transform order of FrFT, and the chirp rate parameter in the simulated ultrasonic echoes. Benchmark and ultrasonic experimental data are used to evaluate the FrFT-CSD algorithm. Signal processing results show that FrFT-CSD not only reconstructs signal successfully, but also characterizes echoes and estimates echo parameters accurately. This study has a broad range of applications of importance in signal detection, estimation, and pattern recognition.

1. Introduction

In ultrasonic imaging applications, the ultrasonic signal always contains many interfering echoes due to the complex physical properties of the propagation path. The pattern of the signal is greatly dependent on irregular boundaries, and the size and random orientation of material microstructures. For material characterization and flaw detection applications, it becomes a challenging problem to unravel the desired information using direct measurement and conventional signal processing techniques. Consequently, signal processing methods capable of analyzing the nonstationary behavior of ultrasonic signals are highly desirable for signal analysis and characterization of propagation path.

Various methods such as short-time Fourier transform, Wigner-Ville distribution, discrete wavelet transform, discrete cosine transform, and chirplet transform have been utilized to examine signals in joint time-frequency domain and to reveal how frequency changes with time in those signals [1–8]. Nevertheless, it is still challenging to adaptively analyze a broad range of ultrasonic signal: narrowband or broadband; symmetric or skewed; nondispersive or dispersive.

Recently, there has been a growing attention to fractional Fourier transform (FrFT), a generalized Fourier transform with an additional parameter (i.e., transform order). It was first introduced in 1980, and subsequently closed-form FrFT was studied [8–11] for time-frequency analysis. FrFT is a power signal analysis tool. Consequently, it has been applied to different applications such as high-resolution SAR imaging, sonar signal processing, blind source separation, and beamforming in medical imaging [12–15]. Short term FrFT, component-optimized FrFT, and locally optimized FrFT have also been proposed for signal decomposition [16–18].

In practice, signal decomposition problem is essentially an optimization problem under different design criteria. The optimization can be achieved either locally or globally, depending on the complexity of the signal, accuracy of estimation, and affordability of computational load. Consequently, the results of signal decomposition are not unique due to different optimization strategies and signal models. For ultrasonic signal analysis, local responses from

Table 1: Parameter estimation results of two slightly overlapped ultrasonic echoes.

	τ (us)	f_c (MHz)	β	α_1 (MHz)^2	α_2 (MHz)^2	θ (Rad)
Echo 1						
Actual parameter	2.5	7.0	1	20	35	$\pi/6$
Estimated parameter	2.50	7.00	1.00	20.00	35.00	0.52
Echo 2						
Actual parameter	3.0	5	1	25	20	0
Estimated parameter	3.00	5.00	1.00	25.00	19.98	0

Table 2: Parameter estimation results of two moderately overlapped ultrasonic echoes.

	τ (us)	f_c (MHz)	β	α_1 (MHz)^2	α_2 (MHz)^2	θ (Rad)
Echo 1						
Actual parameter	2.7	7.0	1	20	35	$\pi/6$
Estimated parameter	2.70	7.02	1.00	20.04	33.55	0.67
Echo 2						
Actual parameter	3.0	5	1	25	20	0
Estimated parameter	3.00	5.00	1.00	24.87	20.38	0.01

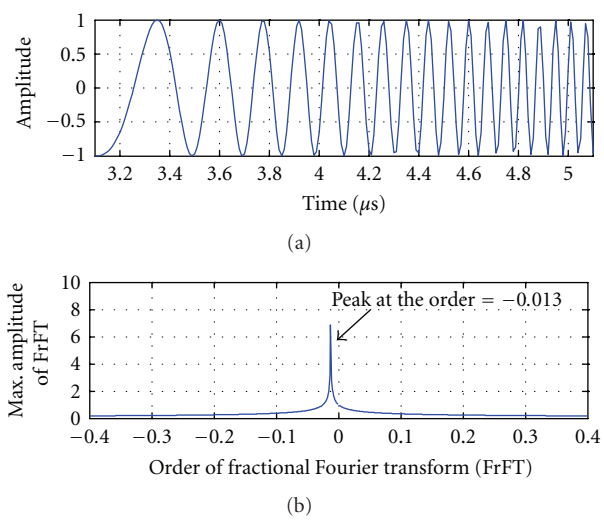

Figure 1: (a) A simulated LFM signal. (b) The optimal transform order tracked by Maximum amplitude of FrFT for different FrFT orders.

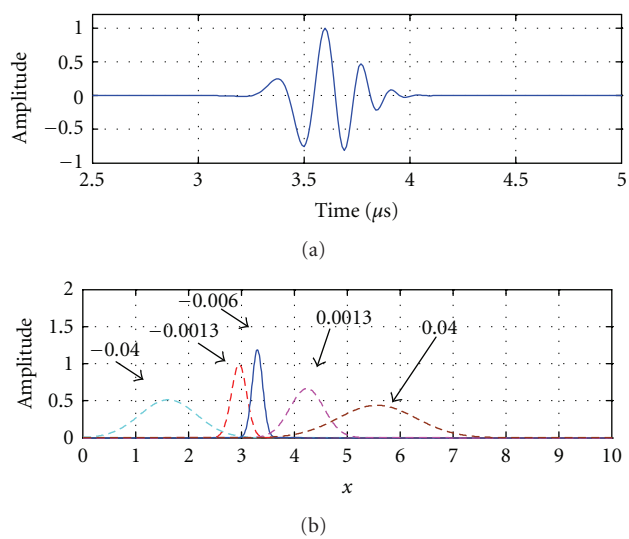

Figure 2: (a) a simulated ultrasonic single echo with $\Theta = [3.6\,\text{us}\quad 5\,\text{MHz}\quad 1\quad 25\,\text{MHz}^2\quad 25\,\text{MHz}^2\quad 0]$. (b) Fractional Fourier transform of the signal in (a) for different transform orders.

microstructure scattering and structural discontinuities are more of importance for detection and material characterization. Chirplet covers a board range of signals representing frequency-dependent scattering, attenuation and dispersion effects in ultrasonic testing applications. This study shows that FrFT has a unique property for processing chirp-type echoes. Therefore, in this paper, the application of fractional Fourier transform for ultrasonic applications has been explored. In particular, FrFT is introduced as a transformation tool for ultrasonic signal decomposition. FrFT is employed to estimate an optimal transform order, which corresponds to highest kurtosis value in the transform domain. The searching process of optimal transform order is based on a segmented signal for a local optimization. Then, the FrFT with the optimal transform order is applied to the entire signal in order to isolate the dominant echo

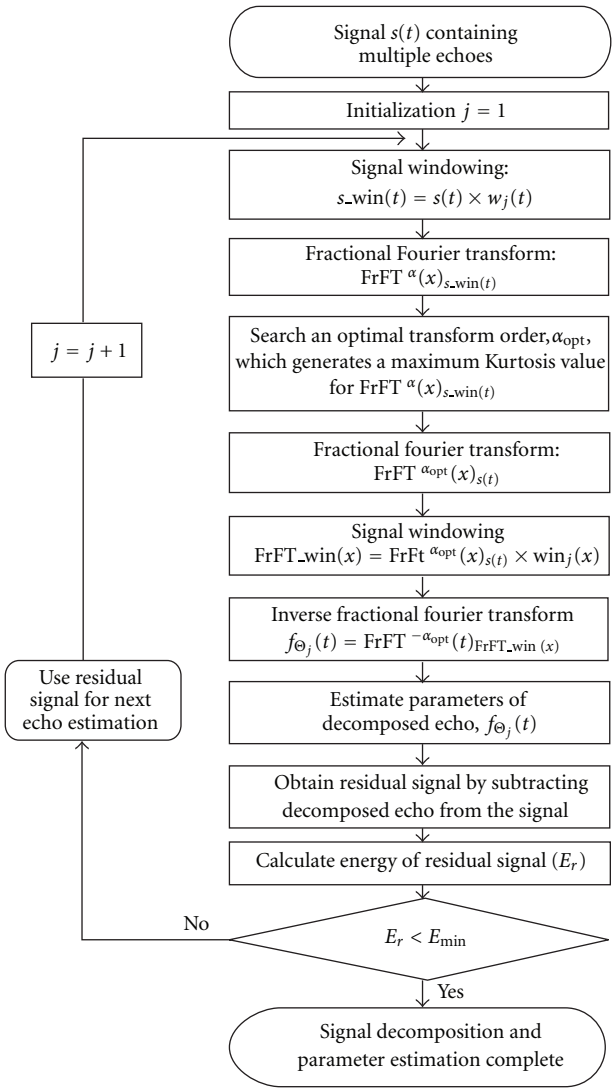

Figure 3: Flowchart of FrFT-CSD algorithm.

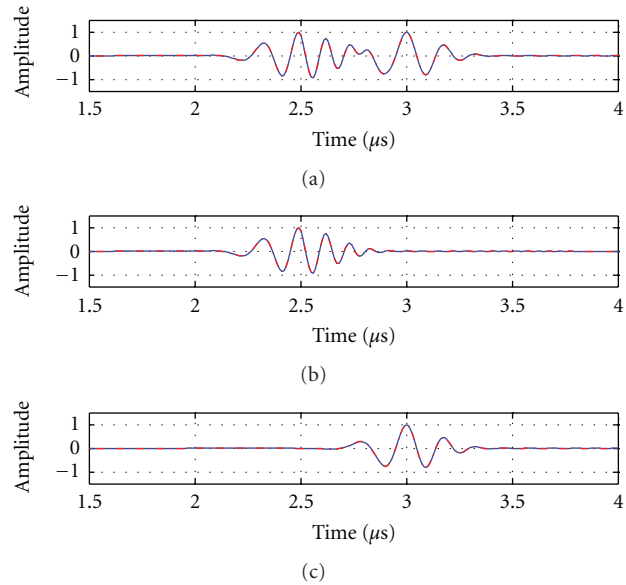

Figure 4: (a) Simulated ultrasonic echoes (20% overlapped). (b) The first signal component. (c) The second signal component (simulated signal in blue, estimated signal in red).

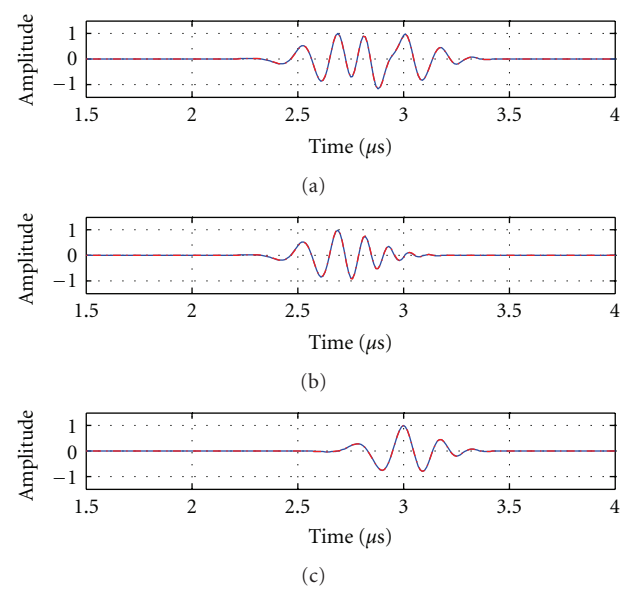

Figure 5: (a) Simulated ultrasonic echoes (50% overlapped). (b) The first signal component. (c) The second signal component (simulated signal in blue, estimated signal in red).

for parameter estimation. This echo isolation is applied iteratively to ultrasonic signal until a predefined stop criterion such as signal reconstruction error or the number of iterations is satisfied. Furthermore, each decomposed component is modeled using six-parameter chirplet echoes for a quantitative analysis of ultrasonic signals.

A bat signal is utilized as a benchmark to demonstrate the effectiveness of fractional Fourier transform chirplet signal decomposition (FrFT-CSD). To further evaluate the performance of FrFT-CSD, ultrasonic experimental data from different types of flaws such as flat bottom hole, side-drilled hole and disk-type cracks are evaluated using FrFT-CSD.

The outline of the paper is as follows. Section 2 reviews the properties of FrFT and the process of FrFT-based signal decomposition. Section 3 addresses how kurtosis, transformation order and chirp rate are related using simulated data. Section 4 presents the steps involved in FrFT-CSD algorithm. Section 5 performs a simulation study of FrFT-CSD and parameter estimation for complex ultrasonic signals. Sections 5 and 6 show the results of a benchmark data (i.e., bat signal); the echo estimation results of benchmark data from side-drilled hole, and disk-shape cracks; the results of experimental data with high microstructure scattering echoes.

2. FrFT of Ultrasonic Chirp Echo

FrFT of a signal, $f(t)$, is given by

$$F^{\alpha}(x) = \frac{e^{-i\,((\pi/4)\,\mathrm{sgn}(\pi\alpha/2)-\,(\pi\alpha/4))}}{(2\pi|\sin(\pi\alpha/2)|)^{1/2}} e^{(1/2)ix^2\cot\,(\pi\alpha/2)} \times \int_{-\infty}^{\infty} e^{(-i\,(xt/\sin(\pi\alpha/2))+(1/2)it^2\cot\,(\pi\alpha/2))} f(t)\,dt, \tag{1}$$

where α denotes transform order of FrFT and x denotes the variable in transform domain.

It has been shown that if the transform order, α, changes from 0 to 4, (i.e., the rotation angle, ϕ, changes from 0 to 2π), $F^{\alpha}(x)$ rotates the signal, $f(t)$, and projects it onto the line of angle, ϕ, in time-frequency domain [19]. This property contributes to FrFT-based decomposition algorithm when applied to ultrasonic signals.

For ultrasonic applications, ultrasonic chirp echo is a type of signal often encountered in ultrasonic backscattered signals accounting for narrowband, broadband, and dispersive echoes. It can be modeled as [8]:

$$f_{\Theta}(t) = \beta \exp\Big[-\alpha_1(t-\tau)^2 + i2\pi\ f_c(t-\tau) + i\alpha_2\ (t-\tau)^2 + i\theta\Big], \tag{2}$$

where $\Theta = [\tau\ f_c\ \beta\ \alpha_1\ \alpha_2\ \theta]$ denotes the parameter vector, τ is the time-of-arrival, f_c is the center frequency, β is the amplitude, α_1 is the bandwidth factor, α_2 is the chirp-rate, and θ is the phase.

Hence, for the ultrasonic Gaussian chirp echo, $f_{\Theta}(t)$, the magnitude of $F^{\alpha}(x)$ given by (1) can be expressed as

$$\begin{aligned} |F^{\alpha}(x)| &= \frac{1}{(2\pi|\sin(\pi\alpha/2)|)^{1/2}} \left| \int_{-\infty}^{\infty} e^{(-i(xt/\sin(\pi\alpha/2))\,+(1/2)it^2\cot\,(\pi\alpha/2))} f(t)\,dt \right| \\ &= \frac{1}{\left(2\sqrt{\alpha_1^2 + (\alpha_2 + (1/2)\cot(\pi\alpha/2))^2}|\sin(\pi\alpha/2)|\right)^{1/2}} \left| e^{(B^2-4AC)/4A} \right|, \end{aligned} \tag{3}$$

where the integration part can be written as

$$\begin{aligned} &\left| \int_{-\infty}^{\infty} e^{(-i\,(xt/\sin(\pi\alpha/2))+(1/2)it^2\cot\,(\pi\alpha/2))} f(t)\,dt \right| \\ &= \left| \int_{-\infty}^{\infty} e^{-[t^2(\alpha_1-\alpha_2 i-(1/2)i\cot\,(\pi\alpha/2))+t(2\alpha_2\tau i-2\alpha_1\tau-2\pi f_0 i+xi\csc(\pi\alpha/2))+(\alpha_1\tau^2-\alpha_2 i\tau^2-\theta+2\pi f_0\tau i)]}\,dt \right| \\ &= \left| \sqrt{\frac{\pi}{A}} e^{(B^2-4AC)/4A} \right|, \end{aligned} \tag{4}$$

with $A = \alpha_1 - \alpha_2 i - (1/2)i\cot\,(\pi\alpha/2)$, $B = 2\alpha_2\tau i - 2\alpha_1\tau - 2\pi\ f_0 i + xi\csc(\pi\alpha/2)$, and $C = \alpha_1\tau^2 - \alpha_2 i\tau^2 - \theta + 2\pi f_0\tau i$.

From (3), it can be seen that, for a linear frequency modulation (LFM) signal (i.e., $\alpha_1 = 0$), if the transformation order, α, satisfies the following equation:

$$\left(\alpha_2 + \frac{1}{2}\cot\frac{\pi\alpha}{2}\right)\sin\frac{\pi\alpha}{2} = 0, \qquad \alpha = -\frac{2}{\pi}\tan^{-1}\left(\frac{1}{2\alpha_2}\right), \tag{5}$$

then the $|F^{\alpha}(x)|$ compacts to a delta function. This means that fractional Fourier transform can be used to compress the duration and compact the energy of ultrasonic chirp echo with an optimal transform order. Optimal transform order can be determined using kurtosis. The energy compaction is a desirable property for ultrasonic signal decomposition, which allows using a window in FrFT domain for isolation of an echo of interest.

3. Kurtosis and FrFT Order

Kurtosis is commonly used in statistics to evaluate the degree of peakedness for a distribution [20, 21]. It is defined as the ratio of 4th-order central moment and square of 2nd-order central moment:

$$K(\alpha) = \frac{\mu_4(F^{\alpha}(x))}{[\mu_2(F^{\alpha}(x))]^2}, \tag{6}$$

where $\mu_4(\bullet)$ denotes 4th-order central moment and $\mu_2(\bullet)$ denotes 2nd-order central moment. A signal with high kurtosis means that it has a distinct peak around the mean. In the literatures of FrFT [18, 19, 22], kurtosis is typically used as a metric to search the optimal transform order of FrFT. Different transform order directs the degree of signal rotation caused by FrFT, and this rotation affects the extent of energy compaction of the transformed signal.

Figure 1(a) shows a chirp signal with the parameters, $\Theta = [3.6\,\mathrm{us}\quad 5\mathrm{MHz}\quad 1\quad 0\quad 25\mathrm{MHz}\quad 0]$. For this

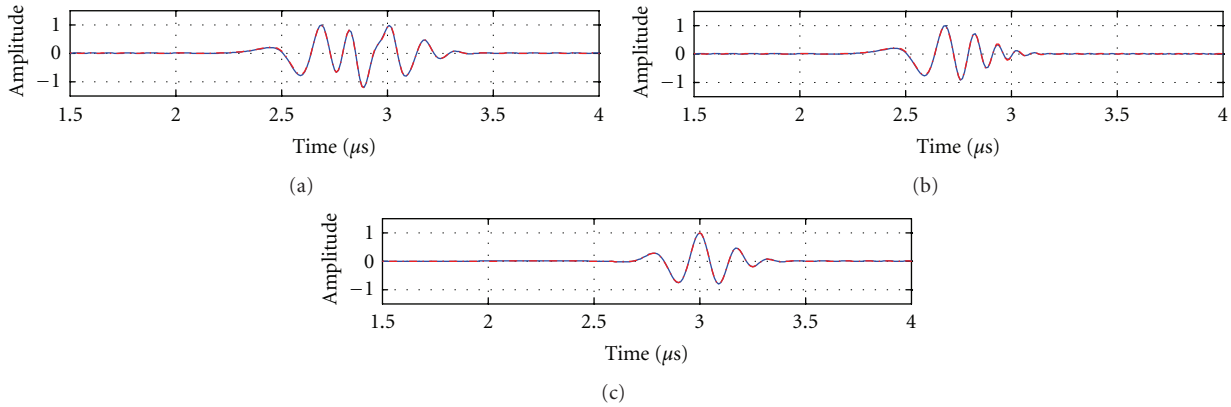

Figure 6: (a) Simulated ultrasonic echoes (70% overlapped). (b) The first estimated echo component. (c) The second estimated echo component (simulated signal in blue, estimated signal in red).

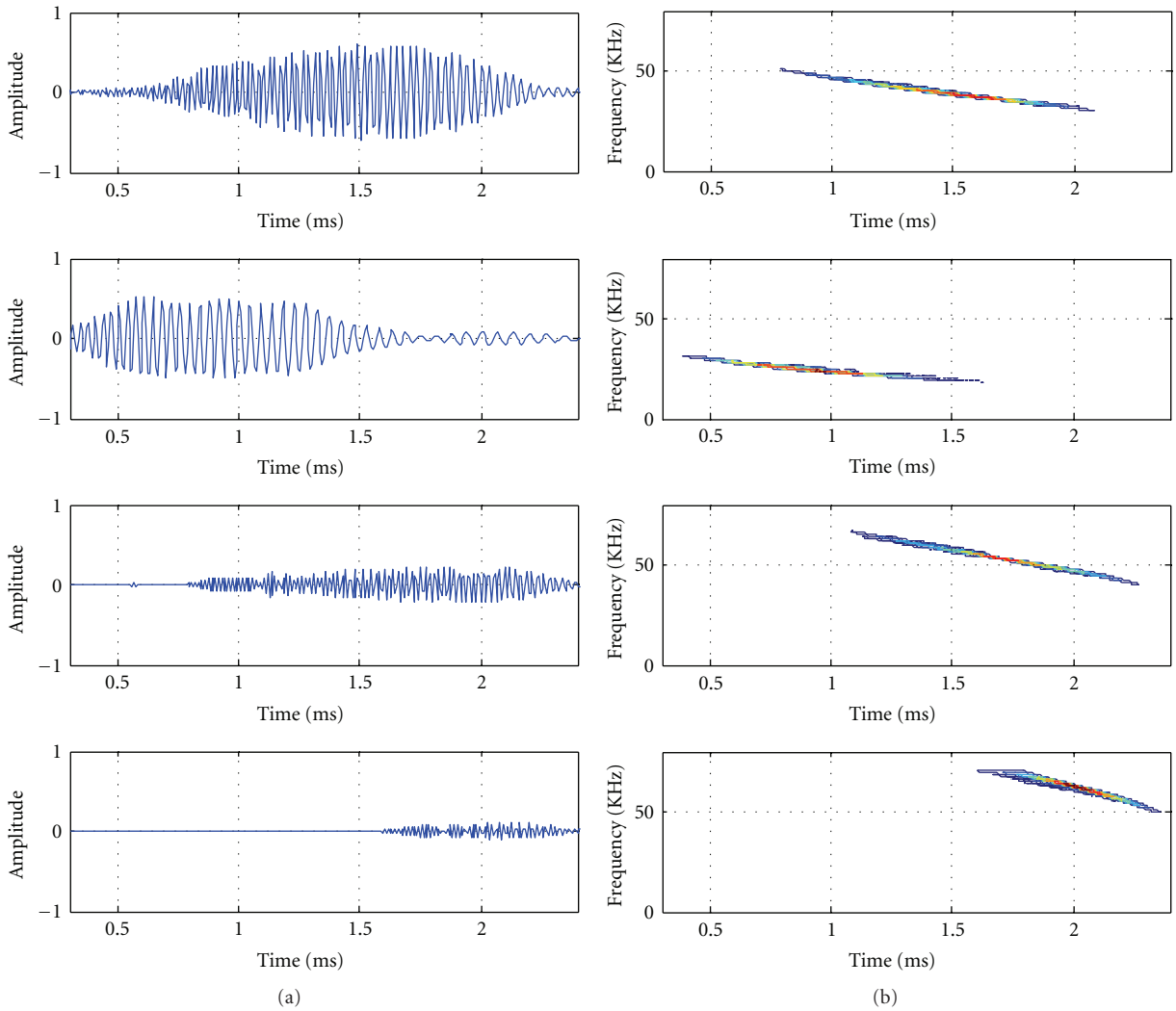

Figure 7: Left column (top to bottom): decomposed bat signal components in time domain. Right column (top to down): Wigner-Ville distribution of the corresponding signals in left column.

Table 3: Parameter estimation results of two heavily overlapped ultrasonic echoes.

	τ (us)	f_c (MHz)	β	α_1 (MHz)^2	α_2 (MHz)^2	θ (Rad)
Echo 1						
Actual parameter	2.7	6	1	20	55	$\pi/6$
Estimated parameter	2.70	6.11	0.97	18.87	53.79	0.72
Echo 2						
Actual parameter	3.0	5	1	25	20	0
Estimated parameter	3.00	5.00	1.00	25.14	20.38	0.01

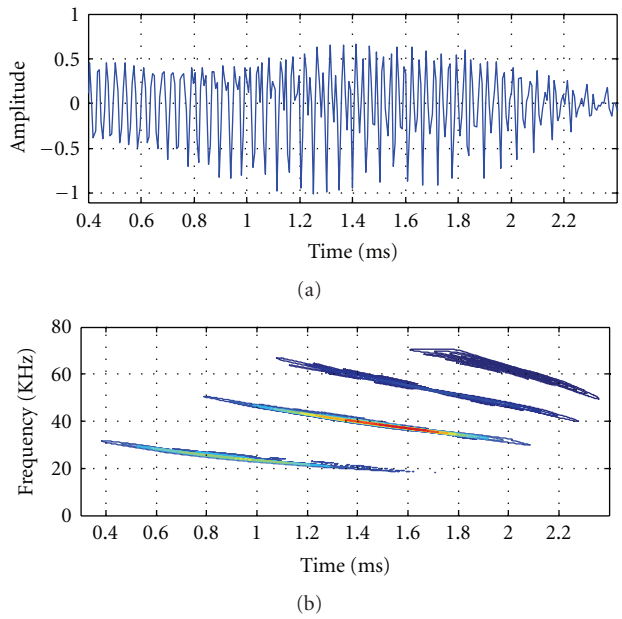

Figure 8: (a) Reconstructed bat signal. (b) Summed Wigner Ville distribution of the decomposed signals in (a).

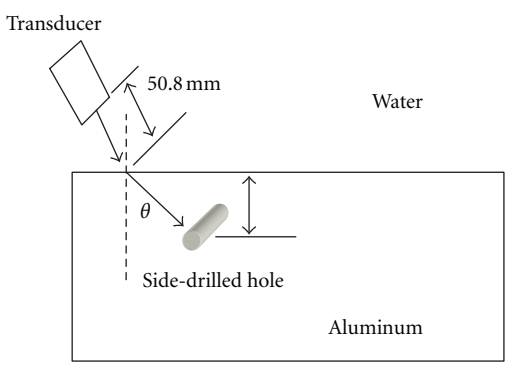

Figure 9: Experiment setup for SDH blocks.

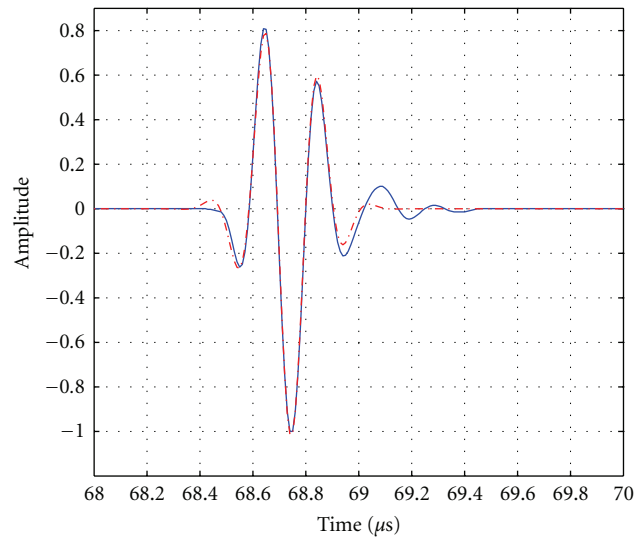

Figure 10: Ultrasonic data from the front surface superimposed with the estimated chirplet (depicted in dashed red color line).

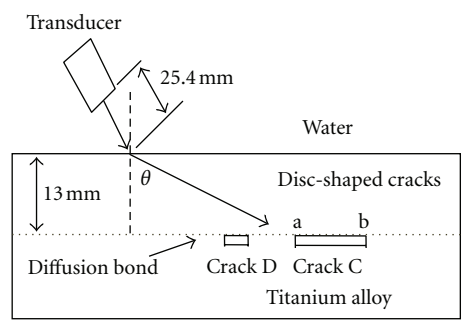

Figure 11: Experiment setup for disc-shaped cracks in a diffusion-bonded titanium alloy.

example, the bandwidth factor equals to zero (see (2)), and according to (5), the optimal transform order can be calculated as

$$\alpha = -\frac{2}{\pi}\tan^{-1}\left(\frac{1}{2\alpha_2}\right) = -0.013. \tag{7}$$

As shown in Figure 1(b), this optimal order can also be determined by direct search for the maximum amplitude of FrFT using different transform orders according to (3). The transform order corresponding to the maximum FrFT among all transform orders matches the theoretical result given in (7).

For ultrasonic applications, the chirp echo is band-limited. For example, Figure 2(a) shows a band-limited single chirp echo with the parameters $\Theta = [3.6\,\text{us} \quad 5\text{MHz} \quad 1 \quad 25\text{MHz} \quad 25\text{MHz} \quad 0]$. Chirplet is a model widely used in ultrasonic NDE applications. Figure 2 illustrates the FrFT of a chirplet using different transform orders. In particular,

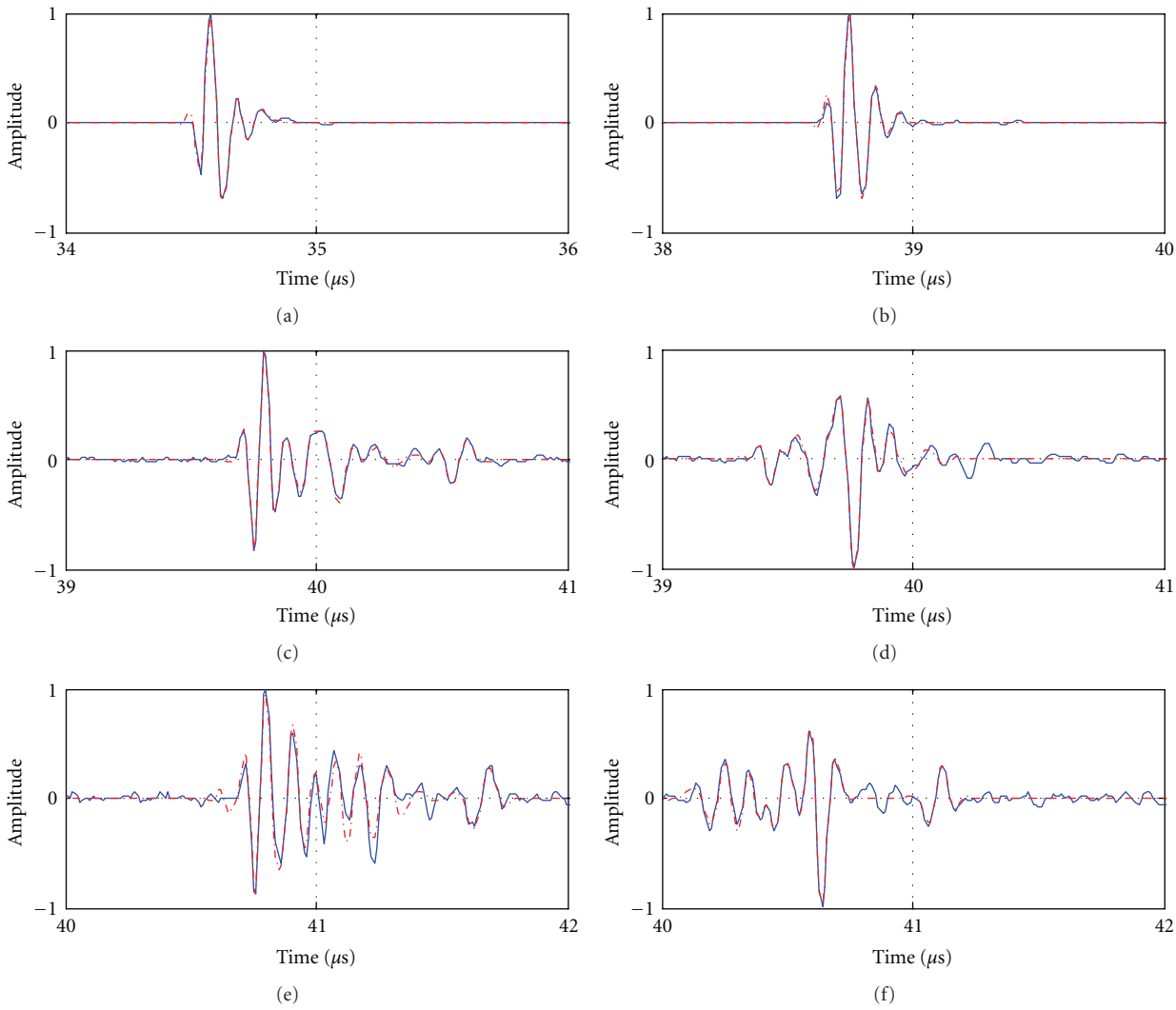

Figure 12: Experimental data of **crack C** (with normalized amplitudes) superimposed with the estimated chirplets. (a) Front surface reference signal superimposed with sum of 2 chirplets. (b) Experimental data (refracted angle 0) superimposed with sum of 2 chirplets. (c) Experimental data (refracted angle 30 at point a) superimposed with sum of 4 chirplets. (d) Experimental data (refracted angle 30 at point b) superimposed with sum of 4 chirplets. (e) Experimental data (refracted angle 45 at point a) superimposed with sum of 4 chirplets. (f) Experimental data (refracted angle 45 at point b) superimposed with sum of 4 chirplets.

Table 4: Estimated parameters of chirplets (block with 1 mm SDH).

	Chirplet parameters	Refracted angle		
		0°	30°	45°
Spherically focused transducer	Amplitude (m-Volt)	42.5	29	16.01
	TOA (us)	76.62	82.6	89.39
	Frequency (MHz)	4.55	4.6	4.32
Planar transducer	Amplitude (m-Volt)	22.71	20.43	14.53
	TOA (us)	76.57	82.80	89.82
	Frequency (MHz)	4.48	4.67	4.81

Table 5: Estimated parameters of chirplets (block with 4 mm SDH).

	Chirplet parameters	Refracted angle		
		0°	30°	45°
Spherically focused transducer	Amplitude (m-Volt)	87.75	59.34	32.61
	Time of arrival (us)	76.10	82.05	88.88
	Frequency (MHz)	4.61	4.54	4.39
Planar transducer	Amplitude (m-Volt)	41.72	37.62	27.97
	Time of arrival (us)	76.11	82.36	89.42
	Frequency (MHz)	4.46	4.67	4.84

the transform order from (7) (i.e., -0.013) is used for a comparison. Our simulation shows that the optimal transform order for the band-limited echo is different compared with the one for the LFM echo due to the impact of bandwidth factor in chirp echoes.

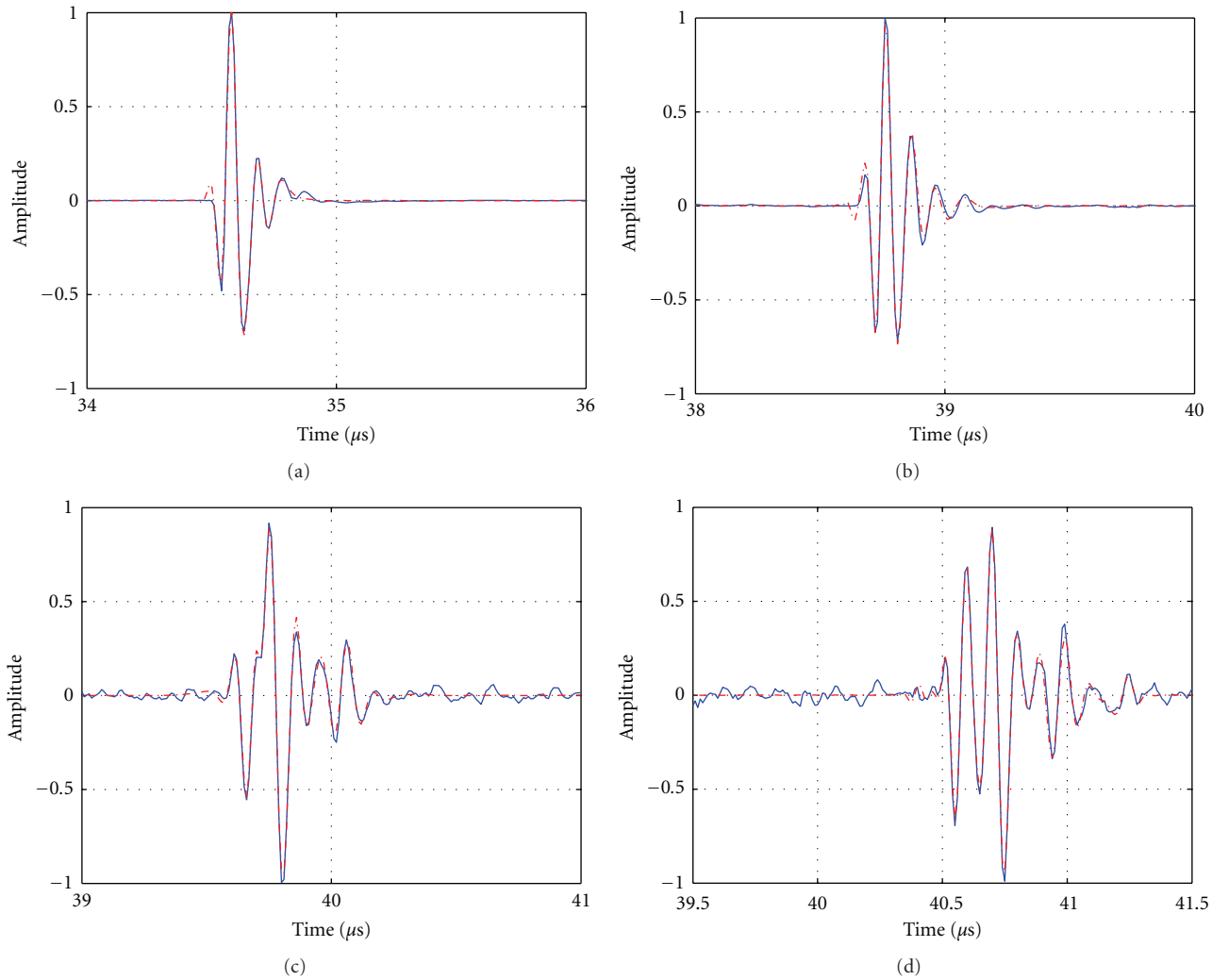

Figure 13: Experimental data of **Crack D** (with normalized amplitudes) superimposed with the estimated chirplets (depicted in dashed red line). (a) Front surface reference signal superimposed with sum of 2 chirplets. (b) Experimental data (refracted angle 0) superimposed with sum of 2 chirplets. (c) Experimental data (refracted angle 30) superimposed with sum of 4 chirplets. (d) Experimental data (refracted angle 45) superimposed with sum of 4 chirplets.

Table 6: Estimated parameters of chirplets (crack D).

	TOA (us)	Center frequency (MHz)	Amplitude (m-Volt)
Reference signal	34.583	9.42	363.3
	34.725	10.60	54.4
Refracted angle 0°	38.776	10.38	4.64
	38.891	13.06	0.50
Refracted angle 30°	39.777	7.68	0.50
	40.040	9.10	0.14
	39.674	12.57	0.18
	39.861	2.18	0.03
Refracted angle 45°	40.677	9.85	0.17
	40.956	9.85	0.07
	40.675	4.51	0.04
	40.620	15.65	0.03

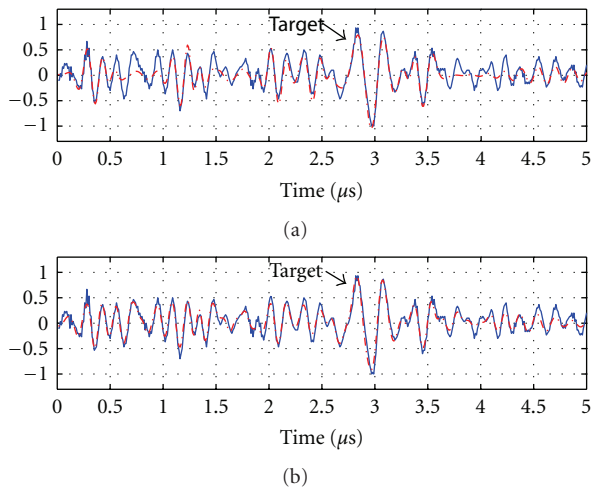

Figure 14: (a) Measured ultrasonic backscattered signal (blue) superimposed with the reconstructed signal consisting of 8 dominant chirplets (red). (b) Measured ultrasonic backscattered signal (blue) superimposed with the reconstructed signal consisting of 23 chirplets (red).

One can conclude that the compactness in the fractional Fourier transform of an ultrasonic echo can be used to track the optimal transform order. It is also important to point out that the optimal transform order is highly sensitive to a small change in the order. Therefore, using kurtosis becomes a practical approach to obtain the optimal FrFT order for ultrasonic signal analysis.

4. FrFT Chirplet Signal Decomposition Algorithm

The objective of FrFT-CSD is to decompose a highly convoluted ultrasonic signal, $s(t)$, into a series of signal components:

$$s(t) = \sum_{j=1}^{N} f_{\Theta j}(t) + r(t), \tag{8}$$

where $f_{\Theta j}(t)$ denotes the jth fractional chirplet component and $r(t)$ denotes the residue of the decomposition process.

The steps involved in the iterative estimation of an experimental ultrasonic signal are

(1) initialize the iteration index $j = 1$;

(2) obtain a windowed signal $s\_\text{win}(t)$ after applying a window, $w_j(t)$, in time domain;

$$s_{\text{win}(t)} = s(t) \times w_j(t). \tag{9}$$

(3) determine the FrFT of the signal, $s\_\text{win}(t)$, $\text{FrFT}^{\alpha}(x)_{s\_\text{win}(t)}$, for different orders, α;

(4) calculate kurtosis of $\text{FrFT}^{\alpha}(x)_{s\_\text{win}(t)}$ for different orders, α:

$$K(\alpha) = \frac{\mu_4\left(\text{FrFT}^{\alpha}(x)_{s\_\text{win}(t)}\right)}{\left[\mu_2\left(\text{FrFT}^{\alpha}(x)_{s\_\text{win}(t)}\right)\right]^2}; \tag{10}$$

(5) estimate the optimal transform order, α_{opt}:

$$\alpha_{\text{opt}} = \arg_{\alpha}\text{MAX}\ (K(\alpha)), \tag{11}$$

α_{opt} corresponds to the FrFT transform order where $K(\alpha)$ has the max value. In our study, a brute-force search is used to estimate the optimal transform order. The step size of searching is set to 0.005. The computation load of calculating the kurtosis and searching for the optimal order is significant. Some researchers used the maximum peak in the transform domain as an alternative metric [17]. For ultrasonic signal decomposition, the optimal transform order is related to the chirp rate of the signal. The search range of transform order can be reduced by considering prior knowledge of ultrasonic transducer impulse response;

(6) apply FrFT with the estimated order α_{opt} to the signal $s(t)$ and obtain $\text{FrFT}^{\alpha_{\text{opt}}}(x)_{s(t)}$;

(7) obtain a windowed signal from $\text{FrFT}^{\alpha_{\text{opt}}}(x)_{s(t)}$:

$$\text{FrFT}_{\text{win}}(x) = \text{FrFT}^{\alpha_{\text{opt}}}(x)_{s(t)} \times \text{win}_j(x), \tag{12}$$

(8) apply the transformation order, $-\alpha_{\text{opt}}$, to the signal $\text{FrFT\_win}(x)$, then reconstruct the jth component by estimating parameters of the decomposed echo:

$$f_{\Theta_j}(t) = \text{FrFT}^{-\alpha_{\text{opt}}}(t)_{\text{FrFT\_win}(x)}, \tag{13}$$

the parameter estimation process here becomes a single-echo estimation problem. A Gaussian-Newton algorithm used in [23–25] is adopted in FrFT-CSD;

(9) obtain the residual signal by subtracting the estimated echo from the signal, $s(t)$, and use the residual signal for next echo estimation;

(10) calculate energy of residual signal (E_r) and check convergence: ($E_{\min}$ is predefined convergence condition) If $E_r < E_{\min}$, STOP; otherwise, go to step 2.

For further clarification, the flowchart of FrFT-CSD algorithm is shown in Figure 3. It is important to mention that two windowing steps are used in FrFT-CSD algorithm. One window is used in step 2 in order to isolate a dominant echo in time domain. It is inevitable to have an incomplete echo due to windowing process. A good strategy of choosing this window is to keep as much of echo information as possible. The other window is applied in step 7. For ultrasonic chirp echoes, the energy compactness of FrFT helps to reduce the window size centered on a desired peak in the transform domain. As shown in Figure 2, a chirplet is compressed to a great extent after the transform. An

automatic windowing process is used to detect the valleys of the dominant echo. In the cases of heavily overlapping echoes and high noise levels (i.e., the cases of poor signal-to-noise ratio), the performance of windowing method may be compromised. In this situation, a window with a predetermined size can be used to isolate desirable peaks.

5. Simulation and Benchmark Study of FrFT-CSD

To demonstrate the advantages of FrFT signal decomposition in ultrasonic signal processing, ultrasonic chirp echoes with three different overlapping scenarios are simulated, where chirp rate models the dispersive effect in ultrasonic testing of materials. Two slightly overlapped (about 20% overlapped) echoes is simulated using the sampling frequency of 100 MHz. The parameters of these two echoes are

$$\begin{aligned} \Theta_1 &= \left[2.5\text{us} \quad 7\,\text{MHz} \quad 1 \quad 20\,\text{MHz}^2 \quad 35\,\text{MHz}^2 \quad \frac{\pi}{6}\right], \\ \Theta_2 &= \left[3.0\,\text{us} \quad 5\,\text{MHz} \quad 1 \quad 25\,\text{MHz}^2 \quad 20\,\text{MHz}^2 \quad 0\right]. \end{aligned} \tag{14}$$

Figure 4 shows the simulated signal (in blue) superimposed with estimated echoes (in red). The estimated parameters perfectly match the parameters of simulation signal as compared in Table 1. One can conclude that the FrFT-CSD not only decomposes the signal efficiently, but also leads to precise parameter estimation results. A moderately overlapped (about 50% overlapped) simulated signal consisting of two echoes is shown in Figure 5. For this simulated signal, Table 2 shows that the estimated parameters are accurate within a few percents.

Finally, Figure 6 and Table 3 show the simulated and estimated two heavily overlapped (about 70% overlapped) echoes. The decomposition results (Figure 6) and estimated parameters (Table 3) confirm the robustness and effectiveness of FrFT-CSD in echo estimation for ultrasonic signal analysis.

An experimental bat data is commonly used as a benchmark signal in time-frequency analysis. It is a 400-sample data digitized 2.5 μs echolocation pulse emitted by a *large brown bat* with 7 μs sampling period. To evaluate the performance of FrFT-based signal decomposition algorithm, the bat data is utilized to demonstrate the effectiveness of algorithm.

Through the processing of FrFT-CSD, there are four main chirp-type signal components identified in the bat signal. The decomposed signals and their Wigner-Ville distribution (WVD) are shown in Figure 7. The reconstructed signal and its superimposed WVD are shown in Figure 8. The results in Figures 7 and 8 are consistent with the analysis results from other techniques in time-frequency analysis [26]. The FrFT-based signal decomposition algorithm not only reveals that the bat signal mainly contains four chirp stripes in time-frequency domain, but provides a high-resolution time-frequency representation.

6. Experimental Studies

For experimental studies, two aluminum blocks with different size of side-drilled hole (SDH) are used [27]. One is with 1 mm diameter, another is 4 mm diameter. The experimental setting is shown in Figure 9. It can be seen that the water path is 50.8 mm and the depth of SDH is 25.4 mm (i.e., from the water-aluminum interface to the center of SDH).

To provide a rigorous test, two 5 MHz transducers are used to acquire ultrasonic data at normal or oblique refracted angles, θ. One is planar transducer. Another is spherically focused transducer with 172.9 mm focal length.

To verify the experiment setup, the FrFT-CSD is utilized to analyze the ultrasonic data from the front surface of the specimen. The ultrasonic data superimposed with the estimated chirplet is shown in Figure 10.

It can be seen that the estimated time-of-arrival (TOA) of the front surface echo is 68.72 μs. In addition, from the experimental setting, the TOA can be calculated as

$$\text{TOA} = \frac{2 \times D}{v}, \tag{15}$$

where D denotes the water distance, and in the case of incidence angle 0 this distance is 50.8 mm. The round trip of ultrasound is twice of the water distance, D. The term v denotes the velocity of ultrasound in medium: $v = 1.484$ mm/μs for water.

From (15), the theoretical value of TOA is 68.47 μs. The estimated TOA is in agreement (within 0.4%) with the theoretical TOA.

Furthermore, the parameters of chirplet are strongly related to the crack size, location, and orientation. For example, the amplitude is a good indicator of crack size. In Tables 4 and 5, the estimated amplitude from a 4 mm SDH is roughly twice of the estimated amplitude from a 1 mm SDH. In NDE applications, the estimated amplitude of a known-size crack could be used as a reference to estimate the size of crack. As shown in (15) and (16), the estimated TOA can be used to approximate the location of crack. In addition, different types of cracks could have different frequency variations. From [8, 26], the response of crack usually shows a downshift in the frequency compared with the responses of grains inside the material.

These results indicate that the estimated parameters from FrFT-CSD algorithm track with reasonable accuracy the physical parameters of experimental setup. Moreover, the FrFT-CSD algorithm provides more detailed information describing the reflected echoes such as phase, bandwidth factor and chirp rate that can be used for further analysis.

Another experiment is set up to evaluate disk-shaped cracks in a diffusion-bonded titanium alloy sample [28]. The ultrasonic data of these synthetic cracks are obtained at normal or oblique refracted angles, θ using a 10 MHz planar transducer. The diameter of the transducer is 6.35 mm. The water depth is 25.4 mm. The surface of diffusion bond is 13 mm below the front surface of water/titanium alloy interface. Two different sizes of cracks are made with the diameter 0.762 mm (i.e., crack D) and the diameter 1.905 mm (i.e., crack C). For crack C, the responded ultrasonic data is

Table 7: Estimated parameters of chirplets (crack C).

	TOA (us)	Center frequency (MHz)	Amplitude (m-Volt)
Reference signal	34.583	9.42	363.3
	34.725	10.60	54.4
Refracted angle 0°	38.754	9.78	14.48
	38.863	12.93	1.86
Refracted angle 30° (point a)	39.784	11.02	0.58
	40.029	6.06	0.19
	40.560	7.68	0.13
	40.122	10.63	0.06
Refracted angle 45° (point a)	40.825	9.88	0.14
	41.157	9.92	0.07
	40.795	15.64	0.04
	41.658	6.87	0.05
Refracted angle 30° (point b)	39.757	7.78	0.49
	39.536	5.32	0.11
	39.905	4.63	0.10
	39.426	11.13	0.10
Refracted angle 45° (point b)	40.632	9.09	0.21
	40.270	9.65	0.07
	40.468	3.40	0.16
	41.100	7.97	0.07

Table 8: Estimated parameters of the 8 dominant chirplets for ultrasonic experimental data.

	τ (us)	f_c (MHz)	β	α_1 (MHz)^2	α_2 (MHz)^2	θ (Rad)
Echo 1	2.95	3.87	1.06	20.16	13.17	2.80
Echo 2	3.47	5.53	0.63	56.86	−41.06	−2.70
Echo 3	0.33	6.57	0.54	37.45	28.66	1.76
Echo 4	1.18	7.24	0.54	27.14	30.17	3.71
Echo 5	2.08	6.66	0.53	39.13	−15.50	2.75
Echo 6	2.40	6.00	0.47	62.91	60.24	2.47
Echo 7	4.64	6.23	0.18	4.75	−0.18	−2.36
Echo 8	1.49	3.97	0.12	0.73	−0.04	−6.64

recorded from the two edges of the crack, which are marked as point a and point b. The thickness of both disk-shaped cracks is 0.089 mm. Figure 11 shows the experiment setup for the alloy sample [28].

From Figure 11, the TOA of crack at refracted angle θ is calculated as follows:

$$\mathrm{TOA}_\theta = \mathrm{TOA}_{\mathrm{ref}} + \frac{2 \times D/\cos\theta}{v}, \tag{16}$$

where $\mathrm{TOA}_{\mathrm{ref}}$ denotes the estimated TOA of reference signal (i.e., 34.58 μs from Tables 6 and 7). The round trip of ultrasound inside titanium from the front surface to the diffusion bound is $2 \times D/\cos\theta$, where D denotes the depth of diffusion bond, which is 13 mm; θ denotes the refracted angle and v denotes the velocity of ultrasound in medium: $v = 6.2$ mm/μs for titanium. Therefore, TOA_θ at the angle 0° is 38.777 μs. TOA_θ at the angle 30° is 39.425 μs. At the angle 45°, TOA_θ is 40.514 μs.

From Tables 6 and 7, it can be seen that the estimated TOA_θ at angle 0° is 38.776 μs and 38.754 μs. Taking the thickness of the cracks (0.089 mm) into consideration, it can be asserted that the estimated TOAs at incident angle 0° are in good agreement with experimental measurements. Experimental signals of crack C and crack D (with normalized amplitudes) superimposed with the estimated chirplets (depicted in dashed line and red color) are shown in Figures 12 and 13. It also can be seen that the front surface reference signal and the experimental data obtained at angle 0° are well reconstructed by the FrFT-CSD algorithm (see Figures 12(a), 12(b), 13(a) and 13(b)). Nevertheless, with the increase of refracted angle, more chirplets needed to decompose the experimental data (see the refracted angle 30 and 45 degree

cases). In addition, Tables 6 and 7 show that the signal energy is more evenly distributed to estimated chirplets in the high refracted angle cases. This spreading of signal might be caused by geometrical effect of the beam profile of the planner transducer and corners/edges of disk-shaped crack.

To further evaluate the performance of FrFT-based signal decomposition algorithm, experimental ultrasonic microstructure scattering signals are utilized to demonstrate the effectiveness of the algorithm. The experimental signal is acquired from a steel block with an embedded defect using a 5 MHz transducer and sampling rate of 100 MHz. The acquired experimental data superimposed with the reconstructed signal consisting of 8 dominant chirplets are shown in Figure 14(a). The estimated parameters of dominant chirplets are listed in Table 8. It can be seen that the 8 dominant chirplets not only provide a sparse representation of experimental data, but successfully detect the embedded defect.

To improve the accuracy of signal reconstruction, FrFT-CSD could be used iteratively to decompose the signal further. A reconstructed signal using 23 chirplets is shown in Figure 14(b). The comparison between the experimental signal and the reconstructed signals clearly demonstrates that the FrFT-CSD is highly effective in ultrasonic signal decomposition.

7. Conclusion

In this paper, fractional Fourier transform is studied for ultrasonic signal processing. Simulation study reveals the link among kurtosis, the transform order, and the parameters of each decomposed components. Benchmark and experimental data sets are utilized to test the FrFT-based chirplet signal decomposition algorithm. Signal decomposition and parameter estimation results show that fractional Fourier transform can successfully assist signal decomposition algorithm by identifying the dominant echo in successive estimation iteration. Parameter estimation is further performed based on the echo isolation. The FrFT-CSD algorithm could have a broad range of applications in signal analysis including target detection and pattern recognition.

Acknowledgments

The authors wish to thank Curtis Condon, Ken White, and Al Feng of the Beckman Institute of the University of Illinois for the bat data and for permission to use it in the study.

References

[1] S. Mallat, *A Wavelet tour of Signal Processing: The Sparse Way*, Academic Press, 2008.

[2] I. Daubechies, "The wavelet transform, time-frequency localization and signal analysis," *IEEE Transactions on Information Theory*, vol. 36, no. 5, pp. 961–1005, 1990.

[3] S. Mann and S. Haykin, "The chirplet transform: physical considerations," *IEEE Transactions on Signal Processing*, vol. 43, no. 11, pp. 2745–2761, 1995.

[4] G. Cardoso and J. Saniie, "Ultrasonic data compression via parameter estimation," *IEEE Transactions on Ultrasonics, Ferroelectrics, and Frequency Control*, vol. 52, no. 2, pp. 313–325, 2005.

[5] R. Tao, Y. L. Li, and Y. Wang, "Short-time fractional fourier transform and its applications," *IEEE Transactions on Signal Processing*, vol. 58, no. 5, pp. 2568–2580, 2010.

[6] S. Zhang, M. Xing, R. Guo, L. Zhang, and Z. Bao, "Interference suppression algorithm for SAR based on time frequency domain," *IEEE Transaction on Geoscience and Remote Sensing*, vol. 49, no. 10, pp. 3765–3779, 2011.

[7] E. Oruklu and J. Saniie, "Ultrasonic flaw detection using discrete wavelet transform for NDE applications," in *Proceedings of IEEE Ultrasonics Symposium*, pp. 1054–1057, August 2004.

[8] Y. Lu, R. Demirli, G. Cardoso, and J. Saniie, "A successive parameter estimation algorithm for chirplet signal decomposition," *IEEE Transactions on Ultrasonics, Ferroelectrics, and Frequency Control*, vol. 53, no. 11, pp. 2121–2131, 2006.

[9] S. C. Pel and J. J. Ding, "Closed-form discrete fractional and affine fourier transforms," *IEEE Transactions on Signal Processing*, vol. 48, no. 5, pp. 1338–1353, 2000.

[10] L. B. Almeida, "Fractional fourier transform and time-frequency representations," *IEEE Transactions on Signal Processing*, vol. 42, no. 11, pp. 3084–3091, 1994.

[11] C. Candan, M. Alper Kutay, and H. M. Ozaktas, "The discrete fractional fourier transform," *IEEE Transactions on Signal Processing*, vol. 48, no. 5, pp. 1329–1337, 2000.

[12] A. S. Amein and J. J. Soraghan, "The fractional Fourier transform and its application to High resolution SAR imaging," in *Proceedings of IEEE International Geoscience and Remote Sensing Symposium (IGARSS '07)*, pp. 5174–5177, June 2007.

[13] M. Barbu, E. J. Kaminsky, and R. E. Trahan, "Fractional fourier transform for sonar signal processing," in *Proceedings of MTS/IEEE OCEANS*, vol. 2, pp. 1630–1635, September 2005.

[14] I. S. Yetik and A. Nehorai, "Beamforming using the fractional fourier transform," *IEEE Transactions on Signal Processing*, vol. 51, no. 6, pp. 1663–1668, 2003.

[15] S. Karako-Eilon, A. Yeredor, and D. Mendlovic, "Blind source separation based on the fractional Fourier transform," in *Proceedings of the 4th International Symposium on Independent Component Analysis and Blind Signal Separation*, pp. 615–620, 2003.

[16] A. T. Catherall and D. P. Williams, "High resolution spectrograms using a component optimized short-term fractional Fourier transform," *Signal Processing*, vol. 90, no. 5, pp. 1591–1596, 2010.

[17] M. Bennett, S. McLaughlin, T. Anderson, and N. McDicken, "Filtering of chirped ultrasound echo signals with the fractional fourier transform," in *Proceedings of IEEE Ultrasonics Symposium*, pp. 2036–2040, August 2004.

[18] L. Stanković, T. Alieva, and M. J. Bastiaans, "Time-frequency signal analysis based on the windowed fractional Fourier transform," *Signal Processing*, vol. 83, no. 11, pp. 2459–2468, 2003.

[19] Y. Lu, A. Kasaeifard, E. Oruklu, and J. Saniie, "Performance evaluation of fractional Fourier transform(FrFT) for time-frequency analysis of ultrasonic signals in NDE applications," in *Proceedings of IEEE International Ultrasonics Symposium (IUS '10)*, pp. 2028–2031, October 2010.

[20] F. Millioz and N. Martin, "Circularity of the STFT and spectral kurtosis for time-frequency segmentation in Gaussian

environment," *IEEE Transactions on Signal Processing*, vol. 59, no. 2, pp. 515–524, 2011.

[21] R. Merletti, A. Gulisashvili, and L. R. Lo Conte, "Estimation of shape characteristics of surface muscle signal spectra from time domain data," *IEEE Transactions on Biomedical Engineering*, vol. 42, no. 8, pp. 769–776, 1995.

[22] Y. Lu, E. Oruklu, and J. Saniie, "Analysis of Fractional Fouriter transform for ultrasonic NDE applications," in *Proceedings of IEEE Ultrasonic Symposium*, Orlando, Fla, USA, October 2011.

[23] R. Demirli and J. Saniie, "Model-based estimation of ultrasonic echoes part I: analysis and algorithms," *IEEE Transactions on Ultrasonics, Ferroelectrics, and Frequency Control*, vol. 48, no. 3, pp. 787–802, 2001.

[24] R. Demirli and J. Saniie, "Model-based estimation of ultrasonic echoes part II: nondestructive evaluation applications," *IEEE Transactions on Ultrasonics, Ferroelectrics, and Frequency Control*, vol. 48, no. 3, pp. 803–811, 2001.

[25] R. Demirli and J. Saniie, "Model based time-frequency estimation of ultrasonic echoes for NDE applications," in *Proceedings of IEEE Ultasonics Symposium*, pp. 785–788, October 2000.

[26] Y. Lu, E. Oruklu, and J. Saniie, "Ultrasonic chirplet signal decomposition for defect evaluation and pattern recognition," in *Proceedings of IEEE International Ultrasonics Symposium (IUS '09)*, ita, September 2009.

[27] Ultrasonic Benchmark Data, World Federation of NDE, 2004, http://www.wfndec.org/.

[28] Ultrasonic Benchmark Data, World Federation of NDE, 2005, http://www.wfndec.org/.

Hindawi Publishing Corporation
Advances in Acoustics and Vibration
Volume 2012, Article ID 957379, 10 pages
doi:10.1155/2012/957379

Research Article

Ultrasonic Flaw Detection and Imaging through Reverberant Layers via Subspace Analysis and Projection

Ramazan Demirli,[1] Moeness G. Amin,[1] Xizhong Shen,[2] and Yimin D. Zhang[1]

[1] *Center for Advanced Communication, Villanova University, Villanova, PA 19085, USA*
[2] *School of Electrical and Electronic Engineering, Shanghai Institute of Technology, Shanghai 201418, China*

Correspondence should be addressed to Ramazan Demirli, ramazan.demirli@villanova.edu

Received 12 March 2012; Revised 30 May 2012; Accepted 31 May 2012

Academic Editor: Erdal Oruklu

Ultrasonic flaw detection and imaging through reverberant layers are challenging problems owing to the layer-induced reverberations and front surface reflections. These undesired signals present a strong clutter and mask the flaw echoes. In this paper, a subspace-based approach is developed for removing, or significantly reducing, the unwanted reverberations, enabling proper flaw detection and imaging. The technique utilizes a set of independent clutter-only reference measurements of the material through the layer. If these measurements are not available, array measurements of the material with flaws are used instead. The clutter, due to its high strength relative to the flaw reflections, forms a subspace spanned by the eigenvectors corresponding to the dominant eigenvalues of the data covariance matrix. The clutter subspace is estimated and removed using orthogonal subspace projection. The clutter usually occupies multidimension subspace that is dependent on the level of coupling, material inhomogeneity, surface roughness, and the sampling rate of the measurements. When the clutter-only reference is not available, information theoretic techniques are used to estimate the dimension of the clutter subspace so that clutter signals are sufficiently suppressed without distorting the flaw signals. The effectiveness of the proposed approach is demonstrated using simulations and real measurement results.

1. Introduction

Ultrasonic detection and imaging of flaws through a layer or screen are challenging problems encountered in ultrasound nondestructive evaluation (NDE). In particular, industrial materials are often manufactured in the forms of multiple layers, which present strong reflections at layer interfaces when exposed to ultrasound testing. These reflections usually repeat themselves in the course of an ultrasonic measurement, giving rise to strong and repeating reverberation patterns [1]. In medical ultrasound, direct access to the tissue of interest is not always possible, and hence ultrasonic measurements are often performed through another tissue or anatomic structure [2]. For example, in ultrasound imaging of brain for abnormalities or tumors, measurements are performed through the skull, which presents strong reverberation signal.

Reverberation signals induced by the top layer (i.e., imaging screen) often mask the target echoes and make the detection and localization of material flaws or tissue abnormalities extremely difficult, if not impossible. Therefore, such reverberation signals (which are also referred to hereafter as reverberation clutter, or simply clutter) must be suppressed or sufficiently mitigated in order to reveal the target echoes. The majority of the existing approaches dealing with reverberation are based on the ideal acoustic wave propagation model in the layered media [1, 3–6]. For example, Saniie and Nagle have developed analytical models of reverberation patterns measured from multilayered media [1]. These models are used for the classification of echoes associated with each layer. The predictive deconvolution technique [7], commonly used in reverberation suppression in seismic explorations, has been applied to ultrasound reverberation suppression [3, 4]. This method also assumes,

although implicitly, an ideal propagation model by relying on the repeatability of reverberating patterns. The methods presented in [5, 6] deal with the identification of reverberation echoes in multilayered media based on time-of-flight analysis of all possible echoes and their power spectrum comparison. In addition to the ideal propagation models mentioned above, these techniques assume nonoverlapping echo patterns amenable to time-of-flight analysis, which requires the thickness of each layer to be relatively large compared to the echo wavelength. Further, the existing approaches often deal with ultrasonic measurements in the far field of the transducer and, as such, use immersion techniques. These techniques are not practical for field testing scenarios in ultrasonic NDE where only contact measurements can be performed in the near field of the transducer. Making contact measurements through the layer is further complicated by the coupling issues and strong irregular echoes from the layer front surface. The reverberation patterns in these cases cannot be simply predicted and removed from the measurements.

Among different possible approaches to considerably attenuate clutter, direct subtraction of background response signal, measured in empty reference scenes, from the response signal with targets (flaws) is commonly used in radar signal processing [8]. Direct application of this method to practical ultrasonic reverberation suppression, however, proves inefficient, due to the significant variations of ultrasound measurements due to the coupling, material inhomogeneity, and surface roughness.

In this paper, we propose an alternative approach based on reverberation subspace learning and projection. This approach has been recently used in through-the-wall radar imaging to remove the wall clutter and enhance the visibility of indoor targets [9, 10] and also in ground penetrating radar for landmine detection [8, 11]. In the proposed approach, the clutter is removed by projecting the received signal onto a subspace that is orthogonal to the bases of possible clutter responses. To construct a comprehensive clutter subspace for efficient clutter removal, we consider two cases of reverberation subspace learning that are of interest to ultrasound NDE, namely, (i) reference-based subspace learning (offline) utilizing a set of flaw-free reverberation measurements and (ii) reference-free subspace learning directly from the online array data. The latter is of particular importance in NDE array imaging when access to a healthy replica is not available [12]. In the first case, we make use of a few independent reverberation measurements from selected locations using a healthy replica of the test material. Then, we construct a clutter subspace utilizing a shift-based perturbation model to account for variations due to surface contacts, material inhomogeneity, and surface roughness. In the second case, we use a physical or synthetic aperture array and form the clutter subspace by exploiting the spatial coherency of the reverberation signals and incoherency of the flaw echoes in the array data. In both cases, the clutter often occupies multiple dimensions of the subspace, dependent on the level of coupling, material inhomogeneity, surface roughness, and the sampling rate of the measurements. Therefore, the dimension of the clutter subspace must be properly estimated before the orthogonal projection is applied. Underestimation of the clutter subspace may result in insufficient clutter removal. On the other hand, particularly in the second case where the flaw signals are present in the clutter subspace construction, overestimation of the clutter subspace will result in flaw signal removal. To avoid this problem, information theoretic techniques are used to estimate the dimension of the clutter subspace so that clutter signals are sufficiently suppressed without distorting the flaw signals.

The effectiveness of the proposed method is examined and demonstrated using both simulations and real experiment data. The results clearly show that strong clutter can be significantly suppressed using the proposed technique based on subspace learning and orthogonal subspace projection. For comparison, we also apply the background subtraction and predictive deconvolution techniques, which show inferior performance to the proposed technique in the presence of irregular variations.

The remainder of the paper is organized as follows. Section 2 presents a clutter subspace construction and projection technique utilizing flaw-free reference measurements of reverberation. Section 3 presents a reference-free clutter subspace construction and projection technique based on transducer array data. Section 4 presents the simulation and experimental results of the clutter removal techniques in both scenarios.

2. Clutter Removal Using Reference Reverberation Measurements

2.1. The Proposed Technique. Consider a flaw detection and imaging problem through a reverberant layer, as depicted in Figure 1. We begin with considering a single sensor measurement, $y(t)$, that may contain flaw echoes, $s_f(t)$, and the reverberation clutter, $r(t)$, in the presence of additive measurement noise

$$y(t) = s_f(t) + r(t) + n(t), \tag{1}$$

where the noise $n(t)$ is zero-mean white Gaussian and is independent of the flaw echoes and reverberation clutter. Measurement noise is usually not considered as a serious impediment since its effect can be mitigated by averaging over multiple observations. The reverberation clutter, $r(t)$, is of quasiperiodic nature damped over time, where the periodicity and the degree of damping depend on the thickness and density of the layer. Under ideal measurement conditions (e.g., the layer is immersed in water in the far field of the transducer), the reverberation signal from the layer can be modeled as the superposition of the time-shifted and amplitude-scaled replicas of the transducer pulse echo wavelet, $s_e(t)$, as [1]

$$r(t) = \rho s_e(t) + \varsigma_{12}\varsigma_{21} \sum_{m=1}^{\infty} (-\rho)^{2m-1} s_e(t - 2m\Delta T), \tag{2}$$

where $2\Delta T$ denotes the time difference of arrival of successive echoes, ρ denotes the reflection coefficient from the propagation path to the layer, and $\varsigma_{12}, \varsigma_{21}$ denote the transmission

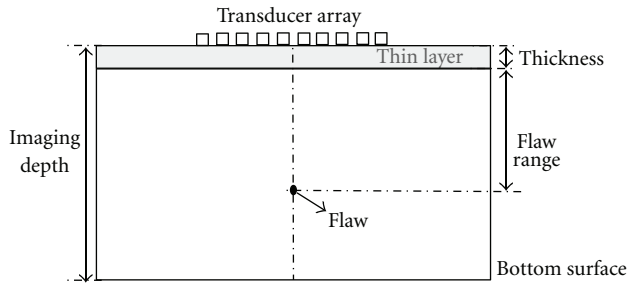

Figure 1: Experimental setup for flaw measurements through a reverberant layer.

coefficients from the propagation path to the layer and layer to the propagation path, respectively. This analytical reverberation model can be interpreted as superimposed echoes with unknown delays and amplitudes. Further, the reverberation signal can be estimated using a maximum likelihood estimation algorithm [13].

For contact measurements considered in this paper, the reverberation signal does not conform to the ideal model for a number of reasons. First, since the measurements are performed in the near field, the strong front-surface reflection (big bang) at the transducer-layer interface makes the reverberating pattern much more complicated. Second, the reverberation signal varies from one measurement to another depending on the coupling between the transducer and the layer as well as the bounding between the layer and the test material. On the other hand, the flaw echoes are short-duration signals with much lower energy compared to the reverberation clutter. Further, depending on the location of the flaw in the material, the flaw echo returns have longer time of arrival than those of the clutter. As such, the flaw echoes have a very low correlation with the reverberation clutter. Our objective is to remove the reverberation clutter without a considerable attenuation of flaw echoes. To this aim, we exploit the high energy and low correlation properties of the reverberation clutter with respect to the flaw echoes.

To model the reverberation clutter, we collect L independent measurements of the clutter, $\mathbf{d}_0, \ldots, \mathbf{d}_{L-1}$, from L different sites of a healthy replica of the material with layer, where $\mathbf{d}_l = [d_l(1), \ldots, d_l(N)]^T$ is the measured signal vector consisting of N time samples and $(\cdot)^T$ denotes matrix transpose. These measurements are stored into an $N \times L$ matrix as

$$\mathbf{Y} = \begin{bmatrix} \mathbf{d}_0 & \mathbf{d}_1 & \cdots & \mathbf{d}_{L-1} \end{bmatrix}. \tag{3}$$

In the absence of flaw echoes, these measurements only contain reverberation clutter and noise. In order to account for local delays of reverberation, we expand these measurements based on a shift-based perturbation model [14]. Basically, all the measurement vectors are shifted by an integer number of samples, both upwards and downwards, up to a maximum potential delay of $d_{\max}$. Since ultrasound signals are typically sampled at a much higher rate than the Nyquist rate, shifting by integer samples will suffice to represent all possible local delays. With the time shifts, the expanded measurement set becomes

$$\mathbf{Y}_e = \begin{bmatrix} \mathbf{Y}^{[-d_{\max}]} & \cdots & \mathbf{Y}^{[-1]} & \mathbf{Y} & \mathbf{Y}^{[+1]} & \cdots & \mathbf{Y}^{[+d_{\max}]} \end{bmatrix}, \tag{4}$$

where $\mathbf{Y}^{[d]}$ is the original measurement matrix shifted by d samples. The dimension of the expanded data set is $N \times M$ with $M = (2d_{\max} + 1)L$. The estimated covariance matrix of the expanded set $\mathbf{Y}_e$ is

$$\mathbf{C}_{\mathbf{Y}_e} = \frac{1}{M}\mathbf{Y}_e\mathbf{Y}_e^T = \mathbf{C}_r + \sigma_v^2\mathbf{I}, \tag{5}$$

where $\mathbf{C}_r$ represents the clutter covariance matrix, $\sigma_v^2\mathbf{I}$ represents the covariance matrix of additive white Gaussian noise (AWGN), and $\mathbf{I}$ denotes the $N \times N$ identity matrix. Matrix $\mathbf{C}_{\mathbf{Y}_e}$ is decomposed into different spectral components using the eigenvalue decomposition

$$\mathbf{C}_{\mathbf{Y}_e} = \sum_{m=1}^{M} \lambda_m \mathbf{u}_m \mathbf{u}_m^T, \tag{6}$$

where λ_m denotes the mth eigenvalue in an ordered set $(\lambda_1 \geq \lambda_2 \geq \cdots \geq \lambda_M)$ and $\mathbf{u}_m$ denotes the corresponding eigenvector. The first η eigenvectors belong to the clutter subspace, whereas the remaining eigenvectors belong to the noise subspace. Since the dimension of the clutter subspace is not known a priori, model-order selection methods must be applied. The techniques found in the literature based on eigenvalue trend analysis such as the differences $(\lambda_m - \lambda_{m+1})$ or ratios $(\lambda_m/\lambda_{m+1})$ of eigenvalues do not always provide satisfactory results. We employ information theoretic criteria such as the Akaike information criterion (AIC) and the minimum description length (MDL) [15]. The AIC is given as

$$\begin{aligned} \operatorname{aic}(\eta) = {} & N \ln\left(\frac{\left[(1/(M-\eta)) \sum_{m=\eta+1}^{M} \lambda_m \right]^{M-\eta}}{\prod_{m=\eta+1}^{M} \lambda_m} \right) \\ & + \eta(2M - \eta), \end{aligned} \tag{7}$$

where M denotes the number of measurements in the expanded data set. Similarly, the MDL is given as

$$\begin{aligned} \operatorname{mdl}(\eta) = {} & N \ln\left(\frac{\left[(1/(M-\eta)) \sum_{m=\eta+1}^{M} \lambda_m \right]^{M-\eta}}{\prod_{m=\eta+1}^{M} \lambda_m} \right) \\ & + \frac{1}{2}\eta(2M - \eta) \ln N. \end{aligned} \tag{8}$$

The clutter subspace is determined as the model order η that minimizes the AIC or MDL. Once the model order is determined, the clutter subspace is formed from the first η dominant eigenvectors, that is,

$$\mathbf{U}_r = \begin{bmatrix} \mathbf{u}_1 & \mathbf{u}_2 & \cdots & \mathbf{u}_\eta \end{bmatrix}. \tag{9}$$

The clutter removal is performed by projecting the received signal (A-scan) onto the orthogonal subspace of the clutter to obtain the flaw enhanced signal, that is,

$$\hat{\mathbf{s}}_f = \left(\mathbf{I} - \mathbf{U}_r\mathbf{U}_r^T\right)\mathbf{y}. \tag{10}$$

2.2. Clutter Removal via Background Subtraction. For comparison, clutter removal via background subtraction is considered. Since a set of reference measurements are available for reverberation clutter, one can employ background subtraction techniques for clutter removal. For this task, we choose the best match signal from the set of expanded measurements matrix, $\mathbf{Y}_e$, to the current measurement $\mathbf{y}$ and subtract this signal from $\mathbf{y}$. The results represent the best possible performance that can be achieved with the background subtraction technique. In this case, the index of the best match reference signal is the one that maximizes the normalized correlation coefficient with $\mathbf{y}$, that is,

$$i_m = \arg_i \max \left| \frac{\mathbf{y}^T \mathbf{Y}_e[i]}{\sqrt{(\mathbf{y}^T\mathbf{y})(\mathbf{Y}_e[i])^T(\mathbf{Y}_e[i])}} \right|, \tag{11}$$

where $\mathbf{Y}_e[i]$ denotes the ith column of the expanded data set matrix $\mathbf{Y}_e$. The clutter removal using background subtraction is then performed as

$$\hat{\mathbf{s}}_f = \mathbf{y} - \left(\frac{\mathbf{y}^T \mathbf{Y}_e[i_m]}{(\mathbf{Y}_e[i_m])^T(\mathbf{Y}_e[i_m])} \right) \mathbf{Y}_e[i_m], \tag{12}$$

where the scalar in the bracket term is the least square estimate of the best match reference signal amplitude.

2.3. Clutter Removal via Predictive Deconvolution. For comparison, the predictive deconvolution technique [3, 4] is also considered for reverberation clutter removal. This technique has been extensively used in seismic signal processing for the suppression of reverberations due to the top layer of the earth [7]. The method is based on the linear prediction filtering and exploits the repetitive patterns in reverberations. The reverberating pattern is predicted based on the past samples of data. The method requires knowledge of the prediction-lag (i.e., the periodicity of reverberation) as well as the pulse duration to set the predictive filter order and error filter length. In this paper, we implemented the technique based on the procedures outlined in [4].

3. Clutter Removal Based on Sensor Array Measurements

3.1. Clutter Removal. When the clutter-only scene is not available, the clutter subspace used for clutter removal must be constructed from data that are measured in the presence of flaw signals. Therefore, care must be exercised not to include the flaw signal in clutter subspace. Toward this end, we consider a K-element array, either consisting of physically present transducers or being formed through aperture synthesis, which measures the material of interest through a reverberant layer as depicted in Figure 1. The signal received at each sensor can be written as

$$y_k(t) = \alpha_k s_f(t - \tau_k) + r(t) + n(t), \quad k = 0, 1, \ldots, K-1, \tag{13}$$

where $y_k(t)$ denotes the signal received at the kth sensor position, $r(t)$ denotes the reverberation clutter due to the layer, $\alpha_k s_f(t - \tau_k)$ denotes the echo signal received at the kth sensor due to the flaw, and $n(t)$ denotes the AWGN. We note that the reverberation signal $r(t)$ is consistent across all sensor measurements except for local delays and small perturbations. On the other hand, flaw echo measurement varies from one sensor to another because each transducer position yields a distinct distance to the flaw. The variation in the flaw echo is modeled in terms of both the delays, (τ_k) due to the spatial arrangement of the array sensors, and the weighting factors (α_k), due to the beamwidth of the transducers and flaw reflection fluctuations. As a result, the reverberation measurements are spatially coherent, whereas flaw measurements are incoherent. In order to exploit the coherency as well as the relative strength of the reverberation, we utilize a subspace construction and projection approach.

For clutter subspace construction, we concatenate the sensor array measurements into a data matrix of size $N \times K$ as

$$\mathbf{Y}_a = \begin{bmatrix} \mathbf{y}_o & \mathbf{y}_1 & \cdots & \mathbf{y}_{K-1} \end{bmatrix}, \tag{14}$$

form the covariance matrix as

$$\mathbf{C}_{\mathbf{Y}_a} = \frac{1}{N} \mathbf{Y}_a \mathbf{Y}_a^T, \tag{15}$$

and then perform eigendecomposition of the above estimated covariance matrix. This time, the dominant eigenvalues will correspond to the clutter subspace, followed by the eigenvalues corresponding to the flaw subspace and those corresponding to the noise subspace. Because the flaw signals are much weaker than the clutter, we can determine the clutter subspace using the AIC or MDL in the same manner as explained before. Finally, the clutter is removed from each sensor data by projecting onto the orthogonal subspace of the clutter to obtain flaw-enhanced signals on each sensor, that is,

$$\hat{\mathbf{s}}_f^{[k]} = \left(\mathbf{I} - \mathbf{U}_r \mathbf{U}_r^T \right) \mathbf{y}_k. \tag{16}$$

Based on the clutter-free array data $\hat{\mathbf{s}}_f^{[k]}$, an ultrasound image can be constructed for flaw imaging. For this task, we present a beamforming algorithm in the next section.

3.2. Ultrasound Imaging of Flaw via Beamforming. The ultrasound measurements from an array composed of K transducers can be used to image the test material [16]. We consider a linear array and assume that the respective positions of transducer elements are known in a three-dimensional Cartesian space, that is, the kth transducer is located at $T_k(x_{Tk}, y_{Tk}, z_{Tk})$. We consider a region of interest (ROI), which is a two-dimensional cross-section under the linear array as depicted in Figure 1. A receiver mode backprojection beamforming algorithm is used to construct internal images of materials [17]. The signal that is reflected from a hypothetical flaw located at the position $P(x_p, y_p, z_p)$ is then received with different delays at each

transducer. The signal corresponding to the direct reflection path recorded at the kth receive transducer is given by

$$r_k(t) = a_k(P)s_e(t - \tau_k(P)), \tag{17}$$

where $a_k(P)$ is the reflectivity of the flaw seen by the transducer that also accounts for the propagation loss and $\tau_k(P)$ denotes the signal propagation delay from the location P to the kth transducer T_k. Assuming a homogeneous material with ultrasound propagation speed of v, the time delay corresponding to any pixel Q in the image, located at $Q(x_q, y_q, z_q)$, can be calculated as

$$\tau_k(Q) = \frac{2}{v}\left\|(x_{Tm}, y_{Tm}, z_{Tm}) - \left(x_q, y_q, z_q\right)\right\|, \tag{18}$$

where $\|\cdot\|$ denotes the Euclidean norm. The image intensity $I(Q)$ of every pixel Q in the imaging plane is obtained by adding the weighted time-delayed K received signals and correlating the resulting signal with the emitted signal. Therefore, the intensity at pixel Q, using the coherent imaging technique, can be written as

$$\begin{aligned} I(Q) &= \left.\sum_{k=1}^{K} w_k(Q) r_k(t + \tau_k(Q)) * s_e(t)\right|_{t=0} \\ &= \left.\sum_{k=1}^{K} w_k(Q) a_k(P) s_e(t + \tau_k(Q) - \tau_k(P)) * s_e(t)\right|_{t=0}, \end{aligned} \tag{19}$$

where $w_k(Q)$ is the weight corresponding to the kth transducer. The cross-correlation performs matched filtering and improves the output signal-to-noise ratio (SNR).

The above synthetic aperture beamforming algorithm is applied for imaging of flaws through layers before reverberation removal using the original array measurements and after reverberation removal using the proposed subspace projection approach. The flaw imaging results will be presented in the next section.

4. Simulations and Experimental Results

4.1. Experiment Settings. An aluminum block (alloy number 6061) of dimensions 6 in×6 in×3 in (152.4 mm×152.4 mm×76.2 mm) is used as the test specimen. A thin metal layer with 2 mm uniform thickness is coupled to the material with a gel. The thin layer is highly reverberant and simulates ultrasonic flaw imaging through reverberant layers. A flat-bottom hole with a diameter of 3 mm and a depth of 21 mm was drilled into the test specimen to emulate a flaw. Figure 1 shows the schematic illustration of the test specimen, the thin layer, and the synthesized sensor transducer used for ultrasonic measurements.

Transducer excitation and signal measurements are performed using an Olympus Panametrics Pulser/Receiver (P/R) (model 5072PR) operated in the monostatic (T/R) mode [18]. The P/R settings are as follows: pulse repetition frequency (PRF) 1 KHz, energy level 3, damping level 4, amplifier gain 30 dB, low-pass filter with a cutoff frequency of 1 MHz, and high-pass filter with a cutoff frequency of 10 MHz. All the ultrasonic measurements are made with an Olympus single-element transducer (model V-110 M) that has a center frequency of 5 MHz [19]. The transducer is placed on the material surface with an ultrasound coupling gel. The acquired signals are digitized with a digital scope (Agilent Technologies DSO7014A Oscilloscope) at a sampling rate of 50 MHz. These signals are collected 32 times and averaged internally by the scope to obtain a signal with a high SNR.

4.2. Simulation Results: Flaw-Free Measurements of Reverberation Clutter Available. We performed a series of simulations using synthetic data based on separate measurements of flaw and reverberation clutter to examine the respective clutter and flaw subspaces and analyze the performance of the subspace-projection-based clutter suppression technique. We first acquired a flaw signal measurement without the thin layer on top of the material. The flaw echo is properly truncated from this measurement and stored in memory. Next, the thin layer is placed on top of the aluminum block using an ultrasound gel as coupling. The reverberation measurement is performed by placing the 5 MHz ultrasonic transducer on the thin layer and covering a healthy (flaw-free) section of the aluminum. We repeated this measurement on different sections of the thin layer for 10 times to obtain a diverse set of reverberation measurements representing clutter.

We used the 10 reverberation measurements with shift-based subspace expansion ($d_{\max} = 1$) to form the clutter subspace as explained in Section 2. A new reverberation measurement (at a location different from the previous measurements) is made to test the clutter removal method. To examine the performance of the clutter removal technique under different conditions, we add the experimentally collected flaw echo and its multipath signals as if they were measured from the top layer to the new reverberation measurement but varied their amplitude and time of arrivals.

Figure 2 illustrates flaw echoes in reverberation and the clutter suppression results after respectively exploiting the subspace projection, background subtraction, and the predictive deconvolution techniques as described in Section 2. Figure 2(a) shows the emulated flaw echo and its multipath signals, whereas Figure 2(b) shows the reverberation measurement with the flaw echoes added. As such, the signal in Figure 2(b) simulates a flaw echo and its multipaths in reverberation. The flaw-echo-enhanced signals processed by the subspace projection, background subtraction, and predictive deconvolution techniques are, respectively, shown in Figures 2(c), 2(d), and 2(e). As evident from these plots, the proposed subspace projection technique highlights the flaw echoes and enhances their visibility. The background subtraction method, on the other hand, retains clutter remnants that can be mistaken as flaw echoes. The predictive deconvolution technique is also applied to this data with prediction lag set equivalent to the measured periodicity of reverberations and prediction filter length set equal to one echo length. The clutter suppression result (see Figure 2(e))

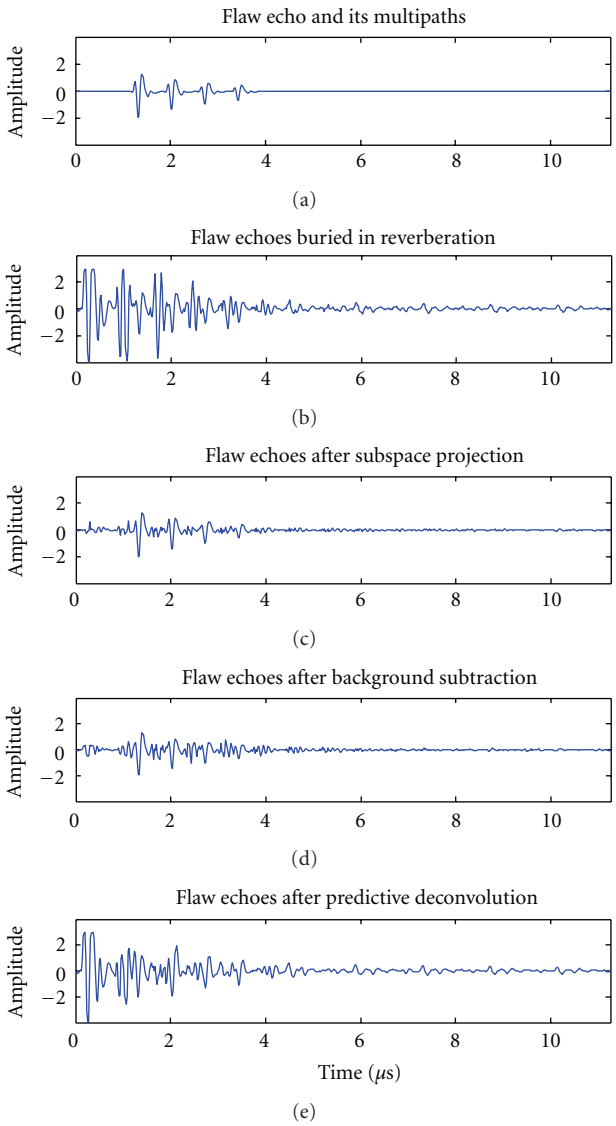

Figure 2: Comparison of reverberation removal techniques. (a) Simulated flaw echo and its multipaths measured through the layer. (b) Flaw echoes added to a real reverberation measurement. (c) Reverberation removal via subspace projection. (d) Reverberation removal via background subtraction. (e) Reverberation removal via predictive deconvolution.

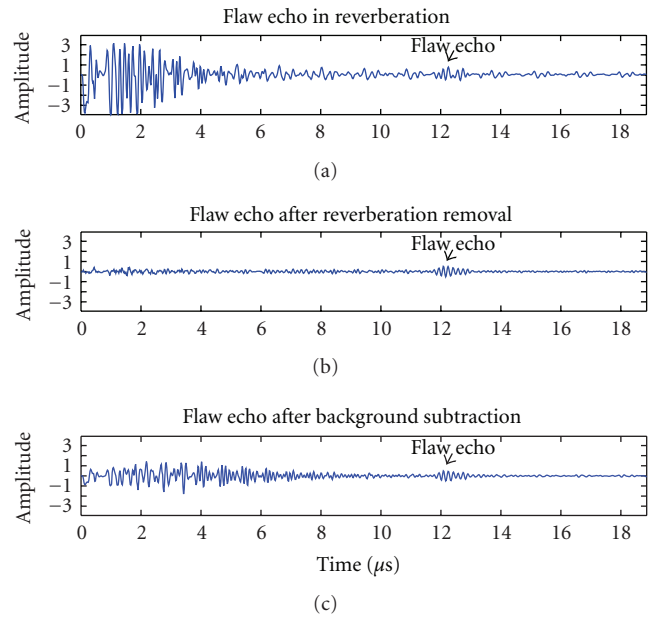

Figure 3: Reverberation removal using experimental data. (a) Ultrasonic measurement of the flaw through a reverberant layer. (b) Reverberation removal via subspace projection. (c) Reverberation removal via background subtraction.

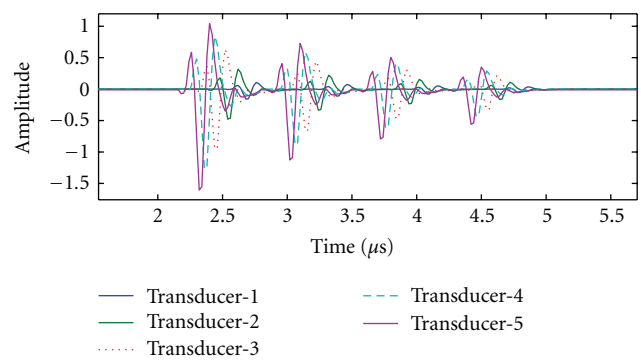

Figure 4: Simulation of flaw and its multipath measurements through the layer with a transducer array shown in Figure 1. The flaw is assumed to be in 1.35 cm depth from about the center of the array (see Figure 1).

is inferior to those obtained from background subtraction and subspace projection. This is due to the fact that, while the predictive deconvolution technique relies on the repeatability of reverberating patterns to predict and remove the future echoes, the actual reverberation echoes vary in their shape due to irregular variations and the existence of different propagation modes. For example, the noticeable difference in shape is observed between the first two echoes shown in Figure 2(b) during the time interval between 0 μs and 1.5 μs. Further, predictive deconvolution always retains the first part of data (e.g., the first echo in Figure 2(e)) before prediction lag. It is noteworthy that the proposed subspace projection technique works for arbitrary signal structures and does not rely on the repeatability of reverberation patterns.

We also made an ultrasonic measurement of a real flaw through the thin layer. To emulate a flaw, a through hole with a diameter of 3 mm is drilled into the aluminum block 3.5 cm down from the top. Then, the thin layer is placed on top of the block with gel coupling. The measurement including reverberations and the flaw echo is shown in Figure 3(a). The clutter-suppressed signals with subspace projection and background subtraction are shown in Figures 3(b) and 3(c), respectively. The subspace expansion technique with $d_{\max} = 5$ samples is utilized. The model order is chosen based on the MDL metric. The flaw echo is located around

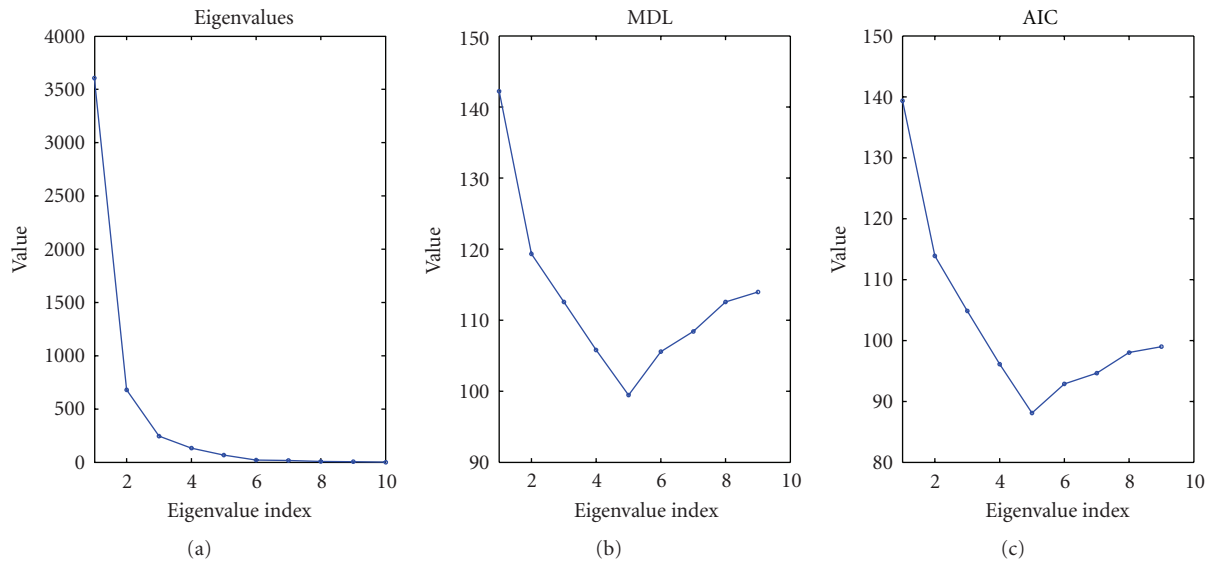

Figure 5: The eigenvalues (a) of the flaw in reverberation measurements with an array: the MDL (b) and AIC (c) metrics.

12 μs. It is seen that the flaw echo is enhanced significantly after subspace-projection-based clutter removal, whereas background subtraction retains a significant portion of clutter.

4.3. Simulations: Independent Measurement of Reverberation Clutter Unavailable. In this section, we examine the reverberation removal technique when reference measurements of the flaw-free reverberation clutter are not available. This can be the case where there is no access to a healthy material. In order to allow clutter subspace estimation, we use multiple positions of the transducers, thus forming a synthetic array aperture that enables ultrasound imaging. By moving the transducer in collinear positions, it becomes equivalent to measuring the flaw with a linear array through the reverberant layer. As such, a subset or all measurements may contain flaw echoes, whereas all measurements contain the strong reverberation signal due to the layer. Clearly, clutter removal in this scenario is more challenging since reference measurements required to form a clutter subspace also contain flaw echoes.

We simulate an array measurement by moving the single-element transducer in small steps on the surface of the thin layer placed on top of the material. To simulate flaw echoes impinged on reverberation measurements, the flaw echoes are generated based on the assumed flaw location, the geometry of the synthesized linear array, the respective delay between the flaw and sensors, and the approximate beamwidth of the measuring transducer. The beamwidth is incorporated as a weighting factor on echo amplitudes based on the flaw location with respect to transducer, as explained in [20]. Further, the flaw echo multipaths are simulated based on the assumed thickness and velocity of the layer and its reflection and transmission coefficients. A typical flaw echo and its multipath signals measured with the first 5 elements of the synthesized linear array (see Figure 1) are shown in Figure 4, where the flaw is located in the range of 1.35 cm from the array boresight. The flaw echo and its multipath signals received by the sensors close to the center are stronger and have a shorter time of arrival than those received by the sensors away from the center. To simulate the flaw measurement through a reverberant layer with a transducer array, we added these simulated flaw echoes to the 10 independent reverberation measurements obtained from the healthy sections of the aluminum block.

Because the flaw signal is contained in the measured waveforms that are used to construct the clutter subspace for orthogonal projection, it is important to accurately estimate the clutter subspace bases that are free of the flaw. As the reverberation clutter is orders of magnitude stronger than the flaw echoes, the clutter subspace can be limited to the eigenvectors associated with the dominant eigenvalues. In order to determine the dominant clutter subspace, we use information theoretic criteria, AIC and MDL, that were presented in Section 2. The flaw echo has a low correlation with the clutter and its energy is much smaller than the clutter energy. As such, its subspace is separate from the clutter subspace and is associated with smaller values of eigenvalues. The estimation of the flaw subspace dimension, however, is not necessary since clutter removal is sufficient to reveal the flaw echoes.

As seen from Figure 5, the dimension of the clutter subspace is chosen as the value that minimizes the AIC (7) or MDL (8) metric. In this case, both criteria provide the same clutter dimension estimate of 5. The subspace-based clutter removal algorithm is tested on the synthetic data containing 10 reverberation measurements in the presence of flaw echoes. Figure 6(a) shows the simulated flaw echo and its multipath signals synthesized from data measured at the 4th transducer in the synthetic array (see Figure 1). Figure 6(b) shows the flaw echo and its multipath signals added to the reverberation. As such, Figure 6(b) simulates

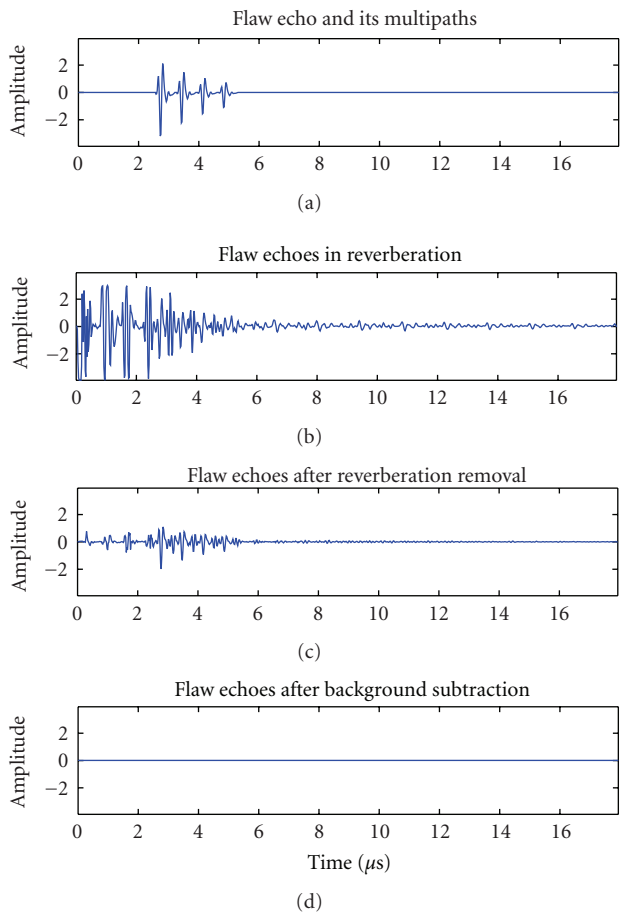

Figure 6: Reverberation removal based on array measurements containing the flaw echoes. (a) Simulated flaw echo and its multipaths received by the 4th transducer shown in Figure 1. (b) Flaw echo and multipaths added to the reverberation measurement from the 4th transducer. (c) Reverberation removal via subspace projection. (d) Reverberation removal via background subtraction.

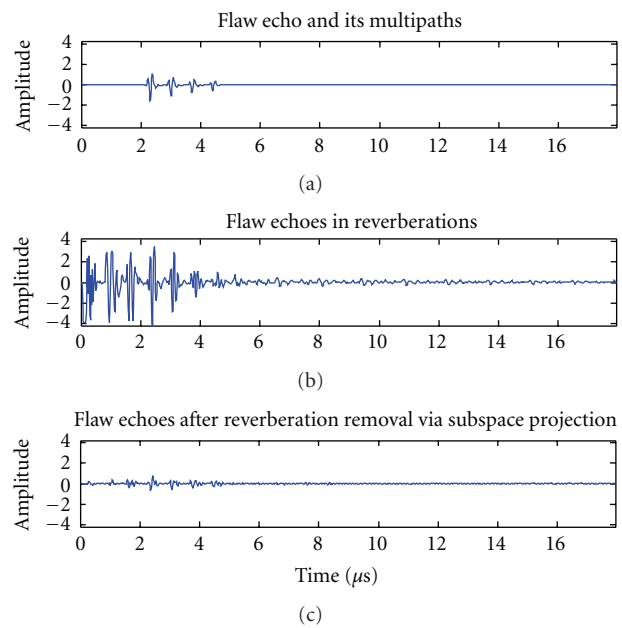

Figure 7: Reverberation removal in a high clutter area. (a) Simulated flaw echo and its multipaths received by the 4th transducer shown in Figure 1. (b) The flaw echo and its multipaths added to the reverberation measurement. The flaw echoes are completely buried in reverberation. (c) Reverberation removal via subspace projection.

the flaw echo measurement with the 4th transducer through the thin layer. We apply the subspace projection technique with clutter subspace dimension set to 5 based on the MDL metric. The reverberation-suppressed signal is shown in Figure 6(c). Although the flaw echo and its multipath signals are clearly revealed, their amplitudes are smaller than the original (Figure 6(a)) owing to the fact that part of their energy lies in the clutter region. As expected, the subspace projection method based on the measurements of reverberations containing flaw echoes is less effective when the clutter and flaw waveforms overlap.

The background subtraction technique does not work for this case since flaw-free reference measurements of reverberation are not available. Direct application of background subtraction yields all-zero signal (Figure 6(d)) since the best match signal to the test signal (Figure 6(b)) is available in the reference set.

In another simulation, the flaw echo and its multipath signals are completely buried in reverberation (see Figure 7). This time, the flaw echo and its multipaths, as shown in Figure 7(a), are much weaker (the first flaw echo amplitude is set to 1) and buried in the dominant part of the reverberation signal as shown in Figure 7(b). As before, this signal is projected to the orthogonal subspace of the clutter with dimension 5 to obtain the flaw-enhanced echoes, as shown in Figure 7(c). The flaw echo and its multipath signals are visible albeit with smaller amplitudes than their original version. The remnants of the clutter are also visible but weaker than the first three flaw echoes.

Finally, we demonstrate the flaw imaging capability of the subspace projection technique in the presence of heavy clutter. For this purpose, we utilize the backprojection beamforming algorithm for synthetic aperture arrays as described in Section 3.1. The imaging results are depicted in Figure 8. Figure 8(a) shows the beamformed image of a flaw in the test material without the thin layer (see Figure 1) based on the simulated measurements of the flaw with the 10-element synthetic array. Figure 8(b) shows the beamformed image when the flaw is measured through the layer. To simulate the array data associated with this image, the flaw and its multipath echoes, as measured through the layer, are added to the 10 independent reverberation measurements collected with the synthetic array. Finally, Figure 8(c) shows the beamformed image after the suppression of the reverberation clutter in the array data using the proposed subspace projection algorithm. The dimension of the clutter subspace is estimated as 5 using the MDL criterion. The positions of the 10-element synthetic arrays with respect to the flaw are shown in the top of the image.

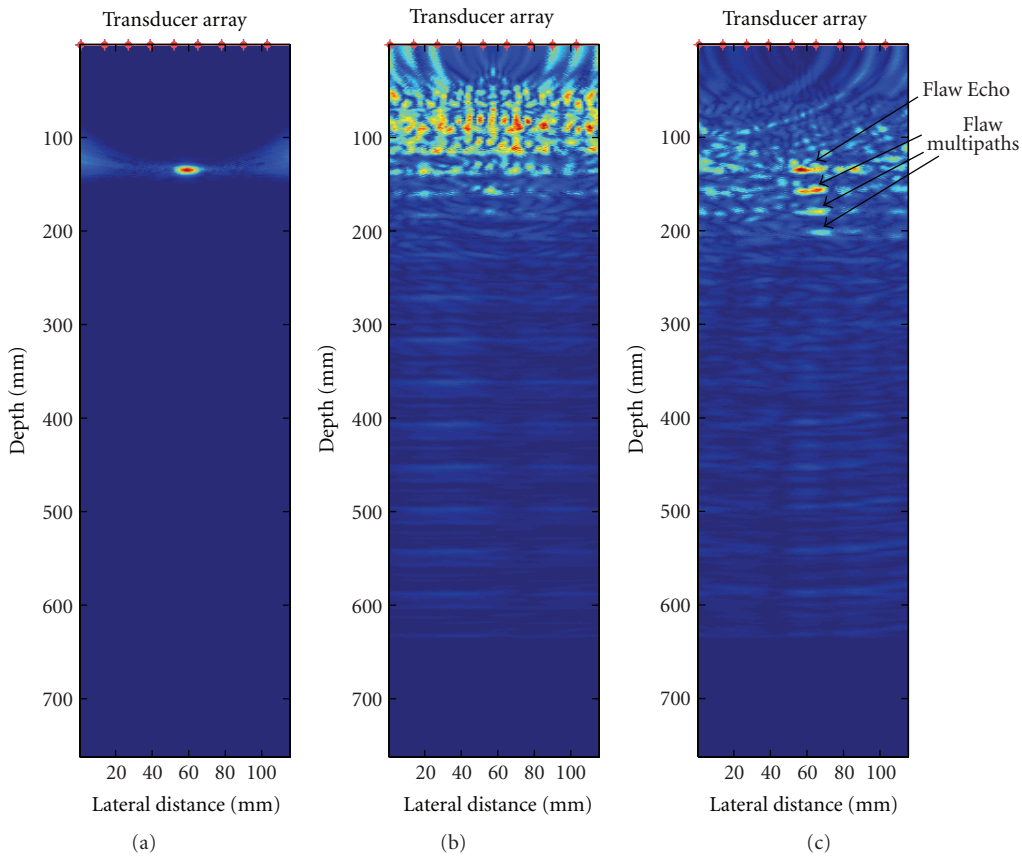

Figure 8: The synthetic aperture array imaging of a flaw through a thin reverberant layer. (a) Simulated flaw echo measurement with a 10-element synthetic linear array. The transducer positions are shown on top of the image. (b) Flaw (a) and its multipath measurements via the thin layer added to 10 reverberation measurements collected with the synthetic array. (c) Imaging after reverberation removed array data. The flaw echo and its multipaths are clearly revealed.

It is evident from Figure 8 that the proposed clutter removal algorithm effectively suppresses the clutter and significantly enhances the visibility of the flaw echo and its first few multipaths, which otherwise are buried in reverberation. Further, the technique is very practical since it operates on the existing array data and adds a negligible computational complexity to the synthetic aperture beamforming imaging algorithm and hence can be incorporated into real-time ultrasound imaging systems.

5. Conclusions

In this paper we proposed a subspace learning and projection technique for suppression of reverberation signals that arise in detection and imaging of flaws through layers. We addressed reverberation clutter removal in ultrasound nondestructive evaluation (NDE) in the presence of very strong reverberation. Two different cases are considered for the application of the proposed technique. The first case uses a set of flaw-free reference measurements of reverberation, whereas the second case is based on array measurements that contain flaws. For the first case, we have shown that, by utilizing a set of reference reverberation signals obtained from the healthy replica of the materials, the clutter can be significantly removed with a negligible effect on the flaw echoes. In the second case that applies to ultrasound NDE imaging, we demonstrated that the clutter can be mitigated by utilizing the array measurements without employing any reference data. The effectiveness of the proposed clutter removal techniques for both cases is verified by analysis and experimental data. The proposed clutter removal technique is computationally efficient and practical for array imaging. It does not require any parameter tuning or the knowledge of the screening layer propagation characteristics. As such, it can be easily incorporated into the existing array imaging systems with minimal complexity.

Acknowledgments

This research is supported in part by the National Science Foundation (NSF) under Grant no. IIP-0917690 and by The Ministry of Railways, China, under Grant no. 2011J011-E.

References

[1] J. Saniie and D. T. Nagle, "Pattern recognition in the ultrasonic imaging of reverberant multilayered structures," *IEEE Transac-*

tions on Ultrasonics, Ferroelectrics, and Frequency Control, vol. 36, no. 1, pp. 80–92, 1989.

[2] S. W. Smith, G. E. Trahey, and O. T. Von Ramm, "Phased array ultrasound imaging through planar tissue layers," *Ultrasound in Medicine and Biology*, vol. 12, no. 3, pp. 229–243, 1986.

[3] D. Kishoni, "Removal of dominant reverberations from ultrasonic time-records of layered material by digital predictive deconvolution," in *Proceedings of the IEEE Ultrasonics Symposium*, pp. 1075–1078, 1986.

[4] Y. F. Chang, Y. Ma, C. M. Lin, and J. H. Lee, "Reverberation reduction in ultrasonic images via predictive deconvolution," *NDT&E International*, vol. 41, no. 4, pp. 235–241, 2008.

[5] M. A. Duarte, J. C. Machado, and W. C. A. Pereira, "A method to identify acoustic reverberation in multilayered homogeneous media," *Ultrasonics*, vol. 41, no. 9, pp. 683–698, 2004.

[6] K. K. Win, J. Wang, C. Zhang, and R. Yang, "Identification and removal of reverberation in ultrasound imaging," in *Proceedings of the 5th IEEE Conference on Industrial Electronics and Applications (ICIEA '10)*, pp. 1675–1680, June 2010.

[7] O. Yilmaz, *Seismic Data Analysis: Processing, Inversion, and Interpretation of Seismic Data*, Society of Exploration Geophysics, Tulsa, Okla, USA, 2000.

[8] A. M. Mayordomo and A. Yarovoy, "Optimal background subtraction in GPR for humanitarian demining," in *Proceedings of the 5th European Radar Conference (EuRAD '08)*, pp. 48–51, October 2008.

[9] Y-S. Yoon and M. G. Amin, "Spatial filtering for wall-clutter mitigation in through-the-wall radar imaging," *IEEE Transactions on Geoscience and Remote Sensing*, vol. 47, no. 9, pp. 3192–3208, 2009.

[10] F. H. C. Tivive, A. Bouzerdoum, and M. G. Amin, "An SVD-based approach for mitigating wall reflections in through-the-wall radar imaging," in *Proceedings of IEEE Radar Conference*, Kansas City, Kan, USA, May 2011.

[11] V. Kovalenko, A. G. Yarovoy, and L. P. Ligthart, "A novel clutter suppression algorithm for landmine detection with GPR," *IEEE Transactions on Geoscience and Remote Sensing*, vol. 45, no. 11, pp. 3740–3750, 2007.

[12] B. W. Drinkwater and P. D. Wilcox, "Ultrasonic arrays for non-destructive evaluation: a review," *NDT&E International*, vol. 39, no. 7, pp. 525–541, 2006.

[13] R. Demirli and J. Saniie, "Model-based estimation of ultrasonic echoes part II: nondestructive evaluation applications," *IEEE Transactions on Ultrasonics, Ferroelectrics, and Frequency Control*, vol. 48, no. 3, pp. 803–811, 2001.

[14] X. Shen, Y. D. Zhang, M. G. Amin, and R. Demirli, "Ultrasound multipath background clutter mitigation based on subspace analysis and projection," in *Proceedings of the IEEE International Conference on Acoustics, Speech and Signal Processing (ICASSP '12)*, March 2012.

[15] M. Wax and T. Kailath, "Detection of signals by information theoretic criteria," *IEEE Transactions on Acoustics, Speech, and Signal Processing*, vol. 33, no. 2, pp. 387–392, 1985.

[16] F. Ahmad, M. G. Amin, and S. A. Kassam, "Synthetic aperture beamformer for imaging through a dielectric wall," *IEEE Transactions on Aerospace and Electronic Systems*, vol. 41, no. 1, pp. 271–283, 2005.

[17] M. G. Amin, Ed., *Through-the-Wall Radar Imaging*, CRC Press, 2010.

[18] Olympus Ultrasonic Pulser/Receiver, http://www.olympus-ims.com/en/5072pr/.

[19] Olympus NDT contact transducers, http://www.olympus-ims.com/en/ultrasonic-transducers/contact-transducers/.

[20] R. Demirli, X. Rivenq, Y. D. Zhang, C. Ioana, and M. G. Amin, "MIMO array imaging for ultrasonic nondestructive testing," in *Nondestructive Characterization for Composite Materials, Aerospace Engineering, Civil Infrastructure, and Homeland Security*, Proceedings of SPIE, San Diego, Calif, USA, March 2011.

Hindawi Publishing Corporation
Advances in Acoustics and Vibration
Volume 2012, Article ID 292695, 12 pages
doi:10.1155/2012/292695

Research Article

Three-Dimensional Acoustic Source Mapping with Different Beamforming Steering Vector Formulations

Ennes Sarradj

Department of Technical Acoustics, Brandenburg University of Technology, Siemens-Halske-Ring 14, 03046 Cottbus, Germany

Correspondence should be addressed to Ennes Sarradj, ennes.sarradj@tu-cottbus.de

Received 12 March 2012; Accepted 20 May 2012

Academic Editor: Mario Kupnik

Acoustic source mapping techniques using acoustic sensor arrays and delay-and-sum beamforming techniques suffer from bad spatial resolution at low-aperture-based Helmholtz numbers. This is especially a problem for three-dimensional map grids, when the sensor array is not arranged around the region spanned by the grid but on only one side of it. Then, the spatial resolution of the result map in the direction pointing away from the array is much worse than in the other lateral directions. Consequently, deconvolution techniques need to be applied. Some of the most efficient deconvolution techniques rely on the properties of the spatial beamformer filters used. As these properties are governed by the steering vectors, four different steering vector formulations from the literature are examined, and their theoretical background is discussed. It is found that none of the formulations provide both the correct location and source strength. As a practical example the CLEAN-SC deconvolution methodology is applied to simulated data for a three-source scenario. It is shown that the different steering vector formulations are not equally well suited for three-dimensional application. The two preferred formulations enable the correct estimation of the source location at the cost of a negligible error in the estimated source strength.

1. Introduction

In the context of acoustic measurements, methods based on acoustic sensor arrays can be used to locate acoustic sources and to estimate their strength [1]. In most cases, these methods are adopted to produce acoustic source maps. In general, such maps can be thought of as an image of the spatial distribution of an indicator quantity of source strength.

Acoustic source mapping techniques using beamforming methods have been widely applied for the study of acoustic sources (e.g., for trains [2], aeroacoustic testing [3, 4], airframe noise [5, 6], noise source characterization at a helicopter [7], and jet noise [8]). These methods use the signals from an array of acoustic sensors (mostly microphones) to filter out the signal from a source at an assumed location. Such a spatial filter behaves like a directional sound receiver with a directional characteristic that favours sound emanating from the assumed source location [9]. If several of such spatial filters are applied in parallel for a number of different assumed source locations, an acoustic source mapping may be generated from the filter outputs. Usually the assumed source locations are arranged in some sort of grid and the amplitude of the output from each individual filter is mapped on the respective grid location. Thus, the filters constitute a mapping device.

The map produced by this device is an image of the spatial source distribution. Ideally, it shall have the following properties: if a certain assumed source location in the grid coincides with an actual source location, the map shows a higher value at this location. If there is no coincidence of assumed and actual source location, the map shows a lower value. Moreover, stronger sources shall result in higher values in the map. Thus, the map provides information about the location of the source, and it allows to estimate the strength of the source.

The feasibility of this approach depends on the properties of the beamformer mapping device as given by the point spread function. The point spread function is the spatial impulse response of the beamformer. It can be thought of being the map that is produced if only one single point

source is present at a certain location. It shows the image of the source as a spot at the source location (main lobe) that is accompanied by a number of spots (side lobes) at other locations and lower in level. This mapping is imperfect for two reasons. First, the width of the main lobe limits the spatial resolution because sources that are too close to each other will produce a mapping very similar to that of a single source. Second, the images of weaker sources may be masked by the side lobes of a stronger source. The point spread function depends on a number of factors: the number and the geometrical layout of the array microphones, the array aperture, the frequency, and the type and properties of the filter. It also depends on the source location.

A number of deconvolution techniques have been developed to recover the true spatial source distribution from the beamformer result by removing the influence of the point spread function. Some rely on precalculated point spread functions (e.g., DAMAS [10]), other approaches assess the point spread function from the acoustic data recorded during the measurement (e.g., CLEAN-SC [11]). A critical point, especially for the latter techniques, is that they require the maximum in the map to coincide with an actual source position.

The beamforming source mapping approach is typically applied using a planar two-dimensional grid. In this case, all sources are mapped into one plane regardless of their actual position. In situations where the acoustic sources under test are not in a common plane (e.g., for complex machinery parts, engines, and some aeroacoustic sources, such as, landing gear and pantographs), this leads to an erroneous source mapping. Therefore, a three-dimensional mapping is desirable that allows source localisation in three dimensions. In principle, the three-dimensional application of beamforming techniques is straightforward and can be easily realised by using a three-dimensional grid [12–20]. However, there appear to be some practical problems in the application.

First, the resolution in the third dimension (depth-wise) is much worse than in the other dimensions unless the microphone array arrangement encloses the source region to be mapped. The second problem is the larger number of points in a three-dimensional grid. While for a two-dimensional mapping some thousand grid points may be sufficient, a three-dimensional grid can easily have some hundred thousand points. Because one filter per grid point is required to calculate the result, the computational effort increases considerably. That is why most applications are using only several ten thousand grid points.

As with two-dimensional map grids, the resolution can be improved using deconvolution techniques also for the third dimension. The computational effort connected with these techniques is generally high and depends on the number of grid points. Those deconvolution techniques that require precalculated point spread functions (e.g., DAMAS [10]) also require to solve a system of equations with as many unknowns as there are grid points. The effort for the estimation of the point spread function increases with the fourth power of the number of grid points in the map grid. The effort to solve the system of equations itself grows with the second to third power. Thus, the large number (hundreds of thousands or more) of grid points required for a three-dimensional mapping with fine spatial resolution renders the application of these techniques inefficient. A possible solution that has been proposed [21] is to assume that the point spread function is assumed to be shift invariant. Thus, the effort would reduce substantially and it would increase then only with the second power of the number of grid points for the estimation of the point spread function and with somewhat less than the second power for the solution of the system of equations based on the fast fourier transform. However, this approach is limited to cases where the source region is small compared with its distance to the array [21]. Thus, it is not applicable to the general case of a larger source region.

Computationally less demanding deconvolution techniques, such as, CLEAN-SC that do not require solving a huge system of equations in turn need to find sources by maximums in the three-dimensional map. Therefore, a final problem in the three-dimensional application of beamforming mapping techniques is to find spatial filters that have the desired properties also in three dimensions to provide these maximums. While this problem arises specifically for deconvolution methods that require maximums in the map to coincide with acoustic sources, it is relevant because the computational cost increases roughly linearly with the number of grid points. This makes these techniques most appropriate for three-dimensional application and allows for practical application with several hundred thousand grid points [17–19].

The problem of desired beamformer filter properties shall be considered here by comparing different spatial filter characteristics given by different steering vectors and analysing their properties with regard to three-dimensional beamforming with deconvolution. In the remainder of this contribution the theoretical basis for the beamforming methods is briefly presented, and four different spatial filter characteristics are discussed. Their properties are demonstrated using a single-source scenario as an example. Finally, a slightly more realistic case is considered. Simulated data for three-dimensional source mapping is analysed using the different beamformers and the CLEAN-SC deconvolution approach. The results are compared with results from two-dimensional source mapping.

2. Theory

First, the analysis of a single sound source located at $\mathbf{x}_s$ using an array of N microphones is assumed. The complex-valued sound pressure p at the i-th microphone at $\mathbf{x}_i$ is

$$p(\mathbf{x}_i) = a(\mathbf{x}_i, \mathbf{x}_0, \mathbf{x}_s) q(\mathbf{x}_s). \tag{1}$$

The strength of the source is characterised by the sound pressure q at the reference location $\mathbf{x}_0$ due to that source. Though in principle $\mathbf{x}_0$ can be freely chosen, for the purpose of the following analysis it is set to the array centre at $(1/N)\sum_{i=1}^{N} \mathbf{x}_i$. The transfer function a depends on the type of the source, its location $\mathbf{x}_s$, and the environmental conditions.

If a monopole source under free-field conditions is assumed and no flow is present, the transfer function is given by:

$$a(\mathbf{x}_i, \mathbf{x}_0, \mathbf{x}_s) = \frac{r_{s,0}}{r_{s,i}} e^{-jk(r_{s,i}-r_{s,0})}, \tag{2}$$

with $r_{s,i} = |\mathbf{x}_s - \mathbf{x}_i|$ and $r_{s,0} = |\mathbf{x}_s - \mathbf{x}_0|$ indicating the distance between the source and the microphone location and the distance between the source and the array centre location, respectively, and k is the wave number. The vector of sound pressures at the microphones due to a source at $\mathbf{x}_s$ is given by $\mathbf{p} = \mathbf{a}(\mathbf{x}_0, \mathbf{x}_s)q(\mathbf{x}_s)$. The transfer vector $\mathbf{a}(\mathbf{x}_0, \mathbf{x}_s)$ contains all respective transfer functions and accounts for the individual time delays and attenuations of the sound that travels from the source to the microphones.

The beamformer filter is realised by calculating the weighted sum of the microphone sound pressures using complex-valued weight factors. The vector $\mathbf{h}(\mathbf{x}_t)$ of these factors is called the steering vector and depends on an assumed source location $\mathbf{x}_t$. The filter output is then:

$$p_F(\mathbf{x}_t) = \mathbf{h}(\mathbf{x}_t)^H \mathbf{p}, \tag{3}$$

where the superscript H denotes the hermitian transpose. Instead of p_F, the real-valued autopower spectrum B of the filter output can be used as a quantity to construct a source map. Using the cross spectral matrix of microphone signals $\mathbf{G}$, it can be written as

$$\begin{aligned} B(\mathbf{x}_t) &= E\{p_F(\mathbf{x}_t)p_F^*(\mathbf{x}_t)\} = \mathbf{h}^H(\mathbf{x}_t)E\{\mathbf{p}\mathbf{p}^H\}\mathbf{h}(\mathbf{x}_t) \\ &= \mathbf{h}^H(\mathbf{x}_t)\mathbf{G}\mathbf{h}(\mathbf{x}_t), \end{aligned} \tag{4}$$

with $E\{\}$ denoting the expectation operator and the superscript $*$ denoting the complex conjugate.

Two properties of the beamformer filter are desirable for a successful application in the case of acoustic source mapping. First, the filter should provide maximum output power when the assumed and the actual source position are the same:

$$B(\mathbf{x}_t = \mathbf{x}_s) > B(\mathbf{x}_t \neq \mathbf{x}_s). \tag{5}$$

This property is essential to have a map showing the peak value at the source position. Second, if the assumed and the actual source coincide, the filter output should be a measure of the source strength. This is true, if

$$B(\mathbf{x}_t = \mathbf{x}_s) = CE\{qq^*\} \tag{6}$$

holds, where C is an arbitrary constant.

The properties of the beamformer filter are governed by the steering vector. This vector depends on the assumed source location x_t also referred to as steering location. While not further considered here, it can be noted that it may also depend on the measured data itself and adapt the filter properties to the data. Sometimes the distance between array and source is very large and a plane wave propagation can be assumed. In this case, x_t is replaced by the direction of arrival and the distance between array and source is set to be practically infinite. However, for three-dimensional application this approach is not feasible.

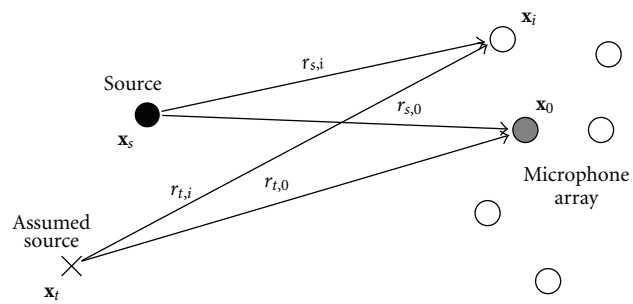

Figure 1: Microphone array and distances to actual and assumed source location.

An in-depth examination of the literature on acoustic beamforming reveals that there are at least four choices available regarding the formulation of the steering vector elements h_i under these circumstances. In the following, these formulations are presented and analysed regarding the desirable properties stated in (5) and (6).

2.1. Formulation I. The most basic idea is to simply compensate for the phase delay [22] between assumed source and the individual microphone. The steering vector elements are then derived from the phase part of the transfer vector elements for the assumed source location:

$$h_i^{\mathrm{I}} = \frac{1}{N}\frac{a_i(\mathbf{x}_0, \mathbf{x}_t)}{|a_i(\mathbf{x}_0, \mathbf{x}_t)|} = \frac{1}{N}e^{-jk(r_{t,i}-r_{t,0})}. \tag{7}$$

The latter part of this equation holds if the transfer function from (2) is assumed and $r_{t,i} = |\mathbf{x}_t - \mathbf{x}_i|$ and $r_{t,0} = |\mathbf{x}_t - \mathbf{x}_0|$ (see Figure 1). Given this steering vector formulation that shall be referred to here as "formulation I", the output power of the beamformer filter can be derived for the case $\mathbf{x}_t = \mathbf{x}_s$:

$$B(\mathbf{x}_t = \mathbf{x}_s) = \left(\frac{1}{N}\sum_{i=1}^{N}\frac{r_{s,0}}{r_{s,i}}\right)^2 E\{qq^*\}. \tag{8}$$

Because $\sum_{i=1}^{N}(r_{s,0}/r_{s,i}) \approx N$, the output is an estimate of the source strength. However, it becomes obvious that the condition (6) is met only approximately.

Condition (5) requires a local maximum of $B(\mathbf{x}_t)$ at $\mathbf{x}_t = \mathbf{x}_s$. A necessary condition for this is that all partial derivatives of B with respect to the elements of $\mathbf{x}_t$ are zero. For this, it is sufficient to have

$$\left.\frac{\partial}{\partial r_{t,i}}B(\mathbf{x}_t)\right|_{\mathbf{x}_t=\mathbf{x}_s} = 0, \qquad \left.\frac{\partial}{\partial r_{t,0}}B(\mathbf{x}_t)\right|_{\mathbf{x}_t=\mathbf{x}_s} = 0. \tag{9}$$

This holds for the partial derivatives that can be computed when the steering vector given by (7) is applied in (4). Thus, the necessary condition to have a maximum response at the source location is met in this case.

2.2. Formulation II. Another formulation of the steering vector that is frequently used in the literature (e.g., [3, 5]) aims at compensating also for the amplitude:

$$h_i^{\mathrm{II}} = \frac{1}{N}\frac{a_i(\mathbf{x}_0,\mathbf{x}_t)}{a_i(\mathbf{x}_0,\mathbf{x}_t)a_i^*(\mathbf{x}_0,\mathbf{x}_t)} = \frac{1}{N}\frac{r_{t,i}}{r_{t,0}}e^{-jk(r_{t,i}-r_{t,0})}. \tag{10}$$

This formulation assures that condition (6) is met because $B(\mathbf{x}_t = \mathbf{x}_s) = E\{qq^*\}$. However, this comes at the cost that the derivatives in (9) do not vanish. There is no maximum at $\mathbf{x}_t = \mathbf{x}_s$, and consequently condition (5) is not met.

2.3. Formulation III. The third formulation of the steering vector [23] that should be discussed is based on the idea that signals from the assumed source position should pass undistorted through the filter, so that $B(\mathbf{x}_t = \mathbf{x}_s) = E\{qq^*\}$. At the same time signals from all other positions should be attenuated as much as possible. This is equivalent to minimising the filter response to spatially white noise [24]. By solving this optimisation problem, the formulation

$$h_i^{\mathrm{III}} = \frac{a_i(\mathbf{x}_0,\mathbf{x}_t)}{\mathbf{a}^H(\mathbf{x}_0,\mathbf{x}_t)\mathbf{a}(\mathbf{x}_0,\mathbf{x}_t)} = \frac{1}{r_{t,0}r_{t,i}\sum_{j=1}^{N}\left(1/r_{t,j}^2\right)}e^{-jk(r_{t,i}-r_{t,0})} \tag{11}$$

arises. The steering vector here is parallel to $\mathbf{a}(\mathbf{x}_0,\mathbf{x}_s)$ when $\mathbf{x}_t = \mathbf{x}_s$. Again, this formulation does not meet condition (5).

2.4. Formulation IV. Formulation IV introduces a steering vector that is also parallel to $\mathbf{a}(\mathbf{x}_0,\mathbf{x}_s)$ when $\mathbf{x}_t = \mathbf{x}_s$ but uses a normalisation to ensure that $h_i^* h_i$ remains constant. This formulation is usually developed via a least square minimisation of the error between modelled and measured sound pressures at the microphones (e.g., [4, 8]). Using the normalisation $h_i^* h_i = 1/N$, the formulation reads

$$\begin{aligned} h_i^{\mathrm{IV}} &= \frac{1}{\sqrt{N}}\frac{a_i(\mathbf{x}_0,\mathbf{x}_t)}{\sqrt{\mathbf{a}^H(\mathbf{x}_0,\mathbf{x}_t)\mathbf{a}(\mathbf{x}_0,\mathbf{x}_t)}} \\ &= \frac{1}{r_{t,i}\sqrt{N\sum_{j=1}^{N}\left(1/r_{t,j}^2\right)}}e^{-jk(r_{t,i}-r_{t,0})}. \end{aligned} \tag{12}$$

In this case condition (5) is met, but the response for $\mathbf{x}_t = \mathbf{x}_s$ is only an approximate measure of the source strength:

$$B(\mathbf{x}_t = \mathbf{x}_s) = \frac{1}{N}\sum_{i=1}^{N}\frac{r_{s,0}^2}{r_{s,i}^2}E\{qq^*\}. \tag{13}$$

2.5. Comparison of Formulations. It can be concluded that in theory neither of this four formulations of the steering vector has both properties desirable for the application of the beamformer to acoustic source mapping. The first formulation (7) and the fourth formulation (12) provide the correct location but produce an error in the source strength and both the second formulation (10) and the third formulation (6) provide the correct source strength, but the maximum does not coincide with the correct location. However, it should be borne in mind that for practical application it suffices to get approximate estimates of both location and source strength with acceptable accuracy.

In contrast to the theoretical model used up to here, in a practical scenario there is often more than one source. The beamformer output is then a superposition of contributions from the individual sources. Thus, the presence of multiple sources has an impact on the performance of the beamformer filter (see [23]). If the signals from these sources are mutually uncorrelated, $B(\mathbf{x}_t)$ is the sum of their nonnegative contributions. In such a case the results will deviate somewhat from those of the mathematical analysis presented for the one source scenario. Any conclusions that were derived for the properties of the different formulations regarding conditions (5) and (6) are not rigorously valid, but only approximately. This becomes especially important when sources are closely spaced with distances less than the wavelength. As a consequence, the low-frequency application of source-mapping beamforming techniques leads to results of limited value. Appropriate deconvolution techniques may improve the results in this case and are frequently applied for this reason.

While for all four formulations of the steering vector meaningful practical results have been reported for acoustic source mapping applications, there are no results available yet that compare the mappings produced by the application of these different steering vectors. Moreover, the vast majority of these applications use two-dimensional mapping grids and assume a priori that all relevant sources are located in the mapping plane. A three-dimensional mapping grid does not need this assumption but will usually require a deconvolution technique to deal with the otherwise inadequate depth-wise resolution.

The large number of points in a three-dimensional mapping grid calls for an deconvolution technique that is computationally efficient. Computationally less demanding deconvolution techniques, like CLEAN-SC, rely on the correct estimation of the source location from the maximum in the map. Because of this requirement, it is important to assess the quality of the results that follow the application of the different formulations of the steering vector for three-dimensional source mapping. In what follows, the effect of using different steering vector formulations shall be analysed for both two- and three-dimensional acoustic source mapping on the basis of simulated measurements.

3. Results

Most practical applications are concerned with sources that are not compact but spatially extended. A usual assumption is to assume that the sources can be seen as spatial distributions of uncorrelated point sources. Thus, in order to analyze the different steering vectors, no extended source is considered here but a simple point source scenario. Results

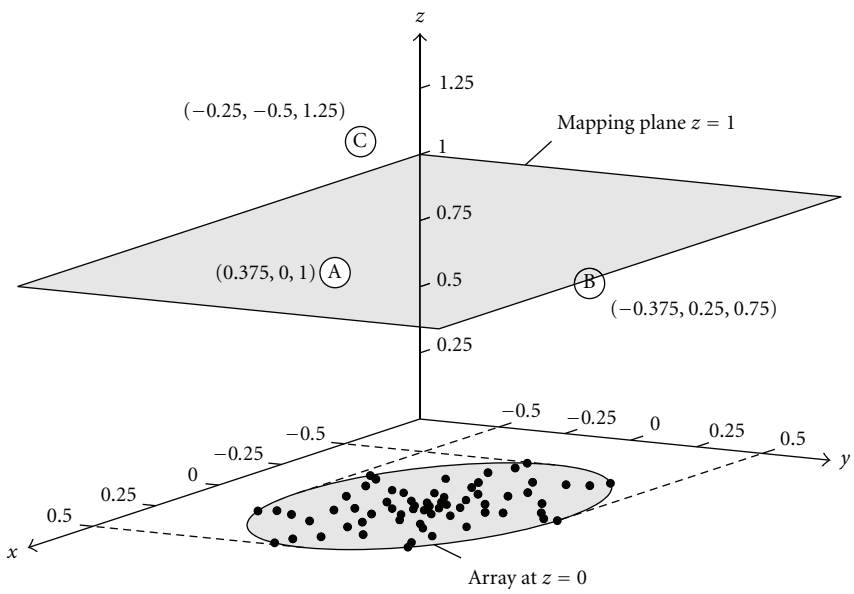

Figure 2: Set-up used for the simulations: 64-channel microphone array and three uncorrelated sources A, B, C with identical source strength, coordinates, and lengths are nondimensionalised by the array aperture.

for practical cases with extended sources that use three-dimensional mapping can be found elsewhere [18, 19, 25].

The source mappings that should be discussed here are based on simulated data that was generated using the set-up shown in Figure 2. It uses a 64 microphone array to analyse three point sources. The microphone array is planar and has a layout that consists of 7 spiral arms that contain 9 logarithmically spaced microphones each and an additional microphone in the centre. The aperture d of the array, defined by the diameter of the smallest circle containing all microphones, is used as a scaling parameter in the analysis. All coordinates and lengths in the analysis are nondimensionalised by the aperture. Frequencies are given in nondimensional form as Helmholtz numbers $\mathrm{He} = d/\lambda = fd/c$ with λ being the wavelength and c being the speed of sound.

The positions of the sources are chosen randomly to span a region with lateral dimensions comparable to the array itself. The distance to the array varies between 0.75 and 1.25 apertures. This choice was made because the application of threedimensional source mapping is most interesting when distances of the sources to the array are somewhat different. However, very large ratios of the distances (i.e., one source very close and another source far away) are not likely to appear in a practical application. Altogether the scenario is somewhat representative of a situation where the object under test has dimensions comparable to the aperture. Typically this would allow for the beamforming analysis at frequencies with wavelengths much smaller than the object. An aperture much larger than the object is desirable for the analysis at lower frequencies. When the application of large aperture arrays is not practicable, the analysis requires deconvolution methods. As results from deconvolution are of special interest here, a scenario representative for this case was chosen as illustrative example.

The simulated microphone signals were calculated using a transfer function similar to (2). The point sources were driven by simulated white noise signals from different gaussian random processes to ensure that they are not coherent. All three sources had the same power. Nevertheless, because of the different distances to the array plane and therefore also to the array centre $\mathbf{x}_0$, the relative sound pressure levels at $\mathbf{x}_0$ due to the individual sources were different: 0 dB, 1.7 dB, and −2.2 dB for source A, B, and C, respectively.

The array was placed in the plane $z = 0$ and two different grids were used. The first grid used for the three-dimensional source mapping covered a block-shaped region with $-1 < x < 1$, $-1 < y < 1$, and $0.125 < z < 2$. It had a uniform grid spacing of 1/32 aperture and the overall number of grid points was 257, 725. The second grid for two-dimensional source mapping in a plane parallel to the array had the same spacing and had the same extent $-1 < x < 1$, $-1 < y < 1$, but for $z = 1$. The overall number of points in this case was 4225. The simulated microphone signals were sampled at a rate that corresponds to $\mathrm{He} = 64$. A fast Fourier transform with prior von Hann weighting was applied for every channel to 1000 consecutive, 50% overlapping blocks of 1024 samples each. All 64^2 cross spectra were calculated and averaged over the 1000 blocks to produce the cross spectral matrix.

The quality of an acoustic source mapping can be determined by evaluating the errors in the source levels and source locations that are estimated using the mapping result. According to the definition in (1), the source level,

$$L_s = 10\log_{10}\frac{E\{qq^*\}}{p_{\mathrm{ref}}^2}\,\mathrm{dB}, \tag{14}$$

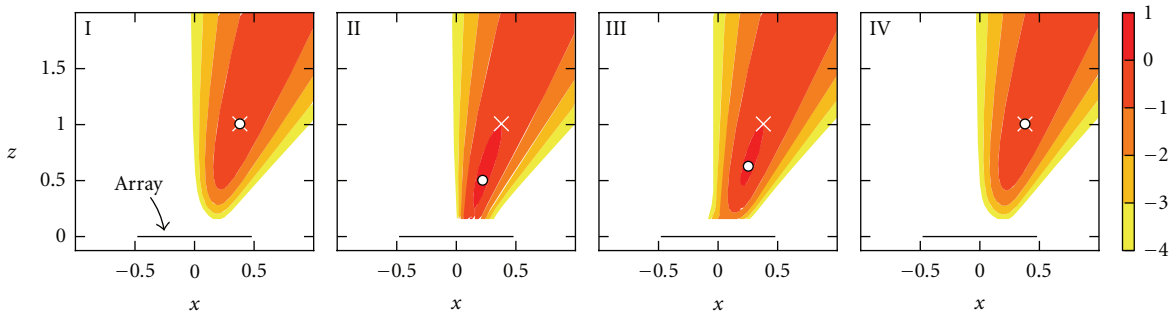

Figure 3: Maps of sound pressure level contributions at the array centre (in dB relative to the correct value) for steering vector formulations I–IV, Helmholtz number He = 2, $y = 0$, white dot: location of the maximum, cross: true source location.

of a certain source is defined as the sound pressure level calculated from the sound pressure q at the array centre caused by that source (p_{ref} is the reference sound pressure). The estimated source level is then

$$L_e = 10 \log_{10} \frac{B}{p_{\text{ref}}^2} \text{dB}, \tag{15}$$

and the error in this level is given by $\Delta L = L_e - L_s$, where L_s is taken to be the true level.

The source location is a vector quantity and involves three components. While the error here could be given as the distance between the true and the estimated location, this quantity is always positive and contains no information on the spatial arrangement. Instead, the error in the estimated source location shall be defined here as an error of the distance r between source and the array centre. It is given by $\Delta r = r_e - r_s$, where r_e and r_s are the estimated and true distances, respectively. As it is reasonable to assume that this error will also increase with the distance, it is used here in the normalised form $\Delta r / r_s$. As the errors in source location and level also depend on the frequency, they are discussed here regarding their dependence on the Helmholtz number.

3.1. Single Source. In the first test case, only source A was operated. In this simple single source scenario it is feasible to use the classic beamforming approach (4) and to do without a deconvolution technique. In Figure 3, the results for all four formulations of the steering vector (I–IV) are compared for He = 2. The source mapping itself is three-dimensional. However, for clarity of presentation only a slice of the mapping along the plane $y = 0$ (perpendicular to the array plane) is shown which contains the true source location. The four formulations obviously lead to different mapping results. In agreement with the theoretical analysis, both formulations I and IV meet the condition (5) that the maximum in the map coincides with the actual source position. For both formulations II and III the maximums in the map are situated somewhere between the actual source position and the array centre. Thus, it would not be possible to estimate the exact source position from the maximum in the source mapping. The actual source position is located on the 0 dB contour for both formulations II and III. In agreement with theory, this shows that condition (6) is met.

While for formulations I and IV the error in source location as shown in Figure 4(a) is zero regardless of He, for formulations II and III; this error becomes less than 5% only above He $\approx$ 5. However, the estimated distance between array centre and source is never larger than the actual distance.

In the present case, the only option to estimate the source level is to use the maximum in the map. Figure 4(b) shows the error in comparison for all four formulations. Formulations I and IV show constant, small errors that follow the theoretical analysis in (8) and (13), respectively. For low Helmholtz numbers, the formulations II and III lead to larger errors because of the error in the estimated source location (the value at the location of the maximum in the map taken as source level). The error vanishes for larger Helmholtz numbers which is in agreement with the theoretical analysis.

3.2. Three Sources, Two-Dimensional Mapping. The second test case where all three sources are operated is a slightly more realistic scenario. In this case, the strength and the location of all three sources are of interest. If a classic beamforming approach with the mapping plane parallel to the array is used, the two-dimensional beamforming maps (Figure 5) show only minor differences for the four formulations. While only source A is actually located in the mapping plane at $z = 1$, contributions from all three sources appear in the maps. Thus, without any further analysis the maps suggest that all sources are located within this plane.

With the exception of source A, the maximums do not coincide with the projected source positions for both Helmholtz numbers shown. The reason is that sources B and C are not located in the mapping plane. The results show the tendency to map the sources nearer to the array more into the direction of the projected array center, while sources with a distance greater than that of the mapping plane are mapped to a an apparent position further away from the center. If there is no information available about the true distance between source and array, there is no way to estimate the exact source positions from the mapping

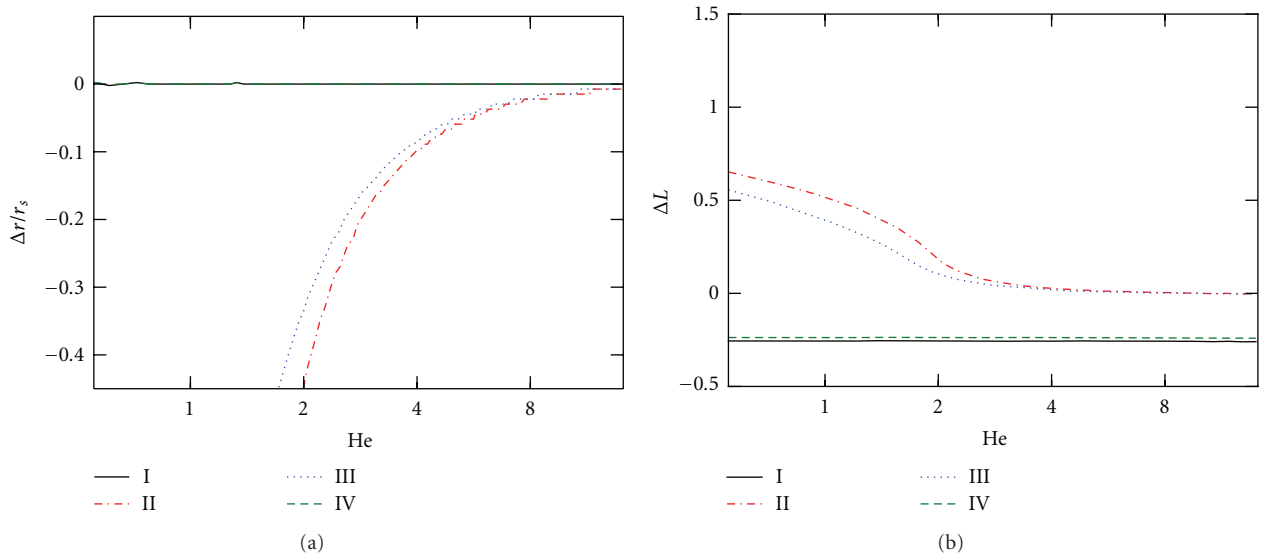

Figure 4: Errors in (a) source location and (b) source strength for formulations I–IV as a function of the Helmholtz number He.

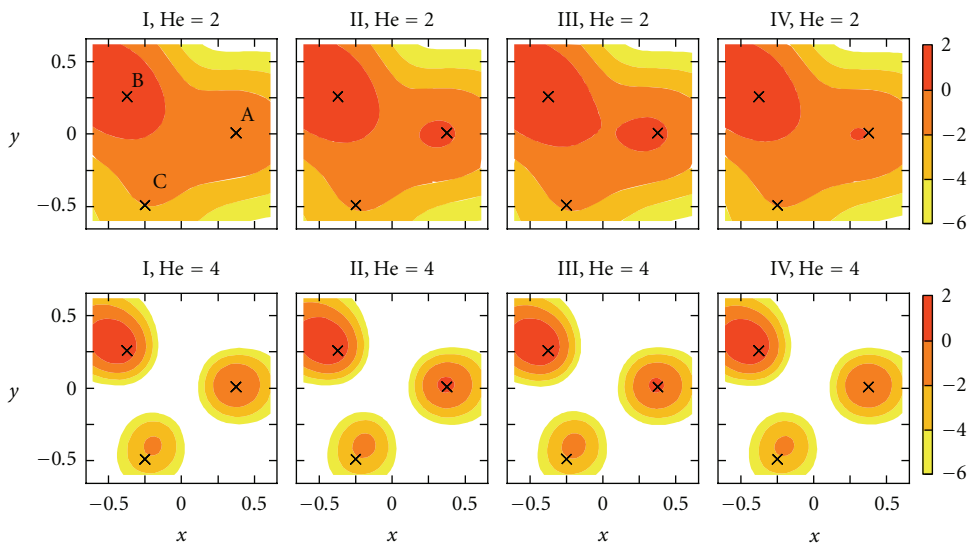

Figure 5: Maps of relative sound pressure level contributions at the array centre (correct values are 0 dB, 1.7 dB, and −2.2 dB for source A, B, and C, resp.) using classic beamforming without deconvolution for steering vector formulations I–IV, Helmholtz numbers He = 2 and 4, $z = 1$, crosses mark the projected position of the sources.

result. For the same reason, it is not feasible to estimate the source strength or to rank the sources using the result from the two-dimensional mapping. While all sources have the same source strength, the result shows the respective sound pressure level contribution at the array centre. If all sources are assumed to be within the mapping plane, B then appears to be the strongest and C appears to be the weakest source.

At the lower frequency shown (He = 2), the sources are less clearly distinguishable because of the large main lobe width at this frequency. If the source spacing would be smaller, the same would happen even at higher frequencies. Thus, the result can be improved if the real beamformer filter properties are taken into account by using a deconvolution technique. In the present case, the deconvolution method CLEAN-SC was applied (see [11] for more details) to the beamforming map. The result is a map that shows nonzero entries only at those grid points where a source is found. This corresponds to a negligible main lobe width regardless of frequency.

When applied to the two-dimensional beamforming results from Figure 5, CLEAN-SC delivers maps that allow for an easy separation of the sources even at the lower

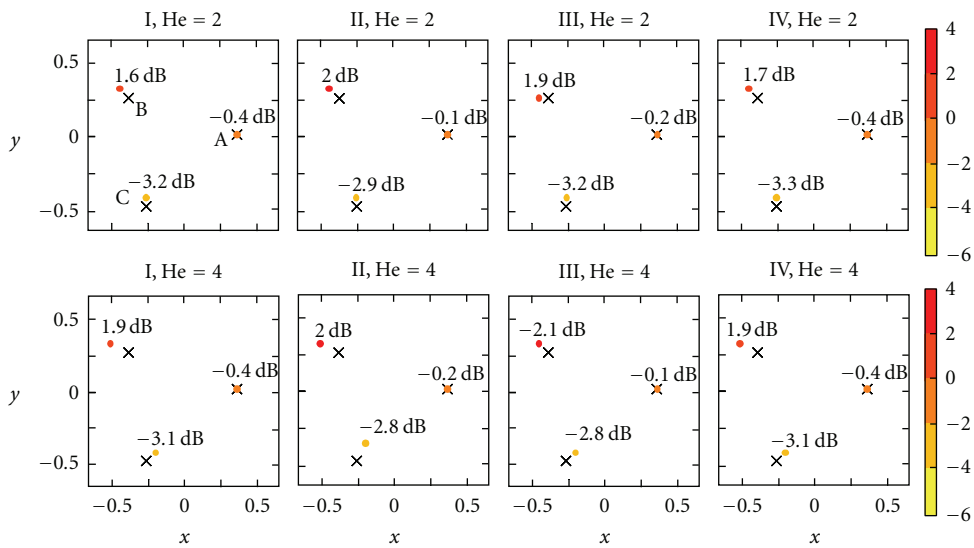

Figure 6: Maps of relative sound pressure level contributions at the array centre (correct values are 0 dB, 1.7 dB, and −2.2 dB for source A, B, and C, resp.) using CLEAN-SC on a two-dimensional grid at $z = 1$, for steering vector formulations I-IV, Helmholtz numbers He = 2 and 4, crosses mark the projected position of the sources.

frequency (Figure 6). Similar to the result from classic beamforming, these maps show all sources as they where situated in the mapping plane. The estimated locations of sources B and C again do not coincide with the projected source positions. The four different steering vector formulations lead to some differences in the estimated source level but show no divergent effects otherwise. To summarise, these results allow to conclude that there are at least three sources, but the information about the (projected) location is limited and a ranking of the sources is not possible.

The effect on the estimated source level as a function of frequency can also be estimated. If the source positions are known, the source level can be estimated from the map by simply taking the values at the grid points that are located at source positions. To allow for small errors in the estimated source positions, in the present case the source level was estimated by integrating over small square regions of the map. These regions were centred at the nominal source positions and had a side length of 0.1 array apertures.

The results in Figures 7(a), 7(c), and 7(e) show that the errors of the estimated source levels tend to be larger at very low Helmholtz numbers and become smaller for He > 2. However, for the sources B and C that are not situated within the mapping plane, the error again increases above He = 8, obviously as a result of the wrong mapping. Similar to the result shown in Figure 6, the four different steering vector formulations show only small differences, with formulations I and IV giving somewhat smaller levels compared to formulations II and III.

3.3. Three Sources, Three-Dimensional Mapping. More information can be gathered when the deconvolution is applied to a three-dimensional beamforming map. To study the results in comparison to two-dimensional beamforming, the analysis of a slice from the three-dimensional result is one option. Figure 8 shows such a slice at $z = 1$ that is equivalent to the mapping plane shown in Figure 2. Sources B and C that are not situated within this plane do not appear in any of the maps. Source A is within the plane but appears only for formulations I and IV and in case of formulation III for the higher frequency (He = 4). The reason for the absence of any source in the remaining maps is that the sources are mapped at the wrong position in the z direction. This becomes obvious in the two-view orthographic projections (Figure 9) of the three-dimensional map that is another option for the graphical representation of the result.

The projections along the y-axis (x-z-plane) reveal that the sources are indeed mapped much closer to the array as they really are for formulations II and III and low frequencies (He = 2). For formulations I and IV, the error in the location is much smaller at this frequency but not zero ($\Delta r/r_s = \pm 0.1 \cdots 0.2$). This effect is present only for the multisource scenario. It can be attributed to the fact that the location of the maximum in the beamforming map for a certain source is slightly shifted by the influence of other sources. For He = 4, no error is visible in the maps with exception of source A and formulation II. This small error also vanishes at even higher frequencies. While the estimated source levels are somewhat different for the different formulations, the errors are small, and no formulation seems to produce distinctly smaller errors than the others.

Finally, the error of the estimated source level shall be examined. Again, the source level was estimated by integrating over regions with a side length of 0.1 array apertures

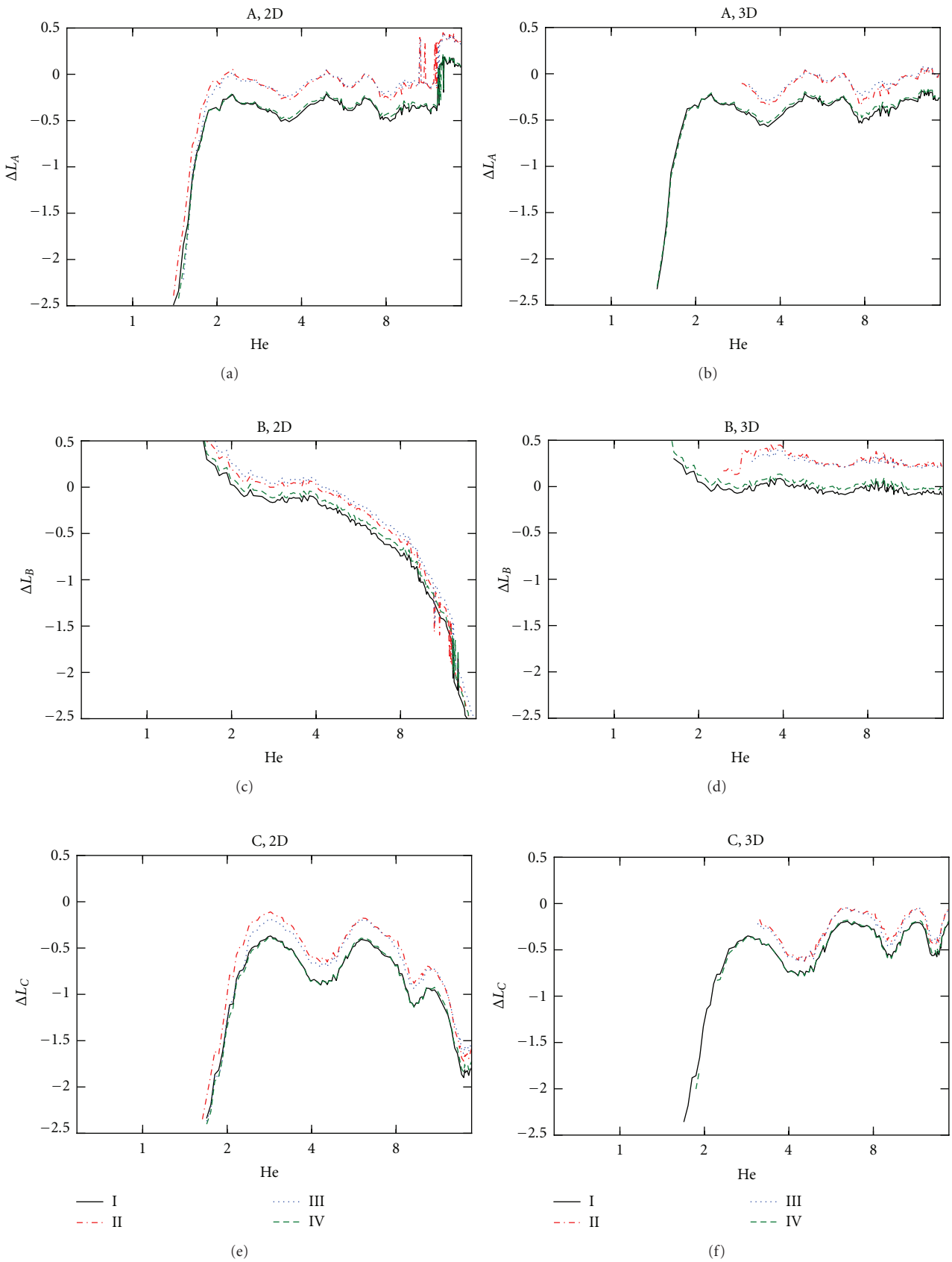

Figure 7: Errors (in dB) in the estimated sound pressure levels for formulations I–IV: (a, b) source A, (c, d) source B, and (e, f) source C.

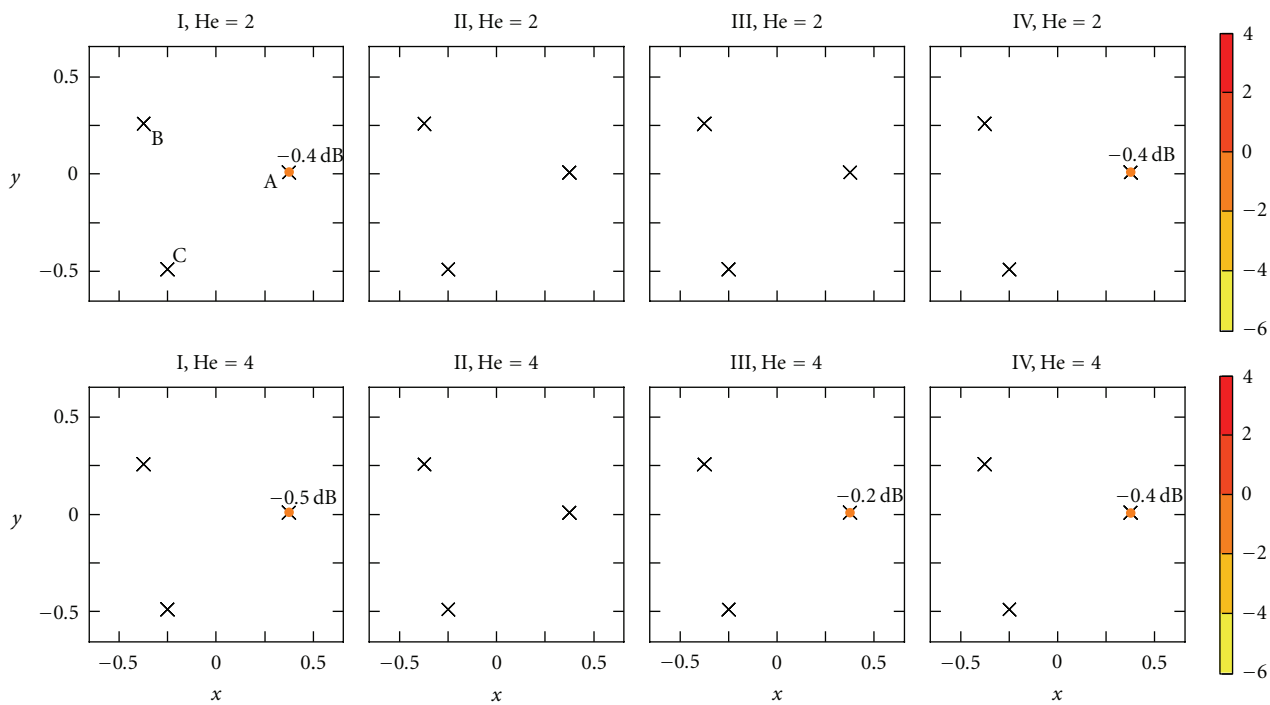

Figure 8: Slices at $z = 1$ of three-dimensional maps of relative sound pressure level contributions at the array centre (correct values are 0 dB, 1.7 dB, and −2.2 dB for source A, B, and C, resp.) using CLEAN-SC on a three-dimensional grid for steering vector formulations I–IV, Helmholtz numbers He = 2 and 4, crosses mark the projected position of the sources.

centred at the source position, but this time the regions were cubic shaped. Figures 7(b), 7(d), and 7(f) show the errors of the estimated source levels for all three sources. The results for formulations I and IV are again very similar and show a small negative error over a wide range of Helmholtz numbers. This error is consistent with the results from the theoretical analysis in (8) and (13) and is negligible for most practical applications. In contrast to the theoretical analysis, the error does not vanish completely for formulations II and III, though it is also negligibly small. For lower Helmholtz numbers, the beamforming and deconvolution method maps the source to a location outside the sector used for the integration. Thus, the estimated source level becomes infinitely small and consequently $\Delta L = -\infty$. While this is the case for He < 2 for all three sources and formulations I and IV, the estimated source level for formulations II and III vanishes already below He $\approx 3 \cdots 4$. The error does not increase for higher Helmholtz numbers as it is the case for the levels estimated from two-dimensional mapping.

It can be concluded that the principal theoretical findings regarding the different formulations I–IV in a single-source scenario remain true for the multiple source case: formulations I and IV deliver the correct source locations already for low Helmholtz numbers but show a small systematic error in the estimated source level. Formulations II and III deliver a slightly less erroneous level, but only for higher Helmholtz numbers, when the error in the estimated source location is small enough to place the source within the integration sector. Thus, for the given scenario the practical differences between the different formulations are generally small for higher Helmholtz numbers. However, in applications where small Helmholtz numbers arise, only formulations I and IV can be applied.

Because the errors in source level are very small for all formulations, formulations I and IV seem to be preferable for the practical application of three-dimensional acoustic source mapping using a beamforming approach. Moreover, once the correct position of a source is estimated, the systematic errors in the source levels for formulations I and IV can be corrected for by taking into account the factors in (8) and (13), respectively. Finally, formulation I has the extraadvantage that the calculation of the steering vectors requires less arithmetic operations.

4. Conclusion

A crucial element for the three-dimensional application of beamforming source mapping techniques using a microphone array is the formulation of the steering vectors. It was shown here that four different formulations found in the literature lead to different results. In theory, no formulation produces both correct source location and strength. Two formulations lead to the correct location at the cost of a

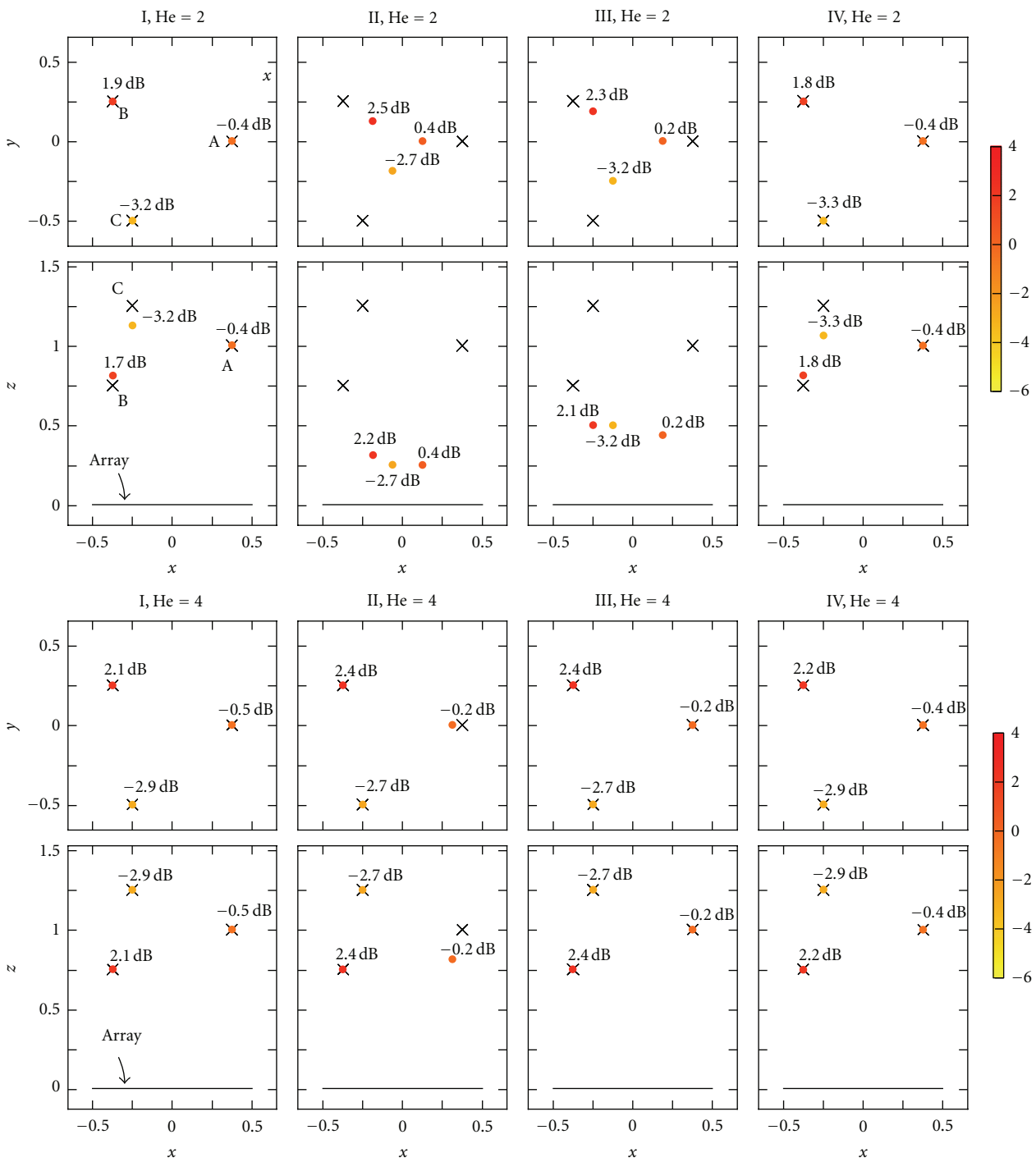

FIGURE 9: Projections of three-dimensional maps of relative sound pressure level contributions at the array centre (correct values are 0 dB, 1.7 dB, and −2.2 dB for source A, B, and C, resp.) using CLEAN-SC on a three-dimensional grid for steering vector formulations I–IV, Helmholtz numbers He = 2 and 4, crosses mark the projected position of the sources.

small error in the estimated source strength. The other two formulations estimate the correct strength but show an error in the estimated location of the source. Using simulated measurement data, it was shown that this error is relevant especially at low Helmholtz numbers based on the array aperture. In a simulated three-source scenario with CLEAN-SC deconvolution, all four formulations lead to small errors in the estimated strength of the sources. Unlike the systematic errors in source location, the systematic errors in the level can be corrected for in principle. Thus, the major conclusion

is that for three-dimensional source mapping those steering vector formulations are preferable that enable the best estimation of the source location, for example, formulations I or IV.

References

[1] P. Nelson, "Source identification and location," in *Advanced Applications in Acoustics, Noise, and Vibration*, F. Fahy and J. Walker, Eds., pp. 100–153, Taylor & Francis, 2004.

[2] B. Barsikow, "Experiences with various configurations of microphone arrays used to locate sound sources on railway trains operated by the DB AG," *Journal of Sound and Vibration*, vol. 193, no. 1, pp. 283–293, 1996.

[3] M. Mosher, "Phased arrays for aerocoustic testing: theoretical development," in *Proceedings of the 2nd AIAA/CEAS Aeroacoustics Conference*, State College, Philadelphia, Pa, USA, May 1996, AIAA-1996-1713.

[4] R. Dougherty, "Beamforming in acoustic testing," in *Aeroacoustic Measurements*, T. Mueller, Ed., pp. 62–97, Springer, Berlin, Germany, 2002.

[5] T. Brooks and W. Humphreys, "Effect of directional array size on the measurement of airframe noise components," AIAA paper 99-1958, 1999.

[6] S. Oerlemans, L. Broersma, and P. Sijtsma, "Quantification of airframe noise using microphone arrays in open and closed wind tunnels," *International Journal of Aeroacoustics*, vol. 6, no. 4, pp. 309–333, 2007.

[7] D. Blacodon, G. Elias, D. Papillier, and J. Prieur, "Noise source localization on a dauphin helicopter in flight," in *Proceedings of the 25th European Rotorcraft Forum*, Roma, Italy, September 1999.

[8] T. Suzuki, "A review of diagnostic studies on jet-noise sources and generation mechanisms of subsonically convecting jets," *Fluid Dynamics Research*, vol. 42, no. 1, Article ID 014001, 2010.

[9] B. D. van Veen and K. M. Buckley, "Beamforming: a versatile approach to spatial filtering.," *IEEE ASSP magazine*, vol. 5, no. 2, pp. 4–24, 1988.

[10] T. F. Brooks and W. M. Humphreys, "A deconvolution approach for the mapping of acoustic sources (DAMAS) determined from phased microphonearrays," AIAA paper 2004-2954, 2004.

[11] P. Sijtsma, "CLEAN based on spatial source coherence," AIAA paper 2007-3436, 2007.

[12] J. Hileman, B. Thurow, and M. Samimy, "Development and evaluation of a 3-D microphone array to locate individual acoustic sources in a high-speed jet," *Journal of Sound and Vibration*, vol. 276, no. 3–5, pp. 649–669, 2004.

[13] T. Brooks and W. Humphreys, "Three-dimensional application of DAMAS methodology for aeroacoustic noise source definition," AIAA paper 2005-2960, 2005.

[14] S. N. Y. Gerges, W. D. Fonseca, and R. P. Dougherty, "State of the art beamforming software and hardware for applications," in *Proceedings of the 16th International Congress on Sound and Vibration*, Krakow, Poland, July 2009, keynote lecture 2.

[15] R. P. Dougherty, "Jet noise beamforming with several techniques," in *Proceedings on CD of the 3rd Berlin Beamforming Conference*, February 2010, BeBeC-2010-17.

[16] K. Oakley, "Noisecam—using 3d beamforming to better localise noise sources on hovercraft," in *Proceedings on CD of the 3rd Berlin Beamforming Conference*, February 2010, BeBeC-2010-22.

[17] H. Brick, T. Kohrs, E. Sarradj, and T. Geyer, "Noise from high-speed trains: experimental determination of the noise radiation of the pantograph," in *Proceedings of the Forum Acusticum*, Aalborg, Denmark, 2011.

[18] T. Geyer, E. Sarradj, and J. Giesler, "Application of a beamforming technique to the measurement of airfoil leading edge noise," *Advances in Acoustics and Vibration*, vol. 2012, Article ID 905461, 2012.

[19] E. Sarradj, "Three-dimensional acoustic source mapping," in *Proceedings on CD of the 4th Berlin Beamforming Conference*, February 2012, BeBeC 2012-11.

[20] M. Legg and S. Bradley, "Comparison of clean-sc for 2d and 3d scanning surfaces," in *Proceedings on CD of the 4th Berlin Beamforming Conference*, February 2012, BeBeC 2012-06.

[21] R. Dougherty, "Extensions of DAMAS and benefits and limitations of deconvolution in beamforming," AIAA paper 2005-2961, 2005.

[22] D. H. Johnson and D. E. Dudgeon, *Array Signal Processing: Concepts and Techniques*, Simon & Schuster, 1992.

[23] E. Sarradj, "A fast signal subspace approach for the determination of absolute levels from phased microphone array measurements," *Journal of Sound and Vibration*, vol. 329, no. 9, pp. 1553–1569, 2010.

[24] P. Stoica and R. Moses, *Introduction to Spectral Analysis*, Prentice Hall, New York, NY, USA, 1997.

[25] T. Geyer, *Trailing edge noise generation of porous airfoils [Ph.D. thesis]*, Brandenburg University of Technology at Cottbus, 2011.

Hindawi Publishing Corporation
Advances in Acoustics and Vibration
Volume 2012, Article ID 275858, 6 pages
doi:10.1155/2012/275858

Research Article

Transducer Field Imaging Using Acoustography

Jaswinder S. Sandhu,[1] Robert W. Schoonover,[2] Joshua I. Weber,[1] J. Tawiah,[1] Vitaliy Kunin,[1] and Mark A. Anastasio[2]

[1] *Santec Systems, Inc., 2924 Malmo Drive, Arlington Heights, IL 60005, USA*
[2] *Department of Biomedical Engineering, Washington University in St. Louis, St. Louis, MO 63130, USA*

Correspondence should be addressed to Jaswinder S. Sandhu, j-sandhu@santecsystems.com

Received 23 December 2011; Accepted 29 March 2012

Academic Editor: Jafar Saniie

A common current practice for transducer field mapping is to scan, point-by-point, a hydrophone element in a 2D raster at various distances from the transducer radiating surface. This approach is tedious, requiring hours of scanning time to generate full cross-sectional and/or axial field distributions. Moreover, the lateral resolution of the field distribution image is dependent on the indexing steps between data points. Acoustography is an imaging process in which an acousto-optical (AO) area sensor is employed to record the intensity of an ultrasound wavefield on a two-dimensional plane. This paper reports on the application of acoustography as a simple but practical method for assessing transducer field characteristics. A case study performed on a commercial transducer is reported, where the radiated fields are imaged using acoustography and compared to the corresponding quantities that are predicted numerically.

1. Introduction

An important aspect of transducer quality control is to assess the radiated ultrasonic field characteristics, which can be affected by factors such as piezoelectric element misalignment with respect to transducer housing, material inhomogeneity, lack of bonding, electrode design and contact placement, acoustic lens quality, and wear plate uniformity and adhesion, to mention a few. A common practice for assessing beam characteristics is to scan a small hydrophone element point-by-point in a plane perpendicular to the transducer's radiation axis [1, 2]. This generates a 2D cross-sectional field distribution at a given distance away from the transducer's radiating surface. To generate a 3D field distribution, 2D cross-sectional distributions are generated at increasing distances along the radiation axis. Hydrophone scanning is slow and tedious, requiring many hours of scanning time to generate the complete field characteristics of the transducer. Moreover, the lateral resolution of the hydrophone scanning method is dependent on the indexing steps between data points as well as the hydrophone element size.

Acoustography [3, 4] is a full-field ultrasonic imaging process wherein an acousto-optical (AO) area sensor is employed to convert ultrasound into a visual image in real time. The AO sensor converts ultrasound energy directly into a visual image by virtue of the inherent acousto-optic effect in our proprietary liquid crystal (LC) or "mesophase" material contained in the AO sensor [3–5]. Theoretical and experimental investigations into the dynamics of liquid crystal devices have been performed to assess the role of geometrical and liquid crystal properties in similar devices [6, 7]. Liquid crystal devices utilizing the AO effect have found utility in acoustic holography [8], medical imaging [9], optical devices [10], and the inspection of composites [11].

In this paper, we report on the application of acoustography for mapping transducer fields. Since it can yield high spatial-resolution recordings of a 2D cross-sectional field distribution without the need for mechanical scanning, acoustography represents a simple and practical method for this application. Experimental studies are conducted in which acoustography is employed to map the fields produced by a commercial transducer at a collection of distances along the transducer's radiation axis. These recordings are compared

to estimates of the fields obtained by numerically solving the associated Rayleigh diffraction integral.

2. Background: Basic Principles of AO Sensors

In the AO sensor used in this work, the LC molecules are initially arranged to be parallel to each other but perpendicular to the confining substrates; confining substrates are acoustically transparent, but one of the substrates is also optically transparent. In this configuration of the molecules, the LC material behaves like a slab of a uniaxial, positive birefringent crystal with optic axis parallel to the LC molecular alignment direction ($\underline{n}$). For such an LC layer, the optical behavior (i.e., brightness change, T) under polarized light can be described by [12]:

$$T = \sin^2\left[\left(\frac{2\pi d}{\lambda}\right)\cdot(n_{\parallel} - n_{\perp})\cdot\sin^2\theta(I)\right], \qquad (1)$$

where d is LC layer thickness; λ is wavelength of light; $n_{\parallel}$ is refractive index of LC along the optic axis ($\underline{n}$); $n_{\perp}$ is refractive index of LC perpendicular to optic axis ($\underline{n}$); $\theta(I)$ is ultrasonically induced tilt angle of the LC molecules that is a function of the ultrasonic intensity I.

In the absence of an ultrasound field, the molecular tilt angle, θ, is zero, and the AO sensor is uniformly dark across the field of view. However, when an area of the AO sensor is exposed to an ultrasonic field, the LC molecules experience a torque [13], which tilts the LC molecules in the ultrasonically exposed region of the AO sensor. As a result, the ultrasonically exposed area of the AO sensor appears bright. Figure 1 illustrates this process. The local induced brightness level of the AO sensor is related to the local ultrasonic intensity [13]; therefore, an ultrasonic intensity image can be created from the visual image of the AO sensor.

The lateral resolution in acoustography is very high because the visual image is created by the local interaction between the ultrasound field and the (~2 nanometer) LC molecules. In practice, the transverse resolution of this method is limited by the optical camera used to image the AO sensor. For this study, an optical system with 0.31 mm pixel size was chosen; however, higher-resolution optical cameras may be used when the application warrants it. The contrast resolution in acoustography depends on the AO sensor's acousto-optic transfer curve [6, 8], which is analogous to the characteristic curve of an X-ray detector. The AO transfer curve expresses the relationship between ultrasonic intensity and the corresponding optical density (brightness level).

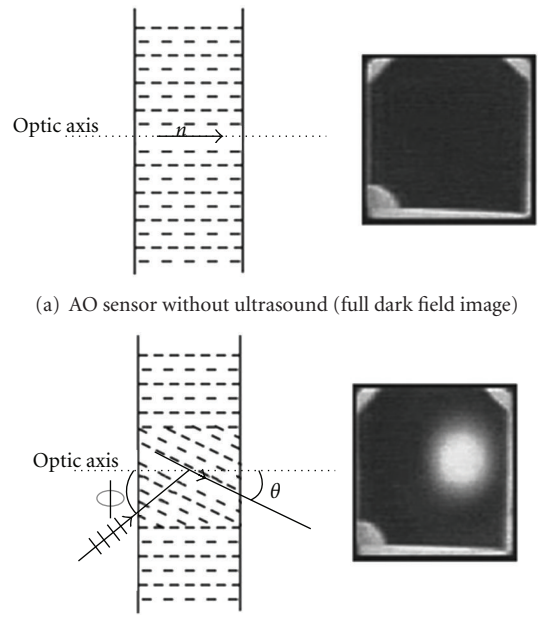

(a) AO sensor without ultrasound (full dark field image)

(b) AO sensor stimulated with ultrasound (area shown as bright spot)

Figure 1: In panel (a), a schematic of the AO sensor before insonification by an ultrasound field is shown alongside an image of the AO sensor, when the LC molecules are aligned along the optical axis. In panel (b), a schematic of the AO sensor after insonification by an ultrasound field is shown alongside an image of the AO sensor, when the LC molecules have been perturbed by an ultrasound field.

3. Methods

3.1. Imaging System. Figure 2 displays an overhead view of the acoustography imaging system. The system consists of a water-immersion tank with dimensions 36″(L) × 36″(W) × 12″(D); a 1″ diameter flat circular test transducer (GE Inspection Technologies) suspended in the water tank; a 5″× 5″ area AO sensor; a digital video camera (Basler A311, not shown) housed in the Optics Box. The optical system has an effective pixel size of 0.31 mm × 0.31 mm. The test transducer was attached to a moveable slide, where the position of the movable slide could be set with an accuracy of ±1 mm with respect to the position of the AO sensor. The beam angle of the test transducer was set with an accuracy of better than 0.5°.

3.2. Experimental Studies. For a flat, circular transducer, such as the one used in this experiment, the ultrasonic intensity along the central axis of the transducer can be expressed as [14]

$$\frac{I(z)}{I(0)} = \sin^2\left[\frac{\pi}{\lambda}\left(\sqrt{r^2+z^2} - z\right)\right], \qquad (2)$$

where $I(0)$ is the maximum intensity, $I(z)$ is the intensity at distance z from the transducer radiating surface, r is radius of the transducer radiating element, and λ is the acoustic wavelength in water. Two-dimensional images of the radiation pattern of the cylindrical transducer were made at four distances, as measured along the central axis of the transducer. Each measurement distance corresponded to either a minimum or maximum of the intensity along the axis (see Figure 3), or a point in the far-field of the transducer. The transition between the near-field and the far-field for this transducer was calculated to be at 35.3 cm.

The nominal frequency of the transducer was 3.5 MHz. However, the transducer was operated at 3.3 MHz to match the operating frequency of the AO sensor. The transducer beam angle was set at 21° with respect to the AO sensor

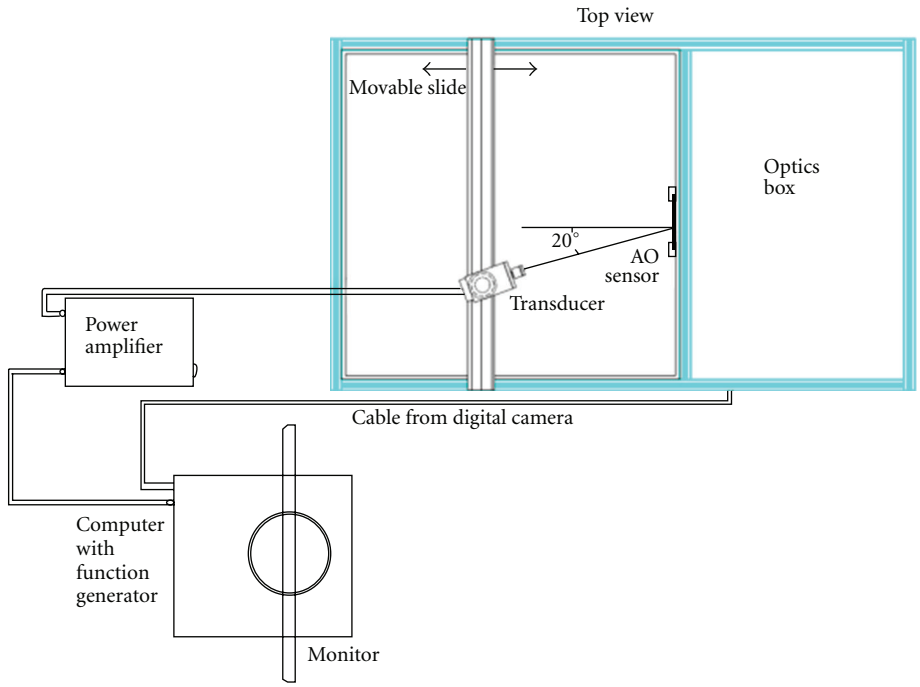

Figure 2: An overhead view of the acoustic imaging system.

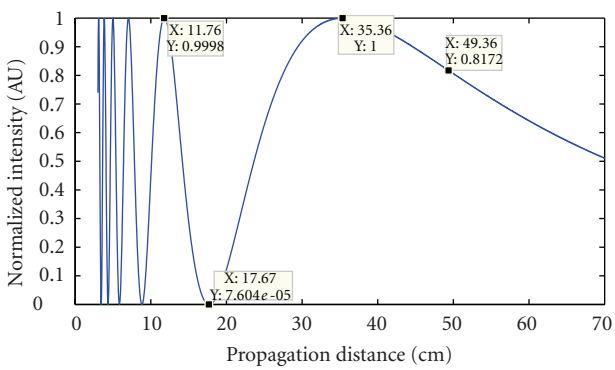

Figure 3: Intensity profile along the central radiation axis of a 1″ diameter transducer element operated at 3.3 MHz.

normal, to avoid reverberations between the AO sensor and the transducer's radiating surface. The transducer was energized using a continuous wave (CW) signal.

For each measurement distance, the intensity map on the AO sensor was captured after less than 10 seconds of insonification. Image capture and processing by the camera system was performed in 30 seconds. The AO sensor has a reset time (to realign the LC molecules) of less than 5 seconds. Thus, the ultrasound intensity at >22,00 distinct spatial positions (142 × 156 array) was measured in less than 35 seconds total.

3.3. Computer-Simulation Studies. Simulations of the ultrasonic field produced by a 1″ transducer were also performed to corroborate the images acquired in the experimental studies. The simulations, performed using the DREAM Toolbox for MATLAB [15], calculated the spatial impulse response of a 0.95″ diameter transducer on a plane rotated by 21° with respect to the central axis of the transducer, a distance z away (where z corresponds to the various measurement distances). The pixel size was chosen to be the same as the effective pixel size of the AO sensor + optical system: 0.31 mm × 0.31 mm. The choice of 0.95″ for the transducer diameter was chosen to best match the experimental data. The spatial impulse response was a 2D × 1D signal (two spatial dimensions to represent the measurement plane and one temporal dimension to represent the time-varying ultrasound field). The discrete Fourier transform of the resulting time series at each pixel in the measurement plane was computed by use of the fast Fourier transform algorithm. The element of the discrete Fourier transform, most closely corresponding to 3.3 MHz at that pixel, was selected. The resulting 2D data, corresponding to a monochromatic ultrasound field at 3.3 MHz on the measurement plane, were then squared to represent the ultrasound intensity. The simulations assume a perfectly flat transducer with specified diameter.

4. Experimental Results

4.1. Experimental and Simulated Images. The first column of Figure 4 displays the ultrasonic field maps recorded by use of the AO sensor in the experimental studies. Specifically, the images depict the field intensity distributions on planes located at distances z = 11.76 cm (panel (a)), 17.67 cm (panel (d)), 35.36 cm (panel (g)), and 49.36 cm (panel (j)) from the transducer face along the radiation axis.

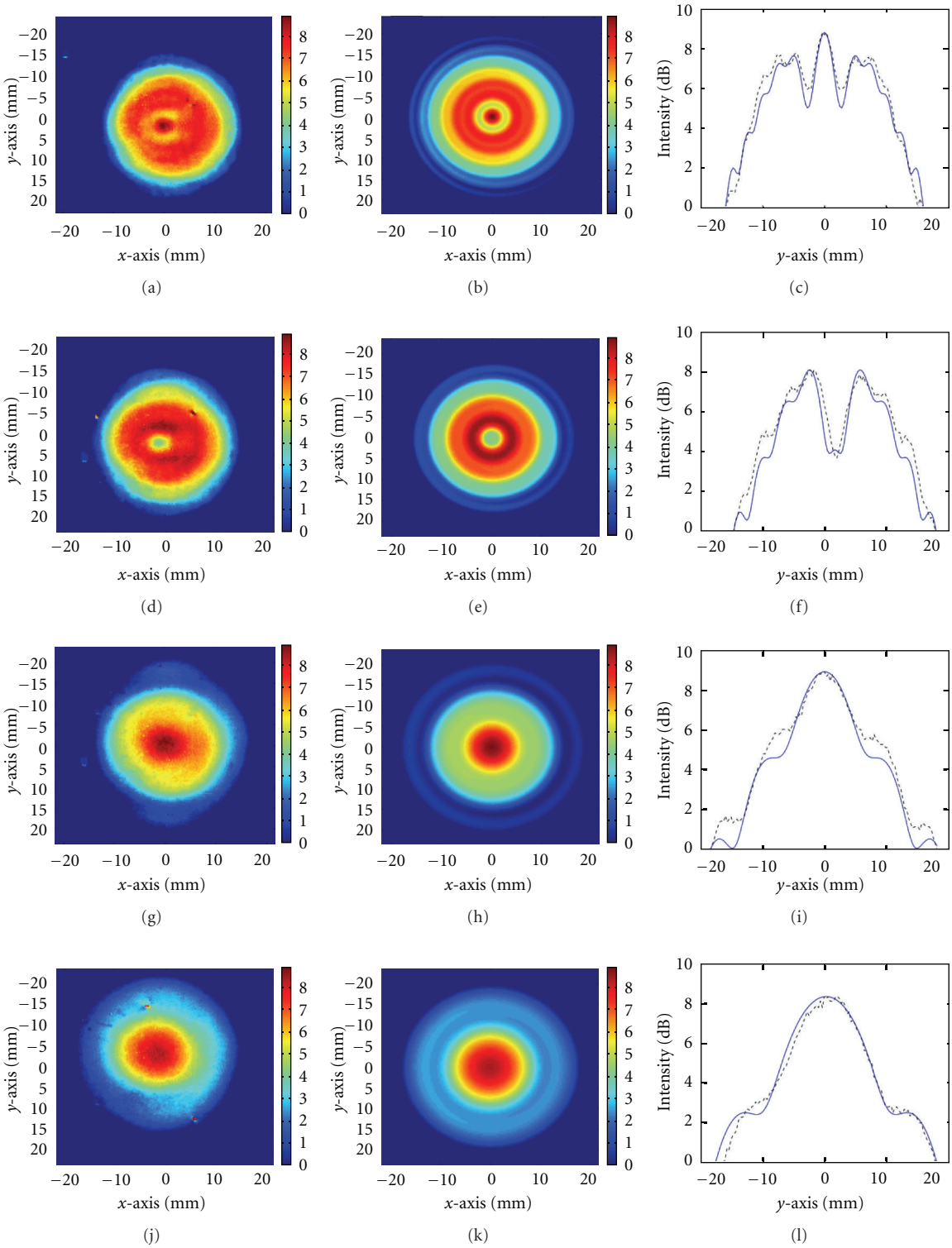

Figure 4: Images of the experimentally determined transducer radiation patterns are shown in the first column. In the second column, theoretically determined transducer radiation patterns are shown. Line plots through the center of the experimental data (black dashed lines) and the theoretical data (blue solid lines) are shown in the third column. The first row corresponds to a propagation distance of 11.76 cm (the location of an intensity maximum on the optical axis in the near zone). The second row corresponds to a propagation distance of 17.67 cm (the location of an intensity minimum on the optical axis in the near zone). The third row corresponds to a propagation distance of 35.36 cm (the near-zone/far-zone transition distance). The fourth row corresponds to a propagation distance of 49.36 cm (a distance in the far zone).

The distances were chosen based on the on-axis intensity profile in Figure 3. The ultrasound intensity in these images was displayed in decibels.

The corresponding simulated intensity images are displayed in the middle column of Figure 4. The simulated intensity data was scaled so that the peak intensity in each simulation matched the peak intensity in the corresponding experimental data. Plots along the y-axis ($x = 0$) of both the experimental (black dashed lines) and theoretical (blue solid lines) results are shown in panels (c), (f), (i), and (l) of Figure 4.

4.2. Discussion of Results. One notes that there is an overall qualitative agreement between the intensity patterns generated through simulation and those obtained with the AO sensor. Comparisons of the intensities in the first and second columns of Figure 4 show strong agreement in predicting the ring structure in the near-zone measurements (first and second rows). For example, in Figure 4(c), the experimental measurements illustrate the same peak-trough-shoulder structure as the theoretical results do for $z = 11.76$ cm. The experimental data also matches the theoretical model in predicting the depth of the trough ($y = 2$ mm) between the two intensity peaks ($y = -3$ mm and $y = 5$ mm) in Figure 4(f) ($z = 17.67$ mm) as well as the predicting the presence of the intensity shoulders at $y = 9$ mm and $y = 14$ mm. The height of the shoulders is slightly underestimated by the simulation results, however. In Figures 4(i) and 4(l), one notes that the simulation matches the experimental results in predicting the width of the radiation pattern as well as predicting the intensity shoulder at $y = \pm 10$ mm in panel (i). The simulation underestimates that shoulder height, however.

The quantitative agreement between the two results may be improved upon through better modeling of the dynamics of the ultrasound field in the AO sensor. The transmission of the ultrasound field through the substrate and into the LC layer of the AO sensor is not accounted for in this analysis. Because of the large speed-of-sound mismatch between the substrate layer (~5000 m/s) and water (~1500 m/s), the transmission of various components of the angular spectrum [16] of the ultrasound field can vary greatly. By accounting for the transmission of sound through the medium, better quantitative accuracy will be achieved.

5. Conclusion

The possibility of applying acoustography to provide a simple but practical tool for mapping ultrasonic fields radiated from ultrasonic transducers has been demonstrated. Since acoustography does not require elaborate mechanical scanning equipment, it is suitable for routine use for quality assessment of transducer fields. The latter capability may be particularly important for calibration of phased array systems, which are being used more and more for nondestructive testing. Other benefits from acoustography have also been demonstrated: each intensity map took <35 seconds compared to hours using current conventional scanning techniques and methods; the entire procedure is user friendly and can be performed by low-skilled operators; the method does not require calibration of the measurement device.

Future plans include a more indepth, head-to-head comparison and validation study of acoustography against the ball reflector method. This will remove any discrepancies that result from simulation modeling errors. In addition, refinement of the process will be pursued including automation, software development, and improved data analysis by obtaining the AO 2D cross-sectional fields and being able to generate true 3D axial profiles using frame-grabbing video output data. This is a distinct advantage over the convention ball reflector method, where the lateral resolution is primarily determined by the indexing step size. Fine indexing steps are required to achieve high resolution but that greatly increases the scan time required to map the ultrasound field. Further improvements in the image processing and analysis will also be pursued to account for the heterogeneous structure of the AO sensor.

Acknowledgment

R.W. Schoonover and M. A. Anastasio acknowledge the support from the National Institute of Health (NIH) awards EB010049 and EB009715.

References

[1] P. G. Kenny, J. J. Gruber, and J. M. Smith, "Ultrasonic transducer characterization," *Materials Evaluation*, vol. 45, no. 6, pp. 730–735, 1987.

[2] R. Lal and D. K. Das-Gupta, "Characterization of ultrasonic transducers," *IEEE transactions on electrical insulation*, vol. 24, no. 3, pp. 473–480, 1989.

[3] J. S. Sandhu, "Acoustography," in *Special Nondestructive Testing Methods, Nondestructive Testing Handbook*, P. O. Moore and P. McIntire, Eds., vol. 9, pp. 278–284, American Society for Nondestructive Testing, Columbus, Ohio, USA, 2nd edition, 1995.

[4] J. S. Sandhu, "Acoustography: a new imaging technique and its applications to nondestructive evaluation," *Materials Evaluation*, vol. 46, pp. 608–613, 1988.

[5] O. A. Kapustina, "Acoustooptical phenomena in liquid crystals," *Molecular Crystals & Liquid Crystals*, vol. 112, pp. 1–164, 1984.

[6] A. P. Malanoski, V. A. Greanya, B. T. Weslowski, M. S. Spector, J. V. Selinger, and R. Shashidhar, "Theory of the acoustic realignment of nematic liquid crystals," *Physical Review E*, vol. 69, no. 2, Article ID 021705, 2004.

[7] V. A. Greanya, A. P. Malanoski, B. T. Weslowski, M. S. Spector, and J. V. Selinger, "Dynamics of the acousto-optic effect in a nematic liquid crystal," *Liquid Crystals*, vol. 32, no. 7, pp. 933–941, 2005.

[8] G. L. Rodríguez, J. Weber, J. S. Sandhu, and M. A. Anastasio, "Feasibility study of complex wavefield retrieval in off-axis acoustic holography employing an acousto-optic sensor," *Ultrasonics*, vol. 51, no. 8, pp. 847–852, 2011.

[9] J. S. Sandhu, R. A. Schmidt, and P. J. La Rivìre, "Full-field acoustomammography using an acousto-optic sensor," *Medical Physics*, vol. 36, no. 6, pp. 2324–2327, 2009.

[10] Y. J. Liu, X. Ding, S. C. S. Lin, J. Shi, I. K. Chiang, and T. J. Huang, "Surface acoustic wave driven light shutters using

polymer-dispersed liquid crystals," *Advanced Materials*, vol. 23, no. 14, pp. 1656–1659, 2011.

[11] J. S. Sandhu, H. Wang, and W. J. Popek, "Acoustography for rapid ultrasonic inspection of composites," in *Nondestructive Evaluation of Materials and Composites*, Proceedings of SPIE, pp. 117–124, December 1996.

[12] M. Born and E. Wolf, *Principles of Optics*, Pergamon Press, New York, NY, USA, 1987.

[13] J. S. Sandhu, H. Wang, and W. J. Popek, "Liquid crystal based acoustic imaging," in *Liquid Crystal Materials, Devices and Flat Panel Displays*, R. Shashidhar and B. Gnade, Eds., vol. 3955 of *Proceedings of SPIE*, pp. 94–108, January 2000.

[14] L. E. Kinsler, A. R. Frey, A. B. Coppens, and J. V. Sanders, *Fundamentals of Acoustics*, Wiley, 1999.

[15] F. Lingvall, T. Olofsson, and T. Stepinski, "Synthetic aperture imaging using sources with finite aperture: deconvolution of the spatial impulse response," *Journal of the Acoustical Society of America*, vol. 114, no. 1, pp. 225–234, 2003.

[16] L. Mandel and E. Wolf, *Optical Coherence and Quantum Optics*, Cambridge University Press, 1995.

Hindawi Publishing Corporation
Advances in Acoustics and Vibration
Volume 2012, Article ID 929174, 15 pages
doi:10.1155/2012/929174

Research Article

High-Frequency Underwater Acoustic Propagation in a Port Modeled as a Three-Dimensional Duct Closed at One End Using the Method of Images

Pierre-Philippe J. Beaujean and Matthew D. Staska

Department of Ocean and Mechanical Engineering, SeaTech, Florida Atlantic University, 101 North Beach Road, Dania Beach, FL 33004, USA

Correspondence should be addressed to Pierre-Philippe J. Beaujean, pbeaujea@fau.edu

Received 15 February 2012; Accepted 4 April 2012

Academic Editor: Jafar Saniie

A computer-efficient model for underwater acoustic propagation in a shallow, three-dimensional rectangular duct closed at one end has been developed using the method of images. The duct simulates a turning basin located in a port, surrounded with concrete walls, and filled with sea water. The channel bottom is composed of silt. The modeled impulse response is compared with the impulse response measured between 15 kHz and 33 kHz. Despite small sensor-position inaccuracies and an approximated duct geometry, the impulse response can be modeled with a relative echo magnitude error of 1.62 dB at worst and a relative echo location error varying between 0% and 4% when averaged across multiple measurements and sensor locations. This is a sufficient level of accuracy for the simulation of an acoustic communication system operating in the same frequency band and in shallow waters, as time fluctuations in echo magnitude commonly reach 10 dB in this type of environment.

1. Introduction

Underwater vehicles and divers routinely operate in ports for security and maintenance operations. Communicating with underwater assets using acoustic modems is a critical feature whenever a tether cannot be used and remains very challenging due to large amounts of noise and fading [1–6]. The reader should note that underwater acoustic communication has become a mature field of research: this reference list is by no means exhaustive.

As in many marine operations, simulation tools play a critical role in optimizing a communication system performance and often in reducing the duration of field tests. Simulating underwater acoustic communications in a port is also a very challenging task, due in part to the complex geometry of the environment. A small displacement between acoustic sensors or a change in the channel geometry can result in a dramatic change in the measured impulse response when using high-frequency sound above 10 kHz. As a result, the channel response varies with time and cannot be modeled exactly. Consequently, stochastic models are used to estimate the performance of an underwater acoustic modem [1, 7]. In this case, the accuracy of the acoustic model is measured in terms of statistical moments rather than absolute accuracy in predicting the impulse response of the channel for a specific configuration. This in turn means that a computer-efficient model of the acoustic channel can provide acceptable results when averaged over a large number of simulations in the presence of small geometrical fluctuations.

To better understand the context of underwater acoustic simulation tools, Figure 1 shows an example of top-level architecture for an underwater acoustic network [7]. The purpose of this tool is to predict the behavior of one or more vehicles, each carrying an acoustic modem and completing a specific mission (helm). All the vehicles evolve in a world, which impacts the acoustic communication quality between any two acoustic modems. Here, each acoustic modem is represented as a protocol stack and a sensor within each vehicle. The passing of information through the acoustic

channel is handled by a medium model within the world. In its simplest form, this model could be a vehicle and a boat, both equipped with an acoustic modem.

Acoustic modems transmit series of acoustic (band-limited) impulses, each containing some binary information, to relay messages between the source and the receiver [1–5]. State-of-the-art acoustic modems transmit hundreds or even thousands of impulses within a message, using either phase or frequency modulation (or a combination of both). The probability that this binary information contains errors is a function of the type of modulation, error coding, signal-to-noise ratio (SNR), and signal-to-multipath ratio (SMR) [1]. The SMR is the energy ratio of the direct echo (traveling directly from the source to the receiver) to the total energy in the reflected (or scattered) echoes measured at the receiver. This SMR is especially critical, as it indicates the amount of fading in the acoustic channel. Modeling the SMR is difficult, as it is a direct function of the acoustic channel response.

A critical issue is the amount of processing required to model the entire network operation, especially in terms of the acoustic channel model. As each acoustic source and receiver moves within the medium, the acoustic channel response changes. A very processor-intensive approach consists in using a powerful acoustic propagation model and recalculates the acoustic channel response given the source and receiver location. For example, Beaujean et al. [8] considered the Parabolic Equation (PE) model approach in a previous paper on a similar problem but realized that this approach was simply too processor-intensive for this application. The impulse response can be precomputed for each combination of source and receiver position, but the sheer number of combinations makes this approach impractical as well.

In contrast, stochastic models are an excellent trade-off between processor requirements and model accuracy, so long as a sufficient number of trials are performed to produce meaningful statistical averages. In the application shown in Figure 1, the authors use the Nakagami model [7, 9]. If A^2 represents the acoustic energy of each impulse within a message, $m_{\text{Nakagami}} = E\{A^2\}^2/\text{Var}\{A^2\}$ is the ratio of the squared expectation (statistical mean) of A^2 to the variance of A^2. Here, the expectation is estimated using the average across all the impulses contained in a message. $E\{A^2\}$ is the average energy of the message. $\sqrt{\text{Var}\{A^2\}}$ is the energy spread. The parameter m_{Nakagami} usually varies from 0.5 to 10.

The main difficulty with stochastic models is to reconcile the statistical parameter(s) with the actual environment in which the acoustic modems operate. In this case, the parameter m_{Nakagami} must be a realistic function of the source and receiver position within the medium. However, this parameter does not have to be extremely accurate either: two significant digits are sufficient to provide a reasonable binary error prediction. Therefore, a simple acoustic propagation model of limited accuracy may be sufficient to provide a realistic value for m_{Nakagami}.

A logical choice is the method of images applied to a specific 3D environment. Although the method is not novel,

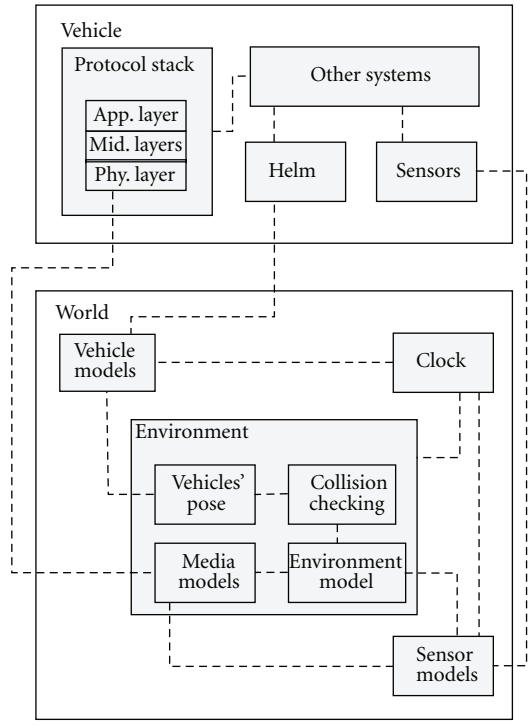

Figure 1: Example of top-level architecture for an underwater acoustic network.

it may predict the amplitude and location of every echo with a sufficient level of accuracy to calculate the parameter m_{Nakagami}. A second option is to convolve the modeled acoustic response with the transmitted modem message to generate an artificial received signal. Once artificial ambient noise has been added, this artificial signal can be decoded. However, this second option is much more processor intensive.

In this context, the authors conduct a comparative analysis between the acoustic response predicted with the proposed 3D model and the acoustic response measured experimentally. A complete sensitivity analysis of the parameter m_{Nakagami} using the acoustic model and the field measurements is beyond the scope of this paper, as it requires a complete description of the actual acoustic message transmitted by the source. Instead, the band-limited impulse response of the acoustic channel is studied, using a pulse transmitted within the entire frequency band of the actual acoustic modem. The comparison is made in terms of the relative error in echo magnitude and time of arrival, across a large number of measurements.

The channel of interest is the south turning basin of Port Everglades, Florida, which is similar in shape to a three-dimensional duct open at one end. Unfortunately, most of the research conducted in underwater acoustic propagation in partial enclosures focuses on three-dimensional wedge geometry. Following the seminal work on horizontal refraction by Weston [10], Deane and Tindle [11] presented a model for the three-dimensional acoustic field in a wedge, leading to the calculation of a loss parameter and to the

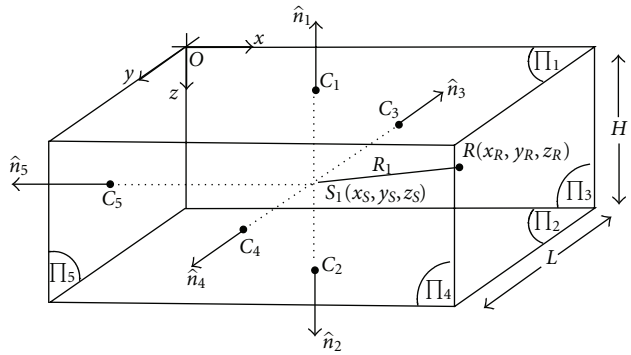

Figure 2: Duct diagram.

modeling of horizontal refraction. The results were also demonstrated experimentally in a wedge-shaped ocean [12–14]. To solve the three-dimensional Helmholtz equation, Buckingham [12] used normal mode theory to derive the mode shapes based on specific boundary conditions and found that the mode shapes varied with frequency and range within the mode coefficients. Borejko [15] created a representation of the image field in a perfect wedge using the ray integral method.

These powerful techniques become overly complex and computer intensive in the present case, due to the short acoustic wavelength and the geometry of the basin. If this duct is filled with seawater of uniform and constant properties and is partially enclosed between a still sea surface, a silt bottom, and three rigid vertical walls, the computer-efficient method of images [16, 17] can be used to model the channel response given specific acoustic sensor locations. The three-dimensional method of images is mostly used to model enclosed environments in airborne audio acoustics [18–22]. Allen and Berkley [18] developed a model to study the basics of room acoustics and were interested only in the point-to-point transmission between source and receiver. Viveiros and Gibbs [19] predicted the field performance of acoustic louvers using an image model compared with impulse measurements. Also using the method of images, Iu and Li [20] computed the acoustic channel in narrow street canyons, modeled as two parallel, infinitely long planes perpendicular to a horizontal ground. The geometry of the duct representing the turning basin is similar to that of the canyon modeled by Iu and Li [20]. However, significant differences exist, namely, in terms of the ultrasound frequency band, sound absorption, and characteristic impedance of the medium and the boundaries. It should be noted that while the image method is not overly complicated for parallelepiped geometries, it can become very complex and processor-intensive for other geometries due to the screening for image sources.

In the following sections, the authors provide the detailed derivation of the method of images applied to the duct representing the basin, followed by a description of a set of experiments and a comparative study between the modeled and the measured channel response.

2. Acoustic Model

Consider the modeled duct shown in Figure 2, where the water mass density ρ and sound velocity c are constant. For now, we also assume that $S_1(x_S, y_S, z_S)$ is a point source producing a complex, harmonic spherical pressure wave $\tilde{p}$ measured at the receiver location $R(x_R, y_R, z_R)$. This complex, harmonic pressure wave is the solution to the Helmholtz equation [23]:

$$\Delta\tilde{p}(x_S, y_S, z_S, x_R, y_R, z_R) + k^2\tilde{p}(x_S, y_S, z_S, x_R, y_R, z_R) = 0. \quad (1)$$

Expressed in Cartesian coordinates and in the complex domain, the free-field harmonic solution to (1) is

$$\tilde{p}(x_S, y_S, z_S, x_R, y_R, z_R, t) = \frac{P_0 e^{i(k(\sqrt{(x_S-x_R)^2+(y_S-y_R)^2+(z_S-z_R)^2})-\omega_c t)}}{\sqrt{(x_S-x_R)^2+(y_S-y_R)^2+(z_S-z_R)^2}}, \quad (2)$$

where $k = \omega_c/c$ is the acoustic wave number, $\omega_c = 2\pi f_c$ is the angular frequency of the transmitted signal, and P_0 (in μPa·m) is the acoustic pressure times unity distance, measured at 1 m from S_1. If we define R_1 as the distance between the source S_1 and the receiver as

$$R_1(x_S, y_S, z_S, x_R, y_R, z_R) = \sqrt{(x_S-x_R)^2+(y_S-y_R)^2+(z_S-z_R)^2}, \quad (3)$$

the complex pressure field produced by the point source becomes

$$\tilde{p}(R_1, t) = \tilde{P}(R_1)e^{-i\omega_c t} = P_0\frac{e^{ikR_1}}{R_1}e^{-i\omega_c t}. \quad (4)$$

The geometry shown in Figure 2 contains a pressure release boundary Π_1, a silt bottom Π_2, and three rigid walls Π_3, Π_4, and Π_5. The duct along the positive x-axis is open ended. The approach in developing the model is to break this three-dimensional problem down to a combination of two-dimensional acoustic models. For simplicity, all the calculations take place in Cartesian coordinates.

2.1. Method of Images Applied between Boundary Π_5 and the Open-End. We first assume that Π_5 is an infinite rigid boundary, as shown in Figure 3. S_2 is located in plane Π_6, which contains $\hat{n}_5$ and $\vec{s_1 r}$. Since Π_5 is a rigid boundary, the pressure gradient along the normal $\hat{n}_5$ is null, so that $(\partial\tilde{P}/\partial x)_{x=0} = 0$. Based on the method of images [16], the pressure at the receiver is the sum of the pressure generated by the source S_1 and the pressure generated by the image S_2, located at equal and opposite distance from the boundary:

$$\tilde{P}(x_S, y_S, z_S, x_R, y_R, z_R) = \tilde{P}(R_1) + \tilde{P}(R_2) = \frac{P_0}{R_1}e^{ikR_1} + \frac{P_0}{R_2}e^{ikR_2}. \quad (5)$$

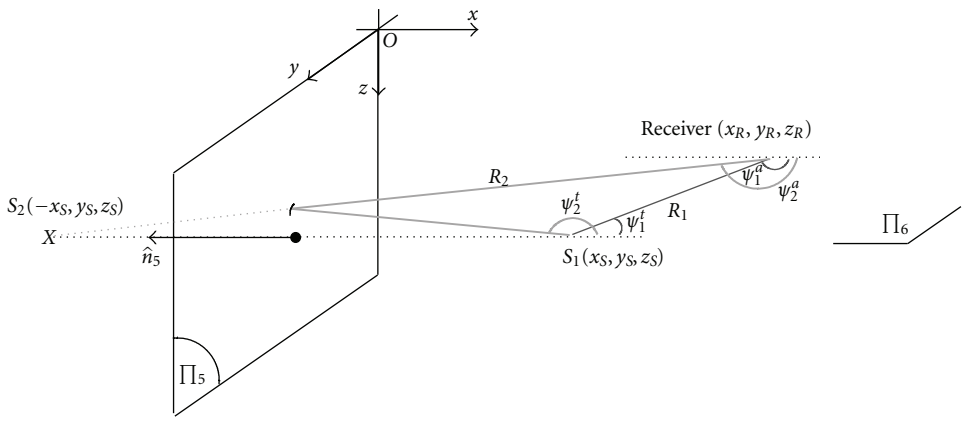

Figure 3: Three-dimensional geometry of image method with a rigid boundary and an open-end.

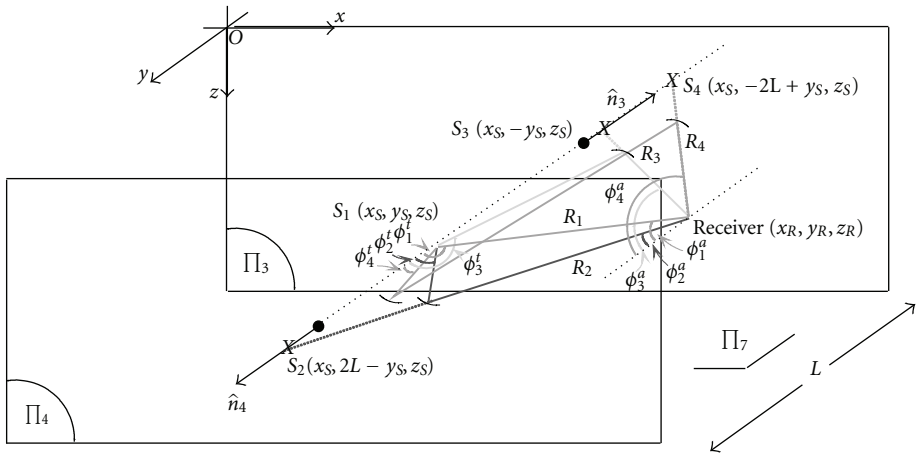

Figure 4: Three-Dimensional Distribution of Images between Rigid Boundaries Π_3 and Π_4, Group $m = 0$.

R_1 is the distance between S_1 and the receiver. R_2 is the distance between S_2 and the receiver:

$$R_1 = \sqrt{(x_S - x_R)^2 + (y_S - y_R)^2 + (z_S - z_R)^2}$$
$$R_2 = \sqrt{(x_S + x_R)^2 + (y_S - y_R)^2 + (z_S - z_R)^2} \tag{6}$$

ψ_l^t and ψ_l^a correspond to the angles of transmission and arrival unique to the source S_l, where $l = 1, 2$ is the image index. Here $l = 1$ corresponds to the physical source S_1:

$$\psi_l^t = \begin{cases} -\arctan\left(\dfrac{\sqrt{(y_S - y_R)^2 + (z_S - z_R)^2}}{x_R - x_{S_l}}\right), & \text{if } l = 1, \\ \arctan\left(\dfrac{\sqrt{(y_S - y_R)^2 + (z_S - z_R)^2}}{x_R - x_{S_l}}\right), & \text{if } l = 2, \end{cases}$$
$$\psi_l^a = \arctan\left(\frac{\sqrt{(y_S - y_R)^2 + (z_S - z_R)^2}}{x_R - x_{S_l}}\right). \tag{7}$$

Note that the calculation of these angles is only useful if either the source or receiver is directional. The time of arrival for each image is given by

$$\tau_l = \frac{R_l}{c}. \tag{8}$$

2.2. Method of Images Applied between Boundaries Π_3 *and* Π_4. We now assume that Π_3 and Π_4 are infinite rigid boundaries, so that the pressure gradient along $\hat{n}_3$ and $\hat{n}_4$ is null, $(\partial\tilde{P}/\partial y)_{y=0} = (\partial\tilde{P}/\partial y)_{y=L} = 0$. In this case, an infinite number of images are modeled. The images are grouped by four, where the very first group contains S_1, S_2, and S_3 and the image of S_2 across Π_3, noted S_4, as shown in Figure 4. The index m corresponds to the group number containing the source S_{ma}. The second index ($a = 1, 2, 3,$ or 4) corresponds to the image number in each group m. The total pressure field is

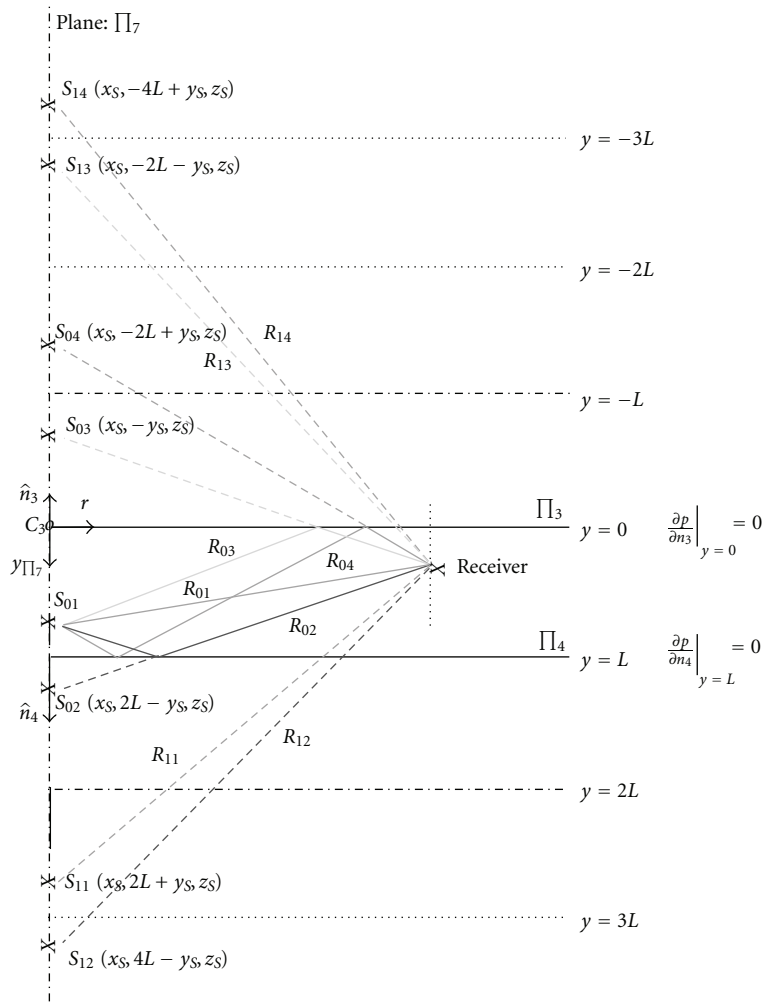

Figure 5: Two-Dimensional Distribution of Images between Rigid Boundaries Π_3 and Π_4, Groups $m = 0$ and $m = 1$.

$$\begin{aligned}
&\widetilde{P}(x_S, y_S, z_S, x_R, y_R, z_R) \\
&= P_0 \sum_{m=0}^{\infty} \left[\frac{1}{R_{m1}} e^{ikR_{m1}} + \frac{1}{R_{m2}} e^{ikR_{m2}} + \frac{1}{R_{m3}} e^{ikR_{m3}} + \frac{1}{R_{m4}} e^{ikR_{m4}} \right] \\
&= P_0 \sum_{m=0}^{\infty} \left[\sum_{a=1}^{4} \left[\frac{1}{R_{ma}} e^{ikR_{ma}} \right] \right].
\end{aligned} \tag{9}$$

Figure 5 shows the first eight images ($m = 0$, $m = 1$) in plane Π_7. Given a group number m, the distance between the receiver and the corresponding image is defined as

$$\begin{aligned}
R_{m1} &= \sqrt{(x_S - x_R)^2 + (z_S - z_R)^2 + (2mL + y_S - y_R)^2}, \\
R_{m2} &= \sqrt{(x_S - x_R)^2 + (z_S - z_R)^2 + [2(m+1)L - y_S - y_R]^2}, \\
R_{m3} &= \sqrt{(x_S - x_R)^2 + (z_S - z_R)^2 + (2mL + y_S + y_R)^2}, \\
R_{m4} &= \sqrt{(x_S - x_R)^2 + (z_S - z_R)^2 + [2(m+1)L - y_S + y_R]^2}.
\end{aligned} \tag{10}$$

The angles of transmission and arrival are defined as

$$\begin{aligned}
\phi_{ma}^{t} &= \begin{cases} -\arctan\left(\dfrac{\sqrt{(x_S - x_R)^2 + (z_S - z_R)^2}}{y_R - y_{S_{ma}}} \right), & \text{if } a = 1, 4, \\ \arctan\left(\dfrac{\sqrt{(x_S - x_R)^2 + (z_S - z_R)^2}}{y_R - y_{S_{ma}}} \right), & \text{if } a = 2, 3, \end{cases} \\
\phi_{ma}^{a} &= \arctan\left(\frac{\sqrt{(x_S - x_R)^2 + (z_S - z_R)^2}}{y_R - y_{S_{ma}}} \right).
\end{aligned} \tag{11}$$

Note that the calculation of these angles is only useful if either the source or receiver is directional. The times of arrival are given by

$$\tau_{ma} = \frac{R_{ma}}{c}. \tag{12}$$

2.3. Method of Images Applied between Boundaries Π_1 *and* Π_2. We now assume that Π_1 and Π_2 are infinite nonrigid boundaries, as shown in Figure 6. Π_1 is a pressure release

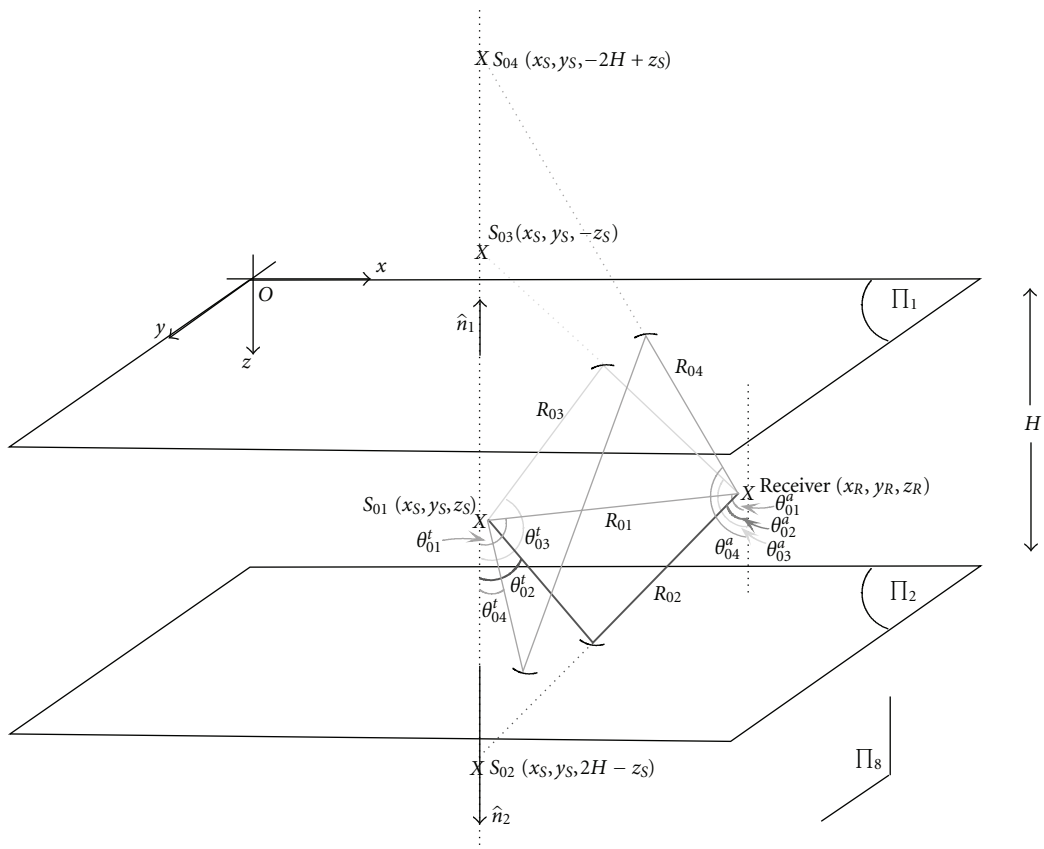

Figure 6: Three-Dimensional Distribution of Images between Pressure Release Boundary Π_1 and Soft Boundary Π_2, Group $m = 0$.

boundary, where the pressure along the normal $\hat{n}_1$ is null. The boundary Π_2 is a silt boundary with a mass density of $\rho_{\text{silt}} = 1500\,\text{kg/m}^3$ and a sound speed $c_{\text{silt}} = 0.985c$ relative to the sound speed in the channel c. The reflection coefficient V_{Π_2} is a function of the angle of incidence θ_{nb} with respect to $\hat{n}_2$. S_{nb} corresponds to the image number b in each group n. Using these parameters, the reflection coefficient $V_{\Pi_2}(\theta_{nb})$ is obtained [23]:

$$\theta^t_{nb} = \sin^{-1}\left(\sqrt{1 - \frac{c^2_{\text{silt}}}{c^2}\cos^2(\theta_{nb})}\right),$$
$$V_{\Pi_2}(\theta_{nb}) = \frac{\rho_{\text{silt}}c_{\text{silt}}/\rho c - \sin\left(\theta^t_{nb}\right)/\sin(\theta_{nb})}{\rho_{\text{silt}}c_{\text{silt}}/\rho c + \sin\left(\theta^t_{nb}\right)/\sin(\theta_{nb})}. \tag{13}$$

θ^t_{nb} is defined with respect to the positive z-axis and corresponds to the angle of transmission from a given image location S_{nb}. The resulting pressure field is the sum of the source pressure field and the pressure fields corresponding to the images of the source S_{01}. Since Π_2 is a partially reflecting boundary, the pressure field of the image S_{02} is multiplied by the reflection coefficient of the boundary. Summing the pressure field of the image source S_{02} to that of the pressure field of the source S_{01}, we obtain

$$\widetilde{P}(x_S, y_S, z_S, x_R, y_R, z_R) = \frac{P_0}{R_{01}}e^{ikR_{01}} + V_{\Pi_2}(\theta_{02})\frac{P_0}{R_{02}}e^{ikR_{02}}, \tag{14}$$

$$R_{01} = \sqrt{(x_S - x_R)^2 + (y_S - y_R)^2 + (z_S - z_R)^2},$$
$$R_{02} = \sqrt{(x_S - x_R)^2 + (y_S - y_R)^2 + (2H - z_S - z_R)^2}. \tag{15}$$

Since Π_1 is a pressure release boundary, S_{03} and S_{04} are out of phase with the actual source. The combined acoustic pressure field due to these images is

$$\widetilde{P}(x_S, y_S, z_S, x_R, y_R, z_R) = \frac{P_0}{R_{01}}e^{ikR_{01}} + V_{\Pi_2}(\theta_{02})\frac{P_0}{R_{02}}e^{ikR_{02}} - \frac{P_0}{R_{03}}e^{ikR_{03}} - V_{\Pi_2}(\theta_{04})\frac{P_0}{R_{04}}e^{ikR_{04}}. \tag{16}$$

The distance between the receiver and the corresponding image is

$$\begin{aligned} R_{01} &= \sqrt{(x_S - x_R)^2 + (y_S - y_R)^2 + (z_S - z_R)^2}, \\ R_{02} &= \sqrt{(x_S - x_R)^2 + (y_S - y_R)^2 + [2H - z_S - z_R]^2}, \\ R_{03} &= \sqrt{(x_S - x_R)^2 + (y_S - y_R)^2 + (z_S + z_R)^2}, \\ R_{04} &= \sqrt{(x_S - x_R)^2 + (y_S - y_R)^2 + [2H - z_S + z_R]^2}. \end{aligned} \tag{17}$$

Given a group number n, the total pressure field at the receiver is

$$\begin{aligned} &\widetilde{P}(x_S, y_S, z_S, x_R, y_R, z_R) \\ &\quad = P_0 \sum_{n=0}^{\infty} (-1)^n \begin{bmatrix} (V_{\Pi_2}(\theta_{n1}))^n \dfrac{1}{R_{n1}} e^{ikR_{n1}} \\ +(V_{\Pi_2}(\theta_{n2}))^{(n+1)} \dfrac{1}{R_{n2}} e^{ikR_{n2}} \\ -(V_{\Pi_2}(\theta_{n3}))^n \dfrac{1}{R_{n3}} e^{ikR_{n3}} \\ -(V_{\Pi_2}(\theta_{n4}))^{(n+1)} \dfrac{1}{R_{n4}} e^{ikR_{n4}} \end{bmatrix}. \end{aligned} \tag{18}$$

The distance between the receiver and each image is

$$\begin{aligned} R_{n1} &= \sqrt{(x_S - x_R)^2 + (y_S - y_R)^2 + (2nH + z_S - z_R)^2}, \\ R_{n2} &= \sqrt{(x_S - x_R)^2 + (y_S - y_R)^2 + [2(n+1)H - z_S - z_R]^2}, \\ R_{n3} &= \sqrt{(x_S - x_R)^2 + (y_S - y_R)^2 + (2nH + z_S + z_R)^2}, \\ R_{n4} &= \sqrt{(x_S - x_R)^2 + (y_S - y_R)^2 + [2(n+1)H - z_S + z_R]^2}. \end{aligned} \tag{19}$$

The angles of transmission and arrival are

$$\begin{aligned} \theta_{nb}^t &= \begin{cases} -\arctan\left(\dfrac{\sqrt{(x_S - x_R)^2 + (y_S - y_R)^2}}{z_R - z_{S_{nb}}}\right), & \text{if } b = 1, 4, \\ \arctan\left(\dfrac{\sqrt{(x_S - x_R)^2 + (y_S - y_R)^2}}{z_R - z_{S_{nb}}}\right), & \text{if } b = 2, 3, \end{cases} \\ \theta_{nb}^a &= \arctan\left(\frac{\sqrt{(x_S - x_R)^2 + (y_S - y_R)^2}}{z_R - z_{S_{nb}}}\right). \end{aligned} \tag{20}$$

Note that the calculation of these angles is only useful if either the source or receiver is directional. The times of arrival are given by

$$\tau_{nb} = \frac{R_{nb}}{c}. \tag{21}$$

Although the objective of this paper is not an in-depth study of the method of images, the reader should be aware that some approximations are made in (13), (14), (16), and (18). While the method of images is perfectly accurate for impenetrable surfaces, either hard (Neumann boundary condition) or soft (pressure release or Dirichlet boundary condition), it loses accuracy in the presence of penetrable surfaces. These issues are covered in detail in [17]. Here we assume that one of the boundaries is made of a uniform, soft sediment, so that sound travels more slowly in this sediment than in water.

We use the geometrical acoustics approximation [17] to the total reflected field to obtain (14), (16), and (18): the energy of the acoustic field reflected off the soft boundary is concentrated about the angle of specular reflection. In reality, a spherical wave incident to the soft bottom would produce weaker levels of sound reflected in every direction: we assume that this secondary sound field is negligible. To further reduce the complexity of the model, we assume that the soft bottom is perfectly flat, uniform, and infinitely deep, so that any possible scattering and diffraction effect is neglected.

The main consequence of these approximations is that the model will overestimate the strength of the reflected sound in the specular direction and omit secondary echoes. In other terms, the modeled channel response will contain strong echoes at times directly related to the specular angles, but will not contain any echo related to wave curvature, scattering, and diffraction effects.

2.4. Pressure Field in the Duct. The final step is to find the analytical expression for the pressure field in the duct. We use the following index notation for each source S_{lmanb}: l corresponds to the image number in the x-direction ($l = 1, 2$), m and a correspond to the group number ($m = 0, 1, 2, \ldots, \infty$) and the image number ($a = 1, 2, 3, 4$) in the y-direction, and n and b correspond to the group number ($n = 0, 1, 2, \ldots, \infty$) and the image number ($b = 1, 2, 3, 4$) in the z-direction. Combining (5), (9), and (18), the acoustic pressure at the receiver is obtained:

$$\widetilde{P}(x_S, y_S, z_S, x_R, y_R, z_R) = P_0 \sum_{l=1}^{2} \left[\sum_{m=0}^{\infty} \left[\sum_{a=1}^{4} \left[\sum_{n=0}^{\infty} (-1)^n \begin{bmatrix} (V_{\Pi_2}(\theta_{lman1}))^n \dfrac{1}{R_{lman1}} e^{ikR_{lman1}} \\ +(V_{\Pi_2}(\theta_{lman2}))^{(n+1)} \dfrac{1}{R_{lman2}} e^{ikR_{lman2}} \\ -(V_{\Pi_2}(\theta_{lman3}))^n \dfrac{1}{R_{lman3}} e^{ikR_{lman3}} \\ -(V_{\Pi_2}(\theta_{lman4}))^{(n+1)} \dfrac{1}{R_{lman4}} e^{ikR_{lman4}} \end{bmatrix} \right] \right] \right]. \tag{22}$$

The summations in (22) account for the reflected paths produced by every wall in the duct. The distance R_{lmanb} between the image S_{lmanb} and the receiver is given in (23):

$$
\begin{aligned}
R_{lm1n1} &= \sqrt{\left[x_S + (-1)^l x_R\right]^2 + (2mL + y_S - y_R)^2 + (2nH + z_S - z_R)^2},\\
R_{lm1n2} &= \sqrt{\left[x_S + (-1)^l x_R\right]^2 + (2mL + y_S - y_R)^2 + [2(n+1)H - z_S - z_R]^2},\\
R_{lm1n3} &= \sqrt{\left[x_S + (-1)^l x_R\right]^2 + (2mL + y_S - y_R)^2 + (2nH + z_S + z_R)^2},\\
R_{lm1n4} &= \sqrt{\left[x_S + (-1)^l x_R\right]^2 + (2mL + y_S - y_R)^2 + [2(n+1)H - z_S + z_R]^2},\\
R_{lm2n1} &= \sqrt{\left[x_S + (-1)^l x_R\right]^2 + [2(m+1)L - y_S - y_R]^2 + (2nH + z_S - z_R)^2},\\
R_{lm2n2} &= \sqrt{\left[x_S + (-1)^l x_R\right]^2 + [2(m+1)L - y_S - y_R]^2 + [2(n+1)H - z_S - z_R]^2},\\
R_{lm2n3} &= \sqrt{\left[x_S + (-1)^l x_R\right]^2 + [2(m+1)L - y_S - y_R]^2 + (2nH + z_S + z_R)^2},\\
R_{lm2n4} &= \sqrt{\left[x_S + (-1)^l x_R\right]^2 + [2(m+1)L - y_S - y_R]^2 + [2(n+1)H - z_S + z_R]^2},\\
R_{lm3n1} &= \sqrt{\left[x_S + (-1)^l x_R\right]^2 + (2mL + y_S + y_R)^2 + (2nH + z_S - z_R)^2},\\
R_{lm3n2} &= \sqrt{\left[x_S + (-1)^l x_R\right]^2 + (2mL + y_S + y_R)^2 + [2(n+1)H - z_S - z_R]^2},\\
R_{lm3n3} &= \sqrt{\left[x_S + (-1)^l x_R\right]^2 + (2mL + y_S + y_R)^2 + (2nH + z_S + z_R)^2},\\
R_{lm3n4} &= \sqrt{\left[x_S + (-1)^l x_R\right]^2 + (2mL + y_S + y_R)^2 + [2(n+1)H - z_S + z_R]^2},\\
R_{lm4n1} &= \sqrt{\left[x_S + (-1)^l x_R\right]^2 + [2(m+1)L - y_S + y_R]^2 + (2nH + z_S - z_R)^2},\\
R_{lm4n2} &= \sqrt{\left[x_S + (-1)^l x_R\right]^2 + [2(m+1)L - y_S + y_R]^2 + [2(n+1)H - z_S - z_R]^2},\\
R_{lm4n3} &= \sqrt{\left[x_S + (-1)^l x_R\right]^2 + [2(m+1)L - y_S + y_R]^2 + (2nH + z_S + z_R)^2},\\
R_{lm4n4} &= \sqrt{\left[x_S + (-1)^l x_R\right]^2 + [2(m+1)L - y_S + y_R]^2 + [2(n+1)H - z_S + z_R]^2}.
\end{aligned}
\tag{23}
$$

For example, if $l = 1, 2$, $m = n = 0$, and $a, b = 1, 2, 3, 4$, thirty-two images are created, as shown in Figure 7. In seawater, a certain amount of the acoustic energy of the propagating signal is also lost in heat originating from viscosity and thermal relaxation. This absorption of sound represents a true loss of acoustic energy within the acoustic channel of propagation. The value of the sound absorption coefficient α_{dB} is given by Schulkin and Marsh [24]:

$$\alpha_{\mathrm{dB}} = 0.0170 \frac{S f_T f_c^2}{f_T^2 + f_c^2} + 0.0245 \frac{f_c^2}{f_T} \ \mathrm{dB/km}. \tag{24}$$

S is the salinity in parts per thousand (ppt), f_c is the central operating frequency in Hertz, and f_T is the temperature-dependent relaxation frequency given by

$$f_T = 21.9 \times 10^{9-(1520/(T+273))} \ \mathrm{Hz}. \tag{25}$$

T is the temperature in degree centigrade. The absorption coefficient α in 1/m is

$$\alpha = \frac{\alpha_{\mathrm{dB}} \cdot \ln(10)}{20 \cdot 10^3} \ 1/\mathrm{m}. \tag{26}$$

To compute the final acoustic pressure field, we assume that the absorption coefficient (in salt water) per unit of wavelength is much smaller than the wave number, $\alpha \ll k$. Using this assumption, we can apply the absorption coefficient to each image individually. Therefore, the final acoustic pressure field in the three-dimensional environment is

$$\widetilde{P}(x_S, y_S, z_S, x_R, y_R, z_R) = P_0 \sum_{l=1}^{2} \left[\sum_{m=0}^{\infty} \left[\sum_{a=1}^{4} \left[\sum_{n=0}^{\infty} (-1)^n \left[\begin{array}{c} \left(V_{\Pi_2}(\theta_{lman1})\right)^n \dfrac{1}{R_{lman1}} e^{(ik-\alpha)R_{lman1}} \\ +\left(V_{\Pi_2}(\theta_{lman2})\right)^{(n+1)} \dfrac{1}{R_{lman2}} e^{(ik-\alpha)R_{lman2}} \\ -\left(V_{\Pi_2}(\theta_{lman3})\right)^n \dfrac{1}{R_{lman3}} e^{(ik-\alpha)R_{lman3}} \\ -\left(V_{\Pi_2}(\theta_{lman4})\right)^{(n+1)} \dfrac{1}{R_{lman4}} e^{(ik-\alpha)R_{lman4}} \end{array} \right] \right] \right] \right]. \tag{27}$$

The corresponding distances R_{lmanb} between the image S_{lmanb} and the receiver are defined in (23).

2.5. In-Band Channel Model. The acoustic model must accommodate broadband chirp signal transmission. One of two approaches is available for broadband analysis: (a) each frequency component of the source signal is analyzed individually to create the modeled transfer function of the acoustic channel, a computer intensive approach; (b) the echo location, magnitude, and phase are computed at the carrier frequency f_c and applied to a short, band-limited impulse of carrier frequency f_c. Although this second approach is less accurate, it is retained as it is far less computer intensive. The simulated transmitted signal $q(t)$ consists of a broadband chirp of bandwidth $W = 18\,\text{kHz}$, central frequency $f_c = 24\,\text{kHz}$, and duration $T_s = 13.54\,\text{ms}$.

Although a complete analysis of using (b) rather than (a) is beyond the scope of this paper, the impact of such an approximation should be briefly discussed. The major impact of using (b) is a distortion of the echo envelope (including the peak value), while the peak location for each echo remains fairly accurate. In addition, since sound absorption increases by 5 dB/km between 15 kHz and 33 kHz, the approximation in (b) leads to a small overestimation of the pressure field above 24 kHz and inversely to an underestimation of the pressure field below 24 kHz. This distortion becomes more severe as the traveled distance associated with a specific echo increases.

The chirp is frequency modulated (linear sweep), and the envelope is a Blackman time window $b_{\text{mdl}}(t)$:

$$q(t) = b_{\text{mdl}}(t) \cdot \sin\left(2\pi\left(f_c + \frac{W \cdot t}{2T_s}\right)t\right)\mu Pa, \tag{28}$$

$$b_{\text{mdl}}(t) = 0.42 - 0.5\cos\left(2\pi\frac{t}{T_s}\right) + 0.08\cos\left(4\pi\frac{t}{T_s}\right). \tag{29}$$

The transmitted signal is expressed in analytical form using a Hilbert transform operation $H\{\}$:

$$\begin{aligned} \widetilde{q}_{\text{mdl}}(t) &= q_{\text{mdl}}(t) + iH\{q_{\text{mdl}}(t)\} \\ &= q_{\text{mdl}}(t) + \int_{-\infty}^{\infty} \frac{i}{\pi t'} q_{\text{mdl}}(t - t')dt'\ \mu\text{Pa}. \end{aligned} \tag{30}$$

Next, the normalized autocorrelation of this complex chirp $\widetilde{q}_{\text{mdl}}(t)$ is computed to produce a band-limited impulse:

$$\widetilde{r}_{\text{mdl}}(t) = \left[\frac{(1/2T_s)\int_{-T_s}^{T_s} \widetilde{q}_{\text{mdl}}(t)\widetilde{q}^*_{\text{mdl}}(t+\tau)d\tau}{(1/2T_s)\int_{-T_s}^{T_s} \left|\widetilde{q}_{\text{mdl}}(t)\right|^2 dt} \right]. \tag{31}$$

The modeled source signal (complex acoustic pressure in μPa) is scaled using the source level SL:

$$\widetilde{s}_{\text{mdl}}(t) = 10^{\text{SL}/20} \cdot \widetilde{r}_{\text{mdl}}(t). \tag{32}$$

Using the approximation aforementioned, the impulse response $\widetilde{h}(t)$ of the duct is calculated for each source and receiver position:

$$\widetilde{h}(t) = \sum_{l=1}^{2} \left[\sum_{m=0}^{\infty} \left[\sum_{a=1}^{4} \left[\sum_{n=0}^{\infty} (-1)^n \left[\begin{array}{c} \left(V_{\Pi_2}(\theta_{lman1})\right)^n \dfrac{\delta(t-\tau_{lman1})}{R_{lman1}} e^{(ik-\alpha)R_{lman1}} \\ +\left(V_{\Pi_2}(\theta_{lman2})\right)^{(n+1)} \dfrac{\delta(t-\tau_{lman2})}{R_{lman2}} e^{(ik-\alpha)R_{lman2}} \\ -\left(V_{\Pi_2}(\theta_{lman3})\right)^n \dfrac{\delta(t-\tau_{lman3})}{R_{lman3}} e^{(ik-\alpha)R_{lman3}} \\ -\left(V_{\Pi_2}(\theta_{lman4})\right)^{(n+1)} \dfrac{\delta(t-\tau_{lman4})}{R_{lman4}} e^{(ik-\alpha)R_{lman4}} \end{array} \right] \right] \right] \right]. \tag{33}$$

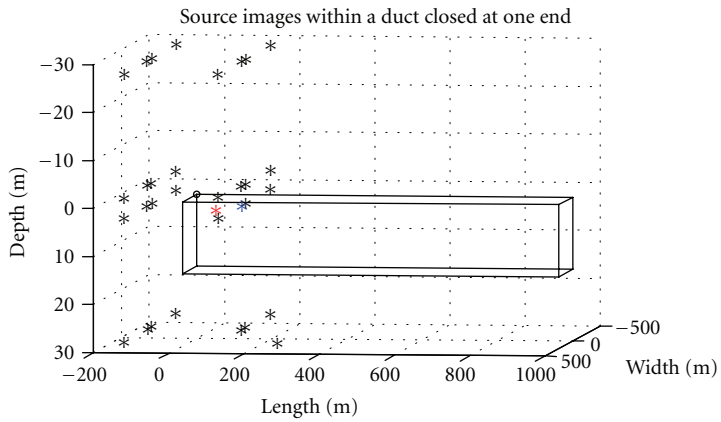

Figure 7: Three-Dimensional Plot of a Block of Thirty-Two Images.

$\delta(t - \tau_{lmanb})$ represents a Dirac delayed by τ_{lmanb} seconds. The in-band impulse response is defined as the convolution between (32) and (33):

$$\tilde{h}_{\mathrm{mdl}}(t) = \tilde{s}_{\mathrm{mdl}}(t) * \tilde{h}(t) = \sum_{l=1}^{2}\left[\sum_{m=0}^{\infty}\left[\sum_{a=1}^{4}\left[\sum_{n=0}^{\infty}(-1)^{n}\left[\begin{array}{c}\left(V_{\Pi_2}(\theta_{lman1})\right)^{n}\dfrac{\tilde{s}_{\mathrm{mdl}}(t-\tau_{lman1})}{R_{lman1}}e^{(ik-\alpha)R_{lman1}}\\ +\left(V_{\Pi_2}(\theta_{lman2})\right)^{(n+1)}\dfrac{\tilde{s}_{\mathrm{mdl}}(t-\tau_{lman2})}{R_{lman2}}e^{(ik-\alpha)R_{lman2}}\\ -\left(V_{\Pi_2}(\theta_{lman3})\right)^{n}\dfrac{\tilde{s}_{\mathrm{mdl}}(t-\tau_{lman3})}{R_{lman3}}e^{(ik-\alpha)R_{lman3}}\\ -\left(V_{\Pi_2}(\theta_{lman4})\right)^{(n+1)}\dfrac{\tilde{s}_{\mathrm{mdl}}(t-\tau_{lman4})}{R_{lman4}}e^{(ik-\alpha)R_{lman4}}\end{array}\right]\right]\right]\right]. \tag{34}$$

$\tilde{h}_{\mathrm{mdl}}$ is computed at fixed time interval $n_\tau \Delta\tau$, where n_τ is defined as

$$n_\tau = \mathrm{int}\left(\frac{\tau_{lmanb}}{F_S}\right), \tag{35}$$

where $\Delta\tau = 1/F_S$ and $\tau_{lmanb} = R_{lmanb}/c$. The function int() corresponds to the integer part of the result, $F_S = 75600\,\mathrm{Hz}$ is the sampling frequency, τ_{lmanb} is the time of arrival of the echo produced by image S_{lmanb}, and c is the sound speed in the channel.

3. Simulated and Experimental Results

3.1. Experimental Setup. A set of field experiments has been conducted on June 8, 2007, in the south turning basin of Port Everglades, Florida. The basin, shown in Figure 8, contains an unobstructed, flat bathymetry silt bottom surrounded with a vertical concrete wall to the south and vertically piled boulders on the west and north sides. The basin is 14 meters deep. The west wall is 255 meters long and the north wall is 290 meters long. Towards the east, the bottom slopes slowly upward towards the shore. The bottom on the east side is a relatively thick layer of mud and very fine silt. Because of the frequency of operations (15–33 kHz), the sound traveling east is for the most part absorbed by this thick layer of mud. Therefore, the acoustic channel can reasonably be approximated as a duct closed on the west end and open on the east end.

The source is an FAU Gateway Buoy [25] configured as a pinger, equipped with an ITC-3460 transducer and Global Positioning System with Wide Area Augmentation System (GPS-WAAS) of ±1 meter accuracy. The source transducer is suspended in the water column at a fixed depth of 1.5 meters below the sea-surface and transmits the chirp signal given in (28). The ITC-6156 receiver transducer is mounted on an air-filled aluminum pressure vessel (6 inches in diameter, 30 inches in length) to simulate the acoustic shading produced by the underwater vehicle of interest. The source signal used in the acoustic model is the signal produced by the omnidirectional source transducer. Therefore, the frequency response of the transducer is taken into account in the model.

This pressure vessel is tethered to a small research vessel at a depth of 1.3 meters. The source is at a stationary location in the turning basin and the receiver produces a record of the impulse response within the basin at multiple locations. The receiver pressure vessel is parallel to the hull of the vessel,

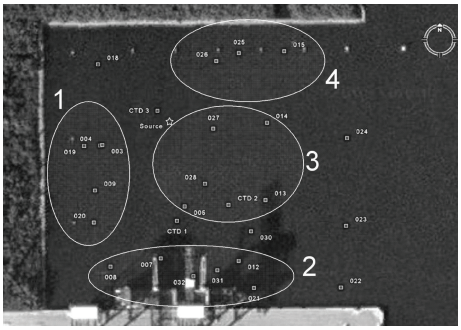

Figure 8: Aerial View of GPS Locations for Each Recorded Sample.

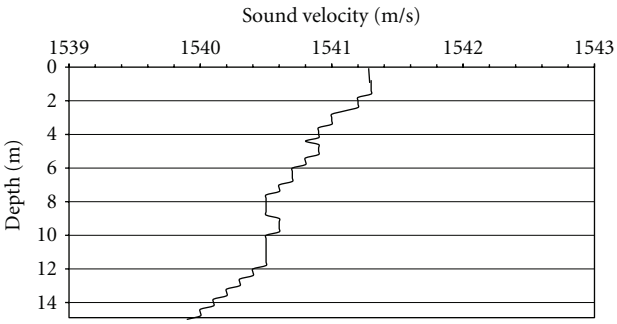

Figure 9: Average Sound Velocity Measured by the CTD.

oriented broadside to the source at each record location. A total of $N_r = 5$ impulse response measurements are collected at each location.

Considering the large number of receiver locations tested, these locations have been grouped in separate regions, labeled 1 to 4 in Figure 8. Region 1 contains the data collected near the western boundary of the turning basin, composed of vertically piled boulders. Region 2 contains the data collected near the flat, concrete southern wall of the turning basin. Region 3 is the most distant from any walls and the deepest portion of the basin. The receiver is also located at fairly close range from the source in this region, so that the echoes originating from the walls are clearly separated from the surface and bottom bounces. Region four contains the data collected near the northern wall, composed of vertically piled boulders.

A series of vertical sound velocity measurements was performed at locations indicated in Figure 8. Figure 9 shows the average sound velocity versus depth for the six casts [26]. The velocity gradient $\Delta c/\Delta H$ in the turning basin is negative:

$$\frac{\Delta c}{\Delta H} = \frac{c_{\max} - c_{\min}}{\Delta H} = \frac{1541.3 - 1540}{14} = 0.092857\,\mathrm{s}^{-1}. \quad (36)$$

Given the limited depth and range, we can reasonably approximate this channel as an iso-velocity channel. Figure 10 shows the actual noise power spectral density (PSD) recorded during the field experimentation [26]. The standard deviation of the in-band noise is $\sigma_n = 110148\,\mu\mathrm{Pa}$ between 15 kHz and 33 kHz.

3.2. Echo Overlap. An issue in estimating the impulse response of an acoustic channel is the limited source bandwidth, which in turn limits the time resolution. Figure 11 shows the magnitude of the modeled impulse response for a receiver located at point 008, with a receiver depth of 1.3 meters and a source depth of 1.5 meters. Two echoes corresponding to the direct path and surface bounce are received between the observation time of 94 ms and 94.5 ms. In (31), the −6 dB pulse width for each echo is 172 μs, causing these two echo partially overlap in Figure 11. This in turn causes echo interference, so that the exact sample spacing and magnitude cannot be determined exactly. Consider two received (complex and band-limited) echoes in (34), noted as:

$$\begin{aligned} \tilde{r}_1(t) &= \left|\tilde{h}_1\right| e^{j\phi_1} \tilde{s}_{\mathrm{mdl}}(t-\tau_1), \\ \tilde{r}_2(t) &= \left|\tilde{h}_2\right| e^{j\phi_2} \tilde{s}_{\mathrm{mdl}}(t-\tau_2). \end{aligned} \quad (37)$$

These echoes may partly overlap and interfere (as depicted in Figure 12), so that the actual peak location for each echo cannot be exactly known. This results in inaccuracies when estimating the time-of-arrival of a given echo. Each echo phase ϕ is the sum of the phase shift ϕ_{boundary} due to boundary interactions and the phase shift ϕ_{travel} due to the relative movement between the source and the receiver:

$$\begin{aligned} \phi &= \phi_{\mathrm{boundary}} + \phi_{\mathrm{travel}}, \\ \phi_{\mathrm{travel}} &= 2\pi f_c \Delta\tau. \end{aligned} \quad (38)$$

$\Delta\tau = \Delta l/c$ is the time shift due to a receiver movement (Δl) in meters, and $\lambda = c/f_c$ is the wavelength of the transmitted signal. In our case, the center frequency for the experimentation is $f_c = 24\,\mathrm{kHz}$ and the measured sound speed within the channel is $c = 1540\,\mathrm{m/s}$. A change in distance of a quarter of a wavelength (0.015 m) results in a change of $\pi/2$ radians in the relative phase between the two echoes. Overall, if $|\tilde{h}_1| = |\tilde{h}_2|$, $|\tilde{r}_1(t) + \tilde{r}_2(t)|$ can vary between 0 and $2|\tilde{r}_1(t)|$ due to small fluctuations in the receiver location. Therefore, the limited time resolution of the experimental setup results in inaccurate measurements of the echo magnitude and location if interference occurs. This in turn means that clearly separated echoes are measured more precisely in terms of both magnitude and time of arrival. Because of the limited time resolution, two or more echoes arriving within a time window of two −6 dB pulse width (344 μs) are treated as a group of overlapping echoes in the field result analysis.

3.3. Model Sensitivity to Geometrical and Physical Inaccuracies. For each receiver location, one record contains $N_r = 5$ impulse responses measured at fixed intervals $T_r = 4$ seconds. The time origin $t = 0$ of the record is the estimated time of arrival of the very first echo of the first impulse response. The modeled echo, corresponding to the direct path of the first record, is also located at $t = 0$. The modeled impulse response is repeated every 4 seconds. For each record $n_r (n_r = 1, \ldots, 5)$ and location n_l within region $n_{\mathrm{reg}} (n_{\mathrm{reg}} = 1, \ldots, 4)$, $\tau_{\mathrm{mdl}}(n_r, n_g, n_l, n_{\mathrm{reg}})$ represents the time

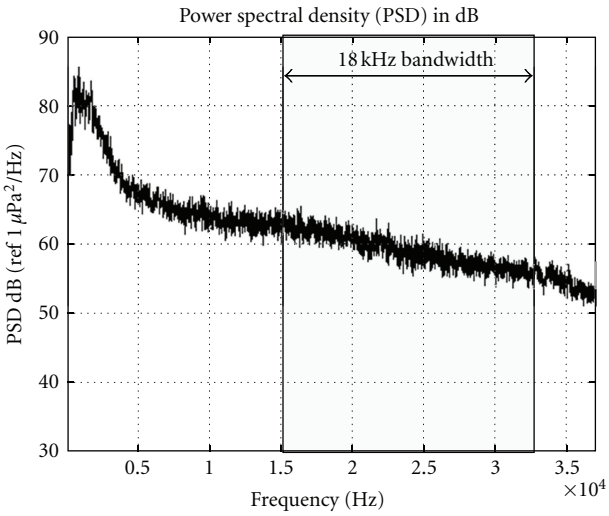

Figure 10: Ambient Noise PSD.

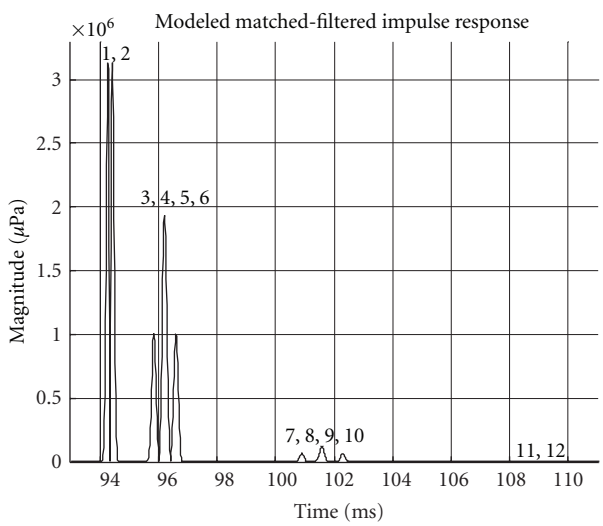

Figure 11: Echo Group 1 of Example Modeled Impulse Response.

delay of the modeled echo group n_g from the time-of-arrival of the modeled direct path. Similarly, $\tau_{\exp}(n_r, n_g, n_l, n_{\text{reg}})$ represents the estimated time delay of the modeled echo group n_g from the time of arrival of the same modeled direct path, including the measured direct path ($n_g = 1$). Each measured echo location is that of the largest echo $|h_{\exp}(n_r, n_g, n_l, n_{\text{reg}})|$ within a 9 ms search window centered on the corresponding modeled echo $|h_{\text{mdl}}(n_r, n_g, n_l, n_{\text{reg}})|$. The specific 9 ms duration is based on the source and receiver position accuracy and the approximated geometry of the duct. As an example, Figure 13 shows the measured and modeled impulse response at location 008 for the first measured impulse response. Note that the location of each search window in Figure 13 is not exact. The relative errors in echo magnitude $\varepsilon_{\text{mag}}(n_r, n_g, n_l, n_{\text{reg}})$ and in echo location

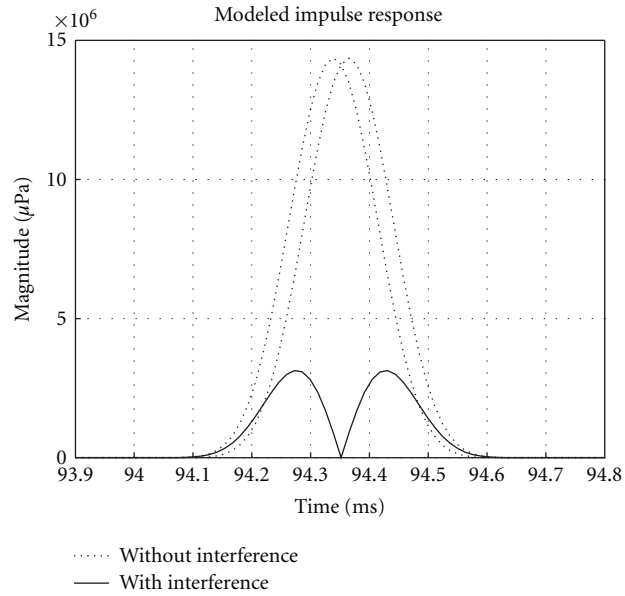

Figure 12: Overlapping Echoes associated with the Direct Path and the first Sea Surface Bounce.

$\varepsilon_{\text{loc}}(n_r, n_g, n_l, n_{\text{reg}})$ between the model and the measurement are

$$\varepsilon_{\text{mag}}\left(n_r, n_g, n_l, n_{\text{reg}}\right) = \left(100 \times \frac{\left|\left|\tilde{h}_{\exp}\left(n_r, n_g, n_l, n_{\text{reg}}\right)\right| - \left|\tilde{h}_{\text{mdl}}\left(n_r, n_g, n_l, n_{\text{reg}}\right)\right|\right|}{\left|\tilde{h}_{\text{mdl}}\left(n_r, n_g, n_l, n_{\text{reg}}\right)\right|}\right)\%,$$

$$\varepsilon_{\text{loc}}\left(n_r, n_g, n_l, n_{\text{reg}}\right) = \left(100 \times \frac{\left|\tau_{\exp}\left(n_r, n_g, n_l, n_{\text{reg}}\right) - \tau_{\text{mdl}}\left(n_r, n_g, n_l, n_{\text{reg}}\right)\right|}{\tau_{\text{mdl}}\left(n_r, n_g, n_l, n_{\text{reg}}\right)}\right)\%. \tag{39}$$

The mean and standard deviation of these errors, computed across all the records at a specific location, region and group, are

$$\overline{\varepsilon_{\text{mag}}\left(n_g, n_l, n_{\text{reg}}\right)} = \left(\frac{1}{N_r}\sum_{i=1}^{N_r}\varepsilon_{\text{mag}}\left(n_r, n_g, n_l, n_{\text{reg}}\right)\right)\%,$$

$$\sigma_{\varepsilon_{\text{mag}}}\left(n_g, n_l, n_{\text{reg}}\right) = \left(\sqrt{\frac{1}{N_r - 1}\sum_{i=1}^{N_r}\left(\varepsilon_{\text{mag}}\left(n_r, n_g, n_l, n_{\text{reg}}\right) - \overline{\varepsilon_{\text{mag}}\left(n_g, n_l, n_{\text{reg}}\right)}\right)^2}\right)\%,$$

$$\overline{\varepsilon_{\text{loc}}\left(n_g, n_l, n_{\text{reg}}\right)} = \left(\frac{1}{N_r}\sum_{i=1}^{N_r}\varepsilon_{\text{loc}}\left(n_r, n_g, n_l, n_{\text{reg}}\right)\right)\%,$$

$$\sigma_{\varepsilon_{\text{loc}}}\left(n_g, n_l, n_{\text{reg}}\right) = \left(\sqrt{\frac{1}{N_r - 1}\sum_{i=1}^{N_r}\left(\varepsilon_{\text{loc}}\left(n_r, n_g, n_l, n_{\text{reg}}\right) - \overline{\varepsilon_{\text{loc}}\left(n_g, n_l, n_{\text{reg}}\right)}\right)^2}\right)\%. \tag{40}$$

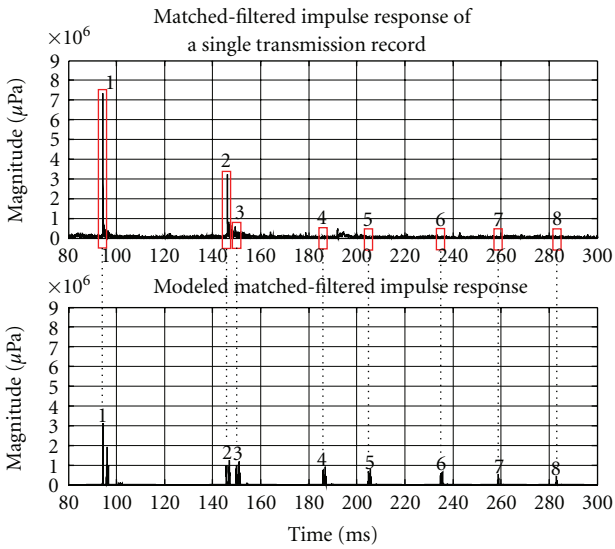

Figure 13: Numbered Echo Groups for Measured and Modeled Impulse Response at Location 008.

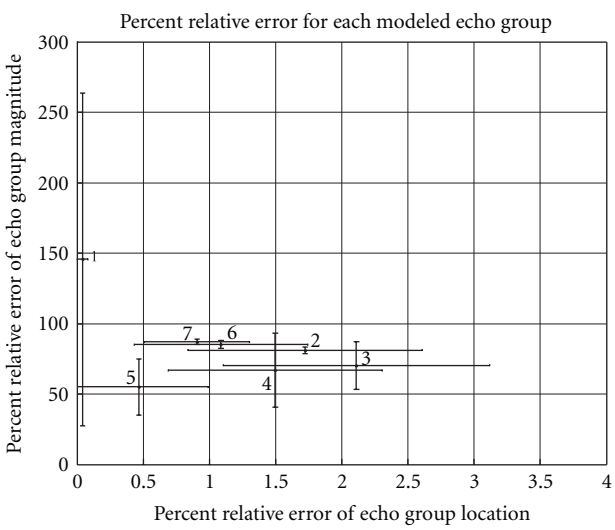

Figure 14: Relative Error in Magnitude and Location for Region 1.

Figures 14 to 17 show the mean and standard deviation of the relative error between the modeled impulse response and the measured impulse response. Each numbered point corresponds to the mean value of the relative error for each echo group. The error bars in each plot represent two standard deviations of the relative error for each echo group. The x-axis corresponds to the relative error for the first arriving echo of each group. The relative error in magnitude for the first arriving echo of each group is displayed on the y-axis. A complete convergence analysis of the model as a function of the number of images is beyond the scope of this paper. However, the authors performed a limited study in [27], which indicated that the model converged using a small number of images.

Figure 14 shows the relative error for region 1. This region corresponds to the receiver locations close to the western wall of the turning basin. This wall is composed of boulders piled vertically in an irregular manner. A significant share of the error observed between the modeled and measured impulse response is attributed to the structure of this wall. Since the boulders create a boundary that is not perfectly flat, the transmitted signal will be scattered at the interaction with the boundary. This scattering differs for different locations even within this region. Across the groups, the mean error in echo location varies between 0.2% and 2.1%. The mean error in echo magnitude varies between 55% (−2.6 dB) and 145% (1.62 dB). The relative error in magnitude of the direct path (group 1) of 145% is due to a significant overlap between the direct path and the surface bounce, caused by the small difference in time of travel between the direct path and the first surface echo. This same observation is made in regions 2 and 4. The standard deviation of the magnitude error varies from 2% (group 7) to 120% (group 1). The standard deviation of the location error varies between 0.1% (group 1) and 1% (group 3).

Figure 15 shows the relative error for each of the eight groups of echoes in region 2. The best match between modeled and measured data is observed in this region, as the relative error in echo group location is less than 1% in most cases. This is due to the fact that the receiver is relatively close to the southern wall of the turning basin and further away from the source. This vertical wall is flat; therefore the flat rigid surface assumed for the model constitutes a fair approximation. This large vertical wall is also an excellent reflector and the scattering is minimal as compared to the rocky walls to the north and west. Echo group 3 produces the largest error in echo location (1.7%) as it includes reflections from the rocky western wall. Across the groups, the mean error in echo location varies between 0.05% and 1.7%. The mean error in echo magnitude varies between 65% (−1.87 dB) and 120% (0.79 dB). The standard deviation of the magnitude error varies from 20% (group 5) to 80% (group 2). The standard deviation of the location error varies between 0.1% (group 1) and 1% (group 3).

Figure 16 shows the relative error for each of the eight groups of echoes in region 3, where all of the receiver locations are relatively close to the source. The relative error in the direct path (group 1) magnitude is significantly lower for this region (55%) as compared with the other regions (115% to 145%). Since the source and receiver depths are constant, the reduced distance between the source and the receiver results in an increased difference in time of travel between the direct path and the first surface echo. As a result, the overlap between these two echoes is reduced and the model prediction for the magnitude of the direct path is more accurate. However, the mean error in echo location for the direct path is 1.7%, which is significantly larger than the corresponding error for regions 1, 2, and 4. This is easily explained by the fact that direct path and surface bounce occur within the same search window with very similar magnitudes, so that the peak location of group $n_g = 1$ is occasionally associated with the surface bounce. The overall accuracy of the model in region 3 is significantly better than that in the other regions. Across the groups, the mean error in echo location varies between 0.4% and 1.7%, while the mean

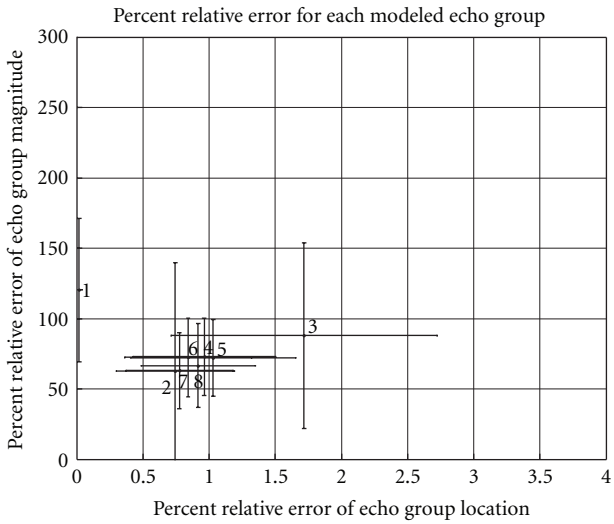

Figure 15: Relative Error in Magnitude and Location for Region 2.

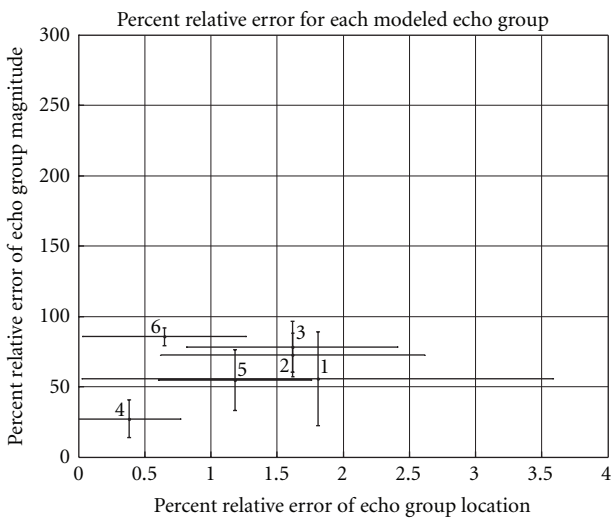

Figure 16: Relative Error in Magnitude and Location for Region 3.

error in echo magnitude varies between 30% (−5.23 dB) and 80% (−0.97 dB). The standard deviation of the magnitude error varies from 5% (group 6) to 30% (group 1). The standard deviation of the location error varies between 0.4% (group 4) and 1.8% (group 1).

Figure 17 shows the relative error for each of the eight groups of echoes in region 4. This region corresponds to the receiver locations that are close to the northern wall of the turning basin. This case is similar to region 1 since the nearest boundary is composed of vertically piled boulders. Across the groups, the mean error in echo location varies between 0.1% and 1.05%, while the mean error in echo magnitude varies between 70% (−1.55 dB) and 120% (0.79 dB). The standard deviation of the magnitude error does not exceed 20%, with the exception of the first group containing the direct path (120%). The standard deviation of the location error varies between 0.1% (group 1) and 1.1% (group 2).

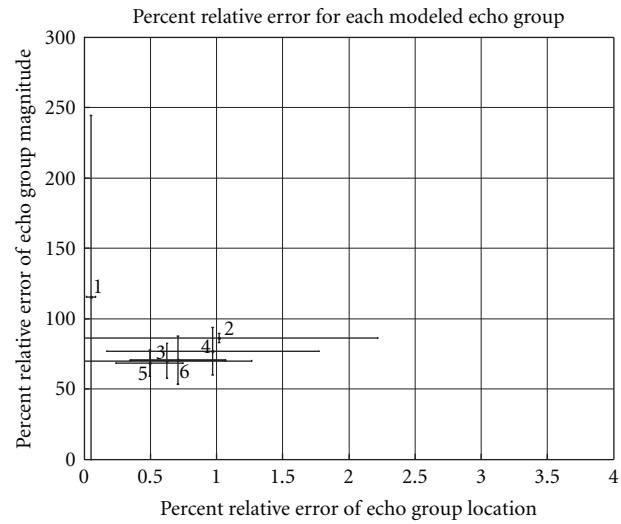

Figure 17: Relative Error in Magnitude and Location for Region 4.

4. Conclusion

At first glance, a mean relative error of up to 145% (1.62 dB) in estimating the echo magnitude appears significant. However, this is a very reasonable number from the standpoint of underwater acoustic communications in nonstationary fading channels. Indeed, fluctuations in echo magnitude of 10 dB are commonly observed in shallow waters [28]. The error in echo location is also very good overall, as it always remains within 4% of the measured echo location. These encouraging results do not mean that the approximations made in the present model (negligible effects of wave curvature, scattering, and diffraction) should be the norm: a more realistic model would be expected to produce more accurate results. Rather, the model may simply be an acceptable trade-off between accuracy and computational load for acoustic communication purposes. Since the performance estimation of underwater acoustic modems is measured in terms of probability of bit error averaged over a very large number of samples, the three-dimensional model presented provides a sufficient level of accuracy to be used in the simulation of an acoustic communication system operating between 15 kHz and 33 kHz, with the benefit of low computing requirements.

Acknowledgments

This work is sponsored by the Center for Coastline Security and Technology at Florida Atlantic University and the Office of Naval Research.

References

[1] P. P. J. Beaujean and E. P. Bernault, "A new multi-channel spatial diversity technique for long range acoustic communications in shallow water," in *Proceedings of the MTS/IEEE Oceans Conference*, vol. 3, pp. 1533–1538, San Diego, Calif, USA, September 2003.

[2] M. D. Green and J. A. Rice, "Channel-tolerant FH-MFSK acoustic signaling for undersea communications and networks," *IEEE Journal of Oceanic Engineering*, vol. 25, no. 1, pp. 28–39, 2000.

[3] K. G. Kebkal and R. Bannasch, "Sweep-spread carrier for underwater communication over acoustic channels with strong multipath propagation," *Journal of the Acoustical Society of America*, vol. 112, no. 5, pp. 2043–2052, 2002.

[4] L. Freitag, M. Johnson, M. Grund, S. Singh, and J. Preisig, "Integrated acoustic communication and navigation for multiple UUVs," in *Proceeding of the MTS/IEEE Oceans Conference*, vol. 4, pp. 2065–2070, November 2001.

[5] P. P. J. Beaujean and E. A. Carlson, "HERMES-A high bit-rate underwater acoustic modem operating at high frequencies for ports and shallow water applications," *Marine Technology Society Journal*, vol. 43, no. 2, pp. 21–32, 2009.

[6] P.-P. J. Beaujean and J. Proteau, "Spatio-temporal processing technique for high-speed acoustic communications in shallow water at the South Florida Testing Facility: theory and experiment," *Journal of Underwater Acoustics*, vol. 56, pp. 317–347, 2006.

[7] E. A. Carlson, P.-P. J. Beaujean, and E. An, "An Ad Hoc wireless acoustic network simulator applied to multiple underwater vehicle operations in shallow waters using high-frequency acoustic modems," *Journal of Underwater Acoustics*, vol. 56, pp. 113–139, 2006.

[8] P. P. J. Beaujean, A. A. Folleco, F. J. Boulanger, and S. A. L. Glegg, "Non-linear modeling of underwater acoustic waves propagation for multi-receiver channels," in *Proceedings of the MTS/IEEE Oceans Conference*, vol. 1, pp. 273–278, San Diego, Calif, USA, September 2003.

[9] R. L. Peterson, R. E. Ziemer, and D. E. Borth, *Introduction to Spread Spectrum Communications*, Prentice-Hall, Upper Saddle River, NJ, USA, 1995.

[10] D. E. Weston, "Horizontal refraction in a three-dimensional medium of variable stratification," *Proceedings of the Physical Society*, vol. 78, no. 1, article 308, pp. 46–52, 1961.

[11] G. B. Deane and C. T. Tindle, "A three-dimensional analysis of acoustic propagation in a penetrable wedge slice," *Journal of the Acoustical Society of America*, vol. 92, no. 3, pp. 1583–1592, 1992.

[12] M. J. Buckingham, "Theory of three-dimensional acoustic propagation in a wedgelike ocean with a penetrable bottom," *Journal of Acoustical Society of America*, vol. 82, no. 1, pp. 198–210, 1987.

[13] S. A. L. Glegg, G. B. Deane, and I. G. House, "Comparison between theory and model scale measurements of three-dimensional sound propagation in a shear supporting penetrable wedge," *Journal of the Acoustical Society of America*, vol. 94, no. 4, pp. 2334–2342, 1993.

[14] S. A. L. Glegg and J. R. Yoon, "Experimental measurements of three-dimensional propagation in a wedge-shaped ocean with pressure-release boundary conditions," *Journal of the Acoustical Society of America*, vol. 87, no. 1, pp. 101–105, 1990.

[15] P. Borejko, "An exact representation of the image field in a perfect wedge," *Acta Mechanica*, vol. 169, no. 1–4, pp. 23–36, 2004.

[16] L. M. Brekhovskikh, *Fundamentals of Ocean Acoustics*, Springer, New York, NY, USA, 3rd edition, 2003.

[17] G. V. Frisk, *Ocean and Seabed Acoustics: A Theory of Wave Propagation*, Prentice-Hall, Upper Saddle River, NJ, USA, 1994.

[18] J. B. Allen and D. A. Berkley, "Image method for efficiently simulating small-room acoustics," *Journal of Acoustical Society of America* , vol. 65, no. 4, pp. 943–950, 1979.

[19] E. B. Viveiros and B. M. Gibbs, "An image model for predicting the field performance of acoustic louvres from impulse measurements," *Applied Acoustics*, vol. 64, no. 7, pp. 713–730, 2003.

[20] K. K. Iu and K. M. Li, "The propagation of sound in narrow street canyons," *Journal of the Acoustical Society of America*, vol. 112, no. 2, pp. 537–550, 2002.

[21] V. Martin and T. Guignard, "Image-source method and truncation of a series expansion of the integral solution—case of an angular sector in two dimensions," *Journal of the Acoustical Society of America*, vol. 120, no. 2, pp. 597–610, 2006.

[22] L. Liu and D. G. Albert, "Acoustic pulse propagation near a right-angle wall," *Journal of the Acoustical Society of America*, vol. 119, no. 4, pp. 2073–2083, 2006.

[23] L. E. Kinsler, A. R. Frey, A. B. Coppens, and J. V. Sanders, *Fundamentals of Acoustics*, John Wiley and Sons, New York, NY, USA, 4th edition, 1983.

[24] M. Schulkin and H. W. Marsh, "Sound absorption in sea water," *Journal of Acoustical Society of America*, vol. 34, no. 6, pp. 864–865, 1962.

[25] F. R. Driscoll, P. P. J. Beaujean, and W. A. Venezia, "Development and testing of an A-sized rapidly deployable navigation and communication GATEWAY buoy," *Marine Technology Society Journal*, vol. 40, no. 1, pp. 36–46, 2006.

[26] D. Sheahan, *An investigation into the acoustic variability and the attenuation of an acoustic signal within a port environment focusing on Port Everglades, Florida*, M.S. thesis, Florida Atlantic University, 2007.

[27] M. D. Staska, *A study of the underwater acoustic propagation in a turning basin modeled as a three-dimensional duct closed at one end using the method of images*, M.S. thesis, Florida Atlantic University, 2007.

[28] P. P. J. Beaujean and L. R. LeBlanc, "Adaptive array processing for high-speed acoustic communication in shallow water," *IEEE Journal of Oceanic Engineering*, vol. 29, no. 3, pp. 807–823, 2004.

Hindawi Publishing Corporation
Advances in Acoustics and Vibration
Volume 2012, Article ID 474039, 16 pages
doi:10.1155/2012/474039

Research Article

Speckle Reduction for Ultrasonic Imaging Using Frequency Compounding and Despeckling Filters along with Coded Excitation and Pulse Compression

Joshua S. Ullom,[1] Michael L. Oelze,[2] and Jose R. Sanchez[3]

[1] *Harris Corporation, Melbourne, FL 32905, USA*
[2] *Electrical and Computer Engineering Department, University of Illinois at Urbana-Champaign, Urbana, IL 61801, USA*
[3] *Electrical and Computer Engineering Department, Bradley University, Peoria, IL 61625, USA*

Correspondence should be addressed to Jose R. Sanchez, jsm@bradley.edu

Received 27 November 2011; Accepted 5 April 2012

Academic Editor: Erdal Oruklu

A method for improving the contrast-to-noise ratio (CNR) while maintaining the −6 dB axial resolution of ultrasonic B-mode images is proposed. The technique proposed is known as eREC-FC, which enhances a recently developed REC-FC technique. REC-FC is a combination of the coded excitation technique known as resolution enhancement compression (REC) and the speckle-reduction technique frequency compounding (FC). In REC-FC, image CNR is improved but at the expense of a reduction in axial resolution. However, by compounding various REC-FC images made from various subband widths, the tradeoff between axial resolution and CNR enhancement can be extended. Further improvements in CNR can be obtained by applying postprocessing despeckling filters to the eREC-FC B-mode images. The despeckling filters evaluated were the following: median, Lee, homogeneous mask area, geometric, and speckle-reducing anisotropic diffusion (SRAD). Simulations and experimental measurements were conducted with a single-element transducer ($f/2.66$) having a center frequency of 2.25 MHz and a −3 dB bandwidth of 50%. In simulations and experiments, the eREC-FC technique resulted in the same axial resolution that would be typically observed with conventional excitation with a pulse. Moreover, increases in CNR of 348% were obtained in experiments when comparing eREC-FC with a Lee filter to conventional pulsing methods.

1. Introduction

In imaging, the ability to detect small or low-contrast structures is of utmost importance. However, ultrasonic images are riddled with speckle, which reduces the ability to detect low-contrast and/or small-sized targets. Speckle is formed by subresolution scatterers that cause constructive and destructive interference of backscattered ultrasonic signals within the resolution cell volume of an ultrasonic source [1]. In ultrasound, the difference in contrast between different soft tissues could be as small as 1%. Consequently, speckle reduction techniques must be applied to improve image contrast and enhance the detectability of structures having low contrast with the background [2].

Speckle-reduction techniques can be classified into two categories: compounding methods and postprocessing techniques. The compounding speckle-reduction methods include spatial [3–6] and frequency compounding [7–11]. These schemes rely on making separate images that have uncorrelated or partially correlated speckle patterns. These images are then averaged to reduce the speckle but at the expense of spatial resolution. Postprocessing speckle-reduction techniques [12–17] reduce speckle after the ultrasound image is formed. The engineering tradeoffs vary based on the postprocessing speckle-reduction technique employed but typically include increased contrast and reduced speckle versus edge preservation, image blurring, and image texture.

A recently developed speckle-reduction technique—resolution enhancement compression with frequency compounding (REC-FC)—can improve the visibility of ultrasonic images while extending the tradeoff between spatial

resolution and visibility [18, 19]. REC-FC used the coded excitation and pulse compression technique, REC, which has the potential to improve the axial resolution of an ultrasonic imaging system by a factor of two [20]. A larger axial resolution translated into a larger bandwidth. In addition to increases in bandwidth, the REC technique has the typical benefits of coded excitation and pulse compression such as increased time bandwidth product (TBP) [21]. An excitation signal with a longer duration than a conventional excitation signal contains more energy, resulting in an increased echo signal-to-noise ratio (eSNR) [22]. Consequently, increased eSNR results in deeper penetration depth. However, because the pulse duration is increased, the axial resolution degrades. To restore the axial resolution, pulse compression techniques, such as a Wiener filter, are used [21].

In REC, the larger bandwidth was exploited by combining the technique with FC. FC is a speckle reduction technique that subdivides the spectrum of the radio-frequency (RF) echoes into subbands to make partially uncorrelated images [7]. These images were then compounded to reduce the speckle variance. REC-FC was found to improve contrast-to-noise ratio (CNR) by as much as 231% compared to a conventional pulsing (CP) scheme. Overall, REC-FC improved image quality, CNR, and lesion boundaries. However, the drawback of REC-FC was that subband filters only contained a fraction of the original system bandwidth, which resulted in a reduction of axial resolution.

In this study, an improvement to the REC-FC technique is proposed, which enhances the visibility of an ultrasonic image while maintaining the axial resolution to comparable levels when exciting a transducer with a pulse. The resulting image can be further enhanced by reducing the speckle and improving the visibility by applying postprocessing despeckling filters.

2. Methods and Procedures

2.1. REC. In REC, a preenhanced chirp, $x(t)$, is used to excite an ultrasonic focused source, $h(t)$. The preenhanced chirp is obtained through convolution equivalence as discussed in [18, 20]. The goal of the preenhanced chirp is to boost the energy in the band edges of the source's frequency response.

With REC, the spectral support of the echo signal is much larger than the bandwidth of the source. However, the pulse duration of the excitation signal, $y(t)$, is longer than an echo from the same source when the excitation is $\delta(t)$, which will be described as conventional pulsing (CP) in this study. Therefore, in order to recover the benefits of the larger bandwidth, the resolution must be restored through pulse compression. Pulse compression is performed using a Wiener filter, which is described by [21]:

$$H_{\text{wiener}}(f) = \frac{\Psi^*(f)}{|\Psi(f)|^2 + \gamma\overline{\text{eSNR}(f)}^{-1}}, \tag{1}$$

where f is frequency, and γ is a smoothing parameter that controls the tradeoff between sidelobe levels, axial resolution, and eSNR. The term $\overline{\text{eSNR}}$ is the echo signal-to-noise ratio per frequency channel and $\Psi(f)$ corresponds to the Fourier transform of a linear chirp excitation, which is part of convolution equivalence scheme used to obtain the preenhanced chirp as discussed in [18, 20]. In practice, the eSNR is estimated for the imaging system by pointing the imaging system to a region where no scatterers exist, for example, water, and the noise of the system can be isolated for a particular excitation. The compressed echo waveform and the log-compressed envelope of the echo waveform for a point target are shown in Figure 1 along with the CP reference. The Wiener filter allows the compression to balance between matched filtering and inverse filtering. Matched filtering provides the best gain in SNR but results in larger sidelobes and loss in axial resolution. An inverse filter provides the best compression terms of axial resolution and sidelobes but amplifies noise in the system.

2.2. REC-FC. In REC-FC, the wideband RF spectrum of each scan line was partitioned into N subbands by using Gaussian bandpass filters. These Gaussian bandpass filters contained a fraction of the original system bandwidth. The resulting images from the N subbands were compounded to form an image with reduced speckle variance. A reduction in speckle variance translated into CNR improvements. However, because the subband width was smaller in bandwidth than the original system, the axial resolution in the compounded images deteriorated. For example, with REC the axial resolution is doubled compared to CP. If overlapping subbands with a width of half the REC bandwidth (full width) are applied, then the resulting axial resolution is the same as CP and the image has improved visibility because of the compounding effects. The tradeoff of axial resolution versus image visibility is shown in Figure 2 for various subband widths. All subband widths are compared to CP, for example, third width implies that subbands with one-third of the CP bandwidth are applied and then compounded.

2.3. Enhanced REC-FC. In this study, a method is proposed that could provide the improvements in visibility that were obtained with REC-FC but without degrading the -6 dB axial resolution beyond the axial resolution obtained for CP. The proposed method consists of compounding REC-FC images obtained from different subband widths, which will reduce the speckle variance even further and result in an improvement of image visibility. This technique will be known as enhanced REC-FC or eREC-FC [23]. Moreover, the method has no impact on the lateral resolution of the imaging system. In this study, eREC-FC utilized the uniformly weighted sum of the following images (Figure 2): REC reference image, REC-FC (full-width), REC-FC (half-width), REC-FC (third-width), REC-FC (fourth-width), and REC-FC (eighth-width) to form a final enhanced REC-FC image. The original REC image was included because the borders of the lesion in the eREC-FC image become much more distinct because of the high spatial resolution of the REC technique. REC-FC (eight-width) was the final image compounded because smaller subband widths require too much computation time for the minimal improvements in CNR. Combining REC with REC-FC (eighth-width) resulted

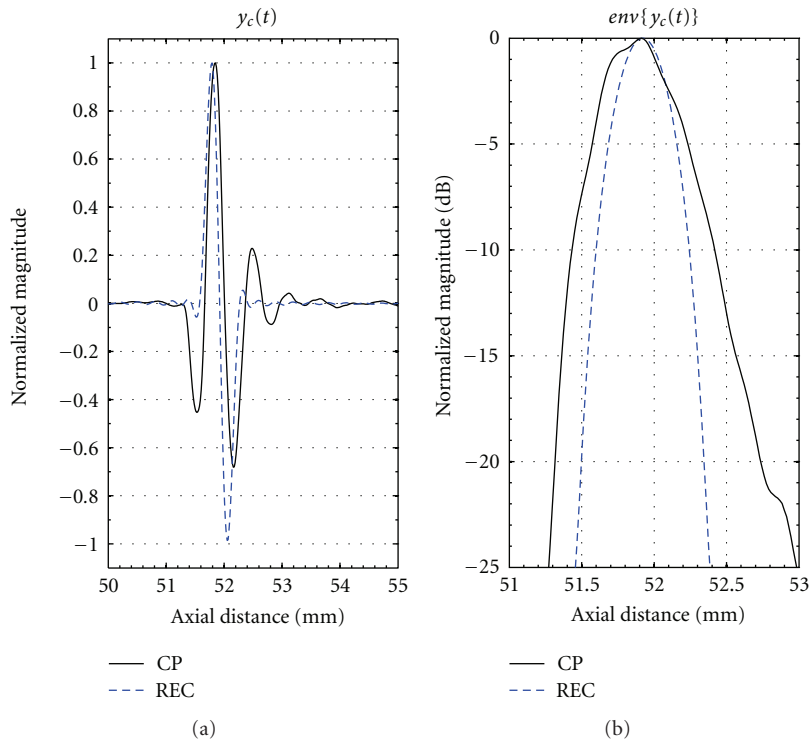

Figure 1: Compression of the $y(t)$ is represented by $y_c(t)$ and the log-compressed and envelope-detected version of $y_c(t)$.

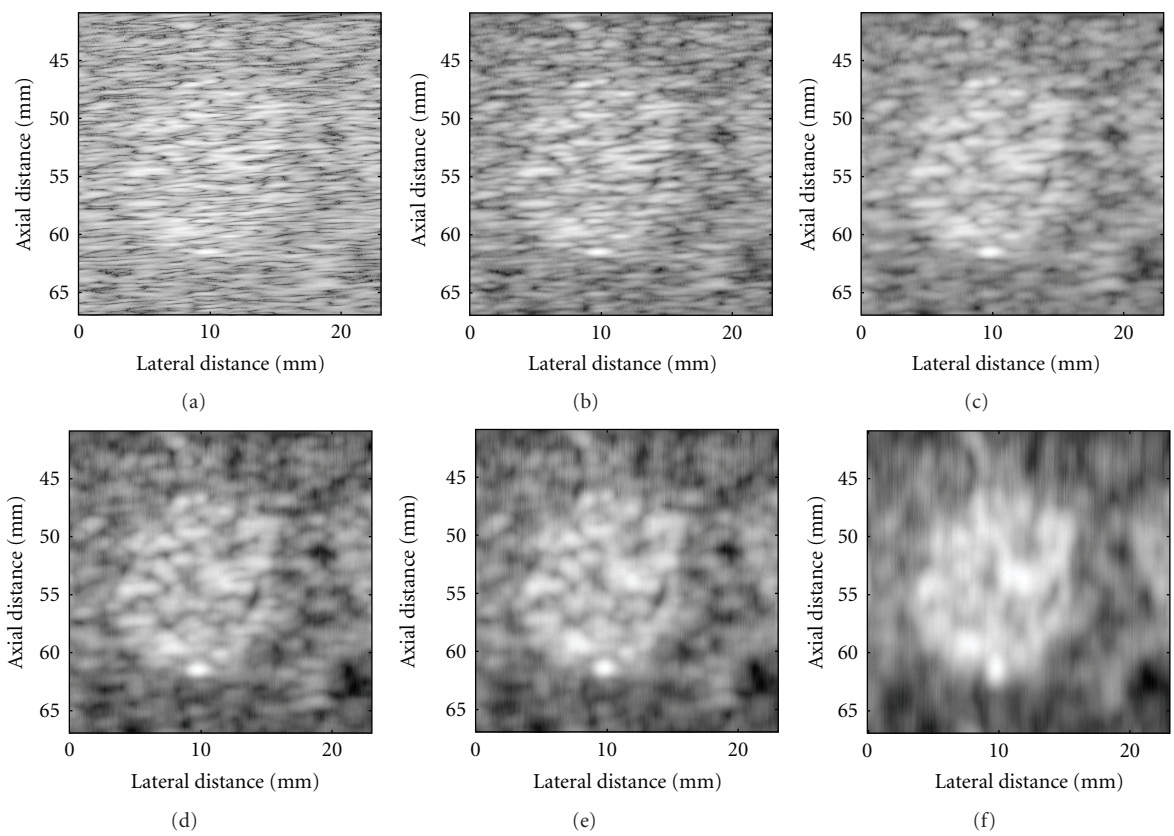

Figure 2: B-mode images for (a) REC reference, (b) REC-FC (full-width), (c) REC-FC (half-width), (d) REC-FC (third-width), (e) REC-FC (fourth-width), and (f) REC-FC (eighth-width). Image dynamic range is −50 dB.

in similar CNR as in the eREC-FC technique presented herein; however, the spatial resolution in the image would be far worse than the eREC-FC technique. Therefore, by combining more images of varying subbands improvements in axial resolution could be obtained.

Theoretically, by summing all the compounded images along with the reference, the final enhanced image would have a -6 dB axial resolution similar to the full-width REC-FC scenario or equivalent to the original resolution obtained with CP. The results of summing the envelope of the reference and subbands are shown in Figure 3. Evaluation of the eREC-FC envelope at -6 dB in Figure 3(b) indicated that a loss of 10 μm in axial resolution was obtained when compared to CP. Compared to the wavelength of the source, the loss is 1.5%. Furthermore, every drop of -6 dB in amplitude is followed by a slight deterioration in the axial resolution. However, this degradation should not affect the image quality unless there is a large contrast difference, such as in a cystic lesion (i.e., no scatterers).

2.4. Despeckling Filters. Images obtained with the eREC-FC technique were further processed with several despeckling filters. These techniques could also be applied to CP and REC excitations. However, the goal of this particular study was to judge how well image quality would be improved by applying coded excitation, novel compounding techniques, and postprocessing filters. Therefore, to better manage the amount of data for comparisons, only filtering techniques will be applied to the eREC-FC images. Similar improvements provided to eREC-FC by the filtering techniques are also expected for CP and simple REC excitations (except that the starting point for eREC-FC in terms of image quality is already improved leading to overall better improvement using filtering for eREC-FC). Despeckling filters make use of a moving, overlapping window of size $(n \times n)$, where n is an odd integer, that advances through the entire image one pixel at a time. The center pixel of the window is the location that will be adjusted in the filtered image. Some despeckling filters use iterative techniques, where after the first iteration (filtering of the original image) the filtered image becomes the input to the filter for each successive iteration. The despeckling filters used in this study were as follows.

2.4.1. Median Filtering [12, 13]. Median filtering makes use of a moving, overlapping window. The median of the pixels in the window is the resulting value of the center pixel in the window for the filtered image. Median filtering is used to smooth an image and minimize or eliminate noise spikes, with the idea that all pixels in a small region of an image should be similar.

2.4.2. Lee Filtering [14]. Lee filtering also uses a moving, overlapping window. The Lee filter uses statistics within that window such as mean and variance to adjust the resulting center pixel of the window. The equation that governs this filtering process [24, 25] is

$$f_{i,j} = \overline{g}_{i,j} + k_{i,j} \cdot \left[g_{i,j} - \overline{g}_{i,j}\right], \tag{2}$$

where i and j are pixel coordinates, $f_{i,j}$ is the filtered pixel at location (i, j), $\overline{g}_{i,j}$ is the mean of the pixel intensities in the window, $g_{i,j}$ is the center pixel in the window, and

$$k_{i,j} = \frac{1 + \overline{g}_{i,j}\sigma^2}{\sigma^2\left(1 + \sigma_n^2\right)}, \tag{3}$$

where σ^2 is the variance in the window and σ_n^2 is the noise variance in the whole image. This will result in $k \in [0, 1]$. Because the variance in noise, or speckle, is not known, it is estimated by [24]

$$\sigma_n^2 = \sum_I \frac{\sigma_{w_b}^2}{\overline{w}_b}, \tag{4}$$

where w_b is a window that is 10 times larger than the filtering window, and $\sigma_{w_b}^2$ and $\overline{w}_b$ are the variance and mean of pixel intensity of the larger window, w_b, respectively. This window moves through the entire image, I. Statistics obtained for each region are combined over the entire image to obtain a single estimate of speckle noise.

2.4.3. Homogeneous Mask Area Filtering [24, 26]. Two windows are used in the homogeneous mask area filtering technique, a large main window, which determines the pixel location to filter, and a smaller subwindow within the main window. For each subwindow, a speckle index is calculated as

$$S = \frac{\sigma^2}{\mu}, \tag{5}$$

where μ and σ^2 are the mean and variance of the pixel intensity in the subwindow, respectively. The mean pixel intensity of the subwindow with the smallest speckle index becomes the filtered pixel value. For this study, the dimension of the subwindow was $(n - 2) \times (n - 2)$.

2.4.4. Geometric Filtering [27]. Geometric filtering uses a moving, overlapping window of size 3×3. In addition, the geometric filter uses an iterative approach to make the center pixel of the window more like its neighboring pixels. The idea behind the geometric filter is that a very small region of an image should be homogeneous. There are four directions the geometric filter iterates through north-south, east-west, northwest-southeast, and northeast-southwest. In each case, a line of three pixels is created and evaluated. The algorithm for computing the filtered pixel update is shown hereinafter. In the first iteration, a would correspond to the pixel in the

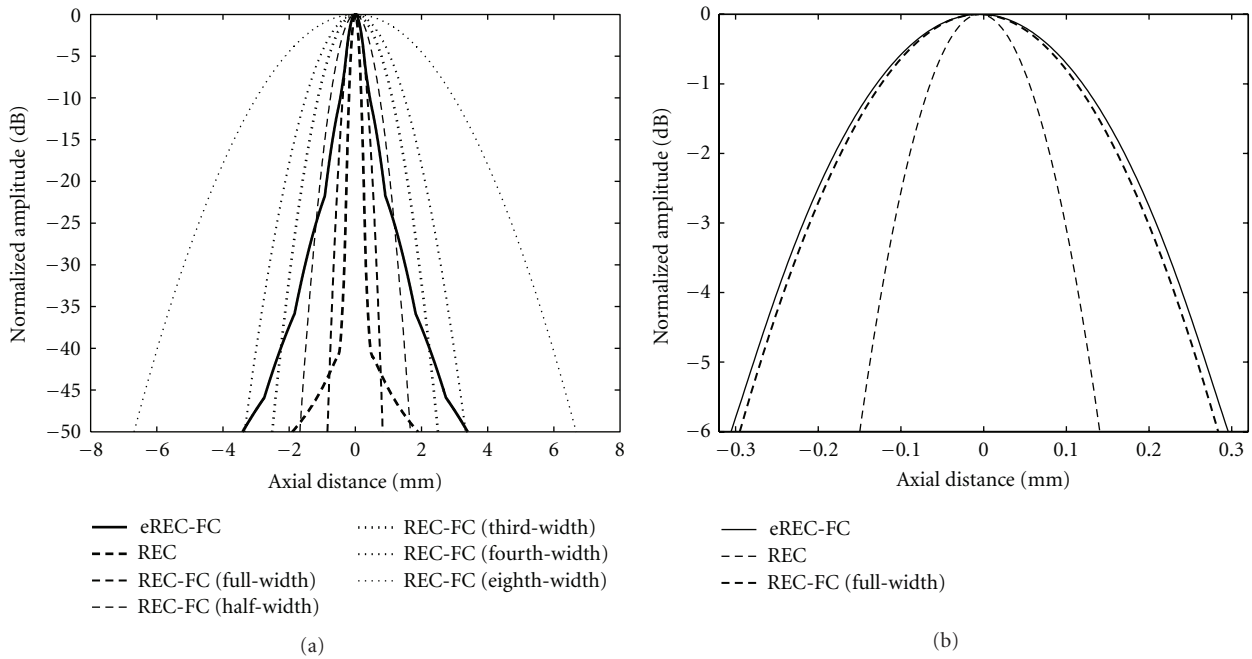

Figure 3: (a) Individual envelopes showcasing the axial resolution for the REC reference case. the REC-FC cases, and the eREC-FC case. (b) Zoomed version of eREC-FC showing that the axial resolution was similar to REC-FC (full-width). Note that the axial resolution for REC-FC (full-width) is the same as CP.

north direction, b is the center pixel, and c would correspond to the pixel in the south direction [24, 27]:

$$\begin{aligned}
&\text{if } a \geq b+2, \text{ then } b = b+1,\\
&\text{if } a > b \text{ and } b \leq c, \text{ then } b = b+1,\\
&\text{if } c > b \text{ and } b \leq a, \text{ then } b = b+1,\\
&\text{if } c \geq b+2, \text{ then } b = b+1,\\
&\text{if } a \leq b-2, \text{ then } b = b-1,\\
&\text{if } a < b \text{ and } b \geq c, \text{ then } b = b-1,\\
&\text{if } c < b \text{ and } b \geq a, \text{ then } b = b-1,\\
&\text{if } c \leq b-2, \text{ then } b = b-1.
\end{aligned} \tag{6}$$

2.4.5. Speckle-Reducing Anisotropic Diffusion [16]. Speckle-reducing anisotropic diffusion (SRAD) is an algorithm that smears the pixel intensities within homogeneous regions while preserving edges by not smearing across inhomogeneous regions. SRAD is based on anisotropic diffusion [28] and is used by solving the diffusion equation described as a nonlinear partial differential equation:

$$\begin{aligned}
\frac{\partial I}{\partial t} &= \operatorname{div}[c(|\nabla I|) \cdot \nabla I],\\
I(t=0) &= I_0,
\end{aligned} \tag{7}$$

where div is the divergence operator, ∇ is the gradient operator, I_0 is the original image, and is greater than zero. c is the instantaneous coefficient of variation and is described by

$$c(x) = \frac{1}{1+(x/k)^2}, \tag{8}$$

where x is a spatial position and k is an edge magnitude parameter.

2.5. Image Quality Metrics. To evaluate the performance of the eREC-FC technique and the eREC-FC with despeckling filters compared with CP the following image quality metrics were used.

2.5.1. Contrast-to-Noise Ratio (CNR) [2]. CNR, also known as contrast-to-speckle ratio, is a quantitative measure that will assess image quality and describe the ability to perceive a target from the background region. CNR is defined as

$$\text{CNR} = \left| \frac{\mu_B - \mu_T}{\sqrt{\sigma_B^2 + \sigma_T^2}} \right|, \tag{9}$$

where μ_B and μ_T are the mean brightness of the background and the target lesion and σ_B^2 and σ_T^2 are the variance of the background and target, respectively. To avoid possible errors in the calculations due to attenuation, the evaluated regions of interest in the background and the target lesion will be of the same size and are located at the same depth. A larger CNR represents better contrast.

2.5.2. Histogram Pixel Intensity (HPI). HPI is the mean of the frequency distribution of gray-scale pixel intensities and is described by

$$\text{HPI} = E\{B\}, \tag{10}$$

where B is the histogram being evaluated and is described by

$$B(i) = c_i, \tag{11}$$

where c_i represents the number of pixels in the image within a particular intensity level, i, which is an integer between 0 and 255 that represents the grayscale levels used in B-mode images. Histograms will be made for same-sized regions for the target lesion and the background and located at the same depth. Ideally, for superior target detectability, there is no overlap present between the target histogram and the background histogram. Therefore, histogram overlap (HO), the percentage of overlapping pixels between these two regions, will be considered as well. In addition to HO, the difference between the distributions for mean pixel intensity for the target and the background will be quantified in order to assess the separation between both distributions. This quantity will be known as H_{diff}. Consequently, the technique with the least amount of overlap and the greatest separation would represent the technique with the best target detectability.

2.5.3. Margin Strength (MS). Estimates of MS [29] were used to detect the edges in the B-mode images. First, a thresholding scheme was applied to the images. Then, MS was estimated to detect the strength of the boundaries using the following expression:

$$\text{MS} = E\left\{\sqrt{\left(\frac{d\text{ROI}}{dx}\right)^2 + \left(\frac{d\text{ROI}}{dy}\right)^2}\right\}, \tag{12}$$

where E is the expectation operator, ROI is the region of interest within the envelope, and x and y correspond to the image coordinates. The margin strength is then imaged, which provides a mechanism to qualitatively study the edge of the targets being imaged.

2.5.4. Comparative Signal-to-Noise Ratio (cSNR) [24, 30]. cSNR is a comparative measure that quantifies the amount of noise/speckle reduction between the filtered and the unfiltered image. cSNR is described by

$$\text{cSNR} = 10\log_{10}\frac{\sum_{i=1}^{M}\sum_{j=1}^{N}\left(g_{i,j}^2 + f_{i,j}^2\right)}{\sum_{i=1}^{M}\sum_{j=1}^{N}\left(g_{i,j} - f_{i,j}\right)^2}. \tag{13}$$

A larger cSNR represents a larger reduction of speckle noise. In this study, each filtered image, g, is compared to the reference image using CP, f.

2.6. Computer Simulations. Computer simulations were carried out in MATLAB (MathWorks, Natick, MA) to characterize the performance of the eREC-FC technique along with the despeckling filters. The simulations used a received pulse-echo pressure field model [31] described as

$$g(x, y, t) = h_1(t) * f(x, y) * h_{\text{pe}}(y, t), \tag{14}$$

where x represents the axial spatial coordinate, y represents the lateral spatial coordinate, $h_1(t)$ is the pulse-echo impulse response of the transducer, $f(x, y)$ is the scattering function, and $h_{\text{pe}}(y, t)$ is the modified pulse-echo spatial impulse response that takes into consideration the geometry of the transducer to the spatial extent of the scattered field (beam diffraction). The pulse-echo impulse response, $h_1(t)$, for CP was generated by gating a sinusoid of 4-cycles with a Hann window:

$$w(n) = \begin{cases} 0.5\left(1 - \cos\left(\dfrac{2\pi n}{L_H - 1}\right)\right), & 0 \le n \le L_H - 1, \\ 0, & \text{otherwise}, \end{cases} \tag{15}$$

where n is an integer and L_H is the number of samples in the window. The window and sinusoid parameters were chosen such that they match the transducer used in experiments. As a result, the pulse-echo impulse response generated was located at the focus of a 2.25-MHz single-element transducer (f/2.66) with a fractional bandwidth of 50% at -3 dB, which would correspond to a window length of $n = 128$. For REC, the desired impulse response function, $h_2(t)$, was constructed to have double the fractional bandwidth or 100% at -3 dB, compared with CP method; therefore, a Hann window of size of half the length, $n = 64$, was used. The spatial response for a circular focused piston source can be simulated as a circular Gaussian beam that is defined as

$$h_{\text{pe}}(y, t) = \delta\left(t - \frac{2R_d}{c}\right)e^{-y^2/\sigma_y^2}, \tag{16}$$

where R_d is the distance from the source to target in space, c is the speed of sound of the medium, and σ_y, which is equal to 1.28 mm, is the nominal lateral beamwidth of the source at -6 dB.

The received RF backscatter data were sampled at a rate of 100 MHz and the transducer was translated laterally in increments of 0.1 mm. The received RF data have a size of 4096×58 samples, axially and laterally. The object being imaged was a simulated phantom that was 20 mm long, 30 mm wide, and 1.92 mm high. A cylindrical target with a radius of 7.5 mm was located at the center of the phantom. To generate a hyperechoic target with a contrast of approximately +6 dB, the amplitude of the scatterers in the target lesion region was twice of the amplitude at the background. To achieve fully developed speckle, the phantom contained an average of 20 point scatterers per resolution cell volume. The scatterers were uniformly distributed throughout the phantom with random spatial locations. Thirty phantoms were simulated and evaluated with the image quality metrics discussed in Section 2.5. Attenuation and noise were not modeled in the simulations to examine the relationship of eREC-FC/despeckling filters to speckle effect only.

2.7. Experiments. Experiments were performed to validate the simulated results. A single-element weakly focused (f/2.66) transducer (Panametrics, Waltham, MA) with a center frequency of 2.25 MHz was used to image a phantom by translating the transducer laterally. The transducer had a -3-dB bandwidth of 50% along with a pulse-echo beamwidth of 1.28 mm. These parameters were measured using the wire technique [32] for transducer characterization. Using REC, the -6-dB pulse-echo bandwidth was

enhanced to 100%. There were two different experimental setups used: one for CP methods and another one for REC experiments. These setups would contain different noise levels due to the use of different excitation systems; therefore, to avoid errors in the comparisons, the noise levels were normalized to an eSNR of 28 dB. Normalization of eSNR was accomplished by adding zero mean Gaussian white noise to the CP RF echo waveform after characterizing the eSNR from measurements of the signal with no scatterers. The two experimental setups are described as follows.

2.7.1. CP Experimental Setup. The transducer was excited by a pulser-receiver (5800, Panametrics, Waltham, MA) and the receive waveform was displayed on an oscilloscope (9354 TM, Lecroy, Chester Ridge, NY) for visual verification. The echo signal was recorded at a rate of 100 MHz by a 12-bit A/D (Digitizing Board UF3025, Strategic Test, Woburn, MA) for further processing by a PC.

2.7.2. REC Experimental Setup. The preenhanced chirp was generated in MATLAB (MathWorks, Natick, MA) and downloaded to an arbitrary waveform generator (W1281A, Tabor Electronics, Tel Hanan, Israel). The excitation signal was sampled at a rate of 100 MHz and amplified by an RF power amplifier (3251, ENI, Rochester, NY). The amplified signal (50 dB) was connected to the transducer through a diplexer (RDX-6, Ritec Enterprises, Warwick, RI). The echo signal was received by a pulser-receiver (5800, Panametrics, Waltham, MA), which was displayed on an oscilloscope (9354 TM, Lecroy, Chester Ridge, NY) for visual verification. The echo signal was recorded at a rate of 100 MHz by a 12-bit A/D (Digitizing Board UF3025, Strategic Test, Woburn, MA) for further processing by a PC.

A tissue-mimicking phantom (Model 539, ATS Laboratories, Bridgeport, CT) was used to assess the performance of eREC-FC and the despeckling filters with the image quality metrics described in Section 2.5. The material from the tissue-mimicking phantom consisted of urethane rubber, which has a speed of sound of 1450 m/s ±1.0% at 23°C and an attenuation coefficient of 0.5 dB/cm/MHz ±5.0%. A +6-dB echogenic gray-scale target structure with a 15 mm diameter at a depth of 4 cm was imaged for both CP and REC. All measurements were conducted at room temperature in a tank of degassed water.

3. Results and Discussion

3.1. Computer Simulations. The CP reference, REC, REC-FC, and eREC-FC B-mode images along with the postprocessing despeckling filtered B-mode images are shown in Figure 4. The CNR, HO, and cSNR for the B-mode images are listed in Table 1. Histograms of the background and target regions for all of the images in Figure 4 are shown in Figure 5 while edge detection images are shown in Figure 6.

3.1.1. eREC-FC. Examination of the reference scans in Figures 4(a) and 4(b) revealed that by using the REC technique the speckle size was finer when compared with CP. This finer speckle comes from the fact that the bandwidth was doubled, which translates into improvements in axial resolution. This smaller speckle size obtained by using REC is critical because the object boundaries are more defined compared with CP [18]. Application of frequency compounding to REC resulted in the B-mode image shown in Figure 4(c). In this scenario, subband widths that are 1/3 of the CP bandwidth were applied to the REC images. With REC-FC (third-width), significant improvements in visibility were observed but at the expense of blurring the image. Specifically, the CNR for REC-FC (third-width) resulted in an average improvement of 197% over 30 phantoms. CNR estimates are listed in Table 1. For eREC-FC, the CNR improved by an average of 148%. However, in addition to the CNR enhancement, it was observed in the eREC-FC results shown in Figure 4(d) that the CNR enhancement was achieved while maintaining the axial resolution, as suggested in Figure 3, to comparable levels when exciting a transducer with a pulse. This result is significant as it suggests that improvements in CNR can be achieved without significantly degrading the axial resolution as shown in the REC-FC technique.

Histogram analysis was performed over the same regions used to obtain the estimates of CNR. The HO and H_{diff} between the target region and the background regions are listed in Table 1. Previously, it was identified that using REC resulted in an image with a smaller speckle size. This improvement had no effect in minimizing the overlap between the target and background regions when compared to CP. However, by applying frequency compounding techniques such as REC-FC and eREC-FC, a substantial reduction in the HO was discovered. It should be noted that a 3.6% reduction in HO was observed in REC-FC (third-width) over eREC-FC. Although eREC-FC has a slightly higher HO, a reduction of 16.3% in HO was observed when compared to CP. Furthermore, REC-FC (third-width) did not provide any improvements in terms of the separation between the target and the background regions as measured in H_{diff} compared to CP. On the contrary, eREC-FC provided a separation of 12 levels of pixel intensities to provide superior target detectability over REC-FC (third-width). Therefore, the slight increase in HO observed in eREC-FC compared to REC-FC (third-width) is acceptable given the benefits of improved spatial resolution and improved target detectability brought by using the eREC-FC technique.

As previously stated, REC-FC is known to enhance the boundaries of the lesions as shown in [18]. However, in eREC-FC, because images with variable speckle sizes are being compounded, it was observed that the transition between the target and the background was slightly blurred. Applying thresholding along with MS resulted in Figure 6. From the MS results, it was observed that REC-FC (third-width) had a more pronounced boundary compared to eREC-FC. Consequently, the tradeoff in using eREC-FC is a degradation of the enhanced edges obtained with the REC-FC technique in order to gain CNR while maintaining the same axial resolution as CP.

In terms of cSNR, REC-FC (third-width) provided the greatest amount of speckle reduction when compared to

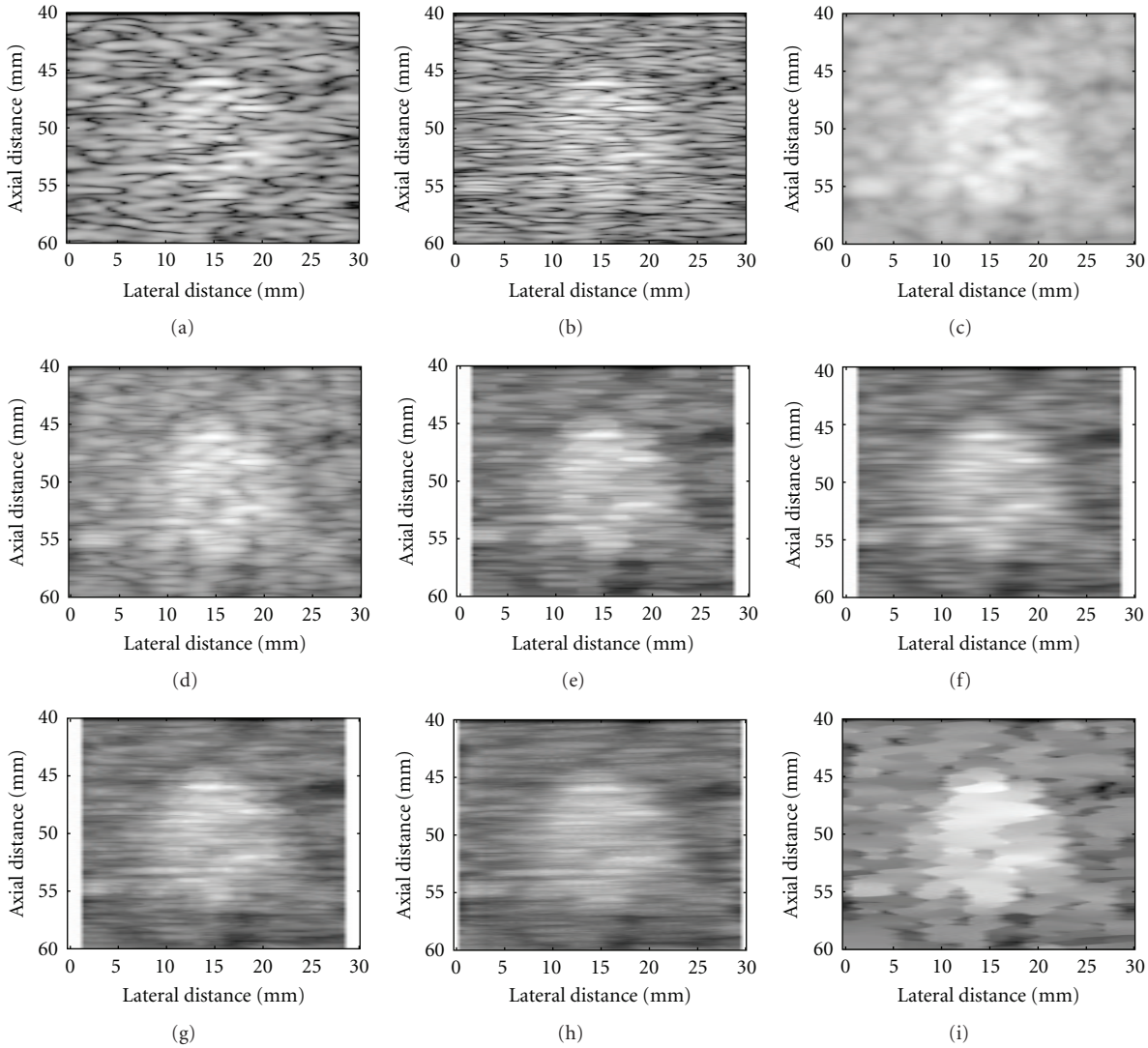

Figure 4: B-mode images of simulated results for the following: (a) CP and (b) REC reference scans, (c) REC-FC (third-width), (d) eREC-FC, (e) eREC-FC with median filtering, (f) eREC-FC with Lee filtering, (g) eREC-FC with homogeneous mask area filtering, (h) eREC-FC with geometric filtering, and (i) eREC-FC with SRAD. Image dynamic range equals −50 dB.

Table 1: CNR, HO, H_{diff}, and cSNR for the 30 cases of simulated RF data for a 15 mm target.[1]

Technique[2]	CNR	HO	H_{diff}	cSNR
CP	0.728 ± 0.172	26.609 ± 4.351	36.358 ± 8.265	—
REC	0.730 ± 0.146	26.820 ± 3.819	35.920 ± 6.809	8.182 ± 0.735
REC-FC (third-width)	2.164 ± 0.388	6.699 ± 3.258	36.500 ± 5.551	14.200 ± 0.564
eREC-FC	1.806 ± 0.301	10.307 ± 3.653	48.590 ± 7.496	10.361 ± 0.771
eREC-FC and median filtering	2.192 ± 0.405	6.366 ± 3.567	58.334 ± 8.923	9.898 ± 0.741
eREC-FC and Lee filtering	2.296 ± 0.401	5.665 ± 3.347	57.477 ± 8.563	9.934 ± 0.724
eREC-FC and HMA filtering	2.214 ± 0.352	6.335 ± 3.073	56.950 ± 8.070	9.873 ± 0.712
eREC-FC and geometric filtering	2.154 ± 0.363	6.962 ± 3.099	50.248 ± 7.148	11.027 ± 0.647
eREC-FC and SRAD filtering	2.328 ± 0.454	5.167 ± 3.170	58.866 ± 9.649	17.338 ± 0.480
P value	2.252×10^{-77}	3.900×10^{-105}	2.482×10^{-047}	1.922×10^{-142}

[1]The values in the table are described in terms of the mean plus/minus one standard deviation.
[2]CP: conventional pulsing; REC: resolution enhancement compression; FC: frequency compounding; eREC-FC: enhanced REC-FC; HMA: homogeneous mask area filtering; SRAD: speckle-reducing anisotropic diffusion.

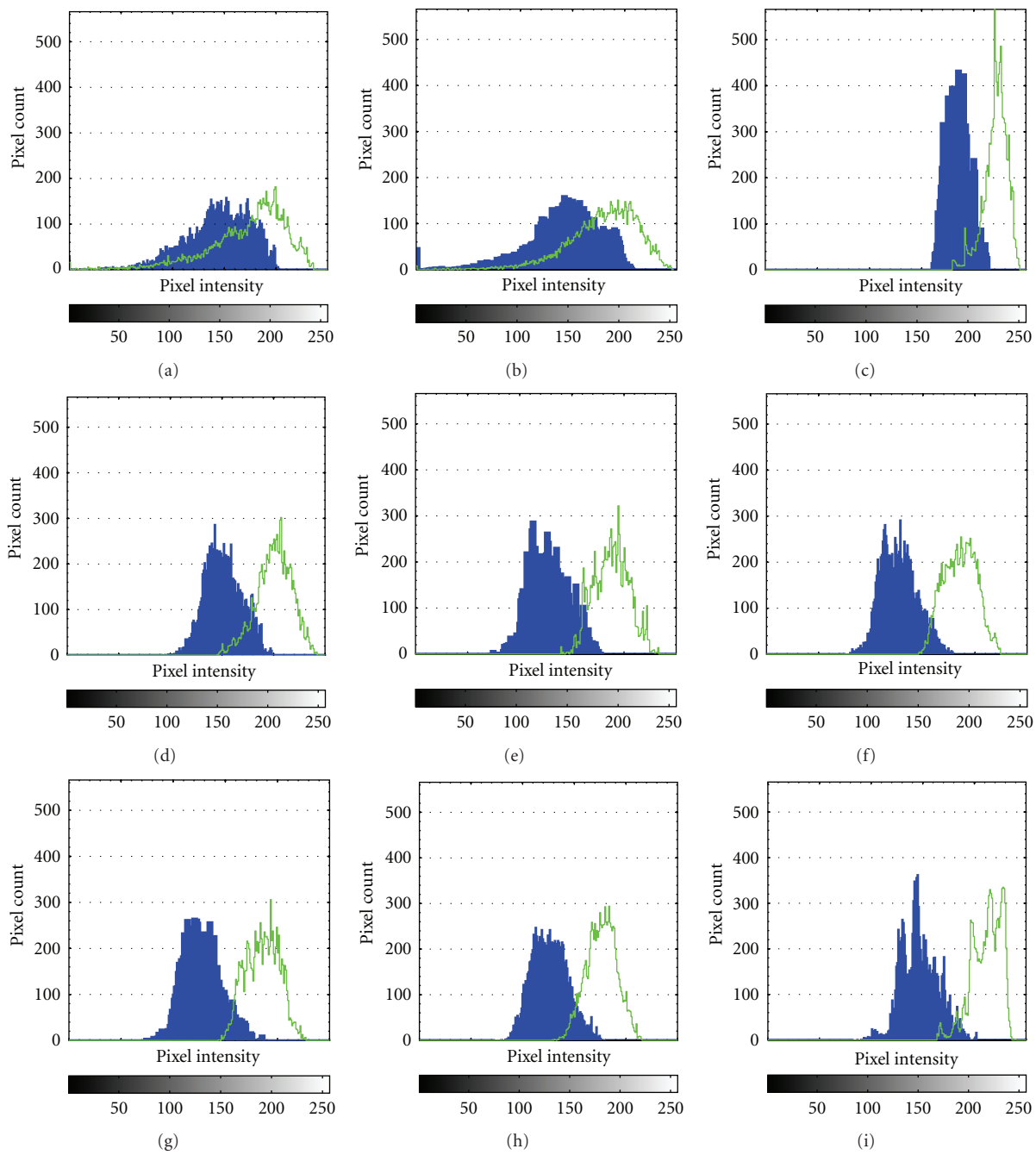

Figure 5: Histograms of simulated results for the following: (a) CP and (b) REC reference scans, (c) REC-FC (third-width), (d) eREC-FC, (e) eREC-FC with median filtering, (f) eREC-FC with Lee filtering, (g) eREC-FC with homogeneous mask area filtering, (h) eREC-FC with geometric filtering, and (i) eREC-FC with SRAD (dark: background region; light: target region).

the reference CP image. However, REC-FC (third-width) suffers from a degradation in axial resolution as the subband widths were 1/3 of the original CP bandwidth. Conversely, eREC-FC provided some reduction in speckle without the deterioration in axial resolution obtained in REC-FC (third-width). Consequently, because eREC-FC provided CNR improvements while maintaining spatial resolution along with improvements as indicated by the comparative metrics, eREC-FC was further evaluated by applying postprocessing despeckling filters.

3.1.2. Postprocessing Speckle Reduction Techniques. In this section, the images generated using the eREC-FC technique were modified by applying several postprocessing despeckling filters discussed in Section 2.4. For this study, the size of the filtering window for the median, Lee, and the homogeneous mask area techniques was 7×7. The units of the pixels are one beamwidth by one time sample. For the geometric and SRAD techniques, 5 and 3300 iterations were applied, respectively. In this study, the main focus was to quantify the improvements provided by each technique using the image

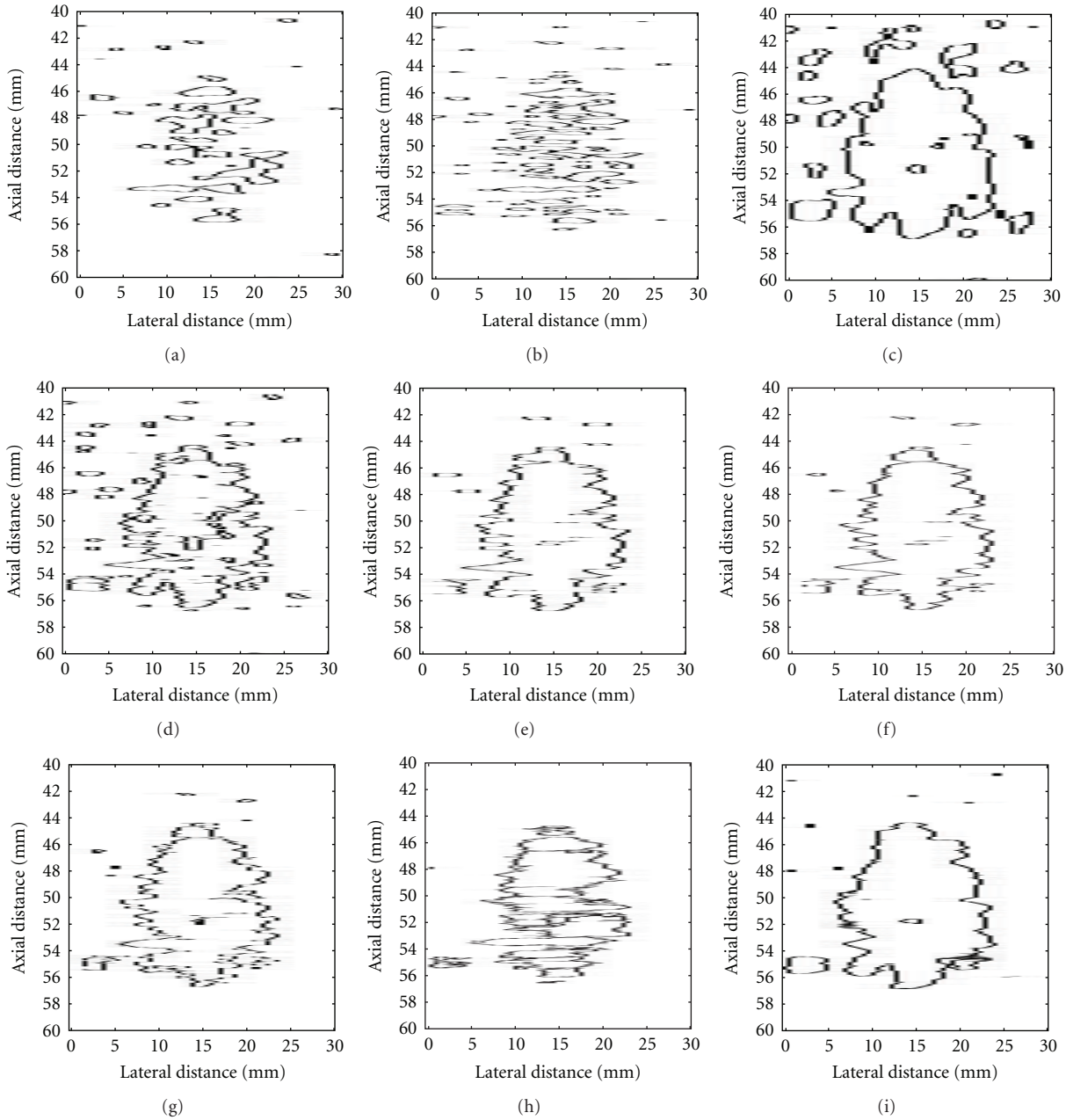

Figure 6: Edge detection images of simulated results for the following: (a) CP and (b) REC reference scans, (c) REC-FC (third-width), (d) eREC-FC, (e) eREC-FC with median filtering, (f) eREC-FC with Lee filtering, (g) eREC-FC with homogeneous mask area filtering, (h) eREC-FC with geometric filtering, and (i) eREC-FC with SRAD.

quality metrics discussed in Section 2.5. Filter computational requirements for all the filters studied herein are evaluated in [33]. Moreover, several real-time implementations of the iterative SRAD technique are evalulated in [34].

Examination of the filtered images in Figures 4(e) and 4(i) revealed that CNR improvements were obtained when using postprocessing despeckling filters compared to CP and eREC-FC. When compared to REC-FC (third-width) all cases resulted in improvements except in the case where the geometric filter was applied. However, the difference in CNR between REC-FC (third-width) and eREC-FC with geometric filtering was almost negligible (0.01). For the eREC-FC image with a median filter shown in Figure 4(e) it was observed that a smearing of the pixels with similar intensities in the lateral extent occurred. A similar smearing was observed in Figure 4(f), which shows the eREC-FC image with a Lee filter. However, the smearing is more prominent across the target and background boundary. For the eREC-FC image with homogeneous mask area filtering, shown in Figure 4(g), a noisy pattern appears around the boundary between the target and the background. In Figure 4(h), the eREC-FC image with a geometric filter is

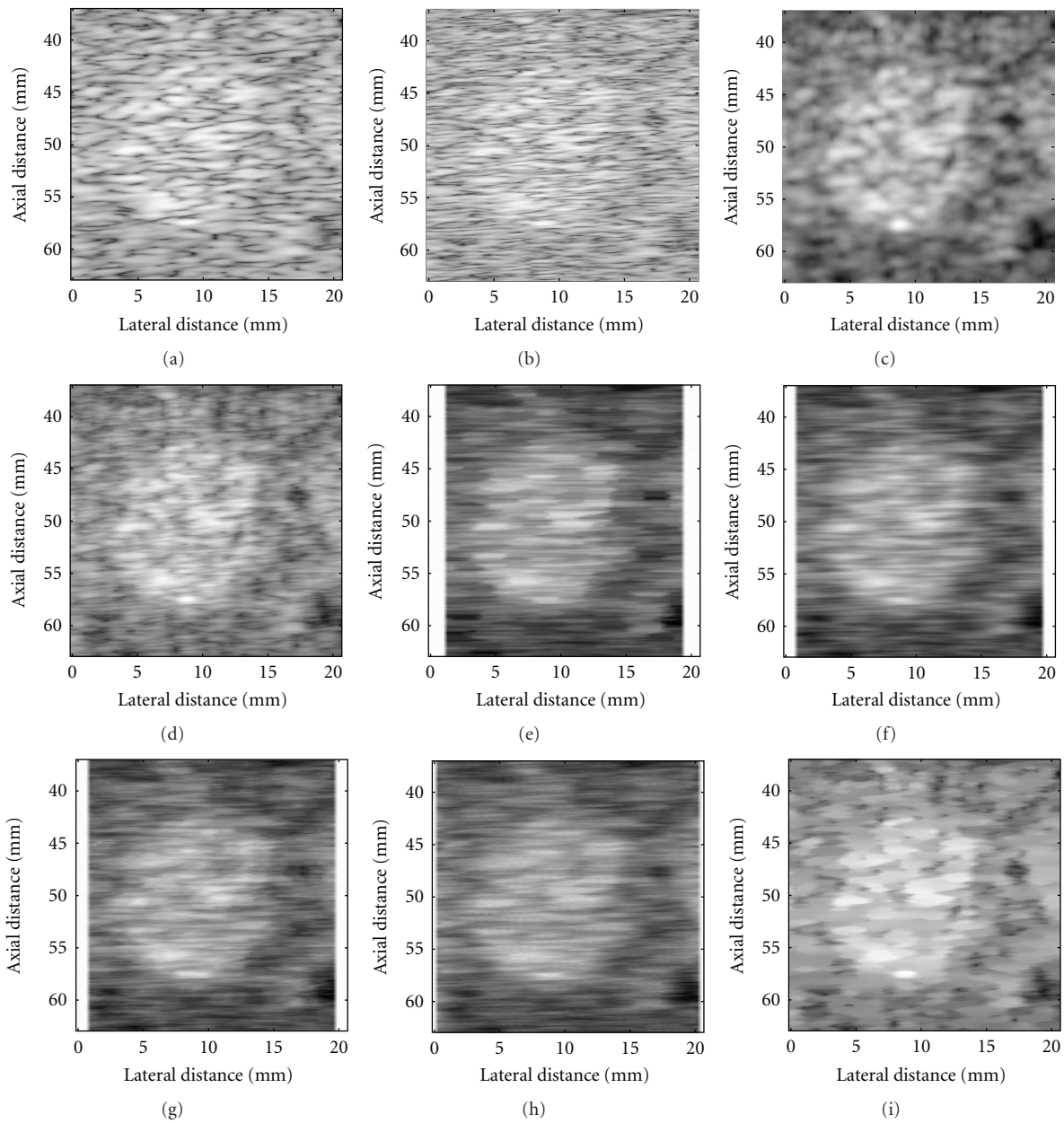

Figure 7: B-mode images of experimental measurement for the following: (a) CP and (b) REC reference scans, (c) REC-FC (third-width), (d) eREC-FC, (e) eREC-FC with median filtering, (f) eREC-FC with Lee filtering, (g) eREC-FC with homogeneous mask area filtering, (h) eREC-FC with geometric filtering, and (i) eREC-FC with SRAD. Image dynamic range equals −50 dB.

shown. For the geometric filtering case a similar appearance to Lee filter was observed. Finally, it was observed that for eREC-FC with SRAD, shown in Figure 4(i), the speckle was replaced by a blotchy appearance that was able to enhance or clearly demarcate the edges in the image. The CNR for eREC-FC in conjunction with postprocessing despeckling filters is listed in Table 1. The highest CNR was achieved when applying SRAD to the eREC-FC images. Overall, by using despeckling filters in conjunction with eREC-FC the levels of CNR estimated for REC-FC (third-width) were exceeded.

Histogram analysis was performed over the same regions used to obtain the estimates of CNR. The HO and H_{diff} between the target region and the background regions are listed in Table 1. Application of postprocessing despeckling filters to the eREC-FC images resulted in decreases in the range from 3.35 to 5.14 for HO. In addition, improvements in terms of the separation between the target and the background mean pixel intensities in the range of 1.57 to 10.27 were observed. This separation improves the overall target detectability. In Section 3.1.1 it was identified that the HO was the smallest for REC-FC (third-width) and the biggest separation between the target and background mean pixel intensities was for eREC-FC. By using despeckling filters, the HO was reduced beyond REC-FC (third-width)

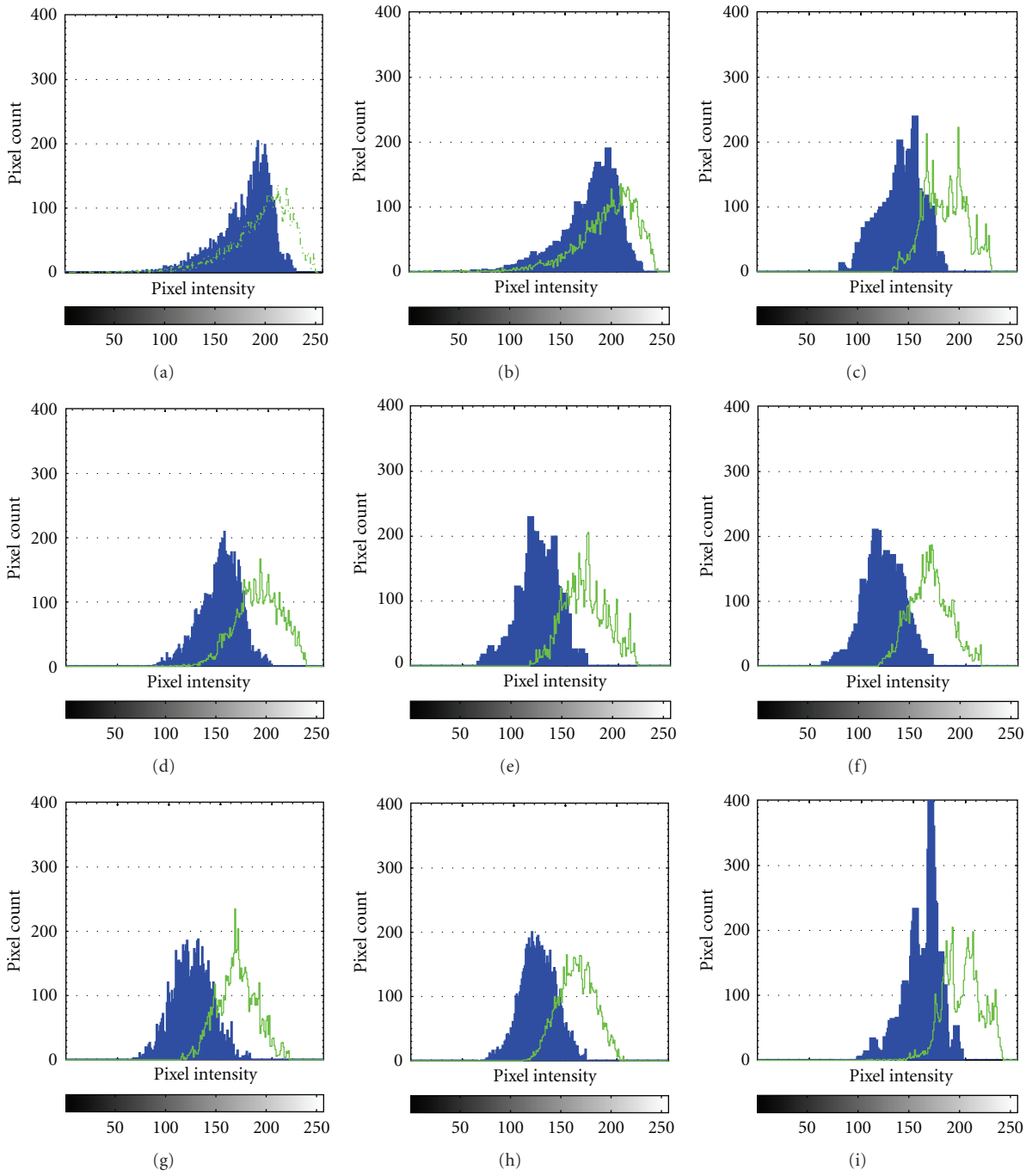

Figure 8: Histograms of experimental measurements for the following: (a) CP and (b) REC reference scans, (c) REC-FC (third-width), (d) eREC-FC, (e) eREC-FC with median filtering, (f) eREC-FC with Lee filtering, (g) eREC-FC with homogeneous mask area filtering, (h) eREC-FC with geometric filtering, and (i) eREC-FC with SRAD (dark: background region; light: target region).

levels while separating the target and background mean pixel intensities beyond the levels for eREC-FC. Consequently, improved CNR and target detectability was achieved with all despeckling filters.

Application of thresholding along with MS to the eREC-FC images that were processed with despeckling filters resulted in Figures 6(e) and 6(i). From the MS results, it was observed that the median, Lee, homogeneous mask area, and SRAD produced improved target delineation when compared to eREC-FC. eREC-FC with geometric filtering showed some horizontal striations that masked the outline of the target. Furthermore, it was noted that SRAD had a similar outline as REC-FC (third-width). Recall that with eREC-FC a tradeoff of degradation in edges versus CNR enhancement while maintaining the same axial resolution as CP was observed. Application of despeckling filters, except for the geometric filtering case, extended this tradeoff. Consequently, postprocessing despeckling filters in conjunction

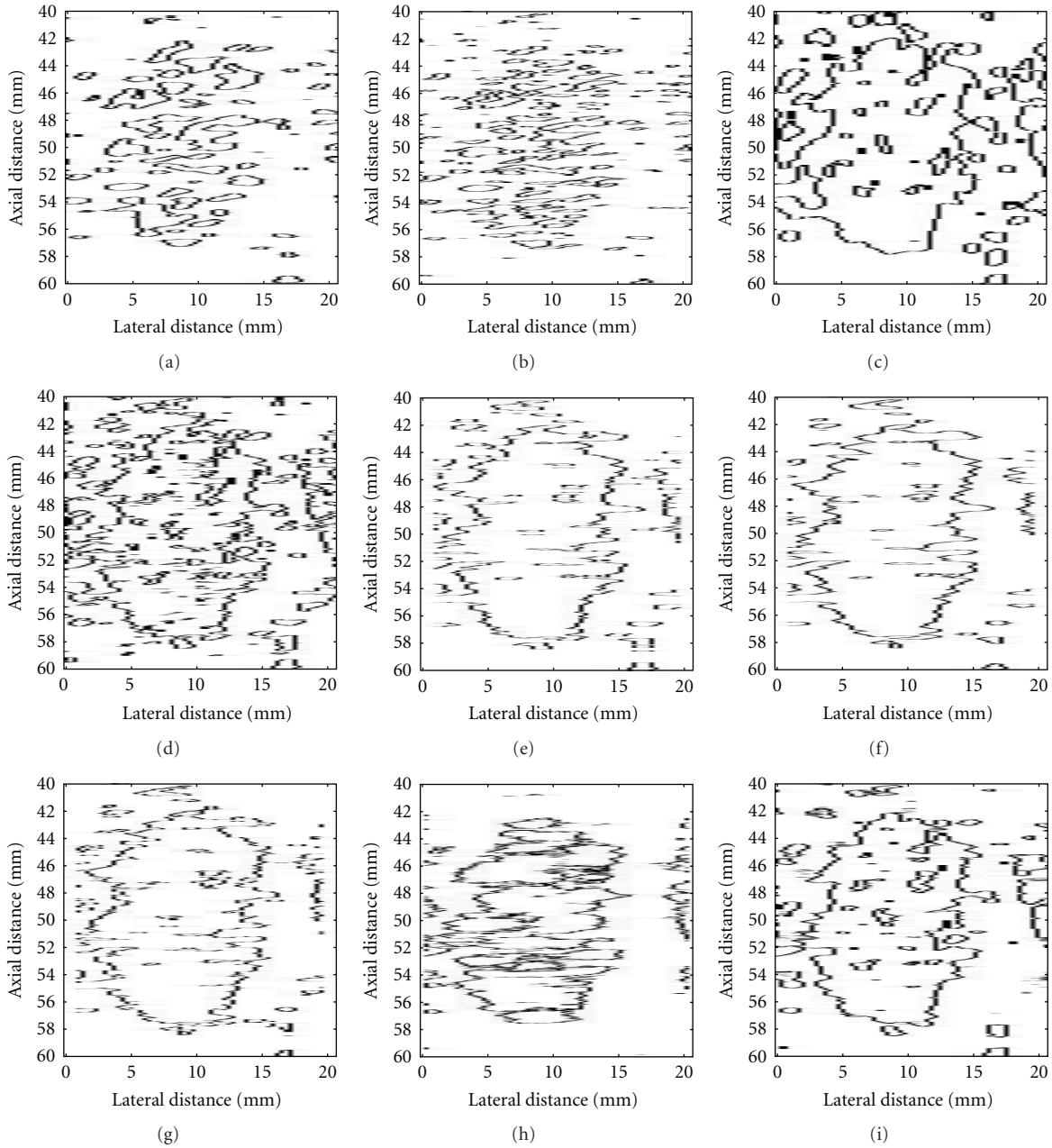

Figure 9: Edge detection images of experimental measurements for the following: (a) CP and (b) REC reference scans, (c) REC-FC (third-width), (d) eREC-FC, (e) eREC-FC with median filtering, (f) eREC-FC with Lee filtering, (g) eREC-FC with homogeneous mask area filtering, (h) eREC-FC with geometric filtering, and (i) eREC-FC with SRAD.

with eREC-FC improved the overall target outline while improving target detectability.

Evaluation of the comparative metric indicates that the performance of the various despeckling filters varies. For example, there was observed a reduction in the cSNR for eREC-FC with median, Lee, and homogeneous mask area filtering while an improvement in cSNR was achieved for the geometric and SRAD filtering. The implication is that only the geometric and SRAD filtering reduced the speckle beyond the eREC-FC image. Although reduced cSNR was observed for the median, Lee, and homogeneous mask area filtering techniques, the reductions were small. Overall, eREC-FC combined with SRAD resulted in the best cSNR when compared to the other despeckling filters.

For the simulations, the aforementioned results suggest that eREC-FC is a useful technique to enhance target detectability while improving image CNR and maintaining a spatial resolution comparable to CP. The performance of eREC-FC was further improved by applying postprocessing despeckling filters. In summary, eREC-FC combined with

Table 2: CNR, HO, H_{diff}, and cSNR for the 15 mm ATS phantom target.

Technique[1]	CNR	HO	H_{diff}	cSNR
CP	0.56	32.49	16.06	—
REC	0.62	32.49	17.61	8.23
REC-FC (third-width)	1.73	14.07	43.17	12.82
eREC-FC	1.60	17.22	37.64	8.72
eREC-FC and median filtering	2.29	12.12	45.43	8.08
eREC-FC and Lee filtering	2.57	12.09	44.89	8.14
eREC-FC and HMA filtering	2.51	13.41	43.98	8.12
eREC-FC and geometric filtering	1.83	15.17	37.67	10.07
eREC-FC and SRAD filtering	1.86	10.65	40.49	18.32

[1]CP: conventional pulsing; REC: resolution enhancement compression; FC: frequency compounding; eREC-FC: enhanced REC-FC; HMA: homogeneous mask area filtering; SRAD: speckle reducing anisotropic diffusion.

SRAD, as quantified by the metrics discussed in Section 2.5, emerged as the best technique that significantly improves the quality of ultrasonic images.

3.2. Experiments. The CP reference, REC, REC-FC, and eREC-FC B-mode images along with the postprocessing despeckling filtered B-mode images are shown in Figure 7. The CNR, HO, and cSNR for the B-mode images are listed in Table 2. Histograms of the background and target regions for all of the images in Figure 7 are shown in Figure 8 while edge detection images are shown in Figure 9.

3.2.1. eREC-FC. Similar to simulations, eREC-FC resulted in CNR, HO, and H_{diff} improvements when compared to CP without significantly degrading the axial resolution. A significant deviation from the simulations was observed when evaluating the H_{diff} for REC-FC (third-width). Both schemes, REC-FC (third width) and eREC-FC, improved target detectability by separating the mean of the target and background regions. In simulations, only deviations were observed for eREC-FC. Evaluating the histogram data listed in Table 2 suggests that the best target detectability was obtained with REC-FC (third-width) because of the combination of a smaller HO and a greater separation between the target and background mean intensity. However, the difference between eREC-FC and REC-FC (third-width) were minimal compared to the improvement both techniques obtained compared to CP. Therefore, by averaging the CNR of all the REC-FC cases used to generate the eREC-FC image also resulted in a CNR value in between the half width and third-width REC-FC cases. This would suggest that an approximation of the CNR improvements obtained with eREC-FC can be established by averaging the CNR of the images being compounded. Furthermore, the CNR improvements obtained with eREC-FC were achieved without deteriorating the axial resolution beyond CP levels, which is the main detriment of the REC-FC technique.

3.2.2. Postprocessing Speckle Reduction Techniques. In this section, the images generated from experimental measurements using the eREC-FC technique were modified by applying several postprocessing despeckling filters discussed in Section 2.4.

Examination of the filtered images in Figures 7(e)–7(i) revealed that CNR improvements were obtained when using postprocessing despeckling filters compared to CP and eREC-FC. Unlike simulations, all cases resulted in improvements when compared to REC-FC (third-width). The CNR for eREC-FC in conjunction with postprocessing despeckling filters is listed in Table 2. The highest CNR was achieved when applying the Lee filter to the eREC-FC technique. In terms of CNR, the Lee filter in conjunction with the eREC-FC technique was the second best technique as determined by the simulations. Moreover, it was determined in the simulations that eREC-FC in conjunction with SRAD provided the best visibility. However, this was not true in the experiments although the relative improvements for simulations and experiment were quite similar when using SRAD. The significant difference between the eREC-FC images for the simulation and experiment is that a larger overlap in pixel intensity between the background and the target occurs during the experiment. Consequently, the experimental measurements allow for improvements without saturating the effectiveness of the despeckling filters, which could have occurred during the simulations. Moreover, unlike simulations, all of the despeckling filters when combined with eREC-FC improved the image CNR beyond what was obtained when using REC-FC (third-width). In fact, in simulations the largest improvement over REC-FC (third-width) was approximately 7% when combining eREC-FC with SRAD, while in the experiments an improvement of 49% was achieved over REC-FC (third-width) when combining eREC-FC with the Lee filter. Overall, by using despeckling filtering in conjunction with eREC-FC significant improvements in CNR were obtained over REC-FC (third-width) along with improvements in terms of the spatial resolution because the eREC-FC image was used as the reference filtered image.

For histogram analysis and cSNR, similar trends were observed in the experimental measurements as predicted by the computer simulations. As in simulations, all postprocessing despeckling filters reduced the HO below REC-FC (third-width) levels except the geometric filtering case. However,

in the experimental measurements, H_{diff} for the geometric filtering case resulted in a smaller separation between the target and background histograms when compared to the REC-FC (third-width) case.

The aforementioned experimental results validate the simulation findings listed in Section 3.1. Overall, the results suggest that eREC-FC is a useful technique to enhance target detectability while improving image CNR and maintaining a spatial resolution comparable to CP. Also, the performance of eREC-FC was further improved by applying postprocessing despeckling filters. In summary, eREC-FC combined with Lee provided the best improvement in terms of CNR while SRAD provided the best improvement in terms of target detectability and speckle reduction. Therefore, both of these techniques significantly improved the quality of ultrasonic images beyond what is available when using CP, REC, REC-FC (third-width), and eREC-FC.

4. Conclusions

A technique that improves target visibility in ultrasound images, known as eREC-FC, was proposed. It was observed that with eREC-FC the quality of the B-mode images generated from echoes of simulated and experimental tissue-mimicking phantoms was drastically improved by increasing the CNR. The CNR values obtained with eREC-FC were observed to be within the CNR values estimated for the half-width and third-width REC-FC cases that were determined in a previous study [18]. A potential detriment to eREC-FC technique would be if the difference in contrast between the background and the target is larger than 20 dB. As shown in Figure 3 the axial resolution at -20 dB is double of that for CP. Therefore, a smearing in the image, similar to that observed in the REC-FC study, is possible under targets with large contrast difference with the background (i.e., cystic targets). A potential solution would be to evaluate the image using a sliding window by applying spatial filter that preserves brightness at the edges (i.e., keep the original pixel in the image) and smooths the original image otherwise (i.e., replace original pixel in the image by the pixel obtained with eREC-FC technique). The potential tradeoff with this solution could be that small targets, depending on the size of the sliding window, may not be improved using a spatial eREC-FC technique.

By itself, the eREC-FC provided substantial improvements in image visibility compared to CP and REC. However, the REC-FC (third-width) appeared to provide better image visibility compared to eREC-FC. Although eREC-FC improved the CNR of ultrasonic B-mode images, further improvements were obtained by applying several postprocessing despeckling filter schemes. These techniques include median filtering, Lee filtering, homogeneous mask area filtering, geometric filtering, and speckle-reducing anisotropic diffusion. Simulations and experimental measurements were used to establish the usefulness of the combination of the eREC-FC technique with despeckling filters in enhancing image CNR, improving target detectability, and reducing speckle noise. Simulations and experimental measurements suggest that eREC-FC combined with despeckling filters was a useful tool to obtain substantial improvements in terms of image visibility and to enhance the boundaries between the target and the background.

References

[1] C. B. Burckhardt, "Speckle in ultrasound B-mode scans," *IEEE Transactions on Sonics and Ultrasonics*, vol. 25, no. 1, pp. 1–6, 1978.

[2] M. S. Patterson and F. S. Foster, "The improvement and quantitative assessment of B-mode images produced by an annular array/cone hybrid," *Ultrasonic Imaging*, vol. 5, no. 3, pp. 195–213, 1983.

[3] S. K. Jespersen, J. E. Wilhjelm, and H. Sillesen, "Multi-angle compound imaging," *Ultrasonic Imaging*, vol. 20, no. 2, pp. 81–102, 1998.

[4] G. E. Trahey, S. W. Smith, and O. T. von Ramm, "Speckle pattern correlation with lateral aperture translation: experimental results and implications for spatial compounding," *Modelling, Measurement and Control A*, vol. 33, no. 3, pp. 257–264, 1986.

[5] A. R. Groves and R. N. Rohling, "Two-dimensional spatial compounding with warping," *Ultrasound in Medicine and Biology*, vol. 30, no. 7, pp. 929–942, 2004.

[6] P. Soler, C. Delso, N. Villain, E. Angelini, and I. Bloch, "Super-resolution spatial compounding techniques, with application to 3D breast ultrasound imaging," in *Medical Imaging 2006: Ultrasonic Imaging and Signal Processing*, vol. 6147 of *Proceedings of SPIE*, pp. 281–292, San Diego, Calif, USA, February 2006.

[7] J. G. Abbott and F. L. Thurstone, "Acoustic speckle: Theory and experimental analysis," *Ultrasonic Imaging*, vol. 1, no. 4, pp. 303–324, 1979.

[8] S. M. Gehlbach and F. G. Sommer, "Frequency diversity speckle processing," *Ultrasonic Imaging*, vol. 9, no. 2, pp. 92–105, 1987.

[9] P. A. Magnin, O. T. von Ramm, and F. L. Thurstone, "Frequency compounding for speckle contrast reduction in phased array images," *Ultrasonic Imaging*, vol. 4, no. 3, pp. 267–281, 1982.

[10] H. E. Melton and P. A. Magnin, "A-mode speckle reduction with compound frequencies and compound bandwidths," *Ultrasonic Imaging*, vol. 6, no. 2, pp. 159–173, 1984.

[11] V. L. Newhouse, N. M. Bilgutay, J. Saniie, and E. S. Furgason, "Flaw-to-grain echo enhancement by split-spectrum processing," *Ultrasonics*, vol. 20, no. 2, pp. 59–68, 1982.

[12] T. S. Huang, G. J. Yang, and G. Y. Tang, "A fast two-dimensional median filtering algorithm," *IEEE Transactions on Acoustics, Speech and Signal Processing*, vol. 27, no. 1, pp. 13–18, 1979.

[13] M. O. Ahmad and D. Sundararajan, "A fast algorithm for two-dimensional median filtering," *IEEE Transactions on Circuits and Systems*, vol. 34, no. 11, pp. 1364–1374, 1988.

[14] J. S. Lee, "Digital image enhancement and noise filtering by using local statistics," *IEEE Transactions on Pattern Analysis and Machine Intelligence*, vol. 2, no. 2, pp. 165–168, 1980.

[15] D. T. Kuan, A. A. Sawchuk, T. C. Strand, and P. Chavel, "Adaptive restoration of images with speckle," *IEEE Transactions on Acoustics, Speech, and Signal Processing*, vol. 35, no. 3, pp. 373–383, 1987.

[16] Y. Yu and S. T. Acton, "Speckle reducing anisotropic diffusion," *IEEE Transactions on Image Processing*, vol. 11, no. 11, pp. 1260–1270, 2002.

[17] K. Z. Abd-Elmoniem, A. B. M. Youssef, and Y. M. Kadah, "Real-time speckle reduction and coherence enhancement in ultrasound imaging via nonlinear anisotropic diffusion," *IEEE Transactions on Biomedical Engineering*, vol. 49, no. 9, pp. 997–1014, 2002.

[18] J. R. Sanchez and M. L. Oelze, "An ultrasonic imaging speckle-suppression and contrast-enhancement technique by means of frequency compounding and coded excitation," *IEEE Transactions on Ultrasonics, Ferroelectrics, and Frequency Control*, vol. 56, no. 7, pp. 1327–1339, 2009.

[19] M. L. Oelze, "System and method for ultrasonic image processing," U.S. Patent 20090209858, 2009.

[20] M. L. Oelze, "Bandwidth and resolution enhancement through pulse compression," *IEEE Transactions on Ultrasonics, Ferroelectrics, and Frequency Control*, vol. 54, no. 4, pp. 768–781, 2007.

[21] T. Misaridis and J. A. Jensen, "Use of modulated excitation signals in medical ultrasound. Part I: basic concepts and expected benefits," *IEEE Transactions on Ultrasonics, Ferroelectrics, and Frequency Control*, vol. 52, no. 2, pp. 177–191, 2005.

[22] J. K. Tsou, J. Liu, and M. F. Insana, "Modeling and phantom studies of ultrasonic wall shear rate measurements using coded pulse excitation," *IEEE Transactions on Ultrasonics, Ferroelectrics, and Frequency Control*, vol. 53, no. 4, pp. 724–734, 2006.

[23] J. R. Sanchez, M. Orescanin, and M. Oelze, "Improving image contrast using coded excitation for ultrasonic imaging," in *Proceedings of the IEEE International Conference on Electro/Information Technology (EIT '10)*, pp. 1–6, Normal, Ill, USA, May 2010.

[24] C. P. Loizou, C. S. Pattichis, C. I. Christodoulou, R. S. H. Istepanian, M. Pantziaris, and A. Nicolaides, "Comparative evaluation of despeckle filtering in ultrasound imaging of the carotid artery," *IEEE Transactions on Ultrasonics, Ferroelectrics, and Frequency Control*, vol. 52, no. 10, pp. 1653–1669, 2005.

[25] Y. Yu and S. T. Acton, "Speckle reducing anisotropic diffusion," *IEEE Transactions on Image Processing*, vol. 11, no. 11, pp. 1260–1270, 2002.

[26] M. Nagao and T. Matsuyama, "Edge preserving smoothing," *Computer Graphics and Image Processing*, vol. 9, no. 4, pp. 394–407, 1979.

[27] L. J. Busse, T. R. Crimmins, and J. R. Fienup, "A model based approach to improve the performance of the geometric filtering speckle reduction algorithm," in *Proceedings of the IEEE Ultrasonics Symposium. Part 1*, pp. 1353–1356, November 1995.

[28] P. Perona and J. Malik, "Scale-space and edge detection using anisotropic diffusion," *IEEE Transactions on Pattern Analysis and Machine Intelligence*, vol. 12, no. 7, pp. 629–639, 1990.

[29] P. M. Shankar, V. A. Dumane, C. W. Piccoli, J. M. Reid, F. Forsberg, and B. B. Goldberg, "Computer-aided classification of breast masses in ultrasonic B-scans using a multiparameter approach," *IEEE Transactions on Ultrasonics, Ferroelectrics, and Frequency Control*, vol. 50, no. 8, pp. 1002–1009, 2003.

[30] D. J. Sakrison, "On the role of observer and a distortion measure in image transmission," *IEEE Transactions on Communications*, vol. 25, no. 11, pp. 1251–1267, 1977.

[31] J. A. Jensen, "A model for the propagation and scattering of ultrasound in tissue," *Journal of the Acoustical Society of America*, vol. 89, no. 1, pp. 182–190, 1991.

[32] K. Raum and W. D. O'Brienjr Jr., "Pulse-echo field distribution measurement technique for high-frequency ultrasound sources," *IEEE Transactions on Ultrasonics, Ferroelectrics, and Frequency Control*, vol. 44, no. 4, pp. 810–815, 1997.

[33] S. Finn, M. Glavin, and E. Jones, "Echocardiographic speckle reduction comparison," *IEEE Transactions on Ultrasonics, Ferroelectrics, and Frequency Control*, vol. 58, no. 1, pp. 82–101, 2011.

[34] W. Wu, S. T. Acton, and J. Lach, "Real-time processing of ultrasound images with speckle reducing anisotropic diffusion," in *Proceedings of the 40th Asilomar Conference on Signals, Systems, and Computers (ACSSC '06)*, pp. 1458–1464, November 2006.

Hindawi Publishing Corporation
Advances in Acoustics and Vibration
Volume 2012, Article ID 231317, 16 pages
doi:10.1155/2012/231317

Research Article

Frequency Domain Compressive Sampling for Ultrasound Imaging

Céline Quinsac, Adrian Basarab, and Denis Kouamé

University of Toulouse, IRIT UMR 5505 CNRS, 31062 Toulouse Cedex 9, France

Correspondence should be addressed to Adrian Basarab, basarab@irit.fr

Received 9 December 2011; Accepted 5 April 2012

Academic Editor: Erdal Oruklu

Compressed sensing or compressive sampling is a recent theory that originated in the applied mathematics field. It suggests a robust way to sample signals or images below the classic Shannon-Nyquist theorem limit. This technique has led to many applications, and has especially been successfully used in diverse medical imaging modalities such as magnetic resonance imaging, computed tomography, or photoacoustics. This paper first revisits the compressive sampling theory and then proposes several strategies to perform compressive sampling in the context of ultrasound imaging. Finally, we show encouraging results in 2D and 3D, on high- and low-frequency ultrasound images.

1. Introduction

Ultrasound (US) imaging acquisition, like all other imaging modalities, relies on Shannon's theorem. This theorem states that, in order to reconstruct perfectly a signal, its sampling frequency must be at least twice the highest-frequency component present in the signal. Often, US devices use a sampling rate that is at least four times the central frequency (wideband), to guarantee Shannon's theorem. However, the volume of data obtained is large, especially in 3D imaging, and can impair imaging in real-time or data transfer [1–4].

Compressed sensing (CS) or compressive sampling is a novel theory aiming to reduce the volume of data acquired, below the one dictated by Shannon's theorem. First introduced by Candès et al. and Donoho in 2006 [5, 6], CS guarantees the reconstruction of a signal from far fewer samples than usually necessary. CS has led to many applications, including medical imaging (particularly in magnetic resonance imaging (MRI) and tomography), sampling the spatial or frequency domains [7–9]. In ultrasound imaging, a few groups proposed very recently preliminary works for adapting the compressive sampling framework to ultrasound imaging [10–15], to ultrasound Doppler [16, 17], or to photoacoustic tomography [18].

The success of this reconstruction lies on two principles inherent to CS: sparsity and incoherence.

Sparsity reflects the ability of a signal to be compressed. A signal that has a sparse representation in a given basis will have most of its coefficients (or entries) null or very close to zero in this representation. Hence, by suppressing those negligible coefficients, the signal can be compressed, that is, reconstructed from relatively few samples [19]. Of course, during data acquisition, there is no knowledge about which coefficients are significant and which are not. CS overcomes this issue using a sampling basis incoherent with the sparsity basis.

Incoherence in CS expresses the idea that signals that are sparse in a given basis cannot be sampled in this basis but in another where the signal is dense. This property guarantees that the samples acquired contain the same amount of information. If the sparse basis was sampled, there would be a risk of acquiring negligible coefficients, not participating to the signal reconstruction.

The challenge of CS is to design a sampling protocol that will capture the information contained on the relatively few coefficients of the sparse basis. This sampling protocol will also suit any type of images within a specific application, here US imaging, without prior knowledge on the signal or image to sample.

By means of optimization methods, the original signal can then be recovered from those few measurements and

the reconstruction quality will be similar to the one obtained respecting Shannon's theorem.

In summary, CS is a simple acquisition method where only a few samples of a signal are blindly measured. The full signal is later retrieved using reconstruction methods.

The purpose of this paper is twofold: first, make CS familiar to US imaging, and second, show the mechanisms involved in a successful CS reconstruction. The structure of the paper includes a reminder of the theory of sampling. Then, an overview of the CS theory and its components (essentially sparsity, incoherence, and optimization) will be given in detail and illustrated in a US context. Then, an application to US imaging will be proposed and results of US image reconstruction from usually 25%, 33%, and 50% of samples acquired will be shown. Finally, perspectives for CS in US will be drawn and future work will be described.

2. Sampling a Signal

The general framework of sampling can be summarized by measuring linear combinations of an analog signal $f(t)$, possibly considered as projections on a given basis:

$$y_k = \langle \varphi_k, f \rangle, \quad \text{for } k = 1, \ldots, m, \tag{1}$$

where $\langle \cdot, \cdot \rangle$ denotes an inner product, y_k are the measurements, φ_k are sampling vectors, and m is the number of measurements. The most common sampling protocol consists of vectors φ_k of Diracs at equal time laps (ideal sampling). The measurements obtained represent then a simple discretization of $f(t)$.

However, if the sampling vectors φ_k are complex exponentials, then the measurements y_k are Fourier coefficients. This sampling protocol is used in MRI, for example.

In CS, the number of measurements m is far below the criteria established by Shannon's theorem for a given signal duration. If f is a digital signal of size n (respecting Shannon's theorem), then $m \ll n$. This situation can rise with slow imaging devices, for example, or when the number of sensors is limited. When it is possible to sample signals respecting Shannon's theorem, like in US imaging, it might be more advantageous to reduce the volume of data or the acquisition time.

However, when the number of measurements is smaller than the signal size, then we are facing an ill-posed inverse problem. If Φ is a matrix of size $m \times n$, concatenating the sampling vectors φ_k, then $y = \Phi f$. When we want to recover the signal $\hat{f}$ corresponding to the measurements y, then there is an infinity of solutions possible.

CS shows that it is possible to recover $\hat{f}$, provided that it has a *sparse* representation in a given basis and that the measurements are *incoherent* with that basis [20]. The following two sections explain those two concepts.

3. The Concept of Sparsity

Sparsity is the idea that signals may have a concise representation in a given basis. For example, a signal composed of three sinusoids will be sparse in the Fourier domain as its representation in this domain is very concise: namely 12 coefficients (6 symmetrical magnitudes and phases). Hence a dense signal in the time domain can be coded with only a few samples.

Other examples include photographic images. On the image, almost all the pixels have a nonzero value. However, in the wavelet domain, these images are sparse; that is, they contain a majority of null or very small coefficients. By discarding those negligible samples, an approximation of the original image can be obtained, with minimal loss of information. Usually, this loss of information is not noticeable: that is, the concept of JPEG2000 compression [19].

Mathematically, it translates as follows:

$$f(t) = \sum_{i=1}^{n} x_i \psi_i(t), \tag{2}$$

where $f(t)$ is the original signal, x_i are the coefficients of the signal in the sparse basis, and $\psi_i(t)$ is an orthonormal basis (Fourier or wavelets e.g.). The S largest coefficients x_i are noted x_S, and the corresponding signal $f_S(t)$. If $f(t)$ is sparse in the basis Ψ composed of the vectors ψ_i, then $f = \Psi x$ and the error $\|f - f_S\|_2$ is small.

Figure 1 illustrates the sparsity of radio-frequency (RF) US signals. Because the sparse representation of the RF US signal (here, its Fourier transform) concentrates the information on a few coefficients, it is possible to reconstruct almost perfectly the signal from only 30% of its largest Fourier coefficients (keeping only 30% of the largest x_i in (2)).

This concept of concentrated information is also visible when plotting the Fourier coefficients in order of magnitude (Figure 2). If they decay rapidly, then the compressed signal $f_S(t)$ including the S largest coefficients will be close to the original signal $f(t)$.

Sparsity therefore leads to the compressive nature of a signal: if a signal has a sparse representation, then the information coding that signal can be compressed on a few coefficients. A reconstruction from those few coefficients can be obtained with minimal loss compared to the original signal. Note however that CS and compression are different in that when sampling a signal, it is impossible to directly acquire the significant coefficients as their positions are not known *a priori*. CS overcomes this issue via an incoherent sampling.

4. Incoherent Sampling

The term incoherent sampling conveys the idea that the sampling protocol φ_k in (1) has to be as little correlated as possible with the sparse representation ψ_i in (2). This requirement prevents from the risk of sampling insignificant bits of information (the close-to-zero coefficients described in Section 3). Instead, the idea of an incoherent sampling is to introduce noise-like interferences to the signal to recover.

The mathematical definition of incoherence is [21, 22]:

$$\mu(\Phi, \Psi) = \sqrt{n} \max_{1 \le k, j \le n} \left| \left\langle \phi_k, \psi_j \right\rangle \right|, \tag{3}$$

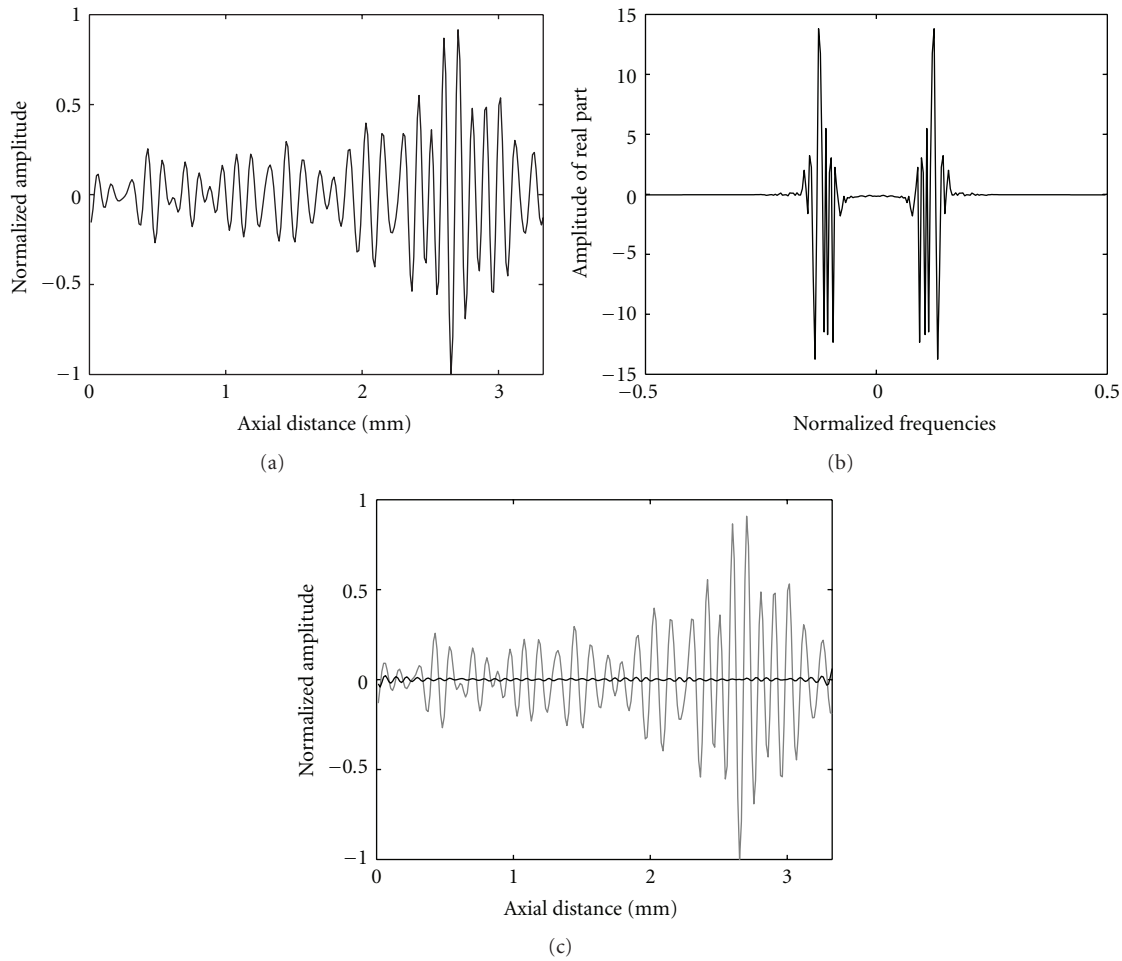

Figure 1: (a) A full US RF signal and (b) its sparse representation via Fourier transform. Most of the coefficients are equal or close to zero. (c) Compressed US RF signal (gray), corresponding to 30% of the largest Fourier coefficients, the rest of them being set to zero. The difference between the full and compressed US RF signal (black) is minimal.

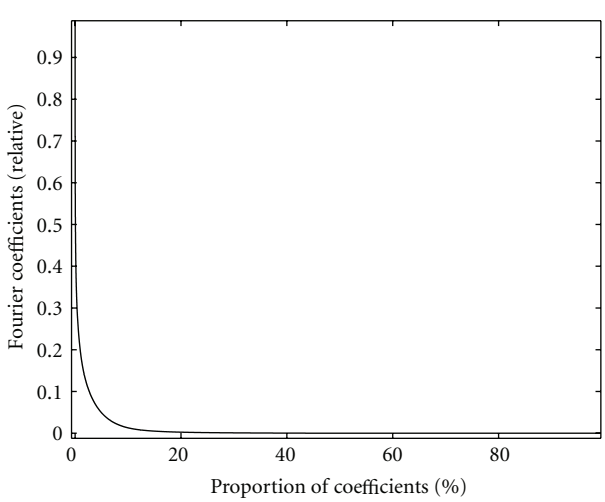

Figure 2: Ordered relative values of a thyroid *in vivo* US image Fourier magnitude coefficients (see Figure 13). They decay very rapidly, indicating a sparse representation of the image by Fourier transform.

where Φ is the sampling basis and Ψ is the sparsifying basis. According to (3), if the two bases are strongly correlated, then μ will be close to $\sqrt{n}$, and if they are not correlated at all, then it will be close to 1. CS requires a low coherence between the bases. In other words, incoherence is guaranteed provided that the two bases are not correlated.

Pairs of bases with minimum coherence include, for example, a basis of Diracs associated with a Fourier basis (a spatial Dirac contains information about all the frequencies). In addition, if the sampling basis is completely random, then it will be maximally incoherent with any sparsifying fixed basis (wavelets, curvelets, etc.) [21].

Figure 3 shows an example of coherent and incoherent samplings of a US RF signal. When the sampling is incoherent with the sparsifying basis (Figures 3(c) and 3(d)), then the measurements (namely, in practical situations) in that basis are dense (by opposition to sparse). The original sparse signal is polluted by noise-like interferences and can be reconstructed by optimization. However, when the sampling basis and the sparsifying basis are coherent (Figures 3(e) and 3(f)), the measurements in the sparsifying basis are

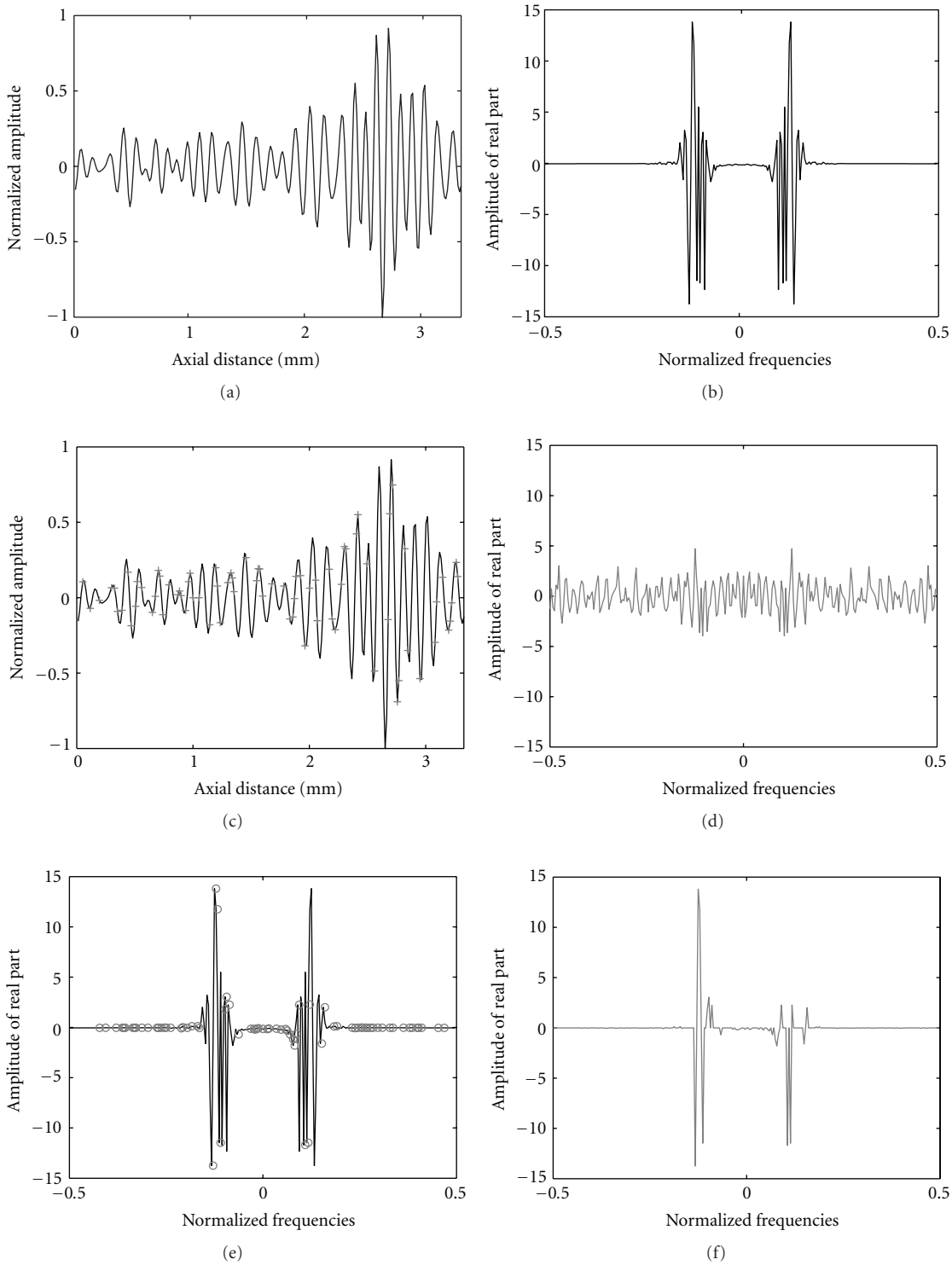

Figure 3: (a) A full US RF signal and (b) its sparse representation via Fourier transform. (c) Sampling 30% of the US RF signal using a basis of random Diracs (crosses), maximally incoherent with the Fourier basis, leads to (d) a dense signal in the sparsifying basis (Fourier transform). However, (e) sampling 30% of the US RF signal using a basis of random sinusoids (circles), coherent with the sparsifying basis, is equivalent to sample random Fourier coefficients of the signal. (e) The resulting measurements in the sparsifying basis (Fourier transform) are sparse as well.

themselves sparse. There is significant information (large Fourier coefficients) missing and CS will not be able to recover the original signal.

From those incoherent measurements and knowing the sparsifying basis, CS theory states that it is possible to recover the original signal using an optimization routine.

5. Signal Reconstruction through Optimization

Knowing that the signal to recover $\hat{f}$ has a sparse representation x in a given basis Ψ, it is possible to reconstruct it from the incomplete incoherent measurements y obtained using the sampling basis Φ. This reconstruction is performed via a convex optimization program:

$$\min||\hat{x}||_1 \quad \text{subject to } y = \Phi f = \Phi\Psi\hat{x}, \tag{4}$$

where $\hat{x}$ is the reconstructed sparse signal and $\|\cdots\|_1$ denotes the ℓ_1 norm.

This optimization searches amongst all the signals that verify the measurements y, the one with the smallest ℓ_1 norm, that is, the sparsest. The choice of the ℓ_1 norm (sum of magnitudes) over the ℓ_0 norm (size of support) is mainly practical: while solving of the ℓ_0 norm minimization is computationally infeasible, the ℓ_1 norm minimization can easily be recast as a linear program. The ℓ_2 norm (sum of magnitudes squared) is unsuited to CS because the minimization would not recover the sparsest signal [23].

In other words, the optimization routine (4) removes the interferences caused by the incoherent undersampling from the sparse representation of the measurements (as in Figure 3(d)). Figure 4 illustrates the process of ℓ_1 norm minimization applied to the Fourier transform of an RF signal: the significant coefficients tend to be amplified while the others, corresponding to the interferences, are attenuated.

In this example, at the last iteration, the recovered signal is exactly equal to the original signal. Generally speaking, recovering the signal is true with overwhelming probability if the number of measurements m follows:

$$m \geq C \cdot \mu^2(\Phi, \Psi) \cdot S \cdot \log n, \tag{5}$$

where C is a positive constant, μ is the coherence as defined in (3), S is the degree of sparsity, and n is the signal size. From (5) it follows that the number of measurements depends on the sparsity S of the signal (the sparsest, the best) in a given basis and the coherence μ of the sampling protocol with that basis.

In practice, many researchers observed that accurate reconstructions can be achieved if the number of measurements m is roughly 2 to 5 times the sparsity S of the signal [24–26]. The work herein matches this statement. For an offline reconstruction, plots in Figure 2 could be used to determine the degree of sparsity and consequently the minimum number of measurements required. For online reconstruction, priors on the US imaging device bandwidth could be exploited. Classic US scanners bandwidth ranges from 50% to 100% or more (depending on the scanner) and is practically estimated at 3 or 6 dB attenuations. An example of an experimental PSF together with its Fourier transform showing the bandwidth at 6 dB is given in Figure 5. Thus, we can observe that, taking into account the device bandwidth, the k-space may be considered even sparser than the impression given by Figure 2. The sparsity could then be set as the number of significant coefficients in the practical bandwidth, or two times this number.

The optimization routine utilizes no prior knowledge about the positions or amplitudes of the sparse coefficients or about the signal to recover.

In practical situations, the measurements y are often corrupted by noise η, originating from the instrumentation. Therefore, the term guaranteeing data consistency in (4) has to be relaxed, so that $y = Ax+\eta$. In addition, the signal might not have an exact sparse representation but an approximate sparse representation where very small but not exactly nil coefficients will be neglected. Again, this approximation will introduce some noise.

In those cases, the CS method will still allow a reconstruction of the signal, provided that the CS matrix A ($A = \Phi\Psi$) respects the Restricted Isometry Property (RIP) [21, 27]:

$$(1 - \delta_S)\|x\|_2^2 \leq \|Ax\|_2^2 \leq (1 + \delta_S)\|x\|_2^2, \tag{6}$$

where S are integers and δ_S is the isometry constant. A obeys (6) when the smallest δ_S that verifies (6) for all S-sparse signals x is not too close to 1. In other words, if A obeys the RIP, then the Euclidean lengths, or norms, will be preserved in A: this is the isometry. This property basically ensures that a sparse signal x will not fall in a null space in A, where it would be impossible to recover.

If (6) is true, then the minimization will allow an accurate reconstruction of the signal. More precisely, the reconstruction of an approximately sparse signal will approach the corresponding compressed signal.

Interestingly, random matrices obey the RIP with overwhelming probability if $m \geq C \cdot S \cdot \log(n/S)$ with C being a constant.

The minimization in the case of noisy data is as follows:

$$\min||\hat{x}||_1 \quad \text{subject to } \left\|A\hat{x}_y\right\|_2 \leq \varepsilon, \tag{7}$$

where the fidelity of the measurement constraint is relaxed to take into account the level of noise ε. This is again a convex minimization, computationally feasible.

6. Sampling Protocols in Ultrasound Imaging

The sampling protocols in US imaging are designed to fulfill both the requirements of CS and of the US instrumentation. The CS theory has been described in the previous section and, from this perspective, the sampling basis mainly has to be incoherent with the sparsifying basis. The US imaging devices have physical constraints that limit the sampling strategies one can adopt for CS.

The data acquisition in US imaging is performed in the image space (spatial domain), unlike MRI, for example

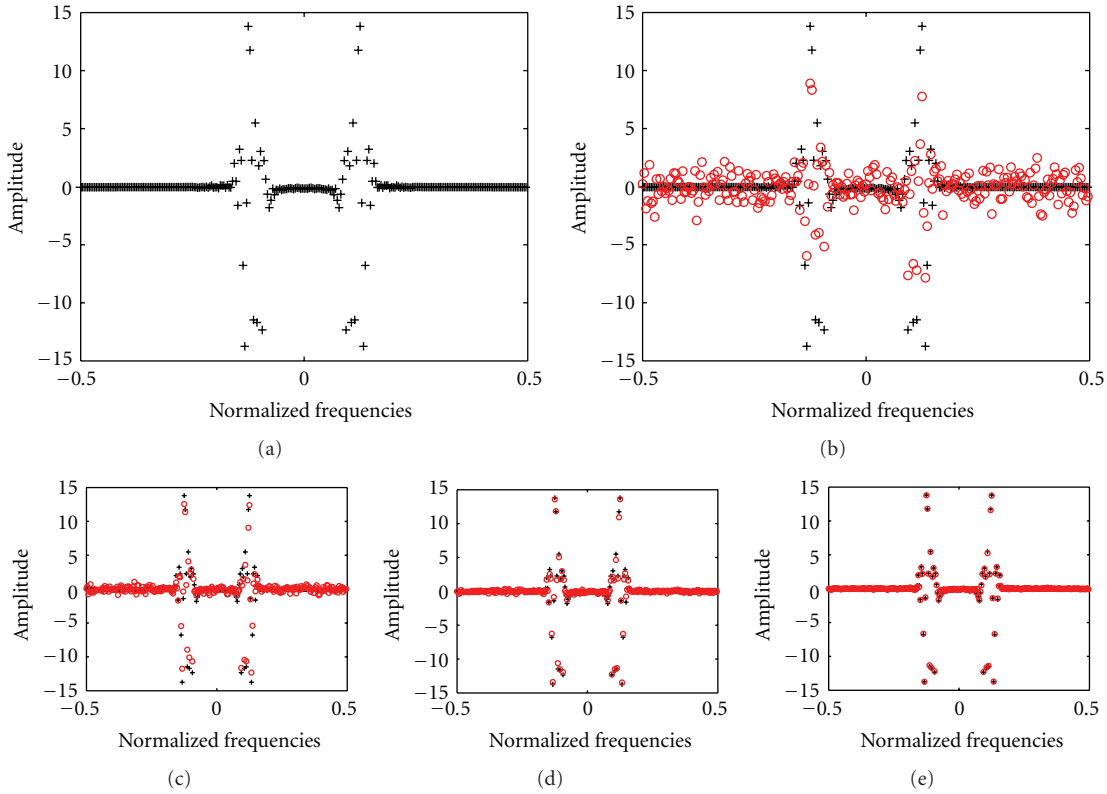

Figure 4: (a) Fourier transform (real part) of an RF signal (256 points) and (b) the initial guess (circles) of the ℓ_1 norm minimization for 128 random measurements. (c) Evolution of the reconstructed sparse signal using a primal-dual algorithm for linear programming at iterations 3, (d) 5 and (e) 11. After 11 iterations the reconstructed signal corresponds exactly to the original.

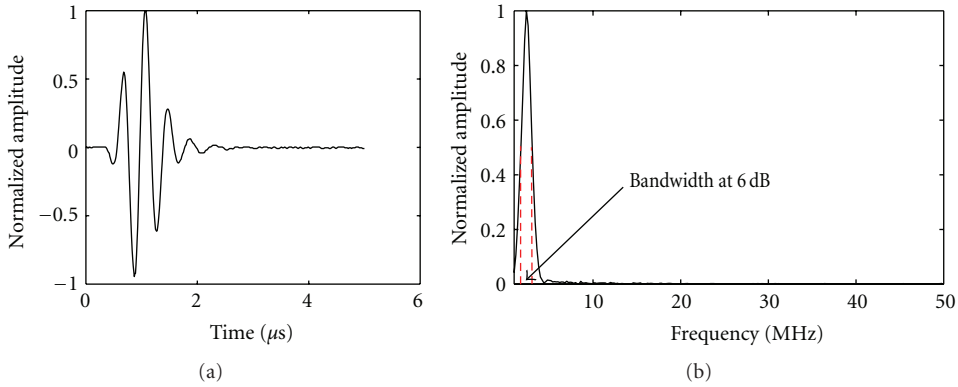

Figure 5: (a) Experimental PSF. (b) Fourier transform of the PSF (only positive frequencies are plotted), showing the bandwidth at 6 dB and reflecting the sparsity of the ultrasound k-space.

[7, 24]. There are several possible sampling protocols adapted to US imaging and incoherent with the sparsifying basis. They all consist in taking samples of that image at more or less random locations. This is equivalent to taking samples at specific times on the RF signals or taking RF lines at specific locations.

In this paper, eight different sampling protocols are proposed: three 2D masks and five 3D masks. In two dimensions, the CS uniformly random mask, denoted Φ_1 and shown in Figure 6(a), will be studied on different types of RF US images. This sampling protocol is maximally incoherent with the Fourier transform (considered as the sparse decomposition basis in this paper) and therefore should give the best results.

However, switching rapidly from one position to the next in this kind of sampling pattern might be difficult from the instrumentation point of view. Consequently, two other sampling masks denoted by Φ_2 and Φ_3 where studied

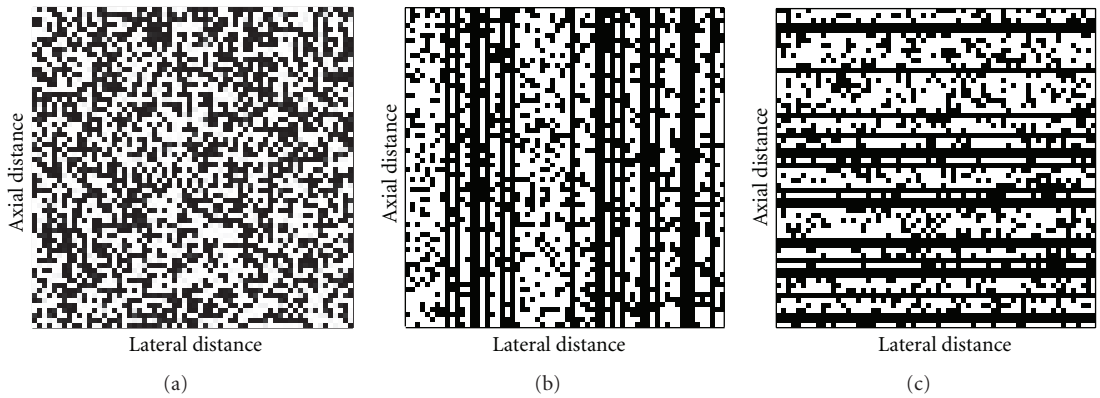

Figure 6: Sampling masks Φ_1 (a), Φ_2 (b), and Φ_3 (c) adapted to a spatial sampling of the US images. The white pixels correspond to the samples used for CS. The proportion of samples here is 50% of the original image.

were whole lines or columns of the images are not sampled at all (Figures 6(b) and 6(c), resp.). The sampled lines or columns are chosen in a uniformly random fashion. On the remaining lines or columns, random points are sampled. The total number of points sampled and chosen was the same as for the sampling mask Φ_1 to be able to compare the quality of the CS reconstructions. The sampling masks Φ_2 and Φ_3 are slightly less incoherent than Φ_1 (due to a certain coherence in the direction that is not sampled at all), so the results are expected to be worse than for Φ_1. However, these two strategies could translate as a gain of time from the instrumentation point of view as some lines (resp., columns) of the image will not be acquired at all.

For 3D US datasets, five sampling strategies are proposed. The first, similar to Φ_1, and maximizing incoherence is a uniformly random mask in three directions, denoted Θ_1 (Figure 7(a)).

The other four, Θ_2 to Θ_5, are inspired by Φ_2 and Φ_3, that is, sampling only certain RF lines. Whereas Θ_2 and Θ_3 consist in sampling different RF lines or columns on each slice of the azimuthal direction (see Figures 7(b) and 7(c)), with Θ_4 and Θ_5, the set of unsampled RF lines or lateral profiles is always the same in each slice (see Figures 7(d) and 7(e)). Consequently, with Θ_4 (resp., Θ_5), some whole axial-azimuthal (resp., lateral-azimuthal) plans of the volume are not sampled.

7. Reconstructions of Ultrasound Images and Volumes

In US imaging, the acquisition consists in taking samples of the image (or of the RF signals). This sampling protocol is similar to a basis of Diracs (sampling mask). To guarantee the success of the CS reconstruction, a basis incoherent with Diracs and where the US images are sparse is needed. The basis chosen in this paper is the Fourier basis as it is maximally incoherent with Diracs and because the US image k-space is sufficiently sparse. The function to minimize is

$$\arg\min_{M} ||AM - y||_2 + \lambda |M|_1, \tag{8}$$

where M is the k-space of the US RF image m ($M = \mathcal{F}m$), and A is the sampling scheme ($A = \Phi\mathcal{F}^{-1}$ here, where Φ corresponds to Φ_k ($k = 1,\ldots,3$), the RF random sample locations in 2D, or to Θ_k ($k = 1,\ldots,5$) in 3D). $\mathcal{F}^{-1}$ stands for the inverse Fourier transform, y are the RF US image measurements and λ is a coefficient weighting for sparsity.

Other bases of sparsity such as the wavelet transform of the US image k-space have been investigated in previous work and give similar results to those presented here [12].

The first term of (8) represents the fidelity of the measurements and the second term guarantees the signal sparsity in the Fourier basis. The balance between those two terms is given by λ. The choice of λ is crucial to a good reconstruction as it corresponds to a threshold for the recovery of significant coefficients in the sparse basis.

In this paper, the optimal λ chosen was the one giving the minimum errors of reconstruction. However, finding the optimal λ by trials and errors is obviously not possible during acquisition where no comparison with the real signal can be performed.

One solution to minimize the fluctuations in the CS reconstructions due to a poor choice of lambda is to add an elastic-net regularization, that is, ℓ_2 minimization term on the sparse coefficients [28]. The resulting reconstruction errors around the optimal λ were however quite large compared to the minimum errors found with only the ℓ_1 minimization.

Another method, based on an adapting λ and called reweighted ℓ_1 minimization, has been developed [29] to address that issue. It consists in performing (8) with an initial λ (equal to one e.g.). Then, (8) is reiterated using a new λ, which value is calculated from the results of the first iteration of (8). Thus, the optimization performed is given as follows:

$$\arg\min_{M} ||AM - y||_2 + \sum_i \left(w_i^{(\ell)} |M_i|_1\right). \tag{9}$$

Namely, the weighted λ at each iteration is $w_i^{(\ell+1)} = 1/(|M_i^{(\ell)}| + \varepsilon)$ where ℓ is the iteration number, $M_i^{(\ell)}$ are the sparse coefficients estimated after ℓ iterations, and ε is a coefficient ensuring stability (that should be slightly

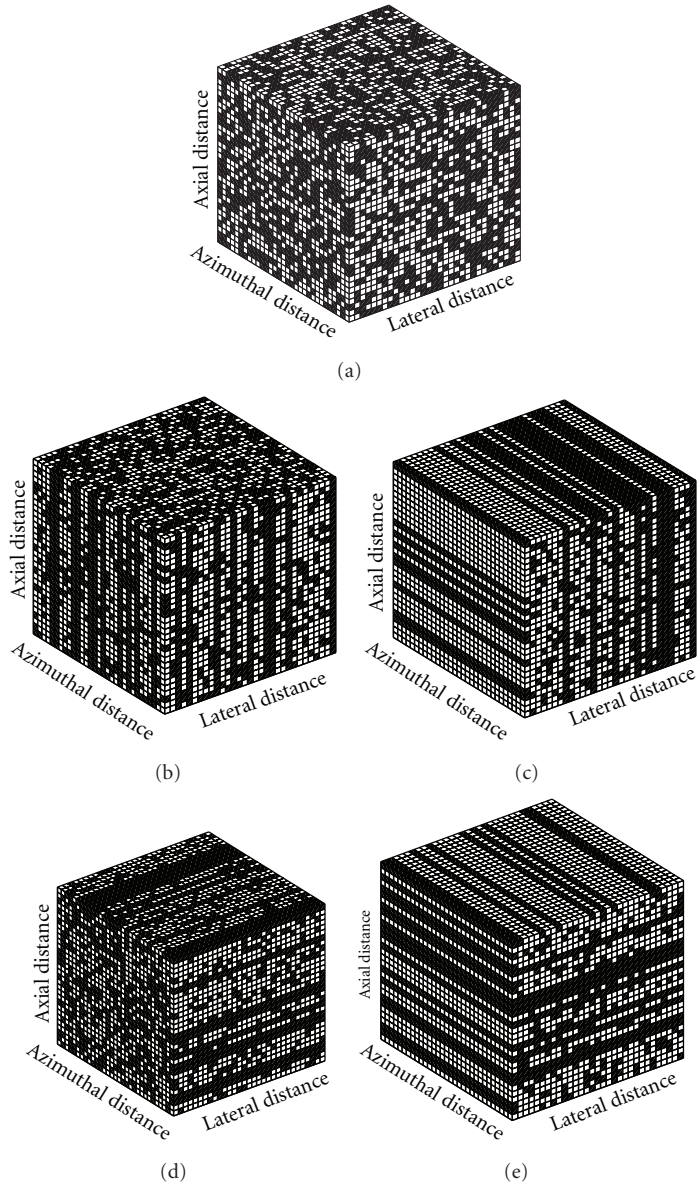

Figure 7: Sampling masks Θ_1 (a), Θ_2 (b), Θ_3 (c), Θ_4 (d), and Θ_5 (e) adapted to a spatial sampling of the 3D US volumes. The white pixels correspond to the samples used for CS. The proportion of samples here is 50% of the original volume.

smaller than the smallest nonnil sparse coefficient). At the first iterations, all w_i coefficients are set to 1 ($w_i^{(0)} = 1$, for all i). In this setting, the choice of lambda is replaced by the choice of ε. However, we observed that the results of the CS reconstructions were a lot less dependant on ε than λ. A major drawback of the reweighted ℓ_1 minimization method is its iterative process. Thus, at least two classic optimizations are performed (corresponding to a minimum of two iterations) in order to get an accurate result.

In Section 8, the two techniques of CS reconstruction: using a fixed optimal λ and the reweighted ℓ_1 minimization were compared for the sampling patterns described in Section 6. In both cases, a nonlinear conjugate gradient algorithm was used for numerical optimization. This algorithm is particularly suited to large-scale data and is used for similar convex optimization problems (see, e.g., [30]).

In addition, different undersampling ratios were tested.

8. Results on a 2D Simulation Image

The CS strategy described in (8) was used to reconstruct the k-space of an RF image simulated using the Field II US simulation program [31]. The parameters and the example scatterer map of a kidney used were as follows Transducer centre frequency = 5 MHz, sampling frequency = 20 MHz, number of scatterers = 50,000, number of RF lines generated = 256, size of the object = 88 × 147 mm. The image was then cropped to a 1792 by 128 size matrix.

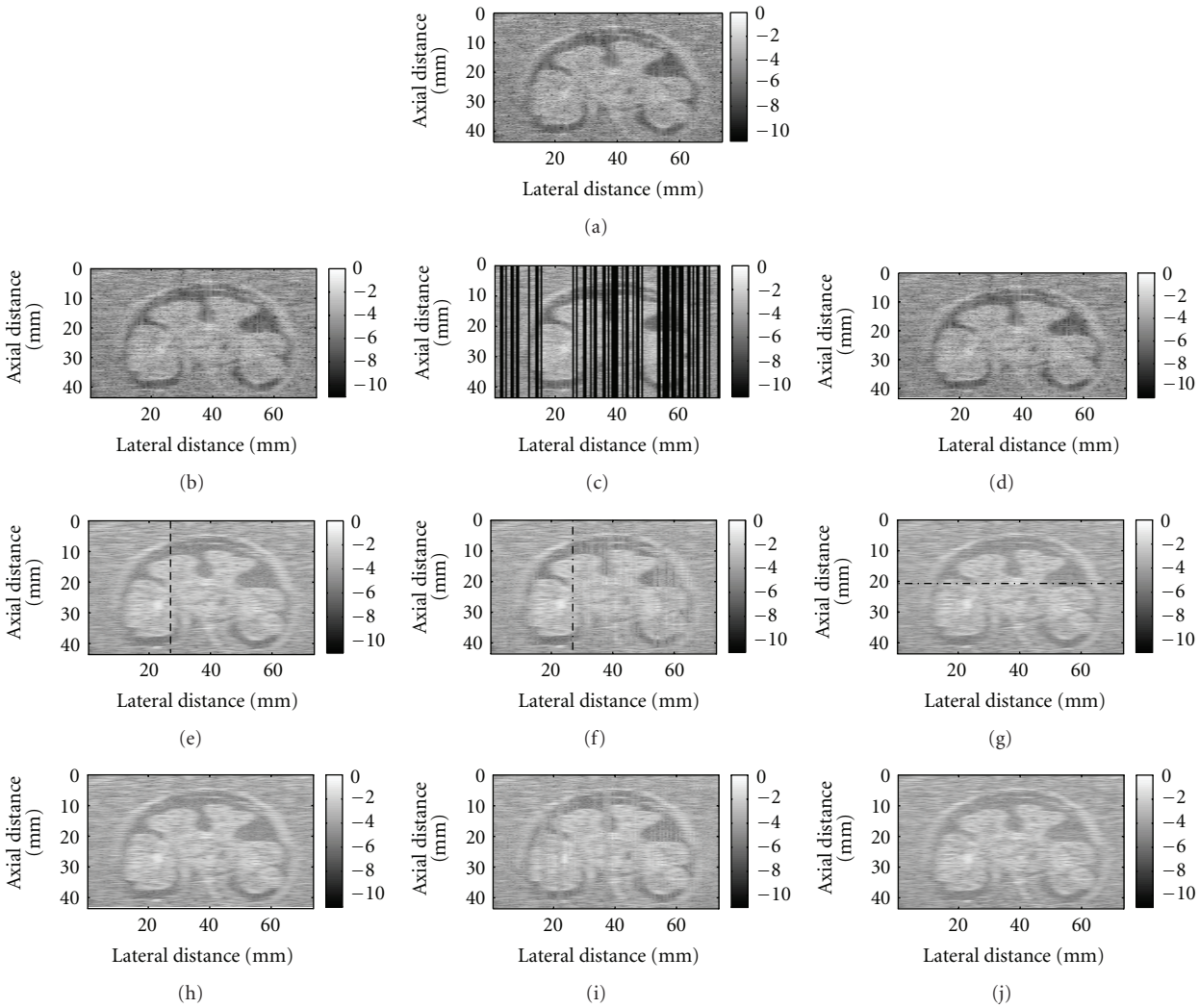

Figure 8: CS on a simulated US image (a) using a two-dimensional random sampling pattern Φ_1 (b) and two alternative sampling mask Φ_2 (c) and Φ_3 (d) using 33% of the samples. The B-mode images of the RF random measurements are shown on the second row. Those from the CS reconstructed k-spaces with the optimal $\lambda = 0.005$ are on the third row: (e) to (g), and those from the CS-reconstructed k-spaces with the reweighted ℓ_1 minimization on the fourth row: (h) to (j). The dotted lines correspond to the position of the RF signals plotted in Figures 9, 10, and 11.

The three different schemes of sampling, Φ_1, Φ_2, and Φ_3 (Figure 6), were studied to compare the CS reconstructions, using a fixed optimal λ set to 0.005 and the reweighted ℓ_1 minimization. The results are shown in Figure 8 for the three sampling patterns (using 33% of the samples).

For the classic 2D random sampling pattern Φ_1, one RF line of the reconstructed signal was plotted against the corresponding RF lines of the original signal and of the random measurements (Figure 9).

For the sampling pattern Φ_2, one RF line of the reconstructed signal was displayed in Figure 10, corresponding to a line that was not sampled at all (shown with the dash-dotted line on Figure 8(f)). RF lines that were partially sampled are very similar to the ones shown in Figure 9.

Figure 11 shows one lateral profile that was not sampled at all with the sampling mask Φ_3 (denoted by a dash-dotted line on Figure 8(g)). Again, the reconstruction quality of lateral profiles that were partially sampled was similar to Figure 9.

Table 1 shows the errors of CS reconstructions for the three sampling masks Φ_1, Φ_2, and Φ_3 at three undersampling ratios: 25%, 33%, and 50%.

For the reconstruction from Φ_1 (Figure 8(e)), the parts of the image that contained less signal, shown in black on the B-mode images, were less successfully reconstructed, but the diagnostic information was maintained. On the RF signals (Figures 9, 10, and 11), the amplitudes of the reconstructed signals were sometimes reduced. However, the differences in amplitude were constant and the timing information of the signal was maintained. Consequently, the CS-reconstructed images would give very close visualizations in B-mode and could also be used for tissue motion estimation or tissue

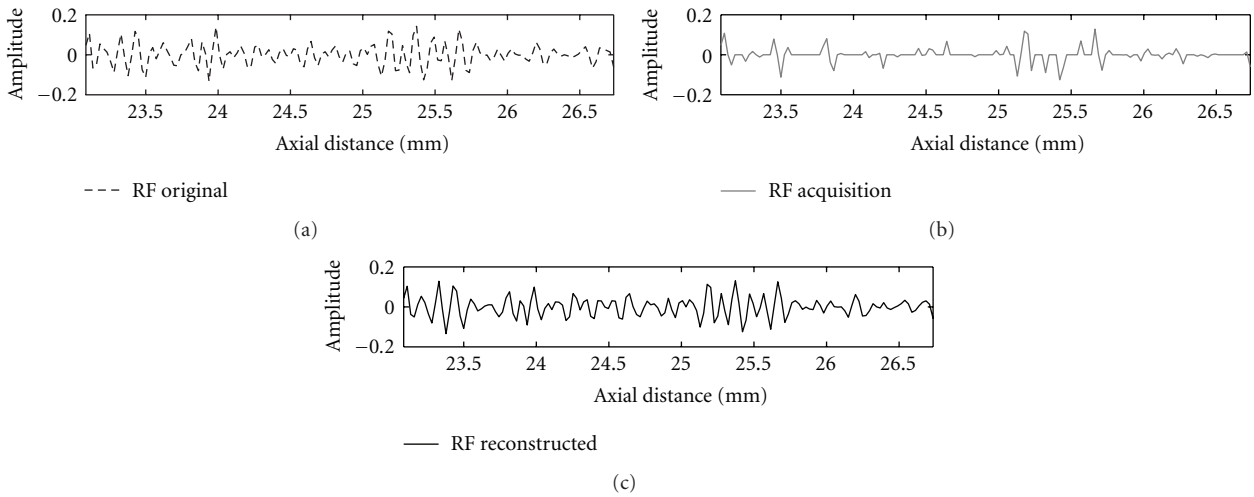

Figure 9: An example of a local region of an RF line after CS reconstruction using Φ_1 sampling pattern, corresponding to the dotted line in Figure 8(e).

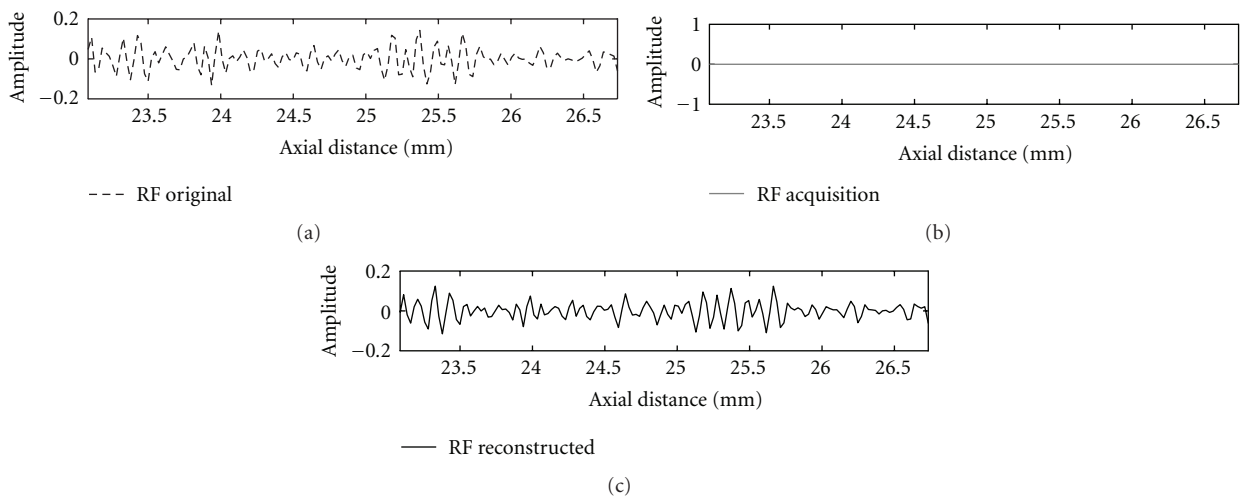

Figure 10: An example of a local region of an RF line after CS reconstruction using Φ_2 sampling mask, corresponding to the dotted line in Figure 8(f). This line was not sampled at all.

characterization. The errors of reconstruction increased with a smaller undersampling ratio as one would expect. In addition, the errors were always reduced when Φ_1 was used, due to a greater incoherence.

With Φ_2, the reconstruction of partially sampled RF lines was again very close to the original signal. For the RF lines that were not sampled at all (Figure 10), a good reconstruction was performed as well, showing the potential of CS for US imaging with reduced pulse emissions. The visualizations in B-mode were again very satisfactory in terms of diagnostic power.

When the sampling mask Φ_3 was used, partially sampled and unsampled lateral lines were well reconstructed (Figure 11). The overall CS reconstruction displayed in B-mode did not exhibit any line artifact.

Results obtained from the reweighted minimization (i.e., with an adaptive λ) were similar to those with the optimal λ, found experimentally.

9. Results on *In Vivo* 2D Images

In this section, US CS is performed using high- and low-frequency ultrasound images. These images were sampled *a posteriori* using CS.

First, results of a CS reconstruction using method (8) on *in vivo* images of the skin are shown. The central frequency was 20 MHz and the sampling frequency 100 MHz (ATYS Medical). Results from three different sampling patterns Φ_1, Φ_2, and Φ_3 (Figure 6) are shown in Figure 12.

The same CS method (8) was used to reconstruct a US image of the right lobe of a normal human thyroid.

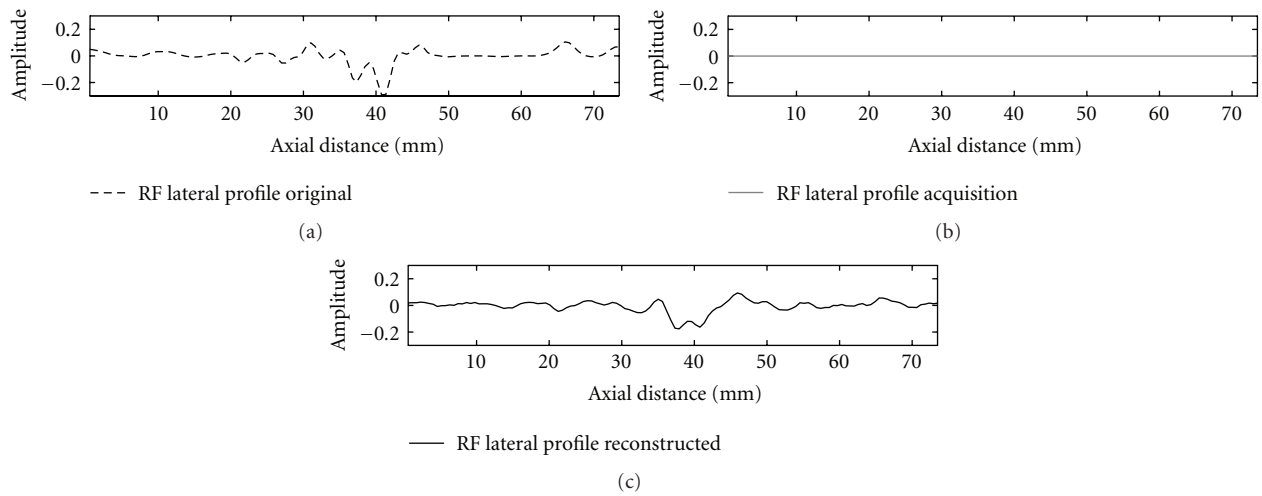

Figure 11: An example of a lateral profile of aN RF image after CS reconstruction using Φ_3 sampling mask, corresponding to the dotted line in Figure 8(g). This lateral profile was not sampled at all.

Table 1: NRMSE between the CS-reconstructed RF US image and the original simulated image of a kidney for different sampling ratios and patterns.

		Φ_1	Φ_2	Φ_3
	25%	0.48	0.58	0.6
Classic ℓ_1 minimization ($\lambda = 0.005$)	33%	0.33	0.45	0.49
	50%	0.15	0.28	0.29
	25%	0.51	0.56	0.64
Reweighted ℓ_1 minimization	33%	0.36	0.47	0.49
	50%	0.17	0.24	0.3

The imaging was performed using a clinical scanner that was modified for research with a 7.5 MHz linear probe (Sonoline Elegra, Siemens Medical Systems, Issaquah, WA, USA). The sampling frequency was adjusted to 40 MHz. For the image presented here, $\lambda = 0.01$ and 33% of the samples were measured *a posteriori*. The three different sampling patterns Φ_1, Φ_2 and Φ_3 (Figure 6) were used. The reconstructed US images of the thyroid are shown in Figure 13.

On *in vivo* US images, similarly to simulation images, the CS reconstruction using both sampling patterns was very good. The tissue structures were restored and the diagnostic information was maintained. Note that the results do not depend on the US frequency used. Tables 2 and 3 show the reconstruction errors for both *in vivo* images and for the different sampling schemes proposed.

10. Results on an *In Vivo* 3D Volume

In vivo US volumes of mouse embryos, acquired on anaesthetised mice, were reconstructed using the sampling masks described in Section 6 (Figure 7).

A single element-high-resolution scanner SHERPA, developed and commercialized by Atys Medical (Lyon, France) where RF data was available, was used (central frequency 22 MHz, frame rate 10 images per second, scanning width 16 mm, sampling frequency 80 M samples/second, emission frequency 20 MHz, exploration depth 7.8 mm). The volume was then cropped to a 128^3 size volume for illustration purposes.

The CS reconstruction of the volume was performed using (8) and $\lambda = 0.4$.

Figure 14 shows the CS reconstruction obtained from the sampling masks Θ_1, Θ_2, Θ_3, Θ_4, and Θ_5 for a 50% undersampling factor. Figure 14(a) represents the original volume and Figures 14(g), 14(h), 14(i), 14(j), and 14(k) the CS reconstructions obtained from each mask, whereas Figures 14(b), 14(c), 14(d), 14(e), and 14(f) are the measurements obtained from Θ_1 to Θ_5 masks, respectively.

The first observation to make is that for all the sampling masks, the CS method (8) provided good reconstructions of the whole volume from only 50% of the samples. The plan that was best reconstructed in each case was always the axial-lateral plan, where the 2D masks were applied (and then repeated along the azimuthal direction). However this setting could easily be changed for other applications where another plan is more crucial.

When the coherence increased, that is, from Θ_3 to Θ_2 to Θ_1 and from Θ_5 to Θ_4 to Θ_1, the reconstructions were degraded, as expected. This is particularly visible on the axial-azimuthal plans of Figures 14(g), 14(h), and 14(i). However, considering that absolutely no samples were kept for the axial-azimuthal plan visible on Figure 14(i), the result

Table 2: NRMSE between the CS-reconstructed RF US image and the original *in vivo* image of the skin for different sampling ratios and patterns.

		Φ_1	Φ_2	Φ_3
Classic ℓ_1 minimization ($\lambda = 0.01$)	25%	0.64	0.71	0.64
	33%	0.48	0.57	0.35
	50%	0.28	0.35	0.35
Reweighted ℓ_1 minimization	25%	0.65	0.67	0.73
	33%	0.51	0.65	0.61
	50%	0.38	0.44	0.43

Table 3: NRMSE between the CS-reconstructed RF US image and the original *in vivo* image of a human thyroid right lobe for different sampling ratios and patterns.

		Φ_1	Φ_2	Φ_3
Classic ℓ_1 minimization ($\lambda = 0.01$)	25%	0.34	0.63	0.38
	33%	0.22	0.53	0.26
	50%	0.12	0.38	0.13
Reweighted ℓ_1 minimization	25%	0.36	0.64	0.39
	33%	0.24	0.56	0.26
	50%	0.15	0.40	0.16

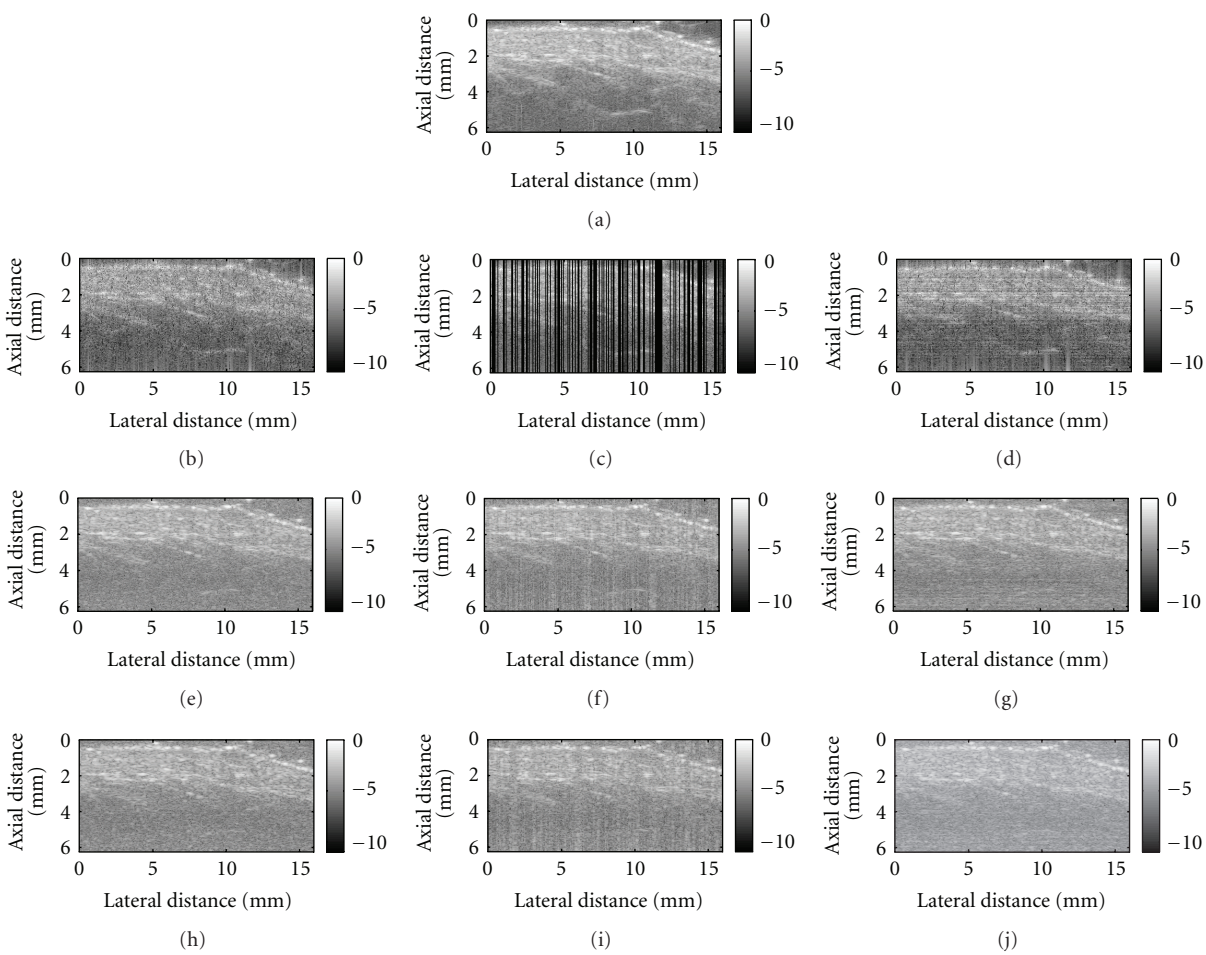

Figure 12: CS reconstruction on a US image of the skin (a) using a two-dimensional random sampling pattern Φ_1 (b) and two alternative sampling masks Φ_2 (c) and Φ_3 (d) and 33% of samples. The B-mode images of the samples are shown on the second row from (b) to (d). The B-mode images of the CS-reconstructed k-spaces with the optimal λ are shown on the third rows (e) to (g). Those from the CS-reconstructed k-spaces using the reweighted ℓ_1 minimization are on the fourth row: (h) to (j).

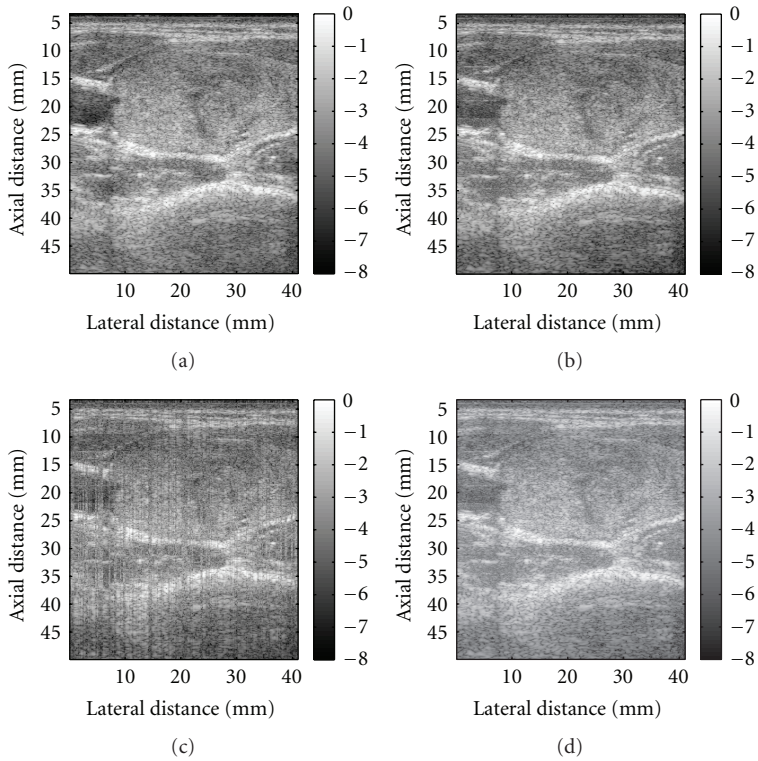

Figure 13: CS reconstruction on a US image of a human thyroid right lobe (a) using a two-dimensional random sampling pattern Φ_1 (b) and two alternative sampling masks Φ_2 (c) and Φ_3 (d) and 33% of samples. The B-mode images of the CS-reconstructed k-spaces with the optimal $\lambda = 0.01$ are shown on the second row from (b) to (d).

Table 4: NRMSE between the reconstructed RF US volume and the original volume for different sampling ratios and patterns.

	Sampling	25%	33%	50%
	Θ_1	0.61	0.49	0.27
	Θ_2	0.69	0.57	0.40
Cubic spline interpolation	Lateral regular	1.09	1.02	0.83

is still quite impressive. This setting could be used in a situation where the speed of imaging would prevail on the quality of the reconstruction. In addition, despite being less sharp, the image still exhibits the tissue structure and might be sufficient in many applications.

For puropse of illustration, Table 4 shows the normalised root mean squared errors of reconstruction between the RF original and reconstructed US volumes for the two sampling patterns Θ_1 and Θ_2 and different rates of decimation (25%, 33%, and 50%). In addition, the NRMSE of the CS reconstructions was compared with results from an interpolation reconstruction method, based on a 2D cubic spline interpolation. The decimation used for the interpolation was a regular lateral undersampling corresponding to the sampling ratios 33% (no axial decimation). As expected, CS outperforms interpolated regular subsampling.

11. Some Hints for Practical Implementation

As shown previously, one of the key points for compressive sampling success is the incoherence of the acquired samples. For this, random sampling schemes are necessary, in both axial and lateral directions.

Regarding the axial direction for the sampling masks Φ_1 and Φ_2, one way to incoherently sample one RF line is to fix a constant sampling frequency f_e, to consider a vector of random integers n_r and to only acquire samples situated at n_r/f_e. This can be achieved by programming specific acquisition devices such as FPGA or CPLD. If the mask Φ_3 is considered, the same n_r random vector is repeated on each RF line.

Alternatively, for all the masks proposed in the paper, the whole RF line can be acquired respecting Shannon's theorem and random samples subsequently discarded, in order to speed up the transfer to the scanner memory.

In the lateral direction, for RF lines selection, the acquisition scheme depends on the type of scanner. For multiple element transducers, each element can be randomly set to be active or not. For single-element transducers, each RF line is acquired separately. Thus, RF lines at random lateral positions can be omitted.

Table 5: Qualitative assessment of the speed of acquisition, the quality of reconstruction, and the ease of a practical implementation of different sampling masks and undersampling ratios (+++ denotes high-speed), high-quality reconstruction and easy implementation.

	Speed	Reconstruction	Implementation
Φ_1	+	+++	+
Φ_2	+++	++	+++
Φ_3	++	++	++

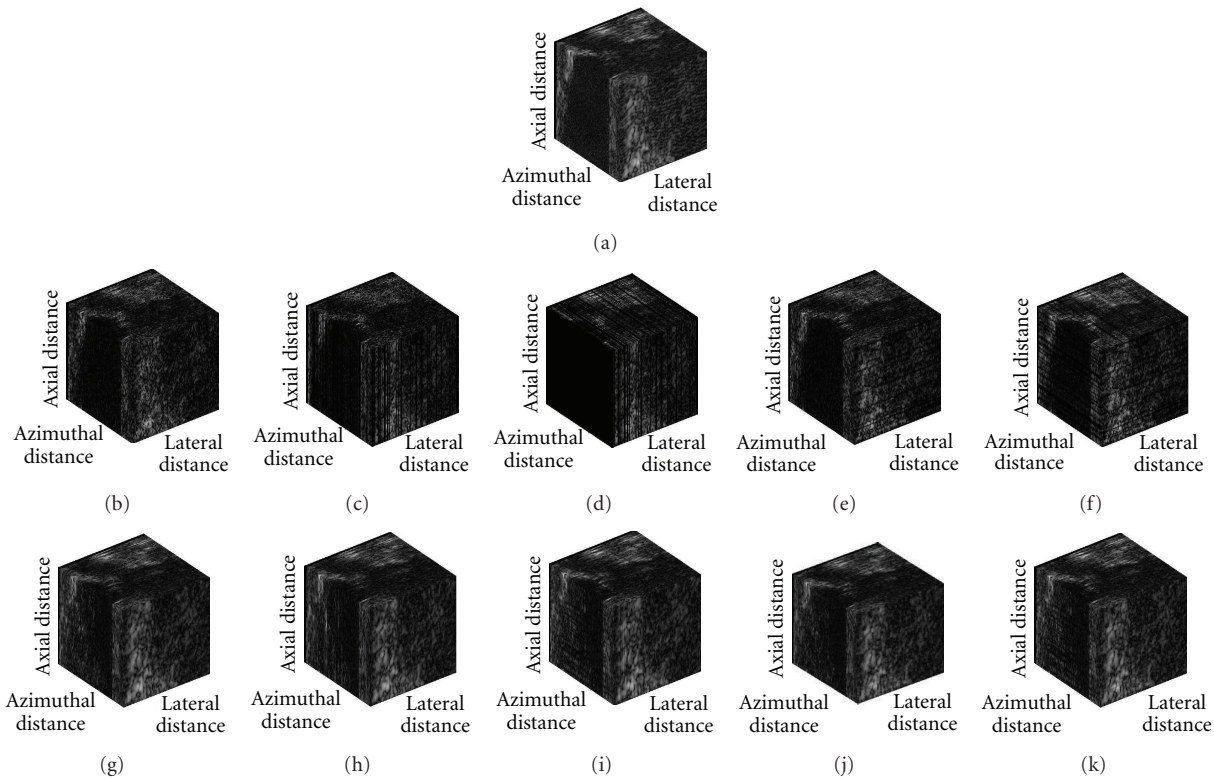

Figure 14: 3D CS reconstructions following (8) on an *in vivo* US volume of a mouse kidney (a) using 50% of the samples and the sampling masks Θ_1, Θ_2, Θ_3, Θ_4, and Θ_5. The B-mode volumes of the RF random measurements are shown in (b), (c), (d), (e), and (f) and of CS reconstructed US volume in (g), (h), (i), (j), and (k).

This methodology could be suitable to all the sampling strategies presented in this paper.

Of course, one could also implement direct random acquisitions through random triggering acquisition board. But this possibility needs more sophisticated electronic design.

12. Summary

Table 5 summarizes the different results presented so far and qualitatively compares the speed of the acquisition, the quality of the reconstruction in term of errors, and the ease of a practical implementation of the different masks and undersampling ratios tested in this paper.

13. Discussion and Conclusion

This paper investigates the feasibility of CS in ultrasound imaging. From this presentation many questions are opened.

13.1. Sparsity of Ultrasound Signals. Sparsity is key point in the success of CS. We dealt here with the fact that the Fourier transform of US is sparse. This may of course be questionable.

US signals exhibit bandpass characteristics and thus are sparse in frequency domain. Consequently, a highly oversampled version of the ultrasound signal could be reconstructed from fewer regular samples. However, it is well known that sampling using high sampling rate is neither easy nor cost-effective particularly in high-frequency US applications. The interest of CS lies in the ability of allowing under sampling from Nyquist limits. Indeed when sampled at Nyquist (which is cost-effective), by taking the demodulated I/Q signal, which remains sparse, CS allows correct reconstruction, whereas no reconstruction is possible after under sampling from Nyquist rate, according to the regular sampling theory.

In addition CS allows skipping RF line in lateral and azimuthal directions.

13.2. Real-Time Nature. In this paper, we showed the powerful potential of CS to reduce data volume and speed up acquisitions at the price of a reconstruction using the l_1 norm. However, using dedicated circuits (GPU type) for the CS reconstruction could allow a great improvement in processing times and overall increase the imaging rate, keeping the real-time nature of US imaging.

In addition, various sampling protocols suited to US imaging were proposed here where the RF signals can be sampled at random times to provide measurements of the final image k-space. Through the l_1 minimization, the original k-space can be reconstructed and the RF US image subsequently recovered with minimal loss of information.

The method presented here differs from inpainting methods as the reconstruction is performed in another domain than the image itself.

Future work will include the identification of optimal conditions as well as an investigation of several optimization routines and better sparsity basis. Additional knowledge about the US images will be inserted in the reconstruction process (statistics of the signal, attenuation). The aim is to reach the fastest and most reliable reconstruction from as little samples as possible. Various applications will also be considered (multidimensional Doppler and tissue characterization).

Acknowledgments

This work was supported by the French National Agency of Research (ANR) under the SURFOETUS Grant. The authors would like to thank Jean-Marc Gregoire and Hugues Herault for ultrasound imaging software development.

References

[1] A. Elen, H. F. Choi, D. Loeckx et al., "Three-dimensional cardiac strain estimation using spatio-temporal elastic registration of ultrasound images: a feasibility study," *IEEE Transactions on Medical Imaging*, vol. 27, no. 11, pp. 1580–1591, 2008.

[2] W. Lees, "Ultrasound imaging in three and four dimensions," *Seminars in Ultrasound CT and MRI*, vol. 22, no. 1, pp. 85–105, 2001.

[3] T. R. Nelson and D. H. Pretorius, "Three-dimensional ultrasound imaging," *Ultrasound in Medicine and Biology*, vol. 24, no. 9, pp. 1243–1270, 1998.

[4] A. Fenster and D. B. Downey, "3-D ultrasound imaging: a review," *IEEE Engineering in Medicine and Biology Magazine*, vol. 15, no. 6, pp. 41–51, 1996.

[5] E. J. Candès, J. Romberg, and T. Tao, "Robust uncertainty principles: exact signal reconstruction from highly incomplete frequency information," *IEEE Transactions on Information Theory*, vol. 52, no. 2, pp. 489–509, 2006.

[6] D. L. Donoho, "Compressed sensing," *IEEE Transactions on Information Theory*, vol. 52, no. 4, pp. 1289–1306, 2006.

[7] M. Lustig, D. L. Donoho, J. M. Santos, and J. M. Pauly, "Compressed sensing MRI: a look at how CS can improve on current imaging techniques," *IEEE Signal Processing Magazine*, vol. 25, no. 2, pp. 72–82, 2008.

[8] H. Yu, G. Cao, L. Burk et al., "Compressive sampling based interior reconstruction for dynamic carbon nanotube micro-CT," *Journal of X-Ray Science and Technology*, vol. 17, no. 4, pp. 295–303, 2009.

[9] J. Provost and F. Lesage, "The application of compressed sensing for photo-acoustic tomography," *IEEE Transactions on Medical Imaging*, vol. 28, no. 4, pp. 585–594, 2009.

[10] D. Friboulet, H. Liebgott, and R. Prost, "Compressive sensing for raw RF signals reconstruction in ultrasound," in *Proceedings of the IEEE International Ultrasonics Symposium (IUS '10)*, pp. 367–370, October 2010.

[11] A. Achim, B. Buxton, G. Tzagkarakis, and P. Tsakalides, "Compressive sensing for ultrasound RF echoes using α-stable distributions," in *Proceedings of the 32nd Annual International Conference of the IEEE Engineering in Medicine and Biology Society (EMBC '10)*, pp. 4304–4307, September 2010.

[12] C. Quinsac, A. Basarab, J. M. Girault, and D. Kouame, "Compressed sensing of ultrasound images: sampling of spatial and frequency domains," in *Proceedings of the IEEE Workshop on Signal Processing Systems (SiPS '10)*, pp. 231–236, October 2010.

[13] C. Quinsac, A. Basarab, J. M. Gregoire, and D. Kouame, "3D compressed sensing ultrasound imaging," in *Proceedings of the IEEE International Ultrasonics Symposium (IUS '10)*, San Diego, Calif, USA, October 2010.

[14] C. Quinsac, F. de Vieilleville, A. Basarab, and D. Kouame, "Compressed sensing of ultrasound single-orthant analytical signals," in *Proceedings of the IEEE International Ultrasonics Symposium (IUS '10)*, San Diego, Calif, USA, October 2010.

[15] R. Tur, Y. C. Eldar, and Z. Friedman, "Innovation rate sampling of pulse streams with application to ultrasound imaging," *IEEE Transactions on Signal Processing*, vol. 59, no. 4, pp. 1827–1842, 2011.

[16] J. Richy, H. Liebgott, R. Prost, and D. Friboulet, "Spectral doppler using compressive sensing," in *Proceedings of the IEEE International Ultrasonics Symposium (IUS '10)*, October 2010.

[17] S. M. S. Zobly and Y. M. Kakah, "Compressed sensing: doppler ultrasound signal recovery by using non-uniform sampling and random sampling," in *Proceedings of the 28th National Radio Science Conference (NRSC '11)*, pp. 1–9, April 2011.

[18] Z. Guo, L. Song, and L. Wang, "Compressed sensing in photoacoustic tomography in vivo," *Journal of Biomedical Optics*, vol. 15, no. 2, Article ID 021311, 2010.

[19] A. Skodras, C. Christopoulos, and T. Ebrahimi, "The JPEG 2000 still image compression standard," *IEEE Signal Processing Magazine*, vol. 18, no. 5, pp. 36–58, 2001.

[20] E. Candès and J. Romberg, "Sparsity and incoherence in compressive sampling," *Inverse Problems*, vol. 23, no. 3, pp. 969–985, 2007.

[21] E. J. Candès and M. B. Wakin, "An introduction to compressive sampling: a sensing/sampling paradigm that goes against the common knowledge in data acquisition," *IEEE Signal Processing Magazine*, vol. 25, no. 2, pp. 21–30, 2008.

[22] D. L. Donoho and X. Huo, "Uncertainty principles and ideal atomic decomposition," *IEEE Transactions on Information Theory*, vol. 47, no. 7, pp. 2845–2862, 2001.

[23] J. Romberg, "Imaging via compressive sampling: Introduction to compressive sampling and recovery via convex programming," *IEEE Signal Processing Magazine*, vol. 25, no. 2, pp. 14–20, 2008.

[24] M. Lustig, D. Donoho, and J. M. Pauly, "Sparse MRI: the application of compressed sensing for rapid MR imaging," *Magnetic Resonance in Medicine*, vol. 58, no. 6, pp. 1182–1195, 2007.

[25] Y. Tsaig and D. L. Donoho, "Extensions of compressed sensing," *Signal Processing*, vol. 86, no. 3, pp. 549–571, 2006.

[26] E. Candès and J. Romberg, "Signal recovery from random projections," in *IS and T Electronic Imaging—Computational Imaging III*, vol. 5674 of *Proceedings of SPIE*, pp. 76–86, January 2005.

[27] R. Baraniuk, M. Davenport, R. DeVore, and M. Wakin, "A simple proof of the restricted isometry property for random matrices," *Constructive Approximation*, vol. 28, no. 3, pp. 253–263, 2008.

[28] C. de Mol, E. de Vito, and L. Rosasco, "Elastic-net regularization in learning theory," *Journal of Complexity*, vol. 25, no. 2, pp. 201–230, 2009.

[29] E. J. Candès, M. B. Wakin, and S. P. Boyd, "Enhancing sparsity by reweighted $\ell 1$ minimization," *Journal of Fourier Analysis and Applications*, vol. 14, no. 5-6, pp. 877–905, 2008.

[30] J. Nocedal and S. J. Wright, *Numerical Optimization*, Springer, New York, NY, USA, 2nd edition, 2006.

[31] J. A. Jensen and N. B. Svendsen, "Calculation of pressure fields from arbitrarily shaped, apodized, and excited ultrasound transducers," *IEEE Transactions on Ultrasonics, Ferroelectrics, and Frequency Control*, vol. 39, no. 2, pp. 262–267, 1992.

Hindawi Publishing Corporation
Advances in Acoustics and Vibration
Volume 2012, Article ID 214839, 28 pages
doi:10.1155/2012/214839

Review Article

Advanced Applications for Underwater Acoustic Modeling

Paul C. Etter

Northrop Grumman Corporation, P.O. Box 1693, Baltimore, MD 21203, USA

Correspondence should be addressed to Paul C. Etter, paul.etter@ngc.com

Received 29 October 2011; Accepted 30 January 2012

Academic Editor: Jafar Saniie

Changes in the ocean soundscape have been driven by anthropogenic activity (e.g., naval-sonar systems, seismic-exploration activity, maritime shipping and windfarm development) and by natural factors (e.g., climate change and ocean acidification). New regulatory initiatives have placed additional restrictions on uses of sound in the ocean: mitigation of marine-mammal endangerment is now an integral consideration in acoustic-system design and operation. Modeling tools traditionally used in underwater acoustics have undergone a necessary transformation to respond to the rapidly changing requirements imposed by this new soundscape. Advanced modeling techniques now include forward and inverse applications, integrated-modeling approaches, nonintrusive measurements, and novel processing methods. A 32-year baseline inventory of modeling techniques has been updated to reflect these new developments including the basic mathematics and references to the key literature. Charts have been provided to guide soundscape practitioners to the most efficient modeling techniques for any given application.

1. Introduction

Over the past several decades, the soundscape of the marine environment has responded to changes in both natural and anthropogenic influences. A soundscape is a combination of sounds that characterize, or arise from, an ocean environment. The study of a soundscape is sometimes referred to as acoustic ecology. The idea of a soundscape refers to both the natural acoustic environment (consisting of natural sounds including animal vocalizations, the sounds of weather, and other natural elements) and anthropogenic sounds (created by humans) including sounds of mechanical origin associated with the use of industrial technology. The disruption of the natural acoustic environment results in noise pollution.

This paper is concerned with the underwater soundscape. The field of underwater acoustics enables us to observe quantitatively and predict the behavior of this soundscape and the response of the natural acoustic environment to noise pollution. Specifically, underwater acoustics entail the development and employment of acoustical methods to image underwater features, to communicate information via the oceanic waveguide, or to measure oceanic properties. In the present context, underwater acoustics encompasses both the science and the technology necessary to deploy functioning acoustical systems in support of naval and commercial operations.

Broadly defined, modeling is a method for organizing knowledge accumulated through observation or deduced from underlying principles. Modeling applications fall into two basic categories: prognostic and diagnostic. *Prognostic applications* include prediction and forecasting functions where future oceanic conditions or acoustic sensor performance must be anticipated. *Diagnostic applications* include system-design and analysis functions typically encountered in engineering tradeoff studies.

The challenges of managing the underwater soundscape are being met by enabling technologies and by emerging solutions. Throughout this paper, the utility of the available inventory of models is stressed and relevant examples from the recent literature are provided in support.

After a brief background in Section 1, the balance of this paper is divided into three main sections. Section 2 addresses evolving challenges. Section 3 discusses enabling technologies. Section 4 reviews emerging solutions. Finally, Section 5 summarizes the notable advances in underwater acoustic modeling that support management of the underwater soundscape.

2. Evolving Challenges

2.1. Background. The soundscape baseline is defined by ambient noise, which is the prevailing background of sound at a particular location in the ocean at a given time of the year. It does not include transient sounds such as the noise of nearby ships and marine organisms, or of passing rain showers. In practice, ambient noise excludes all forms of self-noise, such as the noise of current flow around the sonar. For sonar processing, however, it is the background of noise (including interfering sounds), typical of the time, location, and depth against which an acoustic signal must be detected.

2.2. Naval Operations in Coastal Environments

2.2.1. The Coastal Environment. Coastal environments are generally characterized by high spatial and temporal variabilities. When coupled with attendant acoustic spectral dependencies of the surface and bottom boundaries, these natural variabilities make coastal regions very complex acoustic environments. Specifically, changes in the temperature and salinity of coastal waters affect the refraction of sound in the water column. These refractive properties have a profound impact on the transmission of acoustic energy in a shallow-water waveguide with an irregular bottom and a statistically varying sea surface. Thus, accurate modeling and prediction of the acoustic environment is essential to understanding sonar performance in coastal oceans.

Physical processes controlling the hydrography of shelf waters often exhibit strong seasonal variations. Annual cycles of alongshore winds induce alternating periods of upwelling and downwelling. The presence of coastal jets and the frictional decay of deep-water eddies due to topographic interactions further complicate the dynamics of coastal regions. Episodic passages of meteorological fronts from continental interiors affect the thermal structure of the adjacent shelf waters through intense air-sea interactions. River outflows create strong salinity gradients along the adjacent coast. Variable bottom topographies and sediment compositions with their attendant spectral dependencies complicate acoustic bottom boundary conditions. At higher latitudes, ice formation complicates acoustic surface boundary conditions near the coast. Waves generated by local winds under fetch-limited conditions, together with swells originating from distant sources, conspire to complicate acoustic surface boundary conditions and also create noisy surf conditions. Marine life, which is often abundant in nutrient-rich coastal regions, can generate or scatter sound. Anthropogenic sources of noise are common in coastal seas including fixed sources such as drilling rigs and mobile sources such as merchant shipping and fishing vessels. Surface weather, including wind and rain, further contribute to the underwater noise field. Even noise from low-flying coastal aircraft can couple into the water column and add to the background noise field.

2.2.2. Littoral Operations. Over the past decade, naval mission requirements have shifted from open-ocean operations to shallow-water (or littoral) scenarios. For convenience, shallow water will be defined by water depths less than 200 meters. This has not been an easy transition for sonar technologists since sonar systems that were originally designed for operation in deep water seldom work optimally in coastal regions. This has also held true for modeling and simulation (M&S) technologies, which have undergone a redefinition and refocusing to support a new generation of multistatic naval systems that are intended to operate efficiently in littoral regions while still retaining a deepwater capability. Shallow-water geometries increase the importance of boundary interactions, which diminish acoustic energy through scattering and also complicate localization of diesel submarines and coastal mines due to multipath propagation. Moreover, the higher levels of interfering noises encountered in coastal regions combined with higher levels of boundary reverberation mask signals of interest. In advance of naval deployments, synoptic meteorological and oceanographic (METOC) measurements are often required in remote or hostile (i.e., harsh or heavily defended) coastal environments to forecast acoustic sensor performance. Coupled atmosphere-ocean-acoustic models could reduce the need for hazardous *in situ* data collection by numerically computing initial states for the embedded acoustic models.

In support of naval operations in littoral regions, acoustical oceanographers have employed ocean-acoustic models as adjunct tools that can be used to conduct rapid environmental assessments (REAs) in remote locations. Due to an increased awareness of the potential technological impacts on marine life, naval commanders and acoustical oceanographers must also be aware of new environmental regulations governing the acoustic emissions of their sonar systems.

In shallow water, interactions of the acoustic fields with the sea bed require an understanding of the sedimentary structure of the bottom to a level of detail that is usually not required in deep-water environments. In the forward-propagation case, this means that a significant amount of information is necessary to properly characterize the bottom boundary to ensure the generation of high-fidelity model outputs. This generally requires a good understanding of the physics of bottom-interacting acoustics in diverse ocean environments.

Sonar clutter, particularly in shallow-water environments, introduces false targets that change the statistics of the reverberation signal. Specifically, clutter increases the probability of false alarm for a given probability of detection. This is because clutter adds to the length of the tails of the reverberation-envelope PDF (probability distribution function), moving the statistics away from the Rayleigh canonical form. Clutter can be caused by target-like features, either natural or man-made, or by non-Gaussian distributions of the scatterers. Typically, high-bandwidth or highly directive systems (or both) have more problems with clutter since, as the size of the scattering patch is reduced, the PDF of the generally non-Gaussian scatterer distributions becomes resolved by the system [1].

2.2.3. Training Ranges. At issue here is operational naval training with active sonars. These high-power multistatic

sonars have become more important in the face of improved diesel-electric submarine threats operating in complex coastal environments.

The US Navy has explored the environmental consequences of installing and operating an undersea warfare training range (USWTR) in conjunction with appropriate coordination and consultation with the National Marine Fisheries Service (NMFS) and in compliance with applicable laws and executive orders including the Marine Mammal Protection Act (MMPA), the Endangered Species Act (ESA), the National Environmental Policy Act (NEPA), and the Coastal Zone Management Act (CZMA).

2.2.4. Underwater Networks. Ocean-bottom sensor nodes are used for oceanographic data collection, pollution monitoring, offshore exploration, tactical surveillance applications, and rapid environmental assessments [2, 3]. Factors that determine the temporal and spatial variability of the acoustic channel also limit the available bandwidth of the ocean channel and make it dependent on range and frequency. Specifically, long-range systems (~10 km) have bandwidths of a few kilohertz while short-range systems (~0.1 km) have bandwidths on the order of a hundred kilohertz. A moored-buoy ocean observatory system comprising oceanographic sensors was linked by acoustic communications to retrieve data from sensors in the water column at ranges of approximately 3 km [4]; the observatory was deployed off Vancouver Island in the northeastern Pacific Ocean in May 2004 (for 13 months) to study the correlation of seismicity and fluid flow in a seep area along the Nootka fault.

Underwater networks consist of variable numbers of sensors and vehicles deployed in concert to perform collaborative monitoring tasks over a given area. Underwater sensor networks comprise nodes that communicate via acoustic waves over multiple wireless hops to perform collaborative tasks such as environmental monitoring, naval surveillance, and oceanic exploration. Nodes in underwater sensor networks are constrained by harsh physical environments. Data delivery schemes originally designed for terrestrial sensor networks are unsuitable for use in the underwater environment. Relatively few new schemes have been proposed for underwater use, and no single scheme has yet emerged as the *de facto* standard.

Underwater acoustic communications are influenced by spreading loss, noise, multipath discrimination, Doppler spread, and high and variable propagation delays. Moreover, underwater acoustic channels normally have low data rates and time-varying fading. These factors determine the temporal and spatial variability of the acoustic channel and make the available bandwidth of the ocean channel both limited and dependent on range and frequency. Challenges due to the presence of fading, multipath, and refractive properties of the sound channel necessitate the development of precise underwater-channel models. Some existing channel models are simplified and do not consider multipaths or fading. Multipath interference due to boundary reflection in shallow-water acoustic communications poses major obstacles to reliable high-speed underwater communication systems.

Cooperative transmission is a new wireless communication technique in which diversity gain can be achieved by utilizing relay nodes as virtual antennae. These transmission techniques have been investigated for underwater acoustic communications. First, the performance of several cooperative transmission schemes was studied in an underwater scenario. Second, by taking advantage of the relatively low propagation speed of sound in water, a new wave cooperative transmission scheme was designed in which the relay nodes amplified the signal received from the source node and then forwarded the signal immediately to the intended destination. The goal was to alter the multipath effect at the receiver. Third, the upper bound of performance was derived for the proposed wave cooperative transmission scheme. The simulation results showed that the proposed wave cooperative transmission had significant advantages over both the traditional direct transmission and the existing cooperative transmission schemes originally designed for radio wireless networks [5].

Localization algorithms are relevant to underwater sensor networks, but there are challenges in meeting requirements imposed by emerging applications for such networks in offshore engineering [6]. Localization algorithms can be broadly categorized into *range-based* and *range-free* schemes. Range-based schemes use precise distance or angle measurements to estimate the location of nodes in a network. Range-free schemes are simpler than range-based schemes, but they only provide a coarse estimate of a node's location.

Underwater networking is an enabling technology for the operation of autonomous underwater vehicles. In particular, *ad hoc* networks entail wireless communications for mobile hosts called nodes. In these networks, there is no fixed infrastructure. Mobile nodes that are within range communicate directly via wireless links, while those that are far apart rely on other nodes to relay messages as routers. Node mobility in an *ad hoc* network causes frequent changes of the network topology. Since *ad hoc* networks can be deployed rapidly with relatively low cost, they are attractive for military, emergency, commercial and scientific applications [2, 3]. A channel simulator was developed for testing the performance of unmanned undersea vehicle (UUV) communications [7].

2.2.5. Unmanned Underwater Vehicles. Autonomous underwater vehicles (AUVs), or unmanned undersea vehicles (UUVs), constitute part of a larger group of undersea systems known as unmanned underwater vehicles, a classification that includes nonautonomous remotely operated vehicles (ROVs) that are controlled and powered from the surface by an operator (or pilot) via an umbilical connection.

Underwater gliders actually constitute a new class of autonomous underwater vehicles that glide by controlling their buoyancy and attitude using internal actuators [8]. Gliders have useful applications in oceanographic sensing and data collection because of their low cost, autonomy, and capability for long-range extended-duration deployments. They serve as adjuncts to ship-based hydrographic casts, towed sensors, UUV/AUV and satellite-based sensors, but they also present challenges in communications common to all untethered subsurface sensors.

2.3. Marine Seismic Operations

2.3.1. Seismic Exploration. Marine seismic surveys are used to assess the location of hydrocarbon resources, including gas and oil. There are two acquisition methods: 2D and 3D. The 2D method tows a single seismic cable (or streamer) behind the seismic vessel, together with a single source. The reflections from the subsurface of the sea floor are assumed to lie directly below the path (sail line) of the vessel. In a 3D survey, groups of sail lines (or swathes) are used to acquire orthogonal or oblique lines relative to the acquisition direction. By utilizing more than one source together with many parallel streamers towed by the seismic vessel, the acquisition of many closely spaced subsurface 2D lines can be achieved by a single sail line. Computationally intensive processing is necessary to produce a 3D image of the subsurface of the sea floor. The source arrays are powered by high-pressure air that is compressed onboard the seismic vessel. These compressors are capable of recharging the airguns rapidly and continuously, enabling the airgun source arrays to be fired at approximately 10-second intervals for periods of up to 12 hours. Typical towing depths range from 4-5 meters for shallow high-resolution surveys or 8–10 meters for deeper penetration, lower-frequency targets in open waters. Typical source outputs are approximately 220 dB re 1 μPa/Hz at 1 m. Other types of seismic sources include water guns and marine vibrators.

2.3.2. Marine Mammal Impacts. In 2002, the International Association of Geophysical Contractors (IAGC) hosted an informal meeting to discuss future *Acoustics Research* relevant to seismic operations related to the effects of seismic exploration on sperm whales in the Gulf of Mexico [9]. The IAGC offered its support for sperm-whale research through the contribution of a seismic-source vessel for controlled-exposure experiments. In response, a proposed sperm whale seismic study (SWSS) was approved by the Minerals Management Service (MMS) in 2002. (The MMS is now the Bureau of Ocean Energy Management, Regulation and Enforcement, or BOEMRE.) In subsequent years, IAGC was joined by a number of oil and gas companies to form the Industry Research Funders Coalition (IRFC) that has continued to provide contributions in support of SWSS studies.

Long-term (monthly to seasonal) movements and distributions of sperm whales were studied using satellite-tracked radio telemetry tags (S-tags). Short-term (hours) diving and swimming behavior and vocalizations of sperm whales were examined using recoverable digital-recording acoustic tags (D-tags) that logged whale orientation (i.e., pitch, roll, heading) and depth, as well as the sounds made by the whale and received at the whale from the environment. Diving depths and movements were examined using 3D passive acoustic tracking techniques.

To examine potential changes in the behavior of sperm whales when subjected to seismic airgun sounds, controlled exposure experiments (CEEs) were conducted using the D-tags in conjunction with a seismic-source vessel. The location and level of airgun sounds delivered at the tagged sperm whales were controlled by the science team. These CEEs provided data on the immediate and short-term (hours) response of sperm whales to airgun sounds. Longer-term avoidance or displacement behaviors of sperm whales to seismic vessel airgun sounds were examined using location data from the S-tags and from proprietary commercial seismic shot data.

The 3D tracking method requires at least two widely separated hydrophones to obtain the horizontal range and depth of acoustically active sperm whales and would thus be suited for eventual use on a standard seismic vessel, where the passive acoustic arrays (streamers) can be over a kilometer long. Instead of relying on four hydrophones deployed as a three-dimensional array (which would be difficult to deploy and process), the method used here exploited surface multipath (or "ghosts") to reduce the number of required hydrophones to three and further permitted the phones to be deployed along a single towed cable. The horizontal separation between the widely-spaced hydrophones needed to be at least 200 m in order to obtain adequate range and depth resolution at 1 km horizontal ranges. The method did not require the use of multipath from the ocean bottom, but when such bottom returns were detected they could provide an independent confirmation of these tracking procedures [10].

2.4. Shipping Activity. Shipping lanes, a term used to indicate the general flow of merchant traffic between two ports, are routes that historically have been optimized for shortest distances and travel times, and which are modified to avoid extreme weather events [11]. Noise from distant shipping generally occupies the frequency band 20–500 Hz.

A comparison of time-series measurements of ocean ambient noise over two periods (1963–1965 and 1994–2001) revealed that noise levels from the latter period exceeded those of the earlier period by about 10 dB in the frequency ranges 20–80 Hz and 200–300 Hz, and by about 3 dB at 100 Hz [12]. The observed increase was attributed to increases in shipping. Ambient noise measurements collected at the same site but separated by an interval of nearly 40 years (1964–1966 and 2003–2004) revealed an average noise increase of 2.5–3 dB per decade in the frequency band 30–50 Hz [13, 14].

2.5. Windfarm Development. Wind power, as an alternative to fossil fuels, is plentiful, renewable, widely distributed, clean, and produces no greenhouse gas emissions during operation. A wind farm, which is a group of wind turbines in the same location used for production of electric power, may be located offshore. The installation of ocean wind farms requires medium water depths (<30 m) and construction logistics such as access to specialized vessels to install the turbines. Economic wind generators require wind speeds of 16 km/h or greater.

A concerted effort has been made by industry to minimize any undesirable effects relating to windfarm development and operation [15]. One potential effect of offshore windfarm development is the creation of underwater noise.

Knowing the length of time the marine environment is exposed to an underwater noise source is useful when assessing environmental effects. Measurements of offshore wind turbine noise showed low-frequency sound levels with a maximum of 153 dB re 1 μPa at 1 m at 16 Hz. These measurements were of individual turbines of a relatively low power (less than 1 MW). Despite the low-level and low-frequency nature of the sound, behavioral reactions of marine mammals have been observed in response to the reproduction of wind-turbine noise.

2.6. Ocean Acidification. Climate change also affects the ocean soundscape. The emission of carbon into the atmosphere through the effects of fossil-fuel combustion and industrial processes increases atmospheric concentrations of carbon dioxide (CO_2). Ocean acidification, which occurs when CO_2 in the atmosphere reacts with water to create carbonic acid (H_2CO_3), is increasing.

The attenuation of low-frequency sound in the sea is pH dependent; specifically, the higher the pH, the greater the attenuation. Thus, as the ocean becomes more acidic (lower pH) due to increasing CO_2 emissions, the attenuation will diminish and low-frequency sounds will propagate farther, making the ocean noisier.

Recent investigations modeled what effect the increasing acidity of the ocean would have on ambient-noise levels in shallow water in the presence of internal waves [16]. This model assumed an isotropic distribution of noise sources. Exploring a scenario typical of the East China Sea, the noise at 3 kHz was predicted to increase by 30%, or about one decibel, as the pH decreased from 8.0 to 7.4. These results are representative of other contemporaneous investigations into this matter.

3. Enabling Technologies

3.1. Background

3.1.1. Regulatory Initiatives. An examination of anthropogenic sound in a global context considered the need for new regulatory initiatives to deal with the conflicting uses of ocean space related to noise [17]. This study identified the existing legal, economic, and political barriers to the creation and implementation of a new international regime designed to manage anthropogenic noise in the ocean.

The Committee on Potential Impacts of Ambient Noise in the Ocean on Marine Mammals was charged by the Ocean Studies Board of the US National Research Council to assess the state of our knowledge of underwater noise and recommend research areas to assist in determining whether noise in the ocean adversely affects marine mammals [18]. One of the findings of this committee was that models describing ocean noise are better developed than are models describing marine mammal distribution, hearing, and behavior. The biggest challenge lies in integrating the two types of models. The National Research Council [19] also examined what constitutes *biologically significant* in the context of Level B harassment as used in the latest amendments to the US Marine Mammal Protection Act (MMPA). The MMPA separates harassment into two levels. Level A harassment is defined as "any act of pursuit, torment, or annoyance which has the potential to injure a marine mammal or marine mammal stock in the wild." Level B harassment is defined as "any act of pursuit, torment, or annoyance which has the potential to disturb a marine mammal or marine mammal stock in the wild by causing disruption of behavioral patterns, including, but not limited to, migration, breathing, nursing, breeding, feeding, or sheltering." The MMPA, enacted in 1972, was the first legislation that called for an ecosystem approach to natural-resource management and conservation; it specifically prohibited the *take* (i.e., hunting, killing, capture, and/or harassment) of marine mammals.

The ocean biogeographic information system (OBIS) is an on-line worldwide atlas for accessing, modeling and mapping marine biological data in a multidimensional geographic context [20]. Also see the website at http://www.iobis.org/home.

3.1.2. Modeling Uncertainty. Uncertainty has been defined as a quantitative measure of our lack of knowledge of the sound-speed field and boundary conditions constituting the waveguide information necessary for simulation of the acoustic field [21]. This uncertainty is distinct from any errors related to numerical solution of the wave equation. Existing methods typically solve a deterministic wave equation separately over many realizations, and the resulting set of pressure fields is then used to estimate statistical moments of the field. Proper sampling may involve the computation of thousands of realizations to ensure convergence of the statistics.

A study of the effects of uncertainty in the modeling of anthropogenic impacts suggested a precautionary approach to regulation [22]. It was further noted that due to the complex patterns of sound propagation encountered in diverse shelf regions, some marine mammals may not necessarily encounter the average sound exposure conditions predicted for any given seismic survey.

3.2. Numerical Modeling Techniques. Four types of models will be discussed: propagation, noise, reverberation, and sonar performance. The order of presentation will follow that indicated in Figure 1. This box-type format will be used throughout the text to present compact summaries of methods that have been developed in detail elsewhere [23].

3.2.1. Propagation Models. As sound propagates through the ocean, the effects of spreading and attenuation diminish its intensity. Spreading loss includes spherical and cylindrical spreading losses in addition to focusing effects. Attenuation loss includes losses due to absorption, leakage out of ducts, scattering, and diffraction. Propagation losses increase with increasing frequency due largely to the effects of absorption. Sound propagation is profoundly affected by the conditions of the surface and bottom boundaries of the ocean as well as by the variation of sound speed within the ocean volume.

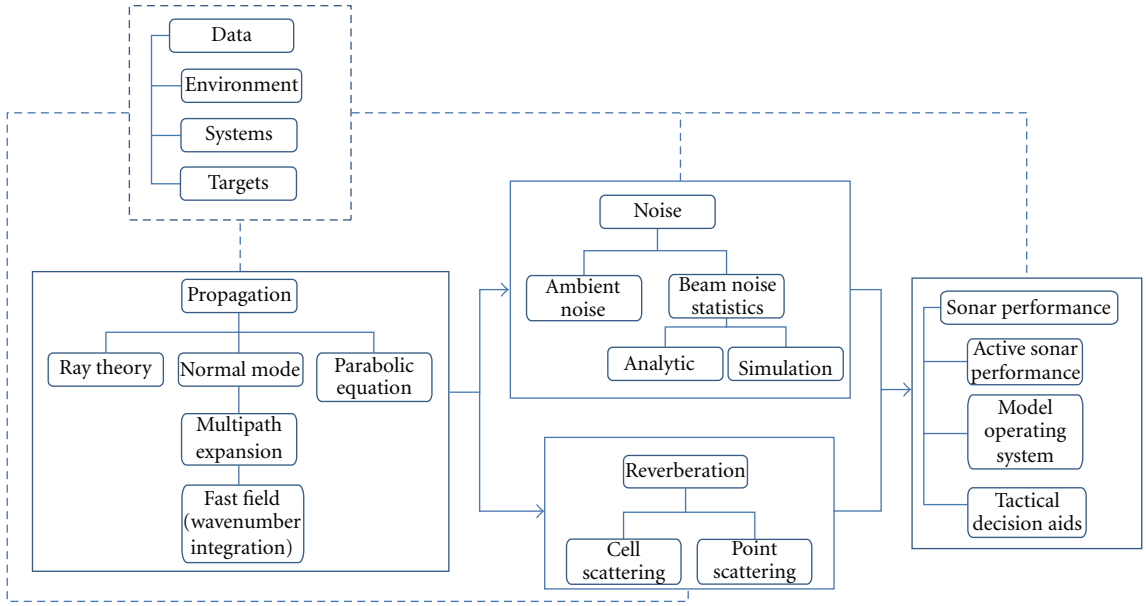

Figure 1: Flow of underwater acoustic modeling from propagation, through noise and reverberation, to sonar performance.

Sound-speed gradients introduce refractive effects that may focus or defocus the propagating acoustic energy.

Formulations of acoustic propagation models generally begin with the three-dimensional, time-dependent wave equation. For most applications, a simplified linear, hyperbolic, second-order, time-dependent partial differential equation is used:

$$\nabla^2 \Phi = \frac{1}{c^2} \frac{\partial^2 \Phi}{\partial t^2}, \tag{1}$$

where $\nabla^2 = (\partial^2/\partial x^2) + (\partial^2/\partial y^2) + (\partial^2/\partial z^2)$ is the Laplacian operator, Φ is the potential function, c is the speed of sound, and t is the time.

Subsequent simplifications incorporate a harmonic (single-frequency, continuous wave) solution in order to obtain the time-independent Helmholtz equation. Specifically, a harmonic solution is assumed for the potential function Φ:

$$\Phi = \phi e^{-i\omega t}, \tag{2}$$

where ϕ is the time-independent potential function, ω is the source frequency $(2\pi f)$, and f is the acoustic frequency. Then the wave equation (1) reduces to the Helmholtz equation:

$$\nabla^2 \phi + k^2 \phi = 0, \tag{3}$$

where $k = (\omega/c) = (2\pi/\lambda)$ is the wavenumber and λ is the wavelength. Equation (3) is referred to as the time-independent (or frequency-domain) wave equation.

Propagation models are integral to the higher-level modeling of noise, reverberation, and, ultimately, sonar performance. The graphic in Figure 1 shows the flow of sonar modeling from propagation, through noise and reverberation, through to sonar performance. Estimates of passive sonar performance would require the input of propagation and noise while active sonar performance would require inputs of both noise and reverberation.

Propagation models can be categorized into five distinct techniques [23].

(a) Ray-theoretical models calculate propagation loss on the basis of ray tracing.

(b) Normal-mode solutions are derived from an integral representation of the wave equation.

(c) Multipath expansion techniques expand the acoustic field integral representation of the wave equation in terms of an infinite set of integrals, each of which is associated with a particular ray-path family. Thus, each normal mode can then be associated with corresponding rays.

(d) In underwater acoustics, fast-field theory is also referred to as "wavenumber integration." In seismology, this approach is commonly referred to as the "reflectivity method" or "discrete-wavenumber method."

(e) The parabolic approximation approach replaces the elliptic reduced wave equation with a parabolic equation (PE). Use of the parabolic approximation in wave propagation problems can be traced back to the mid-1940s when it was first applied to long-range tropospheric radio wave propagation.

As shown in Figure 2, a further division can be made according to range-independent (1D, or depth-dependence only) or range-dependent environmental specifications, where environmental range-dependence can be 2D (depth and range) or 3D (depth, range, and azimuth). Since all five techniques are derived from the wave equation by restricting solutions to the frequency domain, the resulting models

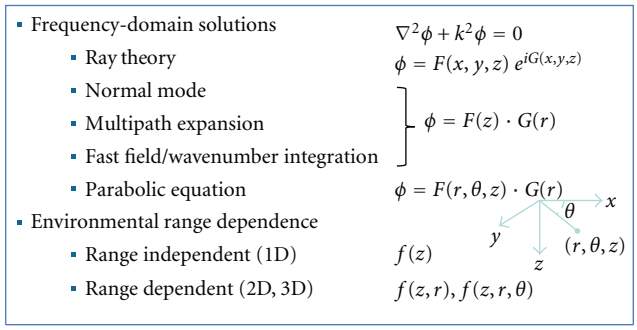

Figure 2: Organization of propagation models into five distinct techniques. A further division is made according to range-independent (1D) or range-dependent (2D or 3D) environmental specifications.

are appropriate for traditional sonar applications. (Solutions obtained in the time domain would be appropriate, e.g., for modeling shock propagation in the ocean.) Each of the five techniques has a unique domain of applicability that can be defined in terms of acoustic frequency and environmental complexity. These domains are determined by the assumptions that were invoked in deriving each solution. Hybrid formulations obtained by combining two or more different techniques are often developed to improve domain robustness.

Table 1 provides a summary of stand-alone propagation models. Superscript letters identify those models that have been added to the inventory since 2003. These letters refer to a brief summary and appropriate documentation. Model documentation can range from informal programming commentaries to journal articles to detailed technical reports containing a listing of the actual computer code. Corresponding information on the legacy models is provided in the 2003 baseline [23] and is not repeated here.

In Table 1: (*Propagation models*), (a) FeyRay was developed to accommodate the speed, fidelity, and implementation requirements of sonar trainers and simulators. It is a broadband, range-dependent, point-to-point propagation model optimized for computa-tional efficiency. FeyRay utilizes the Gaussian-beam approximation, which reduces the acoustic wave equation (a partial differential equation) to a more tractable system of ordinary differential equations [24–28], (b) PlaneRay provides a unique sorting and interpolation routine for efficient determination of a large number of eigenrays in range-dependent environments. No rays are traced into the bottom since bottom interaction is modeled by plane-wave reflection coefficients. The bottom structure is modeled as a fluid sediment layer over a solid half-space. This approach balances two conflicting requirements: ray tracing is valid for high frequencies while plane-wave reflection coefficients are valid for low frequencies where the sediment layers are thin compared with the acoustic wavelength [29–33], (c) PWRC is a ray-based model that performs geoacoustic inversions in range-dependent ocean waveguides. The pressure field is modeled approximately by separating the ocean propagation ray paths from the layered bottom interaction. The bottom interaction is included by using a full-wave description, making PWRC a hybrid model, in contrast to a full-ray theory approach that traces rays into the bottom layers. The field contribution from the bottom interactions partially includes beam-displacement effects associated with internally reflected or refracted returns from the sediment since the complex bottom reflection coefficients are obtained from a full-wave solution. This method is comparable in accuracy to normal mode and analytic solutions (in range-dependent environments) for frequencies >100 Hz [34], (d) Ray5, developed by Trond Jenserud at the Forsvarets forskningsinstitutt (Norwegian Defence Research Establishment), uses direct integration in a sound-speed field specified either analytically or by interpolation from measured data. The Ray5 program is well suited for ray-tracing calculations in acoustic fields described analytically. It needs the sound-speed values, their spatial derivatives and second derivatives at all points within the field. Hence, if these values can be given analytically as functions of the oceanographic and bathymetric parameters, no interpolation is necessary and the program reduces its computing time. Further developments in Ray5 have made it possible to calculate eigenrays. This allows phase information to be retained for a given frequency so that coherent pressure values can be summed for the rays arriving at the receiver. The actual pressure values for the individual rays are calculated by assuming the pressure distribution in the direction normal to the ray to have a Gaussian behavior (i.e., Gaussian beams). It is also possible to calculate the incoherent sound levels [35]. A separate report includes the MATLAB code for Ray5 [36], (e) RAYSON was developed by Semantic (France) to solve the Helmholtz equation using a ray-theoretic approximation for high frequencies. In a stratified (range-independent) environment, analytic solutions are obtained for ray paths that are portions of circles. In range-dependent environments, the ray equations are numerically integrated using a fourth-order Runge-Kutta method to propagate the rays along the range axis. The bottom composition can vary with range and the state of the sea surface can vary in time as well as in range. The software is coded in C++ and is available commercially [37–40], (f) XRAY combines ray tracing in a range-dependent water column with local full-field modeling of interactions with a seabed composed of multiple range-dependent layers of fluid

Table 1: Summary of underwater acoustic propagation models. Superscript letters identify those models that have been added to the inventory since 2003.

Technique	Range independent			Range dependent				
Ray theory	CAPARAY	PLRAY		ACCURAY	GRAB	LYCH	Pedersen	RAYWAVE
	FACT	RANGER		BELLHOP	GRASS	MEDUSA	PlaneRay[b]	RP-70
	FLIRT			Coherent DELTA	HARORAY	MIMIC	PWRC[c]	SHALFACT
	GAMARAY			FACTEX	HARPO	MPC	Ray5[d]	TRIMAIN
	ICERAY			FeyRay[a]	HARVEST	MPP	RAYSON[e]	XRAY[f]
Normal mode	AP-2/5	MODELAB	ORCA	ADIAB	COUPLE	KRAKEN	PROSIM	WKBZ
	BDRM	NEMESIS	POPP[g]	ASERT	CPMS	MOATL	SHAZAM	WRAP
	COMODE	NLNM	PROTEUS	ASTRAL	FELMODE	MOCTESUMA	SNAP/C-SNAP	3D ocean
	DODGE	NORMOD3	SHEAR2	CENTRO	IECM[h]	NAUTILUS	SWAMP[i]	
	FNMSS	NORM2L	Stickler	CMM3D	Kanabis	PROLOS	WEDGE	
Multipath Expansion	FAME	NEPBR				Integrated mode[j]		
	MULE	RAYMODE						
Fast field or wavenumber integration	FFP	OASES	SAFARI	CORE	RD-OASES	SAFRAN		
	Kutschale FFP	pulse FFP	SCOOTER	OASES-3D[k]	RDOASP			
	MSPFFP	RPRESS	SPARC	RDFFP	RDOAST			
Parabolic equation	Use single environmental specification			AMPE/CMPE	FEPES	MONM3D[m]	PE-FFRAME	Two-WayPE
				Cartesian 3DPE[l]	FOR3D	MOREPE	PESOGEN	ULETA
				CCUB/SPLN/CNP1	HAPE	NSPE[n]	PE-SSF (UMPE/MMPE)	UNIMOD
				corrected PE	HYPER	OS2IFD	RAM/RAMS/RAMGEO[p]	3DPE (NRL-1)
				DREP	IFD wide-angle	OWWE[o]	RMPE[q]	3DPE (NRL-2)
				FDHB3D	IMP3D	PAREQ	SNUPE	3DTDPA
				FEPE	LOGPE	PDPE	Spectral PE	3DWAPE[r]
				FEPE-CM	MaCh1	PECan	TDPE	

or solid materials [41], (g) POPP is a range-independent version of the PROLOS normal-mode propagation model [42], (h) IECM is a two-way coupled-mode formalism that provides an exact solution to the wave equation [43]. This model was used to establish a benchmark solution that is an exact numerical solution for the reverberation time series for an environment with a range-dependent, fine-scale rough bottom boundary that induces mode coupling and generates a scattered field. The solution includes scattering effects to all orders in that it sums the infinite series of forward and backward contributions at each range point and maintains energy conservation, (i) SWAMP is a range-dependent normal-mode model that contains closed-analytical forms of the vertical mode functions, which facilitate computation of one-way mode-coupling coefficients between adjacent range-independent regions by neglecting weak backscattering components [44, 45]. The model was used to understand the physics of pulse propagation in double-ducted shallow-water environments where precursors have been observed. The pulse temporal response is modeled using Fourier synthesis in the frequency domain. The model accounts for scattering events along the acoustic signal propagation path and has been extended to model acoustic pulse scattering by spherical elastic-shell targets in inhomogeneous waveguides within the T-matrix approach [46], (j) Integrated Mode extends the multipath expansion method to range-dependent environments [47]. This approach accounts for horizontal variations in bottom depth, bottom type, and sound speed using the stationary phase approximation, (k) OASES-3D target modeling framework is used to investigate scattering mechanisms of flush buried spherical shells under evanescent insonification [48–51], (l) The Cartesian 3D parabolic equation program implements a split-step Fourier algorithm with a wide-angle PE approximation, and is thus a 3D variant of the PE model of Thomson and Chapman [52]. The advantage of employing Cartesian coordinates in the numerical scheme is that the model resolution is uniform over the computational domain [53, 54], (m) MONM3D incorporates techniques that reduce the required number of model grid points. The concept of tessellation (i.e., covering the plane with a pattern in such a way as to leave no region uncovered) is used to optimize the radial grid density as a function of range, reducing the required number of grid points in the horizontal planes of the grid. The model marches the solution out in range along several radial propagation paths emanating from a source position. Tessellation, as implemented in MONM3D, allows the number of radial paths in the model grid to depend on range from the source. In addition, the model incorporates a higher-order azimuthal operator which allows a greater radial separation and reduces the required number of radial propagation paths [55], (n) NSPE, the Navy Standard PE model, consists of two methods of solving the acoustic parabolic wave equation: split-step Fourier parabolic equation model (SSFPE); and split-step Padé (finite-element) parabolic equation (SSPPE) known as RAM. [http://www.nrl.navy.mil/content.php?P=03REVIEW212], (o) OWWE [56] is based on the innovative one-way wave equation developed by Godin [57]. This equation was generalized by Godin to include the source terms and also to account for motion of the medium. The solutions of the differential OWWE are strictly energy conserving and reciprocal. The derivation presented for the multiterm Padé PE model is applicable to a broad class of finite-difference PE models, (p) RAMGEO is a version of RAM modified to handle sediment layers that are range dependent and parallel to the bathymetry [58], (q) RMPE is a ray-mode parabolic-equation solution that is expressed in terms of normal modes in the vertical direction and mode coefficients in the horizontal direction. The model is based on the beam-displacement ray-mode (BDRM) theory and the parabolic equation (PE) method. The BDRM theory is used to analyze the local normal modes. The PE method is used to solve the wave equations for mode coefficients [59], and (r) 3DWAPE incorporates higher-order finite-difference schemes to handle the azimuthal derivative term in a three-dimensional (3D) parabolic equation model [60]. Broadband pulse propagation problems were solved in a 3D waveguide using a Fourier synthesis of frequency-domain solutions (3DWAPE) in a penetrable wedge-shaped waveguide [61]. The 3DWAPE model includes a wide-angle paraxial approximation for the azimuthal component. This version of 3DWAPE was used to investigate broadband sound pulse propagation in two shallow-water waveguides: the 3D ASA benchmark wedge and the 3D Gaussian canyon [62].

The specific utility of these categories is further explained below. In applying ocean-acoustic propagation models, the analyst is normally faced with a decision matrix involving water depth (deep versus shallow), frequency (high versus low), and range-dependence (range-independent versus range-dependent ocean environments). The following assumptions and conditions were imposed in construction of Figure 3, which was originally adapted from F. B. Jensen (see [23]).

(1) Shallow water includes those water depths for which the sound can be expected to interact significantly with the sea floor. Typically, a maximum depth of 200 m is used to delimit shallow water regions. A more accurate definition of shallow water would be expressed in terms of water depth and acoustic wavelength [23].

(2) The threshold frequency of 500 Hz is somewhat arbitrary, but it does reflect the fact that above 500 Hz, many wave-theoretical models become computationally intensive. Also, below 500 Hz, the physics of some ray-theoretical models may become questionable due to restrictive assumptions.

(3) A solid circle indicates that the modeling approach is both applicable (physically) and practical (computationally). Distinctions based on speed of execution may change as progress is made in computational capabilities. A partial circle indicates that the modeling approach has some limitations in accuracy or in speed of execution. An open circle indicates that the modeling approach is neither applicable nor practical.

Model type	Applications							
	Shallow water				Deep water			
	Low frequency		High frequency		Low frequency		High frequency	
	RI	RD	RI	RD	RI	RD	RI	RD
Ray theory	○	○	◑	●	◑	◑	●	●
Normal mode	●	◑	●	◑	●	◑	◑	○
Multipath expansion	○	○	◑	◑	◑	◑	●	◑
Fast field	●	◑	●	◑	●	◑	◑	◑
Parabolic equation	◑	●	○	○	◑	●	◑	◑

Low frequency (<500 Hz) RI: range-independent environment
High frequency (>500 Hz) RD: range-dependent environment

● Modeling approach is both applicable (physically) and practical (computationally)

◑ Limitations in accuracy or in speed of execution

○ Neither applicable or practical

Figure 3: Domains of applicability of underwater acoustic propagation models.

To provide compact summaries, propagation models are arranged in categories reflecting the basic modeling technique employed (i.e., the five canonical approaches) as well as the ability of the model to handle environmental range dependence (Figure 3). Such factors define what is termed *domains of applicability*. Hybrid models occasionally compromise strict categorization, and some arbitrariness has been allowed in this classification process. The environmental range dependence considers variations in sound speed or bathymetry. Other parameters may be considered to be range dependent by some of the models, although they are not explicitly treated in this paper.

Figure 3 has been modified in two important respects relative to previous versions [23]. Specifically, a range-dependent capability has been added to the multipath-expansion and to the fast-field (or wavenumber integration) approaches. This change is warranted by the substantial progress made by modelers over the past several years.

Taken together, Figure 3 and Table 1 provide a useful mechanism for selecting a subset of candidate models once some preliminary information is available concerning the intended applications. Note that range-dependent models can also be used for range-independent environments by inserting a single environmental description to represent the entire horizontal range.

3.2.2. Noise Models. Noise is the prevailing, unwanted background of sound at a particular location in the ocean at a particular time. The local noise field is thus characterized by temporal, spatial, and spectral variabilities. The noise generated by natural or anthropogenic point sources is diminished through the effects of propagation to the sonar receiver.

Noise models can be segregated into two categories: ambient-noise models and beam-noise statistics models, as illustrated in Box 1. Ambient-noise models are applicable over a broad range of frequencies and consider noise originating from surface weather, biologics, shipping, and other commercial activities [63]. Beam-noise statistics models [64] predict the properties of low-frequency shipping noise using either analytic (deductive) or simulation (inductive) methods. Table 2 provides a summary of noise models. Superscript letters identify those models that have been added to the inventory since 2003. These letters refer to a brief summary and appropriate documentation. Model documentation can range from informal programming commentaries to journal articles to detailed technical reports containing a listing of the actual computer code. Corresponding information on the legacy models is provided in the 2003 baseline [23] and is not repeated here.

In Table 2: (*Noise models*), (a) ARAMIS consists of a number of FORTRAN, C++ and MATLAB codes that integrate US Navy standard databases with user-provided sonar system parameters to assess the performance of passive spatial processors [65], (b) DANM is the successor to ANDES. DANM predicts the azimuthal dependence of noise in the 25–5,000 Hz band [18]. The dynamic ambient noise model (DANM) provides a realistic simulation of the temporal noise field in which a passive receive array operates. The total noise field is obtained by separately calculating wind and shipping noise. The temporal variability of the noise field is simulated by moving merchant ships along major shipping lanes. Shipping databases provide seasonal information about shipping lanes between the world's major ports, as well as the type and number of ships that move in the lanes, (c) ISAAC uses a Gaussian ray-tracing approach to determine the acoustic ray paths between source and target, including those reflected from the sea surface and sea bed. The ray paths may refract with changes in bathymetry, water density, salinity, temperature, and sea-bed type. ISAAC

Ambient noise

Given: the directional noise intensity per unit solid angle $[N_s(\theta,\phi)]$.

(i) The horizontal noise directionality $[N(\phi)]$ is calculated from $[N_s(\theta,\phi)]$ as:

$$N(\phi) = \int_{-\pi/2}^{\pi/2} N_s(\theta,\phi)\cos\theta\, d\theta.$$

(ii) The vertical noise directionality $[N(\theta)]$ is calculated from $[N_s(\theta,\phi)]$ as:

$$N(\theta) = (1/2\pi)\int_0^{2\pi} N_s(\theta,\phi)\, d\phi.$$

(iii) The omnidirectional noise level (N) is then calculated as:

$$N = \int_0^{2\pi}\int_{-\pi/2}^{\pi/2} N_s(\theta,\phi)\cos\theta\, d\theta\, d\phi,$$

or

$$N = \int_0^{2\pi} N(\phi)\, d\phi.$$

(iv) The horizontal angle (ϕ) is measured positive clockwise from true North while the vertical angle (θ) is measured positive upward from the horizontal plane. No receiver beam patterns were convolved with the noise levels $N(\theta)$ and $N(\phi)$.

Beam-noise statistics

The averaged noise power at the beamformer output (Y) can be expressed as:

$$Y = \sum_{i=1}^{m}\sum_{j=1}^{n}\sum_{k=1}^{A_{ij}} S_{ijk}Z_{ijk}B_{ijk},$$

where m: number of routes in the basin; n: number of ship types; A_{ij}: number of ships of type j on route i (a random variable); S_{ijk}: source intensity of the kth ship of type j on route i (a random variable that is statistically independent of the source intensity of any other ship); Z_{ijk}: intensity transmission ratio from ship ijk to the receiving point; B_{ijk}: gain for a plane wave arriving at the array from ship ijk

Box 1: Organization of underwater acoustic noise models into two categories.

Table 2: Summary of underwater acoustic noise models. Superscript letters identify those models that have been added to the inventory since 2003.

Ambient noise	Beam-noise statistics
ANDES	*Analytic*
AMBENT	BBN shipping noise
ARAMIS[a]	BTL
CANARY	Sonobuoy noise
CNOISE	USI Array noise
DANES	
DANM[b]	*Simulation*
DINAMO	BEAMPL
DUNES	DSBN
FANM	NABTAM
ISAAC[c]	SIAM-I/II[e]
MONM[d]	
Normal mode ambient noise	
RANDI-I/II/III	

allows sensitive marine areas such as marine mammal locations, migratory routes and fisheries to be displayed in the GIS alongside acoustic propagation results. Noise impacts on individual species can be assessed by comparing the sound pressure levels generated from anthropogenic activities with sensitivity thresholds to perform environmental risk assessments. The system has been configured specifically for use by offshore industries, environmental agencies, regulators and others to help assess the environmental impact of underwater noise. The *dBht (species)* approach provides a measurement of sound that accounts for interspecies differences in hearing ability by passing the sound through a filter which mimics the hearing ability of the species. (The *dBht (species)* metric is a pan-specific metric incorporating the concept of "loudness" by using a frequency-weighted curve based on the species' hearing threshold as the reference unit for a dB scale. A large number of both field and controlled-laboratory measurements have been made of the avoidance of a range of idealized noises, using fish with greatly different hearing as a model. All data, irrespective of source or species, indicate a dependence of avoidance reaction on the dBht(species) level. The data indicate three regions: no reaction below 0 dBht (i.e., below the species' threshold of hearing), a cognitive avoidance region where increasing numbers of individuals will avoid the noise from 0 to 90 dBht, and instinctive reaction at and above 90 dBht where all animals will avoid the noise. This probabilistic model allows the behavioral impact of any noise source to be estimated [66].) This approach provides an indication of the noise level that will be received for the species at various distances from the noise source. These values can then be compared to published data to indicate distances at which a species will demonstrate a strong avoidance reaction, a temporary elevation of hearing threshold or a permanent elevation of hearing threshold [67], (d) MONM (marine operations noise model) incorporates a range-dependent, split-step parabolic equation acoustic model including a shear-wave computation capability. MONM has been used for precise estimation of noise produced by subsea construction noise, marine facilities operation, and seismic exploration, particularly in complex coastal regions. The core algorithm in MONM computes frequency-dependent acoustic transmission loss parameters along fans of radial tracks originating from each point in a specified set of source positions. The modeling is performed in individual one-third octave spectral bands

covering frequencies from 10 Hz to several kHz, which covers the overlap between the auditory frequency range of marine mammals and the spectral region in which sound propagates significantly beyond the immediate vicinity of the source. The MONM software makes use of geo-referenced databases to automatically retrieve the bathymetry and acoustic-environmental parameters along each propagation traverse, and incorporates a tessellation algorithm that increases the angular density of modeling segments at greater ranges from a source to provide more computationally efficient coverage of the area of interest. The grid of transmission-loss values produced by the model for each source location is used to attenuate the spectral acoustic output levels of the corresponding noise source to generate absolute received sound levels at each grid point. These are then summed across frequencies to provide broadband levels. A further step of Cartesian resampling and summing of the received noise levels from all the sources in a modeling scenario yields the aggregate noise level for the entire operation on a regular grid from which contours can be drawn on a GIS map. The model can either generate contours at evenly spaced levels or draw boundaries representing biologically significant threshold levels [68], and (e) SIAM II (S.C. Wales, unpublished manuscript) was designed to provide many replications of surface-ship noise for horizontal array systems, particularly narrow-beam systems, but could also be used for omnidirectional systems. Its predecessor, SIAM I [69, 70], predicted ship-generated noise over the band 20–120 Hz by generating many replications so that ensemble statistics could be examined. A review report provides more details on SIAM (I/II) in addition to other legacy beam-noise statistics models [71]. Plotting packages for SIAM were described elsewhere [72].

3.2.3. Reverberation Models. Reverberation is sound that is scattered by the ocean boundaries (sea surface and sea floor) or by the volumetric inhomogeneities. Reverberation is produced by the sonar itself; therefore, the spectral characteristics are essentially the same as the transmitted sonar signal. The intensity of reverberation varies with the range of the scatterers (due to propagation loss) and also with the intensity of the transmitted signal.

Most traditional active sonars are configured in what is termed a monostatic geometry, meaning that the source and receiver are at the same position. In some sonar systems, however, the source and receiver are separated in range or depth, or both, in what is termed a bistatic configuration. Bistatic geometries are characterized by a triangle of source, target and receiver positions, and by their respective velocities. Such geometries are commonly employed in sonobuoy applications and also in active surveillance applications. Geometries involving multiple sources and receivers are termed multistatic.

Reverberation models can be categorized according to cell-scattering or point-scattering techniques (Box 2). Cell-scattering formulations divide the ocean into cells, where each cell contains a large number of uniformly distributed scatterers [73]. Point-scattering formulations assume a random distribution of (point) scatterers. Table 3 provides a summary of stand-alone reverberation models. Superscript letters identify those models that have been added to the inventory since 2003. These letters refer to a brief summary and appropriate documentation. Model documentation can range from informal programming commentaries to journal articles to detailed technical reports containing a listing of the actual computer code. Corresponding information on the legacy models is provided in the 2003 baseline [23] and is not repeated here.

In Table 3: (*Reverberation models*), (a) C-SNAP-REV computes reverberation using the C-SNAP range-dependent normal-mode model. Range dependence of the environment is treated as a one-way coupled-mode solution. Surface and bottom reverberation is obtained by integrating the received intensity over the area insonified by the emitted pulse and that contributes to the reverberation at a given time. An average sound speed is assumed for all the paths (i.e., no group-velocity dependence). The scattering is described by a mode-coupling matrix that is equivalent to the plane-wave scattering function evaluated at discrete angles corresponding to the modes. The incident and scattered mode angles are modified to take into account the local slope and are given by the local phase velocity and the sound speed at the interface. Coherent summation of mode contributions is used to correctly model the effects of deep-water convergent zones. The empirical scattering function is based on Lambert's rule. The model deals mainly with the monostatic case, though the technique is extendable to bistatic geometries. (Unpublished notes by Ellis, SACLANT Undersea Research Centre, La Spezia, Italy, various dates.) (b) HYREV is a high-frequency, monostatic reverberation model suitable for shallow-water environments. Arrival times and transmission losses from the source to scatterers are obtained from the appropriate eigenrays. The composite-roughness theory is used to predict the boundary scattering [74], (c) NOGRP first runs the normal-mode program POPP (a variant of PROLOS), which calls the normal mode subprogram MODES and writes out a binary file of mode information that is then read by the monostatic reverberation code. ROSELLA, an extension of NOGRP, is used to execute the reverberation calculations with beam patterns [75, 76], (d) PAREQ-REV is a range-dependent wave-theory model based on the parabolic approximation of the wave equation. The numerical method uses the split-step Fourier marching solution with automatic interpolation of environmental data with range. The code allows a choice of either the standard Tappert-Hardin parabolic equation or the wide-angle equation of Thomson-Chapman. Several choices of starting fields are provided, including a Gaussian source beam of varying width and tilt with respect to the horizontal. Reverberation from the ocean boundaries is computed using standard scattering laws: Lambert's rule for bottom backscatter, and either Chapman-Harris curves or Lambert's rule for sea-surface backscatter. The computational scheme uses reciprocity of propagation to compute the reverberation field for arbitrary receiver depths at the source range. (Unpublished notes by Schneider, SACLANT Undersea Research Centre,

Cell scattering:
Cell-scattering models assume:
(1) a homogeneous distribution of scatterers throughout the area or volume producing reverberation at any given time;
(2) a sufficiently high density of scatterers to ensure that a large number of scatterers occurs in an elemental volume (dV) or area (dA) at range r.
The projector beam pattern is denoted by $b(\theta, \phi)$ and the axial intensity at unit distance is I_0.
The receiver beam pattern is denoted by $b'(\theta, \phi)$ and s_v is the ratio of the intensity of the scattering produced by a unit volume at a distance of 1 m from the volume to the intensity of the incident sound wave.
The equivalent plane-wave volume reverberation level (RL_v) is

$$\mathrm{RL}_v = 10\log_{10}[(I_0/r^4)s_v \textstyle\int_v b(\theta,\phi)b'(\theta,\phi)\, dV].$$

The plane-wave level of boundary reverberation is

$$\mathrm{RL}_b = 10\log_{10}[(I_0/r^4)s_b \textstyle\int b(\theta,\phi)b'(\theta,\phi)\, dA].$$

Point scattering:
Point-scattering models are based on a statistical approach that assumes the scatterers are randomly distributed throughout the ocean. The echoes from each individual scatterer are then summed to compute the reverberation level.

Box 2: Organization of underwater acoustic reverberation models into two categories.

La Spezia, Italy, various dates.), (e) PERM-2D computes backscatter from range-dependent bathymetry in the oceanic waveguide [77]. This technique extends the approach of Collins and Evans [78] to problems involving small-scale and large-scale boundary roughness. The PERM-2D model subdivides the oceanic waveguide into range-independent regions and applies the single-scattering approximation (i.e., multiple forward and backward coupling in the scattered fields is neglected) to formulate a scattering problem for the reflected and transmitted pressure field at each range step. Forward-scattering loss, which can be significant at long ranges and very rough surfaces, is included in the solution. Wide-angle operators, which are accurate for the propagating and evanescent spectrum, are applied to yield stable and convergent iteration formulas for the reflected and transmitted fields [79]. Unlike perturbative methods that are restricted to small-roughness amplitudes, the PERM-2D model is valid for arbitrary roughness subject to the single-scattering approximation, (f) REVPA is a parabolic-equation reverberation model intended for shallow-water applications [80], (g) R-SNAP is a coherent monostatic reverberation model employing the range-dependent propagation model SNAP [81, 82], (h) ARTEMIS (adiabatic reverberation and target echo mode incoherent sum) is a general-purpose numerical model of bistatic target echo level and surface and bottom reverberation for bistatic arrangements in an arbitrary range-dependent environment with arbitrary sound-speed variation [83]. The model minimizes computation time while retaining a reasonably accurate power envelope. The approach is based on the adiabatic normal-mode approximation, but with the modal series treated as a continuum and with WKB mode amplitudes (excluding the oscillatory modulation). Outputs are three-dimensional and they can be presented in map form as target echo, reverberation or signal-to-reverberation ratio. Given sparse environmental data, the tradeoff between accuracy and speed is negotiated by intelligent interpolation. This is done by constructing quantities (functions of the desired variables, such as cycle distance, ray angles, etc.) that are more or less linear in space or in mode number. These are converted back to the original variables after linear interpolation, (i) BISTAR is a bistatic, range-dependent reverberation model based on the method of coupled normal modes. The environment is discretized into range-independent segments and the outward propagating field is coupled at the interfaces under the single-scatter hypothesis. The propagation theory and implementation are those of C-SNAP. In order to implement the reverberation prediction, the CW field estimate of C-SNAP has been augmented with a narrowband time-series estimator. The time-domain estimates for the range-dependent environment are available separately and are also used to obtain the reverberation estimates. The scattering process itself can be modeled either as a parametric scattering strength such as Lambert's law or via perturbation theory. The model includes coherent propagation to and from the scattering patch [84–87]. (Also, unpublished notes by K.D. LePage, SACLANT Undersea Research Centre, La Spezia, Italy, various dates.), (j) MURAL, the multistatic reverberation algorithm, supports trainer development, and can be used with any propagation model that produces range-sampled grids of transmission loss, travel time, launch and grazing angles. MURAL contains functions that calculate propagation, scattering and beam patterns. The operation of MURAL couples the algorithm controls to the requested resolution of the prediction with the goal of self-optimizing its performance for the requested resolution [88], (k) S-SCARAB is a range-independent raytracing model for calculating both forward propagating and reverberant acoustic fields. Features include improved algorithms to calculate the coherent forward propagating field, the inclusion of upward refracting rays in the sediment, definition of bistatic source-receiver geometries, and the possibility of specifying 3D beam patterns of the source and receivers. The forward and back propagating acoustic fields are calculated by tracing rays both in the water column and sediment. Only contributions from the ocean bottom are considered in calculation of the reverberation. The local scattering properties of the seabed are described by known power-law expressions for both the interfaces of stratified sediment layers and volume inhomogeneities in the sediment. These scattering kernels

Table 3: Summary of underwater acoustic reverberation models. Superscript letters identify those models that have been added to the inventory since 2003.

Cell scattering	
Monostatic	Bistatic/multistatic
C-SNAP-REV[a]	ARTEMIS[h]
DOP	BAM
EIGEN/REVERB	BiKR
HYREV[b]	BiRASP
MAM	BISAPP
NOGRP/ROSELLA[c]	BISSM
PAREQ-REV[d]	BISTAR[i]
PEREV	MURAL[j]
PERM-2D[e]	OGOPOGO
REVMOD	RASP
REVPA[f]	RUMBLE
REVSIM	S-SCARAB[k]
R-SNAP[g]	
TENAR	
Point scattering	
Monostatic	Bistatic/multistatic
REVGEN	BORIS-SSA[m]
RITSHPA[l]	Under-ice reverberation Simulation

are dependent on physical descriptors of the bottom such as seabed roughness. S-SCARAB is computationally efficient compared to other reverberation tools based on normal-mode or parabolic equation approaches, particularly at higher frequencies [89], (l) RITSHPA is a reverberation module intended for use in high-resolution, wideband sonar simulators [90] in which reverberation is stochastic (non-Rayleigh) and follows the K-distribution [91]. Hybrid multipaths, in which the return path is different from the transmit path, are also considered. RITSHPA assumes spherical propagation loss (i.e., isovelocity water column) and uses widely known formulas to compute reflection and scattering at boundaries, and (m) BORIS-SSA (bottom reverberation from inhomogeneities and surfaces small-slope approximation) simulates time series resulting from acoustic scattering off various seafloor types involving various source-receiver geometries [92–96]. This package is an upgrade of BORIS-3D. The model parameters characterize the sonar directivity and pulse shape, the geometrical configuration of the scattering problem and the geophysical characteristics of the seafloor, the sea surface, or other surfaces. These surfaces can have various statistical behaviors or can be obtained from deterministic data based on measured surface heights.

3.2.4. Sonar Performance Models. Sonar performance models combine environmental models, propagation models, noise models, reverberation models, and appropriate signal-processing models to solve the sonar equations. A further segregation can be made according to source/receiver geometry into monostatic and bistatic categories (Box 3). The monostatic formulation of the sonar equations follows a traditional format [73], while the bistatic formulation is adapted from H. Cox (see [23]). The performance of passive sonars (i.e., those that detect sound emitted from a target of interest) could be modeled using the appropriate environmental descriptors together with suitable propagation-loss and noise models. The performance of active sonars (i.e., those that transmit an interrogation signal and then detect the echo returned from a target of interest) could be modeled similarly with the addition of suitable reverberation models.

Sonar performance models can be further categorized as active sonar models, model operating systems and tactical decision aids. Model-operating systems provide a framework for the direct linkage of data-management software with computer-implemented codes of acoustic models, thus facilitating the construction of versatile simulation capabilities. Model-operating systems are further distinguished from stand-alone active sonar performance models by virtue of their ability to conduct sensitivity analyses by computing components of the active-sonar equation using alternative solution techniques. Since sonar model operating systems normally utilize existing ocean-acoustic models and standard oceanographic databases, these systems are unique only in the sense of the number and types of models and databases included, and the particular architectures, graphical user interfaces (GUIs), and other features employed. Tactical decision aids represent a form of engagement-level simulation that blends environmental information with tactical rules. These decision aids guide system operators and scene commanders in planning missions and allocating resources by exploiting knowledge of the operating environment. Table 4 provides a summary of sonar performance models. Superscript letters identify those models that have been added to the inventory since 2003. These letters refer to a brief summary and appropriate documentation. Model documentation can range from informal programming commentaries to journal articles to detailed technical reports containing a listing of the actual computer code. Corresponding information on the legacy models is provided in the 2003 baseline [23] and is not repeated here.

In Table 4: (*Sonar performance models*), (a) ESPRESSO is a minehunting sonar performance assessment tool developed as a NATO standard for interfacing with NATO planning and evaluation tactical decision aids [97]. It uses BELLHOP as a propagation submodel, which has also been modified to calculate beam-based, high-frequency reverberation [98]. Espresso exists in two versions: one intended for scientific use and the other for military use. The scientific version of Espresso provides greater flexibility than the military version, including the ability to select sub-models and view the results of any sub-model. A user guide addresses the user interface for Espresso and describes the underlying software models and data output options available within Espresso [99]. There is a separate user guide for the military version, Espresso (m), which provides greater tailoring of the user interface, including the ability to customize parameters [100]; (b) LYBIN is a range-dependent, ray-theoretical model developed by Svein Mjølsnes of the Norwegian Defence Logistic Organization [101–103]. Range-dependent environmental inputs include bottom type and topography, volume backscatter, sound speed, temperature, salinity, wind speed, and wave height. Choices of

Active sonar equations (monostatic)

(i) Noise background

$$\mathrm{SL} - 2\mathrm{TL} + \mathrm{TS} = \mathrm{NL} - \mathrm{DI} + \mathrm{RD}_N.$$

(ii) Reverberation background

$$\mathrm{SL} - 2\mathrm{TL} + \mathrm{TS} = \mathrm{RL} + \mathrm{RD}_R.$$

Passive sonar equation

$$\mathrm{SL} - \mathrm{TL} = \mathrm{NL} - \mathrm{DI} + \mathrm{RD}.$$

SL: source level; TL: transmission loss; TS: target strength; NL: noise level; DI: receiving directivity index; RL: reverberation level; RD: recognition differential.

Active sonar equations (bistatic)

The signal excess (SE) can be represented as:

(i) $\mathrm{SE} = \mathrm{ESL} - \mathrm{TL}_1 - \mathrm{TL}_2 - [(N_0 - \mathrm{AG}_N) \oplus R_0] + \mathrm{TS} - \Lambda - L$,

the energy source level (ESL) is related to the intensity source level (SL) as:

(ii) $\mathrm{ESL} = \mathrm{SL} + 10\log_{10} T$

where T is the duration of the transmitted pulse,

The echo energy level (EEL) received from the target at a hydrophone on the receiver array is then:

(iii) $\mathrm{EEL} = \mathrm{ESL} - \mathrm{TL}_1 - \mathrm{TL}_2 + \mathrm{TS}$,

where TS is the target strength, N_0 is the noise spectral level, R_0 represents the reverberation spectral level, AG_N is the array gain against noise, Λ is the threshold on the signal-to-noise ratio (SNR) required for detection,

L is a loss term to account for time spreading and system losses,

$\oplus$ represents power summation, TL_1 is the transmission loss from source (S) to target (T),

and TL_2 is the transmission loss from target (T) to receiver (R).

Box 3: Sonar performance models are based upon the sonar equations, which are the basic building blocks for both monostatic and bistatic sonar geometries.

calculation outputs include ray trace, transmission loss, reverberation (surface, volume, and bottom), noise, signal excess, probability of detection, travel time, and impulse response. The transmission-loss module was evaluated by NURC [104]. LYBIN is available commercially from the Forsvarets forskningsinstitutt (FFI), (c) MOC3D [105] is a 3D model developed from the 2D model MOCASSIN [106]. MOC3D was used to investigate the importance of out-of-plane sound propagation in a shallow-water experiment in the Florida Straits [107], (d) MODRAY was developed in conjunction with DSTO (Australia) to simulate the propagation of sound through the underwater environment [108, 109]. MODRAY uses classical ray-tracing theory to produce sound-pressure time series at one or more receivers. The marine environment is range-independent. Seafloor composition can be specified, the sound-speed profile can be arbitrary, noise includes wind, rain, biological and shipping sources, and scattering by marine organisms is included. MODRAY can model an arbitrary number of sound sources, reflectors and receivers stationed on moving platforms. MODRAY has been used extensively to model the effectiveness of underwater communications algorithms [110, 111], (e) SUPREMO is a multistatic sonar performance model that includes propagation, target echoes, reverberation and noise, all plotted as a function of delay time and bearing using an equivalent map projection. A modular propagation section makes it possible to separate the effects of propagation modeling (e.g., theoretical basis and range-dependence) from those of scattering computations (e.g., computational efficiency, bottom slope and scattering law). Special attention is paid to problems of interference from multiple sources firing in sequence, target aspect dependence from multiple receivers, mixed FM and CW, mismatched source and receivers, multiple displays (one for each bistatic pair), and presentation of results [82, 112–115]. Predictions of acoustic reverberation and target echo intensity made by the SUPREMO sonar performance model were compared with measured data gathered in the Malta Plateau region of the Mediterranean Sea. The observed model-measurement agreement demonstrated the suitability of SUPREMO for use with an environmentally adaptive, low-frequency, active sonar system [116]. Version 2.0 of SUPREMO has been documented [117, 118], (f) SWAMI models range-and-azimuth dependence (N $\times$ 2D) via adiabatic modes [119].

Table 4: Summary of sonar performance models. Superscript letters identify those models that have been added to the inventory since 2003.

Active sonar models		
Active RAYMODE		MINERAY
ALMOST		MOCASSIN
ASPM		MOC3D[c]
CASTAR		MODRAY[d]
CONGRATS		MSASM
ESPRESSO[a]		NISSM-II
GASS		SEARAY
HODGSON		SONAR
INSIGHT		SST
INSTANT		SUPREMO[e]
LIRA		SWAMI/DMOS[f]
LORA		SWAT
LYBIN[b]		UAIM[g]
Model operating systems		
CAAM	GSM - Bistatic	
CALYPSO[h]	HydroCAM	
CASS	PRISM	
ESME/NEMO[i]	SPPS[j]	
Tactical decision aids		
ASPECT SPPS[k]		
IMAT		
NECTA		

SWAMI has been used to support the towed integrated active-passive sonar (TIAPS), which was developed as a technology demonstrator for the Canadian Forces. Software development utilized a system test bed (STB) comprising a collection of scaleable, portable, and reusable components for constructing sensor-based applications. The toolset contains modules to produce predictions of transmission loss, reverberation (MONOGO), signal excess, and probability of detection. SWAMI includes the capability to model various source and receiver configurations including omnidirectional arrays, line-arrays (both horizontal and vertical) and volumetric arrays [120]. DMOS (DRDC Atlantic Model Operating System) is an evolution of the SWAMI suite of programs that enables a user to model transmission loss, reverberation, signal excess, and probability of detection for active sonars [121]. Originally, the suite was based on normal-mode theory (PMODES); however, normal-mode theory is best suited to shallow water and low acoustic frequencies, and users occasionally need to model reverberation and other parameters under other conditions. DMOS was enhanced to include a Gaussian-beam acoustic propagation model, BELLHOP, as an alternate propagation engine. A DRDC-extended version that included a range-dependent capability was chosen. DMOS may now be used to model both active and passive sonars in shallow or deep water; (g) UAIM is a system of computer algorithms designed to predict multibeam sonar performance and image the effects of variations in bathymetry, clutter objects, and bottom type, particularly in complex shallow-water environments [122]. The model addresses perceived weaknesses in existing mine-countermeasure (MCM) sonar performance models. The propagation code in UAIM was derived from RASP while the reverberation and signal excess codes were derived from GSM. Modifications were made to these codes to accommodate high-frequency range-dependent applications. A utility package called SoundGuide assists the operator in creating the large input file, executes UAIM and plots the resulting data, (h) CALYPPSO (ΚΑΛΥΨΩ) is an integrated computer environment that was developed for the analysis of underwater acoustic detection systems [123]. The communication language is Greek. It can treat passive detection, broadband, or LOFAR, as well as active detection, monostatic or multistatic. The system contains compact databases for environmental (coastline, bathymetry, oceanographic, geological) and operational (system parameters, target characteristics) data. Acoustic propagation calculations are performed using normal-mode, parabolic approximation, and ray-theoretical codes supporting broadband calculations in range-dependent environments. The results include transmission loss, reverberation levels, detection thresholds and probabilities of detection for a variety of user-defined operational scenarios. (This work was supported by the Greek MOD.) (i) ESME (effects of sound on the marine environment) is a multidisciplinary research and development effort to explore the interactions between anthropogenic sounds, the acoustic environment and marine mammals [124, 125]. The "ESME workbench" models the entire sound path including the sound sources (impulsive or explosive), the medium (water column and seafloor), and the temporary threshold shift (TTS) models of the marine mammals. (TTS refers to a temporary increase in the threshold of hearing, i.e., the minimum intensity needed to hear a sound at a specific frequency, but which returns to its preexposure level over time.) The goal is to predict impacts of anthropogenic sounds on marine mammals. This entails three elements: (1) accurate estimates of the sound field in the ocean; (2) accurate estimates of the cumulative sound exposure of the marine mammals; (3) reliable predictions of the incidence of TTS for the species of interest given the estimated cumulative exposure. The flexibility and computational efficiency of the ESME Workbench will be enhanced by merging the NEMO (NUWC exposure model) and ESME approaches into the "One Navy Model," which is intended to serve as the standard simulation system for use in predicting impacts of anthropogenic sound sources on marine life for environmental compliance purposes, (j) SPPS, the sonar performance prediction system (developed in Germany), evaluates the performance of sonar systems in various naval-warfare scenarios and assists in sonar-system design efforts. The model accommodates active and passive sonar detection problems involving both broadband and narrowband signals using a variety of sonar antennas. The integrated ocean-acoustic propagation model spans the frequency range 10 Hz to 1 MHz by using a hybrid combination of parabolic-equation, coupled-mode, and ray propagation submodels. Environmental databases describe the ocean environment,

targets, platforms and sonar-system characteristics. The reverberation model predicts volume, surface and bottom components. Noise sources include ambient, biological, rain, shipping, ice, seismic exploration, and self-noise [126], and (k) ASPECT, the active system performance estimate computer tool, is a multistatic tactical decision aid (TDA). It computes estimates of system performance for active underwater acoustic sensors. ASPECT was originally designed to satisfy the requirements of mission planning software for the IEER (improved extended echo ranging) system. However, virtually any multistatic or monostatic active acoustic system can be modeled using this software package. ASPECT uses the FAME (fast multipath expansion) model for range-independent calculations of transmission loss and ASPM (active system performance model) for range-dependent transmission loss and reverberation. These computations are then fed into MSASM, which is capable of estimating the performance of active sonar systems for multiple sources, receivers, and targets. It simulates target motion including such features as normal and uniform probability distribution, various speed, and course distributions, as well as target evasion modeling to a limited degree. ASPECT version 2.0 (and beyond) supersedes the MSASM Interactive Execution and Optimization System (MINEOS), which was the first version of mission planning software developed for the IEER program. ASPECT also exists as a standalone version [127].

3.3. Inversion Techniques

3.3.1. Adjunct Tools for Oceanographers. Inverse acoustic sensing techniques presently constitute adjuncts to direct measurement methods. However, the application of inverse acoustic sensing techniques to dynamical studies of the oceans' boundaries and interior show great promise for three reasons. First, such data can be used to establish comparative baselines for other remote sensors, such as satellites, by providing synoptic portraitures of the interior oceans together with concurrent ground-truth data at the sea surface. Second, inverse acoustic techniques often afford useful insights into a broad class of oceanic phenomena since their successful employment relies heavily on the use of numerical models first to understand the role of the oceans as an acoustic medium. Third, inverse data provide estimates of spatially integrated and temporally averaged oceanic conditions that are not readily available from traditional oceanographic sensors.

Recently, acoustical oceanographers have employed underwater-acoustic models as adjunct tools for inverse-sensing techniques that can be used to obtain synoptic portraitures of large ocean areas or to monitor long-term variations in the ocean.

Useful information about the ocean can be derived from both forward and inverse applications of underwater sound. Direct (or forward) methods include traditional sonar applications. Inverse methods extract information from direct measurements of the physical properties of the ocean. These inverse methods combine the direct physical measurements with theoretical models of underwater acoustics. The objective is to estimate detailed underwater-acoustic fields from sparse physical measurements using the theoretical models as guides. Inversions of controlled-source, noise, and reverberation fields have been performed successfully (Box 4).

Inverse sensing techniques that employ acoustics have been used in several subdisciplines of geophysics including seismology, meteorology, and oceanography. In oceanography, inverse acoustic data provide estimates of spatially integrated and temporally averaged oceanic conditions that are not readily available from a traditional constellation of point sensors. Forward (or direct) models are important in solving inverse problems.

3.3.2. Propagation (Acoustic Field Measurements). Acoustic propagation characteristics in the deep oceans are determined largely by the refractive properties of the water column and, to a lesser extent, by the surface and bottom boundary conditions. Propagation measurements can be used to infer bulk properties of the water column such as temperature, sound speed, density, and currents. In shallow-ocean areas, where propagation characteristics can be strongly affected by the bottom boundary, propagation measurements can be used to infer properties of the sea floor such as composition and scattering characteristics. A wide spectrum of inverse problems has been addressed in underwater acoustics including estimation of geoacoustic parameters, acoustic thermometry, and shallow-water characterization. Inverse acoustic sensing methods utilizing the propagation characteristics of the oceans include matched field processing, ocean acoustic tomography and deductive geoacoustic inversion [23]. A new technique known as a time reversal mirror (TRM) uses inverse methods to refocus received signals back to the source.

Range-dependent ray-theoretical models are typically used for deep-water applications involving tomographic experiments as well as for high-frequency experiments in shallow water. Range-dependent wave-theoretical models based on normal-mode, fast-field (wavenumber integration), or parabolic-equation approaches are preferred for low-frequency experiments in shallow water.

3.3.3. Noise. The ambient noise field in the oceans is described by the spectral, spatial, and temporal characteristics of sound generated by both natural and industrial sources. Measurements of these characteristics can provide useful information regarding the nature of the noise sources themselves as well as physical features within the oceans. Examples of inverse applications of the noise field include wind speed determination, rainfall measurements, object imaging (*acoustic daylight*), and geoacoustic inversion.

3.3.4. Reverberation. The reverberation field in the oceans is the product of acoustic scattering by the surface and bottom boundaries and by inhomogeneities within the oceans. The utility of the reverberation field as an inverse sensing technique is analogous to that of the ambient noise field. For example, the reverberation field can be inverted to

Propagation
(i) Matched field processing:
  (a) source localization,
  (b) marine environment characterization.
(ii) Ocean acoustic tomography:
  (a) density field (eddies, currents),
  (b) temperature (climate monitoring).
(iii) Deductive geoacoustic inversion:
  (a) sediment parameters,
  (b) sea-floor scattering characteristics.
(iv) Time reversal mirror (TRM):
  (a) signal refocusing.
Noise
(i) Field inversion:
  (a) wind speeds,
  (b) rainfall rates.
(ii) Acoustic daylight:
  (a) object imaging.
(iii) Geoacoustic inversion:
  (a) seabed acoustics.
Reverberation
(i) Field inversion:
  (a) sea-floor imaging.
(ii) TRM nulling:
  (a) reverberation attenuation.

Box 4: Summary of inverse ocean acoustic sensing techniques.

image the sea floor. A new development uses time reversal mirror (TRM) methods to attenuate reverberant returns.

4. Emerging Solutions

4.1. Background. This section addresses advanced processing methods in addition to novel methods by which to maximize the interpretation, and thus utility, of archival and experimental data.

4.2. Advanced Integrated Modeling Approaches

4.2.1. Acoustic Integration Model. The acoustic integration model (AIM) combines a movement simulator with underwater acoustic models to predict (and thus minimize and mitigate) the potential effect of sound on marine mammals [128]. Simulated sound sources and animals are programmed to move in location and depth over time in a realistic fashion. AIM is a Monte Carlo statistical model based on a whale movement and tracking model and an underwater acoustic backscattering model for a moving source. Currently, AIM incorporates the BELLHOP and PE propagation models in addition to the ETOP05 bathymetry and GDEM sound-speed profile databases. The ETOP05 data set is the highest resolution topographic data set with global coverage that is publicly available, with elevations posted every 5 arc minutes (approximately 10 km) for all land and sea floor surfaces. ETOP05 is distributed without restriction by the National Oceanic and Atmospheric Administration (NOAA) through its National Geophysical Data Center (NGDC).

4.2.2. Marine Mammal Movement Models. A method has been developed for modeling marine mammal movement and behavior (3MB) for use in environmental impact assessments [129]. Estimating the impact of anthropogenic sound on marine animals entails consideration of animal location and behavior at the time of sound exposure. The ESME model (see Table 4) incorporates 3MB to provide fine-scale control over simulated marine-animal (animat) movement and behavior. Control over the animats is scaleable to the information available regarding the species of concern. Movement and behavior are stochastically determined by sampling from distributions describing rates of movement in the horizontal and vertical planes, direction of travel, time at the surface between dives, time at depth, and time in and transition between behavioral states. Influence of behavior over each of the other distributions is also permitted.

As part of the NATO Undersea Research Centre (NURC) broadband environmentally adaptive concept, the SUPREMO sonar performance model was incorporated within a feedback mechanism for sonar-parameter optimization for any specified ocean environment [130]. The feasibility of using active sonars to monitor the movement of marine mammals was investigated in order to recommend stand-off distances within which an acoustic source should not be deployed [131].

4.2.3. Energy Flux Models. Some applications, such as work relating to acoustic impacts on marine mammals, do not require extremely high-fidelity model outputs. Transmission losses averaged over depth, for example, are often adequate.

An approach referred to as energy-flux models [132] is useful for rapid calculation of transmission loss where the propagation conditions are dominated by numerous boundary-reflected multipaths and when only the coarse characteristics of the acoustic field are needed.

In specific configurations, especially at long ranges in shallow-water environments, the transmitted field can be viewed as being composed of many paths propagating by successive reflections from the surface and bottom boundaries. Here, the acoustic energy will remain trapped between these two boundaries. Furthermore, if the acoustic frequency is high enough that the field oscillations can be considered to be random, then an average intensity can be calculated using simple algebraic formulas [23].

This concept can be extended to ocean environments where the sound speed is not constant, or where there are slight losses at the boundaries. In such cases, the transmitted field cannot be taken as a volumetric average. Rather, it has to be decomposed into its angular components and the cyclic characteristics of the various beams must be detailed [133].

This approach is very useful for predicting incoherent transmission losses in cases where there are a large number of modes (≥ 6). These flux models are fast because there is no requirement to find modes or eigenrays. They can also lead to

very simple and intuitive expressions. This method has been extended for reverberation [134].

4.2.4. Waveguide Invariant Models. In weakly range-dependent ocean environments, it has been observed that the acoustic wavefield can be described in terms of ray-based or mode-based approaches [135, 136]. Using ray-based descriptions, distributions of the ray amplitude and phase (travel time) are largely controlled by the so-called stability parameter (α). Alternatively, using mode-based descriptions in either purely range-independent environments or in range-independent environments upon which weak (range-dependent) perturbations have been superimposed, many wavefield properties are controlled by the so-called waveguide invariant (β). When β is evaluated using asymptotic mode-theoretical results (in a stratified environment), it was found that $\beta = \alpha$, which is consistent with the well-known ray-mode duality. In weakly range-dependent environments, however, α was found to control ray stability and several measures of travel-time dispersion while β controlled the spread of modal-group delays due to mode coupling.

In essence, the waveguide invariant (β) summarizes the pattern of constructive and destructive interference between acoustic modes propagating in the ocean waveguide. It manifests itself as interference fringes (or striations) in a plot of frequency versus source-receiver separation. The waveguide invariant summarizes in a single scalar parameter the dispersive propagation characteristics in a waveguide.

4.3. Advanced Nonintrusive Measurement Approaches

4.3.1. Acoustic Transmission Options. In *acoustic probing*, transmit signals can be adapted according to *in situ* estimates of channel conditions. Waveform characteristics could be set using returns from the previous transmission as an indicator of channel response. Rapidly modifying processing parameters by analyzing previously received signals addresses the problem of fluctuating acoustic channel response owing to variations in environmental factors. Such optimal matching to the estimated channel response would improve target-echo stability [137].

Since sound level, frequency, and duration are critical parameters in causing physical damage to marine life, transmitting over a wider frequency spectrum using spread-spectrum techniques or noise-like signals could avoid tissue damage by reducing the time spent (or energy transmitted) in particular frequency bands. Spread-spectrum techniques use a pseudorandom spreading code to produce a wide-band source signature. Signals must possess high range and Doppler resolution and minimize cross-talk between different users.

Noise-like signals emulate ambient noise by covertly adapting to the fluctuating ambient noise field. Designers could model pseudo-random signals based on bioacoustic noise, surf noise (when high-frequency broadband transients should be useful [138]) or shipping noise (when near CW would be more useful).

Advances in sonar technologies have rendered modern sonar systems useful for *in situ* measurements of the ambient marine environment. For example, through-the-sensor measurements of the ocean impulse response have enabled modern sonars to perform collateral functions as *tactical environmental processors*.

A recent *through-the-sensor* remote-sensing technique for acoustic-parameter estimation has been referred to as SABLE (sonar active boundary loss estimation) [139]. Bottom scattering strengths were derived from active hull-mounted naval sonar data by using eigenray paths modeled by CASS and GRAB to associate sonar-signal attributes with specific propagation paths.

4.3.2. Collision Avoidance. Cetaceans are prone to collisions with fast-moving vessels. In areas of high cetacean and vessel densities, the sperm whale (*Physeter macrocephalus*) is of great concern. Sperm whales are highly vocal and can be localized with passive sonar; however, when at or near the surface (i.e., when they are at greatest risk of collision), they tend to stop vocalizing. Techniques employing active sonars have proved to be inefficient due to short detection ranges and high closing speeds. The efficiency of a passive-sonar solution was evaluated that used vocalizing whale clicks (at depth) as acoustic sources to detect silent whales [140]. This solution could serve as a noninvasive complement to a more complex passive localization and collision-avoidance system. A wideband N $\times$ 2D (range-and-azimuth-dependent) ray model was used to simulate a passive solution comprising an arbitrary number of active acoustic sources (vocalizing whales), an illuminated object (silent whale) and a passive-sonar receiver, all positioned in three-dimensional space with arbitrary bathymetry. Both curved-line and straight-line ray solutions were implemented, with the latter providing greater computational speeds at the expense of temporal and angular fidelity. The simulation recreated the resultant mixture of direct, reverberated and target-backscattered signals arriving at the receiver for any array configuration, any number of sources and one target. In the vicinity of the Canary Islands, the simulations demonstrated the applicability of the concept with a maximum detection range on the order of 1 km.

4.4. Advanced Processing Methods

4.4.1. Adjoint Modeling. The principal application of adjoint models is sensitivity analysis. When quantitative estimates of sensitivity are desired, a mathematical model of the phenomenon or relationship is required. While models have been used to assess the impacts of perturbations and thus estimate sensitivity, a more efficient approach is to use the model's adjoint to determine optimal solutions. The adjoint operates backward in the sense that it determines a gradient with respect to input from a gradient with respect to output. In a temporally continuous model, this would appear as integration backwards in time. If there are no numerical instabilities associated with irreversible processes in the tangent linear model acting forward in time, there will be

none in the adjoint acting backward in time (a tangent linear model provides a first-order approximation to the evolution of perturbations in a nonlinear forecast trajectory). The greatest limitation to the application of adjoints is that the results are useful only when the linearized approximation is valid. The adjoint operator (matrix transpose) back-projects information from data to the underlying model. Geophysical modeling calculations generally use linear operators that predict data from models. The usual task is to find the inverse of these calculations, that is, to find models (or make maps) from the data. The adjoint operator tolerates imperfections in the data and does not demand that the data provide full information.

The concept of adjoint modeling was introduced in shallow water acoustics for solving inverse problems [141]. In related work, the concept of backpropagation was reviewed in the context of adjoint modeling [142]. The different implementations of this concept were compared and discussed in the framework of experimental acoustic inversion in shallow water with application to source localization, ocean acoustic tomography, geoacoustic inversion and underwater communications. Well-established inversion (or focalization) methods based on matched-field processing, model-based matched filter and time-reversal mirror are related to lesser known techniques such as acoustic retrogation and other variants of backpropagation. In contrast to the latter, adjoint-based variational inversion approaches make use of the adjoint of a forward model to backpropagate the model-data mismatch at the receiver toward the source.

An adjoint model was derived from a forward-propagation model (e.g., normal mode or parabolic equation) to propagate data-model misfits at the observation point back through the medium to the site of those medium perturbations that were not accounted for in the forward model and which gave rise to the observed data-model misfits [143]. This property makes adjoint models attractive for use in acoustic inversion experiments.

4.4.2. Stochastic Resonance. Stochastic resonance refers to a phenomenon that is manifested in nonlinear systems whereby weak signals can be amplified in the presence of noise [144]. Three components are necessary: a threshold, a periodic signal and a source of noise. The response of the system undergoes resonance-like behavior as the noise level is varied [145]. Stochastic resonance was applied to enhance the detection of target signals masked by shallow-water reverberation [146]. Specifically, parameter-induced stochastic resonance was used to tune system parameters to recover the spatial signal that was corrupted by Gaussian noise. This method also has applicability when processing spatial signals that are corrupted by K-distributed envelope noise (a standard model for radar clutter).

4.4.3. Optimization Techniques. Ant colony optimization (ACO) has elements in common with genetic algorithms [147]. Both are population-based algorithms that search a discrete space and provide uncertainty analyses. The main difference is the mechanism that handles and recombines components of better candidate solutions (i.e., ant-pheromones trails versus genetic operators). Ant colony optimization is further distinguished by having a form of memory (the ant pheromone trails), while genetic algorithms are without memory. Specifically, when the pheromones evaporate, identifiers of paths with above-average quality fade out. Thus, high rates of evaporation mean that only recent information can be retrieved (typical for short-term memory); alternatively, low rates of evaporation allow recollection of much older information (typical for long-term memory). When applied to inversion, the world of the ants acts as an analogy for the geoacoustic environment.

An efficient and reliable method was proposed for performing the inversion of a neural-network underwater acoustic model to obtain sea-floor parameters [148]. Two different versions of a modified particle-swarm optimization were used: two-step gradient approximation and hierarchical cluster-based approximation. Both approaches worked well.

Tabu search has traditionally been applied to combinational optimization problems [149, 150]. The tabu search begins by marching to a local minimum. This approach avoids entrapment in cycles by forbidding (tabu), or penalizing, moves that take the solution in the next iteration to points in the solution space previously visited.

4.4.4. Chaos. In the presence of weak fluctuations in the sound-speed field, it has been observed that ray trajectories in ocean waveguides exhibit a chaotic behavior in which the travel times along eigenrays form compact clusters, the center of which is close to the arrival time of an unperturbed ray with similar geometry [151]. The deep-water acoustic waveguide was modeled by an unperturbed sound-speed profile $[c_0(z)]$ combined with weak fluctuations of sound speed $[\delta c(r,z)]$ caused by a random field of internal waves conforming to the Garrett-Munk spectrum. Formally, ray equations in a random inhomogeneous medium can be considered as stochastic equations whose parameters are determined by a random function δc. Such nonlinear equations can be solved in the framework of ordinary perturbation theory, but only for short ranges. Instead, the ray structure was analyzed by using the Hamiltonian formalism in terms of action-angle canonical variables whose variation was small under conditions of weak perturbations. It was estimated that ray arrival times at a distance r occupied an interval whose average width increased in proportion with $r^{1.5}$, in agreement with previous investigators. Moreover, for $r < 10^3$ km, the ray trajectories forming the cluster deviated only slightly from the unperturbed ray trajectory and the cluster width grew in proportion with $r^{0.5}$. For $r > 10^3$ km, the width of the cluster grew in proportion with r^2.

Chaotic and stochastic nonlinear ray dynamics can occur in underwater-acoustic waveguides with longitudinal variations in the sound speed caused by internal waves [152]. This situation was investigated using a model of a "frozen" medium in which the temporal variations in the environment were neglected and only the spatial variations due to the comparatively small propagation time of sound

in the ocean were considered. Coherent ray clusters were observed in which large fans of rays with close initial conditions preserved close current dynamical characteristics over long distances. The cluster structure could be considered to consist of statistical and coherent parts. Rays belonging to the statistical part propagated in the same areas of phase space with the same value of the Lagrangian, but did not correlate with each other and demonstrated exponential sensitivity to initial conditions. Rays belonging to the coherent part did not demonstrate sensitivity to initial conditions. This coherent clusterization might be a useful property for acoustic tomography in terms of determining spatio-temporal variations in the hydrological environment under conditions of ray chaos [153].

5. Summary

This paper has reviewed changes in the ocean soundscape, changes that have been driven by both anthropogenic activity and natural factors. New regulatory initiatives have placed additional restrictions on uses of sound in the ocean, and mitigation of marine-mammal endangerment is now an integral consideration in acoustic-system design and operation. Emphasis has been placed on leveraging advanced modeling methods to solve emerging scientific and engineering challenges in this field.

Naval sonars have been redesigned as high-power multistatic systems capable of operating in complex coastal environments against quiet submarines. Littoral training ranges to support this new generation of sonar systems must comply with more stringent environmental regulations. Such compliance is often assessed using advanced modeling techniques coupled with *in situ* data collection. Oceanographic data collection is supported by underwater networks consisting of sensors and vehicles deployed in concert. These networks employ nodes that communicate via acoustic channels that have low data rates and time-varying fading.

Seismic exploration has ventured into deeper waters in search of diminishing energy resources using source arrays that are powered by high-pressure air. Controlled-exposure experiments have studied changes in the behavior of nearby whales due to these powerful sources; however, modeling uncertainty complicates the regulatory interpretation of average sound-exposure conditions.

Increased merchant shipping activity has had a measureable impact on the ocean soundscape over the past four decades: the average noise has increased by 2.5–3 dB per decade in the frequency band 30–50 Hz. Moreover, the growing number of wind farms in coastal waters of medium depth (<30 m) has added to the soundscape at low frequencies and resulted in behavioral reactions of nearby marine mammals.

Climate change has also affected the ocean soundscape. The emission of carbon into the atmosphere through the effects of fossil-fuel combustion and industrial processes has increased atmospheric concentrations of carbon dioxide (CO_2). Ocean acidification, which occurs when CO_2 in the atmosphere reacts with water to create carbonic acid (H_2CO_3), has increased. The attenuation of low-frequency sound in the sea is pH dependent; specifically, the higher the pH, the greater the attenuation. Thus, as the ocean has become more acidic (lower pH) due to increasing CO_2 emissions, the attenuation has diminished and low-frequency sounds propagate farther, making the ocean noisier. Recent investigations have estimated that the noise at 3 kHz would increase by 30% if the pH decreased from 8.0 to 7.4.

Modeling tools traditionally used in underwater acoustics have undergone a necessary transformation; these tools include propagation, noise, reverberation, and sonar-performance models. Advanced modeling techniques now include forward and inverse applications, integrated-modeling approaches, nonintrusive measurements and novel processing methods. The flow of the sonar modeling processes was used to demonstrate advances in modeling technology relevant to assessments of the ocean soundscape. A 32-year baseline inventory of modeling techniques was updated with the latest developments, including basic mathematics and references to the key literature, to guide soundscape practitioners to the most efficient modeling techniques for any given application.

Advanced processing methods included integrated modeling approaches that combine marine-mammal movement simulators with underwater acoustic models to predict (and thus minimize and mitigate) the potential effect of sound on marine mammals. Advances have been achieved using energy-flux and waveguide-invariant techniques that can simplify interpretation of channel models. Nonintrusive measurement approaches included new acoustic transmission options to minimize marine-mammal impacts. Collision avoidance techniques have proved useful in areas of high cetacean and vessel density. Finally, adjoint modeling, stochastic resonance, optimization techniques, and chaos were shown to facilitate understanding of advance underwater acoustic modeling results.

Abbreviations

1D:	One-dimensional
2D:	Two-dimensional
3D:	Three Dimensional
3DWAPE:	3D wide-angle parabolic equation
3MB:	Marine mammal movement and behavior
ACM:	Association for computing machinery
ACO:	Ant colony optimization
AIM:	Acoustic integration model
ARAMIS:	Array response advanced modal integrated simulator
ARTEMIS:	Adiabatic reverberation and target echo mode incoherent sum
ASA:	Acoustical Society of America
ASPECT:	Active system performance estimate computer tool
AUV:	Autonomous underwater vehicle
BISTAR:	Incoherent bistatic reverberation for range-dependent environments

BLM: Bureau of Land Management (now BOEMRE)
BMT: British Maritime Technology Ltd
BOEMRE: Bureau of Ocean Energy Management, Regulation and Enforcement (formerly BLM)
BORIS-SSA: Bottom reverberation from inhomogeneities and surfaces-small-slope approximation
CALYPSO: Model operating system
Cartesian 3DPE: 3DPE Employing Cartesian Coordinates in the Numerical Scheme
CEE: Controlled exposure experiments
CiSE: Computational intelligence and software engineering
CMM: Caractérisation du Milieu Marin
CORDA: Centre for Operational Research and Defence Analysis
COWRIE: Collaborative Offshore Wind Energy Research Into the Environment
C-SNAP-REV: Reverberation using the C-SNAP Normal-Mode Model
CW: Continuous wave
CZMA: Coastal zone Management Act
DANM: Dynamic ambient noise model
dB: Decibel
DMOS: DRDC Atlantic model operating system
DRDC: Defence Research and Development Canada
DREA: Defence Research Establishment Atlantic (Canada)
DSTO: Defence Science and Technology Organisation (Australia)
EIA: Environmental impact assessment
ESA: Endangered Species Act
ESME: Effects of sound on the marine environment
ESPRESSO: Extensible performance and evaluation suite for sonar
ETOP05: Earth topography five-minute grid
FeyRay: Broadband, range-dependent Gaussian-beam propagation model
FFI: Forsvarets forskningsinstitutt (Norwegian Defence Research Establishment)
FFP: Fast field program
FM: Frequency modulation
FORTRAN: Formula translation
GDEM: Generalized digital environmental model
GIS: Geographic information system
GmbH: Gesellschaft mit beschränkter Haftung
GOATS: Generic Ocean Array Technology Sonar
GUI: Graphical User Interface
HYREV: HanYang University Reverberation Model
IAGC: International Association of Geophysical Contractors
IARIA: International Academy, Research, and Industry Association
ICC: International Conference on Communications
IECM: Integral equation coupled-mode
IEEE: Institute of Electrical and Electronics Engineers
IEER: Improved extended echo ranging
Integrated Mode: Multipath expansion method extended to range-dependent environments
IOMEDEX: Ionian Sea/Mediterranean Sea Exercise (part of LRAPP)
IRFC: Industry Research Funders Coalition
ISAAC: Impact on Species from Anthropogenic Acoustic Channels
JASA: Journal of the Acoustical Society of America
LRAPP: Long Range Acoustic Propagation Project
LSMS: Life system modeling and simulation
LYBIN: Range-dependent ray-theoretical propagation model
MATLAB: Matrix Laboratory (Mathworks, Inc.)
MCM: Mine countermeasures
METOC: Meteorology and oceanography
MINEOS: MSASM interactive execution and optimization system
MMPA: Marine Mammal Protection Act
MMS: Minerals Management Service
MOC3D: 3D Version of MOCASSIN
MOCASSIN: Monte Carlo Schall-Strahlen Intensitäten (Monte Carlo Sound Ray Intensities)
MOD: Ministry of Defence
MODRAY: Maritime Operations Division Ray-tracer
MONM: Marine Operations Noise Model
MONM3D: 3D PE Model for MONM
MONOGO: Reverberation Module in SWAMI
M&S: Modeling and Simulation
MTS: Marine Technology Society
MURAL: Multistatic reverberation algorithm
$N \times 2D$: Quasi-3D modeling approach
NATO: North Atlantic Treaty Organization
NEMO: NUWC Exposure Model
NEPA: National Environmental Policy Act
NGDC: National Geophysical Data Center
NMFS: National Marine Fisheries Service
NOAA: National Oceanic and Atmospheric Administration
NOGRP: Fast normal mode (monostatic) reverberation model
NSPE: Navy Standard Parabolic Equation
NTNU: Norwegian University of Science and Technology
NURC: NATO Undersea Research Centre (formerly SACLANTCEN)

NUSC: Naval Underwater Systems Center (now NUWC)
NUWC: Naval Undersea Warfare Center (formerly NUSC)
OASES: Ocean acoustics and seismic exploration synthesis
OASES-3D: Version of OASES incorporating 3D scattering effects
OBIS: Ocean biogeographic information system
OCS: Outer continental shelf
ONR: Office of Naval Research
OWWE: One-way wave equation
PAREQ: Parabolic equation model
PAREQ-REV: Reverberation using the PAREQ parabolic equation model
PDF: Probability density (or distribution) function
PDPE: Pseudo-differential PE
PE: Parabolic equation
PERM-2D: Reverberation model
PlaneRay: Eigenray Model for range-dependent environments
PMODES: Range-independent normal-mode transmission-loss module in SWAMI
POPP: Range-independent version of PROLOS
PWRC: Plane wave reflection coefficient
RAM: Range-dependent acoustic model
RAMGEO: RAM modified for range-dependent sediment layers
Ray5: Range-dependent ray model
RAYSON: Range-dependent ray-theoretic model for high frequencies
RDS: Rapidly deployable system
REA: Rapid environmental assessment
REVPA: Parabolic-equation reverberation model
RITSHPA: Reverberation including the statistics of hybrid path arrivals
RMPE: Ray-Mode Parabolic Equation Model
ROSELLA: Extension of NOGRP to handle beam patterns
ROV: Remotely operated vehicle
R-SNAP: Coherent monostatic reverberation model
SABLE: Sonar active boundary loss estimation
SACLANT: Supreme Allied Commander, Atlantic
SACLANTCEN: SACLANT Undersea Research Centre
SIAM: Simulated ambient noise model
SIGBED: Special Interest Group on Embedded Systems (ACM)
SPPS: Sonar performance prediction system
S-SCARAB: SACLANTCEN-scattering reverberation and backscatter
SSF: Split-step Fourier
SSFEPE: SSF PE Model
SSPPE: Split-step Padé PE model
STB: System test bed
SUPREMO: Multistatic sonar model
SWAMI: Shallow Water Active-Sonar Modelling Initiative
SWAMP: Shallow Water Acoustic Modal Propagation
SWSS: Sperm Whale Seismic Study
TDA: Tactical decision aid
TIAPS: Towed integrated active-passive sonar
TRM: Time-reversal mirror
TTS: Temporary threshold shift
UAIM: Underwater acoustic imaging model
UDT: Undersea defence technology
USWTR: Undersea warfare training range
UUV: Unmanned undersea vehicle
WHOI: Woods Hole Oceanographic Institution
WKB: Wentzel, Kramers, and Brillouin
WUWNet: Workshop on Underwater Networks
XRAY: Range-dependent ray theoretical model combined with full-field modeling of seabed interactions.

References

[1] K. D. LePage, P. Neumann, and C. W. Holland, "Broad-band time domain modeling of sonar clutter in range dependent waveguides," in *in Proceedings of the MTS/IEEE Oceans 2006 Conference (OCEANS'06)*, Boston, Mass, USA, September 2006.

[2] I. F. Akyildiz, D. Pompili, and T. Melodia, "Challenges for efficient communication in underwater acoustic sensor networks," *ACM SIGBED Review*, vol. 1, no. 2, pp. 3–8, 2004.

[3] I. F. Akyildiz, D. Pompili, and T. Melodia, "Underwater acoustic sensor networks: research challenges," *Ad Hoc Networks*, vol. 3, no. 3, pp. 257–279, 2005.

[4] D. Frye, L. Freitag, R. Detrick et al., "An acoustically linked moored-buoy ocean observatory," *EOS, Transactions, American Geophysical Union*, vol. 87, no. 22, pp. 213–218, 2006.

[5] Z. Han, Y. L. Sun, and H. Shi, "Cooperative transmission for underwater acoustic communications," in *Proceedings of the IEEE International Conference on Communications, (ICC '08)*, pp. 2028–2032, Beijing, China, 2008.

[6] V. Chandrasekhar, W. K. G. Seah, Y. S. Choo, and H. V. Ee, "Localization in underwater sensor networks—survey and challenges," in *Proceedings of the 1st ACM International Workshop on Underwater Networks (WUWNet'06)*, pp. 33–40, Los Angeles, Calif, USA, September 2006.

[7] J. Wang, P. Cai, and D. Yuan, "An underwater acoustic channel simulator for UUV communication performance testing," in *Proceedings of the IEEE International Conference on Information and Automation*, pp. 2286–2290, Harbin, China, 2010.

[8] J. G. Graver, *Underwater gliders: dynamics, control and design*, PhD dissertation, Department of Mechanical and Aerospace Engineering, Princeton University, Princeton, NJ, USA, 2005.

[9] A. Jochens, D. Biggs, D. Engelhaupt et al., "Sperm whale seismic study in the Gulf of Mexico," Summary Report, 2002–2004 OCS Study MMS 2006-034, US Department of the Interior, Minerals Management Service, Gulf of Mexico OCS Region, New Orleans, La, USA, 2006.

[10] A. Thode, D. K. Mellinger, S. Stienessen, A. Martinez, and K. Mullin, "Depth-dependent acoustic features of diving sperm whales (*Physeter macrocephalus*) in the Gulf of Mexico," *Journal of the Acoustical Society of America*, vol. 112, no. 1, pp. 308–321, 2002.

[11] W. M. Carey and R. B. Evans, *Ocean Ambient Noise: Measurement and Theory*, Springer, New York, NY, USA, 2011.

[12] R. K. Andrew, B. M. Howe, J. A. Mercer, and M. A. Dzieciuch, "Ocean ambient sound: comparing the 1960s with the 1990s for a receiver off the California coast," *Acoustic Research Letters Online*, vol. 3, pp. 65–70, 2002.

[13] M. A. McDonald, J. A. Hildebrand, and S. M. Wiggins, "Increases in deep ocean ambient noise in the Northeast Pacific west of San Nicolas Island, California," *Journal of the Acoustical Society of America*, vol. 120, no. 2, pp. 711–718, 2006.

[14] M. A. McDonald, J. A. Hildebrand, S. M. Wiggins, and D. Ross, "A 50 year comparison of ambient ocean noise near San Clemente Island: a bathymetrically complex coastal region off Southern California," *Journal of the Acoustical Society of America*, vol. 124, no. 4, pp. 1985–1992, 2008.

[15] J. Nedwell and D. Howell, "A review of offshore windfarm related underwater noise sources," Report 544R0308, Subacoustech Ltd, commissioned by COWRIE (Collaborative Offshore Wind Research Into the Environment), Hampshire, UK, 2004.

[16] D. Rouseff and D. Tang, "Internal waves as a proposed mechanism for increasing ambient noise in an increasingly acidic ocean," *Journal of the Acoustical Society of America*, vol. 127, no. 6, pp. EL235–EL239, 2010.

[17] E. McCarthy, *International Regulation of Underwater Sound: Establishing Rules and Standards to Address Ocean Noise Pollution*, Kluwer Academic Publishers, Dordrecht, The Netherlands, 2004.

[18] National Research Council, *Ocean Noise and Marine Mammals*, The National Academies Press, Washington, DC, USA, 2003.

[19] National Research Council, *Marine Mammal Populations and Ocean Noise: Determining When Noise Causes Biologically Significant Effects*, The National Academies Press, Washington, DC, USA, 2005.

[20] J. F. Grassle, "The ocean biogeographic information system (OBIS): an on-line, worldwide atlas for accessing, modeling and mapping marine biological data in a multidimensional geographic context," *Oceanography*, vol. 13, no. 3, pp. 5–7, 2000.

[21] S. Finette, "Embedding uncertainty into ocean acoustic propagation models," *Journal of the Acoustical Society of America*, vol. 117, no. 3 I, pp. 997–1000, 2005.

[22] J. W. Lawson, "The use of sound propagation models to determine safe distances from a seismic sound energy source," Research Document 2009/060, Department of Fisheries and Oceans, Canadian Science Advisory Secretariat, 2009.

[23] P. C. Etter, *Underwater Acoustic Modeling and Simulation*, Spon Press, London, UK, 3rd edition, 2003.

[24] R.J. Howard, T. Foreman, and D. Clark, "Architectural and design considerations in propagation model selection and design, simulation interoperability standards organization," in *Proceedings of the Simulation Interoperability Workshop*, no. 00S-SIW-054, 2000.

[25] F. C. Newman, A. C. Biondo, M. D. Mandelberg, C. C. Matthews, and J. R. Rottier, "Enhancing realism in computer simulations: environmental effects," *Johns Hopkins APL Technical Digest*, vol. 23, no. 4, pp. 443–453, 2002.

[26] J. Collins, T. Foreman, and D. Speicher, "A new design for a sonar environmental effects server," in *Proceedings of the Simulation Interoperability Workshop*, no. 02F-SIW-114, Simulation Interoperability Standards Organization, 2002.

[27] T. Foreman and D. Speicher, "Expanded sonar environmental acoustic effects server capabilities for fleet battle experiments," in *Proceedings of the Simulation Interoperability Workshop*, no. 03F-SIW-062, Simulation Interoperability Standards Organization, 2003.

[28] J. B. Collins and C. G. Scannell, "Natural environment data services in distributed modeling and simulation," in *Net-Centric Approaches to Intelligence and National Security*, R. Ladner and F. E. Petry, Eds., pp. 149–174, Springer, New York, NY, USA, 2005.

[29] J. M. Hovem, "PlaneRay: an acoustic underwater propagation model based on ray tracing and plane-wave reflection coefficients," FFI-rapport 2008/00610, Forsvarets forskningsinstitutt/Norwegian Defence Research Establishment (FFI), 2008.

[30] J. M. Hovem, S. Yan, X. Bao, and H. Dong, "Modeling underwater communication links," in *Proceedings of the 2nd International Conference on Sensor Technologies and Applications (SENSORCOMM '08)*, pp. 679–686, IEEE Computer Society, 2008.

[31] J. M. Hovem and H. Dong, "PlaneRay: an underwater acoustic propagation model using ray tracing and plane wave reflection coefficients," *Journal of the Acoustical Society of America*, vol. 120, p. 3221, 2006.

[32] J. M. Hovem and D. P. Knobles, "A range-dependent propagation model based on a combination of ray theory and plane-wave reflection coefficients," *Journal of the Acoustical Society of America*, vol. 112, p. 2393, 2002.

[33] J. M. Hovem and D. P. Knobles, "A range dependent propagation model based on a combination of ray theory and plane wave reflection coefficients," in *Proceedings of the 10th International Congress on Sound and Vibration*, pp. 2593–2600, Stockholm, Sweden, July 2003.

[34] S. A. Stotts, D. P. Knobles, R. A. Koch, D. E. Grant, K. C. Focke, and A. J. Cook, "Geoacoustic inversion in range-dependent ocean environments using a plane wave reflection coefficient approach," *Journal of the Acoustical Society of America*, vol. 115, no. 3, pp. 1078–1102, 2004.

[35] U. Kristiansen, "Sound propagation in regions of variable oceanography—a summary of student work at NTNU," FFI-rapport 2010/00812, Norwegian Defence Research Establishment, 2010.

[36] H.S. Olsen, "Lydutbredelse i havområder med avstandsavhengig oseanografi," Norges teknisk-naturvitenskapelige universitet, Institutt for elektronikk og telekommunikasjon, Trondheim, Norway, 2008.

[37] T. S. Semantic, "RAYSON: underwater acoustic rays software," Product description literature, Semantic TS , Sanary, France, 2002.

[38] C. Viala, C. Noël, and G. Lapierre, "RAYSON: a real time underwater communication simulator and performance estimator," in *Proceedings of the 7th French Workshop on Underwater Acoustics*, Brest, France, 2004.

[39] C. Viala, C. Noël, Y. Stéphan, and M. Asch, "Real-time geoacoustic inversion of large band signals," in *Proceedings of the IEEE Oceans 2005 Europe Conference*, pp. 1392–1395, Brest, France, 2005.

[40] C. Viala, C. Noël, Y. Stéphan, and M. Asch, "Real-time geoacoustic inversion of broad band signals in deep water,"

in *Proceedings of the Caractérisation du Milieu Marin (CMM'06)*, Brest, France, 2006.

[41] E. Svensson, I. Karasalo, and J.-P. Hermand, "Hybrid raytrace modelling of an underwater acoustics communication channel," in *Proceedings of the 7th European Conference on Underwater Acoustics*, pp. 1211–1216, Delft, The Netherlands, 2004.

[42] D. D. Ellis, "A two-ended shooting technique for calculating normal modes in underwater acoustic propagation," DREA Report 85/105, Defence Research Establishment Atlantic, Nova Scotia, Canada, 1985.

[43] S. A. Stotts, D. P. Knobles, and R.A. Koch, "Scattering in a Pekeris waveguide from a rough bottom using a two-way coupled mode approach," *Journal of the Acoustical Society of America*, vol. 129, no. 5, pp. EL172–EL178, 2011.

[44] N. A. Sidorovskaia, "A new normal mode program SWAMP as a tool for modeling scattering effects in oceanic waveguides," in *Modelling and Experimental Measurements in Acoustics III*, D. Almorza, C. A. Brebbia, and R. Hernandez, Eds., pp. 267–275, WIT Press, Southampton, UK, 2003.

[45] N. A. Sidorovskaia, "Systematic studies of pulse propagation in ducted oceanic waveguides in normal mode representation," *The European Physical Journal, Applied Physics*, vol. 25, no. 2, pp. 113–131, 2004.

[46] I. M. Tamendarov and N. A. Sidorovskaia, "Unified acoustic model for simulating propagation and scattering effects in oceanic waveguides," *Journal of the Acoustical Society of America*, vol. 116, p. 2527, 2004.

[47] C. A. Clark, "Acoustic wave propagation in horizontally variable media," *IEEE Journal of Oceanic Engineering*, vol. 30, no. 1, pp. 188–197, 2005.

[48] H. Schmidt, A. Maguer, E. Bovio et al., "Generic oceanographic array technologies (GOATS) '98 – Bistatic seabed scattering measurements using autonomous underwater vehicles," Report SR-302, SACLANT Undersea Research Centre, La Spezia, Italy, 1998.

[49] H. Schmidt, I. Veljkovic, and M. Zampolli, "Bistatic scattering from buried targets in shallow water—experiment and modelling," in *Proceedings of the 7th European Conference on Underwater Acoustics*, Delft, The Netherlands, 2004.

[50] H. Schmidt, "Bistatic scattering from buried targets in shallow water," in *Proceedings of the Autonomous Underwater Vehicle and Ocean Modelling Networks (GOATS'00)*, E. Bovio, R. Tyce, and H. Schmidt, Eds., no. CP-46, SACLANT Undersea Research Centre, 2001.

[51] H. Schmidt, "OASES Version 3.1 user guide and reference manual," Department of Ocean Engineering, Massachusetts Institute of Technology, Cambridge, Mass, USA, 2004.

[52] D. J. Thomson and N. R. Chapman, "WIDE-angle split-step algorithm for the parabolic equation," *Journal of the Acoustical Society of America*, vol. 74, no. 6, pp. 1848–1854, 1983.

[53] T. F. Duda, "Initial results from a Cartesian three-dimensional parabolic equation acoustical propagation code," Tech. Rep. WHOI-2006-14, Woods Hole Oceanographic Institution, Woods Hole, Mass, USA, 2006.

[54] L. Y. S. Chiu, Y.-T. Lin, C.-F. Chen, T. F. Duda, and B. Calder, "Focused sound from three-dimensional sound propagation effects over a submarine canyon," *Journal of the Acoustical Society of America*, vol. 129, no. 6, pp. EL260–EL266, 2011.

[55] M. E. Austin and N. R. Chapman, "The use of tessellation in three-dimensional parabolic equation modeling," *Journal of Computational Acoustics*, vol. 19, pp. 221–239, 2011.

[56] D. Mikhin, "Exact discrete nonlocal boundary conditions for high-order Padé parabolic equations," *Journal of the Acoustical Society of America*, vol. 116, no. 5, pp. 2864–2875, 2004.

[57] O. A. Godin, "Reciprocity and energy conservation within the parabolic approximation," *Wave Motion*, vol. 29, no. 2, pp. 175–194, 1999.

[58] L. T. Fialkowski, J. F. Lingevitch, J. S. Perkins, D. K. Dacol, and M. D. Collins, "Geoacoustic inversion using a rotated coordinate system and simulated annealing," *IEEE Journal of Oceanic Engineering*, vol. 28, no. 3, pp. 370–379, 2003.

[59] L. Zhang, L. Da, and Y. Zhou, "A new ocean acoustic model in computational oceanographic physics," in *in Proceedings of the International Conference on Computational Intelligence and Software Engineering, CiSE'09*, Wuhan, China, December 2009.

[60] F. Sturm and J. A. Fawcett, "On the use of higher-order azimuthal schemes in 3-D PE modeling," *Journal of the Acoustical Society of America*, vol. 113, no. 6, pp. 3134–3145, 2003.

[61] F. Sturm, "Examination of signal dispersion in a 3-D wedge-shaped waveguide using 3DWAPE," *Acta Acustica United with Acustica*, vol. 88, no. 5, pp. 714–717, 2002.

[62] F. Sturm, "Numerical study of broadband sound pulse propagation in three-dimensional oceanic waveguides," *Journal of the Acoustical Society of America*, vol. 117, no. 3 I, pp. 1058–1079, 2005.

[63] W. Renner, "User's guide for the ANDES model," Tech. Rep. version 4.2, Science Applications International Corp., 1995.

[64] M. Moll, R. M. Zeskind, and W. L. Scott, "An algorithm for beam noise prediction," Report 3653, Bolt, Beranek and Newman, 1979.

[65] J. Arvelo, "Array response advanced modal integrated simulator (ARAMIS) user's guide, STX-98-010," Johns Hopkins Applied Physics Laboratory, Laurel, Md, USA, 1998.

[66] J. R. Nedwell, J. Lovell, and A. W. H. Turnpenny, "Experimental validation of a species-specific behavioral impact metric for underwater noise," *Journal of the Acoustical Society of America*, vol. 118, p. 2019, 2005.

[67] BMT Cordah EIA and Environmental Services, *Offshore Renewables. Noise Assessment and Modelling, Product Description Literature*, Aberdeen, UK, 2010.

[68] M. H. Laurinolli, C. D. S. Tollefsen, S. A. Carr, and S. P. Turner, "Assessment of the effects of underwater noise from the proposed Neptune LNG project. Part (3): noise sources of the Neptune project and propagation modeling of underwater noise," LGL Report TA4200-3, JASCO Research Ltd for LGL Ltd, Ontario, Canada, 2005.

[69] S. W. Marshall and J. J. Cornyn, "Ambient-noise prediction. Vol. 1–Model of low-frequency ambient sea noise," Report 7755, Naval Research Laboratory, Washington, DC, USA, 1974.

[70] S. W. Marshall and J. J. Cornyn, "Ambient-noise prediction. Vol. 2–Model evaluation with IOMEDEX data," Report 7756, Naval Research Laboratory, Washington, DC, USA, 1974.

[71] Science Applications Inc., "Review of models of beam-noise statistics," SAI-78-696-WA, McLean, Va, USA, 1977.

[72] D. Long, "FANM/SIAM noise plot program," Ocean Data Systems Inc., Rockville, Md, USA, 1974.

[73] R. J. Urick, *Principles of Underwater Sound*, McGraw-Hill, New York, NY, USA, 3rd edition, 1983.

[74] J. W. Choi, K.-S. Yoon, J. Na, J.-S. Park, and Y.N. Na, "Shallow water high-frequency reverberation model," *Journal of the Acoustical Society of Korea*, vol. 21, pp. 671–678, 2002 (Korean).

[75] D.D. Ellis, *Measurements and Analysis of Reverberation and Clutter Data*, DRDC Atlantic ECR 2007-065, Defence Research and Development Canada, Atlantic, 2007.

[76] D. D. Ellis, "Normal-mode models OGOPOGO and NOGRP applied to the 2006 ONR reverberation modeling workshop

problems," DRDC Atlantic TM 2006-289, Defence Research and Development Canada, Atlantic, 2008.

[77] J. F. Lingevitch, "A parabolic equation method for modeling rough interface reverberation," in *Proceedings of the International Symposium on Underwater Reverberation and Clutter*, P. L. Nielsen, C. H. Harrison, and J.-C. LeGac, Eds., Lerici, Italy, 2008.

[78] M. D. Collins and R. B. Evans, "A two-way parabolic equation for acoustic backscattering in the ocean," *Journal of the Acoustical Society of America*, vol. 91, no. 3, pp. 1357–1368, 1992.

[79] F. A. Milinazzo, C. A. Zala, and G. H. Brooke, "Rational square-root approximations for parabolic equation algorithms," *Journal of the Acoustical Society of America*, vol. 101, no. 2, pp. 760–766, 1997.

[80] G. Bouchage and K. D. LePage, "A shallow-water reverberation PE model," *Acta Acustica United with Acustica*, vol. 88, no. 5, pp. 638–641, 2002.

[81] K. LePage, "Monostatic reverberation in range dependent waveguides: the R-SNAP model," Report SR-363, SACLANT Undersea Research Centre, La Spezia, Italy, 2003.

[82] M. K. Prior, C. H. Harrison, and K. D. LePage, "Reverberation comparisons between RSNAP, SUPREMO and analytical solutions," Report SR-361, SACLANT Undersea Research Centre, La Spezia, Italy, 2002.

[83] C. Harrison, "ARTEMIS: a fast general environment reverberation model," in *Proceedings of the International Symposium on Underwater Reverberation and Clutter*, P. L. Nielsen and C. H. Harrison and J.-C. LeGac, Eds., p. 2008, Lerici, Italy, 2008.

[84] K. LePage, "Bottom reverberation in shallow water: coherent properties as a function of bandwidth, waveguide characteristics, and scatterer distributions," *Journal of the Acoustical Society of America*, vol. 106, no. 6, pp. 3240–3254, 1999.

[85] K. D. LePage, "Bistatic reverberation modeling for range-dependent waveguides," *Journal of the Acoustical Society of America*, vol. 112, pp. 2253–2254, 2002.

[86] K. D. LePage and C. H. Harrison, "Bistatic reverberation benchmarking exercise: BiStaR versus analytic formulas," *Journal of the Acoustical Society of America*, vol. 113, pp. 2333–2334, 2003.

[87] K. D. LePage and C. Harrison, "Effects of refraction on the prediction of bistatic reverberation in range dependent shallow water waveguides," *Journal of the Acoustical Society of America*, vol. 114, p. 2302, 2003.

[88] D. M. Fromm, "A computationally efficient multistatic reverberation algorithm," *Journal of the Acoustical Society of America*, vol. 129, p. 2631, 2011.

[89] V. Marconi, P. L. Nielsen, and C. Holland, "S-SCARAB: SACLANTCEN-Scattering reverberation and backscatter user guide and reference manual, NURC/SM-418," NATO Undersea Research Centre, La Spezia, Italy, 2004.

[90] F.-P. A. Lam, N. J. Konijnendijk, J. Groen, and D. G. Simons, "Non-Rayleigh wideband sonar reverberation modeling including hybrid multi-paths," in *Proceedings of the The Oceans'06 MTS/IEEE-Boston Conference*, Boston, Mass, USA, 2006.

[91] D. A. Abraham and A. P. Lyons, "Simulation of non-Rayleigh reverberation and clutter," *IEEE Journal of Oceanic Engineering*, vol. 29, no. 2, pp. 362–374, 2004.

[92] E. Pouliquen, A. P. Lyons, and N. G. Pace, "The Helmholtz-Kirchhoff approach to modeling penetration of acoustic waves into rough seabeds," *Journal of the Acoustical Society of America*, vol. 104, p. 1762, 1998.

[93] G. Canepa and C. Berron, "Characterization of seafloor geoacoustic properties from multibeam data," in *Proceedings of the MTS/IEEE Oceans Conference*, Boston, Mass, USA, 2006.

[94] R. J. Soukup, G. Canepa, H. J. Simpson, J. E. Summers, and R. F. Gragg, "Small-slope simulation of acoustic backscatter from a physical model of an elastic ocean bottom," *Journal of the Acoustical Society of America*, vol. 122, no. 5, pp. 2551–2559, 2007.

[95] P. Staelens, *Defining and modeling the limits of high-resolution underwater acoustic imaging,*, Doctoral dissertation, Universiteit Gent, Belgium, 2009.

[96] P. Blondel and N. G. Pace, "Bistatic sonars: sea trials, laboratory experiments and future surveys," *Archives of Acoustics*, vol. 34, no. 1, pp. 95–109, 2009.

[97] G. L. Davies, "Project 03F–1: phase I completion report," Memo SM-399, SACLANT Undersea Research Centre, La Spezia, Italy, 2002.

[98] M. Meyer and G. L. Davies, "A beam-based high-frequency reverberation model," Report SR-365, SACLANT Undersea Research Centre, La Spezia, Italy, 2002.

[99] G. L. Davies and E. P. Signell, "Espresso—scientific user guide," Report NURC-SP-2006-003, NATO Undersea Research Centre, La Spezia, Italy, 2006.

[100] G. L. Davies and E. P. Signell, "Espresso(m)—user guide," Report NURC-SP-2006-002, NATO Undersea Research Centre, La Spezia, Italy, 2006.

[101] S. Mjølsnes, *LYBIN SGP-180(C)—Model Description*, The Royal Norwegian Navy Materiel Command, Bergen, Norway, 2000.

[102] K.T. Hjelmervik and G.H. Sandsmark, "In ocean evaluation of low frequency active sonar systems," in *Proceedings of the Acoustics '08 Conference*, pp. 2839–2843, Paris, France, 2008.

[103] E. Dombestein, A. Gjersøe, and M. Bosseng, "LybinCom 6.0—description of the binary interface," FFI-rapport 2009/02267, Forsvarets forskningsinstitutt/Norwegian Defence Research Establishment, 2010.

[104] C. M. Ferla, C. Isoppo, G. Martinelli, and F. B. Jensen, "Performance assessment of the LYBIN-2.0 propagation-loss model," Memo SM-384, SACLANT Undersea Research Centre, La Spezia, Italy, 2001.

[105] S. M. Ivansson, "Stochastic ray-trace computations of transmission loss and reverberation in 3-D range-dependent environments," in *Proceedings of the 8th European Conference on Underwater Acoustics*, pp. 131–136, Carvoeiro, Portugal, 2006.

[106] H. G. Schneider, "MOCASSIN: sound propagation and sonar range prediction model for shallow water environments. User's guide," Tech. Rep. 1990–9, Forschungsanstalt der Bundeswehr für Wasserschall- und Geophysik, Kiel, Germany, 1990.

[107] F. Sturm, S. Ivansson, Y.-M. Jiang, and N. R. Chapman, "Numerical investigation of out-of-plane sound propagation in a shallow water experiment," *Journal of the Acoustical Society of America*, vol. 124, no. 6, pp. EL341–EL346, 2008.

[108] K. Frith, "MODRAY underwater sound simulator user manual, Version 5.0," Australia Department of Defence, Defence Science and Technology Organisation, Maritime Operations Division, Aeronautical and Maritime Research Laboratory, Edinburgh, South Australia, 2003.

[109] Ebor Computing, "MODRAY, product description literature," Mile End, South Australia, 2005.

[110] R. Alksne, "Rapidly deployable systems (RDS) underwater acoustic telemetry trials report," Tech. Rep. DSTO-TN-0259, Australia Department of Defence, Defence Science and

Technology Organisation, Maritime Operations Division, Aeronautical and Maritime Research Laboratory, Victoria, Australia, 2000.

[111] D. McCammon, "Active sonar modelling with emphasis on sonar stimulators," Report CR 2004-130 Defence Research and Development Canada—Atlantic, 2004.

[112] A. Baldacci and C. H. Harrison, "SUPREMO prototype version 01 user's guide, M-141," SACLANT Undersea Research Centre, La Spezia, Italy, 2002.

[113] C. H. Harrison, "Scattering strength uncertainty," *Journal of the Acoustical Society of America*, vol. 112, p. 2253, 2002.

[114] C. H. Harrison, "SUPREMO: a multistatic sonar performance model, Memo SM-396," SACLANT Undersea Research Centre, La Spezia, Italy, 2002.

[115] C. H. Harrison, "Closed-form expressions for ocean reverberation and signal excess with mode stripping and Lambert's law," *Journal of the Acoustical Society of America*, vol. 114, no. 5, pp. 2744–2756, 2003.

[116] M. K. Prior and A. Baldacci, "Comparison between predictions made by the SUPREMO sonar performance model and measured data," Report SR-429, SACLANT Undersea Research Centre, La Spezia, Italy, 2005.

[117] M. K. Prior, "SUPREMO v.2.0 user guide," Report NURC-FR-2007-009, NATO Undersea Research Centre, La Spezia, Italy, 2007.

[118] M. K. Prior, "SUPREMO v.2.0 program description," Report NURC-FR-2007-011, NATO Undersea Research Centre, La Spezia, Italy, 2007.

[119] J. A. Theriault and D. D. Ellis, "Shallow-water low-frequency active sonar modelling issues," in *Proceedings of the MTS/IEEE Oceans '97 Conference*, p. 678, 672, Halifax, Canada, 1997.

[120] J. A. Theriault, S. Pecknold, N. Collison, and C. Calnan, "Modelling multibeam reverberation with an N×2D model," in *Proceedings of the 8th European Conference on Underwater Acoustics*, Carvoeiro, Portugal, 2006.

[121] C. Calnan, "DMOS—Bellhop Extension," Tech. Rep. CR 2006-005, DRDC Atlantic, Defence Research and Development Canada—Atlantic, 2006.

[122] M. D. Wagstaff, R. W. Meredith, and H. A. Terrill-Stolper, "Multi-beam high frequency imaging in a range-dependent environment," in *Proceedings of the MTS/IEEE Oceans '97 Conference*, pp. 927–931, Halifax, Canada, 1997.

[123] M. A. Kalogerakis, E. K. Skarsoulis, J. S. Papadakis et al., "An integrated computer system for underwater acoustic detection analysis," in *Proceedings of the Undersea Defence Technology Conference, (UDT'04)*, Nice, France, 2004.

[124] H. J. Shyu and R. Hillson, "A software workbench for estimating the effects of cumulative sound exposure in marine mammals," *IEEE Journal of Oceanic Engineering*, vol. 31, no. 1, pp. 8–21, 2006.

[125] M. Siderius and M. B. Porter, "Modeling techniques for marine-mammal risk assessment," *IEEE Journal of Oceanic Engineering*, vol. 31, no. 1, pp. 49–60, 2006.

[126] "Applied Radar & Sonar Technologies GmbH, Sonar performance prediction system (SPPS)," product description literature, Bremerhaven, Germany, 2002.

[127] Applied Hydro-Acoustics Research Inc., "ASPECT user's guide," Version 2.0.1 Build 664, Centreville, VA, USA, 2001.

[128] A. S. Frankel, W. T. Ellison, and J. Buchanan, "Application of the Acoustic Integration Model (AIM) to predict and minimize environmental impacts," in *in Proceedings of the MTS/IEEE Oceans '02 Conference*, pp. 1438–1443, Biloxi, Miss, USA, October 2002.

[129] D. S. Houser, "A method for modeling marine mammal movement and behavior for environmental impact assessment," *IEEE Journal of Oceanic Engineering*, vol. 31, no. 1, pp. 76–81, 2006.

[130] G. Haralabus and A. Baldacci, "Impact of seafloor and water column parameter variations on signal-to-background ratio estimates—a sensitivity analysis based on sonar performance modeling," in *Proceedings of the 8th European Conference on Underwater Acoustics, 2006*, Carvoeiro, Portugal.

[131] P. D. Ward, P. Varley, and T. Clarke, "Detecting marine mammals using active sonar—a theoretical consideration," in *Proceedings of the Institute of Acoustics*, vol. 26, part 6, no. Symposium on Bio-Sonar Systems and Bioacoustics, 2004.

[132] D. E. Weston, "Acoustic flux formulas for range-dependent ocean ducts," *Journal of the Acoustical Society of America*, vol. 68, no. 1, pp. 269–281, 1980.

[133] X. Lurton, *An Introduction to Underwater Acoustics: Principles and Applications*, Springer, New York, NY, USA, 2002.

[134] C. W. Holland, "Propagation in a waveguide with range-dependent seabed properties," *Journal of the Acoustical Society of America*, vol. 128, no. 5, pp. 2596–2609, 2010.

[135] M. G. Brown, F. J. Beron-Vera, I. Rypina, and I. A. Udovydchenkov, "Rays, modes, wavefield structure, and wavefield stability," *Journal of the Acoustical Society of America*, vol. 117, no. 3, pp. 1607–1610, 2005.

[136] K. L. Cockrell and H. Schmidt, "A relationship between the waveguide invariant and wavenumber integration," *Journal of the Acoustical Society of America*, vol. 128, no. 1, pp. EL63–EL68, 2010.

[137] R. McHugh, D. McLaren, M. Wilson, and R. Dunbar, "The underwater environment—a fluctuating acoustic medium rich in marine life. Implications for active military sonar," *Acta Acustica United with Acustica*, vol. 91, no. 1, pp. 51–60, 2005.

[138] G. B. Deane and M. D. Stokes, "Model calculations of the underwater noise of breaking waves and comparison with experiment," *Journal of the Acoustical Society of America*, vol. 127, no. 6, pp. 3394–3410, 2010.

[139] W. E. Brown and M. L. Barlett, "Midfrequency 'through-the-sensor' scattering measurements: a new approach," *IEEE Journal of Oceanic Engineering*, vol. 30, no. 4, pp. 733–747, 2005.

[140] E. Delory, M. André, J. L. Navarro Mesa, and M. Van Der Schaar, "On the possibility of detecting surfacing sperm whales at risk of collision using others' foraging clicks," *Journal of the Marine Biological Association of the United Kingdom*, vol. 87, no. 1, pp. 47–58, 2007.

[141] J.-P. Hermand, M. Meyer, M. Asch, and M. Berrada, "Adjoint-based acoustic inversion for the physical characterization of a shallow water environment," *Journal of the Acoustical Society of America*, vol. 119, no. 6, pp. 3860–3871, 2006.

[142] M. Meyer and J.-P. Hermand, "Backpropagation techniques in ocean acoustic inversion: time reversal, retrogation and adjoint modeling—a review," in *Acoustic Sensing Techniques for the Shallow Water Environment: Inversion methods and experiments*, A. Caiti, N. R. Chapman, J.-P. Hermand, and S.M. Jesus, Eds., pp. 29–46, Springer, New York, NY, USA, 2006.

[143] P. Hursky, M. B. Porter, B. D. Cornuelle, W. S. Hodgkiss, and W. A. Kuperman, "Adjoint modeling for acoustic inversion," *Journal of the Acoustical Society of America*, vol. 115, no. 2, pp. 607–619, 2004.

[144] L. Gammaitoni, P. Hänggi, P. Jung, and F. Marchesoni, "Stochastic resonance," *Reviews of Modern Physics*, vol. 70, no. 1, pp. 223–287, 1998.

[145] H. Zhang, B. Xu, Z.-P. Jiang, and X. Wu, "Target detection in shallow-water reverberation based on parameter-induced stochastic resonance," *Journal of Physics A*, vol. 41, no. 10, Article ID 105003, 2008.

[146] B. Xu, L. Zeng, and J. Li, "Application of stochastic resonance in target detection in shallow-water reverberation," *Journal of Sound and Vibration*, vol. 303, no. 1-2, pp. 255–263, 2007.

[147] A. V. van Leijen, *The sound of sediments: acoustic sensing in uncertain environments*, PhD dissertation, Universiteit van Amsterdam, The Netherlands, 2010.

[148] B. B. Thompson, R. J. Marks, M. A. El-Sharkawi, W. J. Fox, and R. T. Miyamoto, "Inversion of neural network underwater acoustic model for estimation of bottom parameters using modified particle swarm optimizers," in *in Proceedings of the IEEE International Joint Conference on Neural Networks*, pp. 1301–1306, Portland, Ore, USA, July 2003.

[149] Z.-H. Michalopoulou and U. Ghosh-Dastidar, "Tabu for matched-field source localization and geoacoustic inversion," *Journal of the Acoustical Society of America*, vol. 115, no. 1, pp. 135–145, 2004.

[150] F. Glover and M. Laguna, *Tabu Search*, Kluwer Academic Publishers, Dordrecht, The Netherlands, 1997.

[151] A. L. Virovlyansky, "Signal travel times along chaotic rays in long-range sound propagation in the ocean," *Acoustical Physics*, vol. 51, no. 3, pp. 271–281, 2005.

[152] D. V. Makarov, M. Y. Uleysky, and S. V. Prants, "Ray chaos and ray clustering in an ocean waveguide," *Chaos*, vol. 14, no. 1, pp. 79–95, 2004.

[153] D. Makarov, S. Prants, A. Virovlyansky, and G. Zaslavsky, *Ray and Wave Chaos in Ocean Acoustics: Chaos in Waveguides*, World Scientific Publishing, Singapore, 2010.